STRUCTURAL BASIS OF KEY CONSERVED CELL-SURFACE SIGNALING PATHWAYS INVOLVED IN IRON IMPORT

A Dissertation
Submitted to the Graduate Faculty
of the
North Dakota State University
of Agriculture and Applied Science

By

Beau Dalton Jernberg

In Partial Fulfillment of the Requirements
for the Degree of
DOCTOR OF PHILOSOPHY

Major Department:
Chemistry and Biochemistry

May 2023

Fargo, North Dakota

North Dakota State University
Graduate School

Title

Structural Basis of Key Conserved Cell-Surface Signaling Pathways Involved in Iron Import

By

Beau Dalton Jernberg

The Supervisory Committee certifies that this ***disquisition*** complies with North Dakota State University's regulations and meets the accepted standards for the degree of

DOCTOR OF PHILOSOPHY

SUPERVISORY COMMITTEE:

Christopher Colbert, Ph.D.
Chair

Sangita Sinha, Ph.D.

Glenn Dorsam, Ph.D.

Zhongyu Yang, Ph.D.

Approved:

April 12, 2024
Date

Gregory Cook, Ph.D.
Department Chair

ABSTRACT

Cell surface signaling (CSS) allows Gram-negative bacteria to transcriptionally regulate gene expression in response to external stimuli. CSS pathways involve three key components: an outer membrane transducer for sensing the extracellular stimuli; an inner membrane sigma regulator for relaying the signal; and a cytoplasmic sigma factor, which activates transcription of target genes. The goal of this research was to structurally and biophysically characterize events leading to the processing of the sigma regulator that results in transcription activation. Our model systems are the *Pseudomonas capeferrum* BN7/8 (Pup) and *Escherichia coli* ferric citrate (Fec) uptake pathways.

We detail the X-ray crystal structure of the N-terminal signaling domain (NTSD) of the transducer, PupB, complexed with the C-terminal cell-surface signaling domain (CCSSD) of the sigma regulator, PupR. Stabilization of the PupR CCSSD by the PupB NTSD provides a rationale for the formation of a preformed CSS complex. Additionally, we probed the FecR CCSSD and FecA NTSD interaction and observed similarities. We found the FecA NTSD complexes with the FecR CCSSD and stabilizes the domain in nonsignaling conditions indicating a conserved mechanism.

Further, we show that access to the PupR CCSSD is only possible in the absence of the PupB NTSD. Pulldown assays, isothermal titration calorimetry, protease assays, and mass spectrometry analysis demonstrate the site-1 protease, Prc, only recognizes and degrades PupR in the absence of the PupB NTSD. X-ray crystal structures of Prc mutants and potential product peptides reveal transitions between “closed” and “open” conformations as well as catalytic intermediates in the protease active site. Size exclusion small angle X-ray scattering data

confirms the Prc conformations in solution and an elongated molecular envelope of the Prc:PupR complex. Together this provides new structural insights into protease activation during CSS.

Finally, we studied the TonB C-terminal domain of *P. capeferrum* by size exclusion small angle X-ray scattering. Our results indicate it forms a monomeric structure in solution.

Overall, our results indicate there is a conserved CSS pathway that has been characterized by our individual signal transduction states. Thus, we have provided novel implications in ferric siderophore uptake and the mechanism of iron import mediated CSS.

ACKNOWLEDGMENTS

I am extremely thankful to my dissertation advisor, Dr. Christopher Colbert. Without his continued advice, support, and exceptional experimental knowledge, I would not be the scientist I am today. He constructed many opportunities to learn through conferences and workshops. He also promoted following my curiosity into different research projects, some of which became the core of my graduate work. I'm very happy with my body of work, none of which would've been possible without Dr. Colbert's help.

Additionally, I am grateful to Dr. Sangita Sinha for her immense pool of knowledge and expertise that has been extremely influential on my professional goals. Learning the ins and outs of being a scientist and the ability to critically think about science from her has been a joy over the years. Dr. Sinha provided many resources for my projects and advice that rounded out my work.

My appreciation goes out to my other committee members, Dr. Zhongyu Yang, Dr. Sheela Ramamoorthy, and Dr. Glenn Dorsam. They have all been supportive of my research and aiding in the goal of achieving my PhD. The questions and viewpoints have been extremely valuable and are much appreciated.

Another big thank you goes to my lab mates who were always prepared to troubleshoot problems, run to the convenience store, and vent over a quesadilla. Dr. Jaime Jensen, Dr. Karen Glover, Dr. Yue Li, Dr. Shreya Mukhopadhyay, Dr. Shane Wyborny, Dr. Srini Dasanna, Dr. David Morgan, Dr. Elizabeth Bueno, Ben, Sam, Tajnin, Victor, Robyn, Robin, Subeksha, Tyeaba, Amanda, and Emily all made the lab a great place to learn and have a few laughs along the way.

Finally, I would like to thank all my friends and family that supported me and kept me sane throughout this process. I'm very lucky to have all of you in my life and couldn't have done it without you.

DEDICATION

For my wife, who provided her unending patience, unconditional love, and uncanny ability to put up with me

For my parents and family members, who always loved and encouraged me to be my best

For my grandparents, who have always been great role models in life

"Be aware that there are endless opportunities that occur throughout life. Accept those that appear feasible. Others will emerge if you dedicate your complete effort to their development"

- Dr. Phillip Harein

TABLE OF CONTENTS

LIST OF TABLES

LIST OF FIGURES

Figure Page

LIST OF ABBREVIATIONS

APS ..... Advanced Photon Source

ASD ..... Anti-sigma domain

$CC_{1/2}$ ..... Pearson correlation coefficient between random half-datasets

CCSSD ..... C-terminal cell-surface signaling domain

CD ..... Circular dichroism

CJM ..... C-terminal juxtamembrane

CSS ..... Cell-surface signaling

CTD ..... C-terminal domain

Da ..... Dalton

Dmax ..... maximum dimension

DNA ..... Deoxyribonucleic acid

DTT ..... dithiothreitol

ECF ..... Extracytoplasmic function

FC-13 ..... Fos-choline 13

FNorm ..... Normalized fluorescence change

GSH ..... Glutathione Sepharose

GST ..... Glutathione S-transferase

HEPES ..... 4-(2-hydroxyethyl)-1-piperazineethanesulfonic acid

HRP ..... Horseradish peroxidase

IPTG ..... Isopropyl β-D-1-thiogalactopyranoside

ITC ..... Isothermal titration calorimetry

kDa ..... kilodalton

LB ..... Luria Bertani

LPS ..... Lipopolysaccharide

MBP ..... Maltose binding protein

MR ..... Molecular replacement

MW ..... Molecular weight

MWCO ..... Molecular weight cutoff

NMR ..... Nuclear magnetic resonance

NTD ..... N-terminal domain

NTSD ..... N-terminal signaling domain

OM ..... Outer membrane

PCR ..... Polymerase chain reaction

PDB ..... Protein data bank

PDZ ..... PSD95, Dlg1, zo-1 domain

PEG ..... Polyethylene glycol

PMF ..... Proton motive force

R_{free} ..... Free R-factor

RIP ..... Regulated intramembrane proteolysis

RMSD ..... Root-mean-square deviation

R_{work} ..... Working R-factor

SAXS ..... Small-angle X-ray scattering

SDS-PAGE ..... Sodium dodecyl sulfate polyacrylamide gel electrophoresis

SEC ..... Size exclusion chromatography

SeMet ..... Selenomethionine

STN ..... Secretin and TonB N-terminus short domain

TBDT ..... TonB-dependent transducer

TEV ..... Tobacco etch virus

WT ..... Wild type

LIST OF SYMBOLS

g.....relative centrifugal force (RCF)

I(0)..... scattering intensity at zero-angle

I ..... scattering intensity

I/σI..... signal-to-noise ratio

K_d ..... dissociation constant

mAU.....milli-absorbance units

P(r).....pairwise-distance distribution function

q..... momentum transfer

R_g.....radius of gyration

T_m ..... melting temperature

ΔG ..... change in Gibbs free energy

ΔH ..... change in enthalpy

ΔS .....change in entropy

ε..... extinction coefficient

θ..... angle between incident X-rays, or degree ellipticity

σ ..... transcriptional regulator (sigma factor)

χ.....chi value (goodness of fit)

Å.....angstrom

1. INTRODUCTION

1.1. Influences of Antibiotics

1.1.1. Gram-Negative Infections and our Counterattack

Infectious diseases have long wrought havoc on the world. Of these, a significant contribution can be attributed to Gram-negative bacteria. In the fourteenth century approximately 25 million people in Europe fell victim to the bubonic plague, caused by the Gram-negative bacteria *Yersinia pestis* [2]. A more recent example is Cholera. Millions of people are still affected by *Vibrio cholerae* infections each year, and 90,000+ succumb to the severe dehydration resulting from this infection [3]. Not only do Gram-negative infections pose a serious health risk but a substantial economic cost as well. However, the introduction of antibiotics has significantly aided in reducing both the medical and monetary costs of these infectious diseases. Pneumonia is no longer killing 30-40% of those infected and amputations from skin infections are far less common [4]. Invasive medical procedures are only possible due to the use of antibiotics in healthcare. Additionally, beyond direct healthcare uses, antimicrobials are a staple in many households and limit initial exposures.

The first antibiotic, penicillin, brought about a new era. The discovery, for which Fleming, Howard Florey, and Ernst Chain were awarded the Nobel Prize in 1945, set humanity down a new avenue to combat bacterial infections. Shortly after the discovery of penicillin, antibiotics such as streptomycin, erythromycin, and chloramphenicol began widespread distribution (Figure 1.1). In recent history, combinations of antibiotic cocktails targeting Gram-negative bacterial cell wall synthesis and inhibition of critical nucleic acid and protein synthesis rage a war against these bacterial infections [5]. However, overuse and over prescription of

antibiotics in today's day and age doesn't come without a cost. With use comes resistance, and an additional battle to be won against bacterial infections.

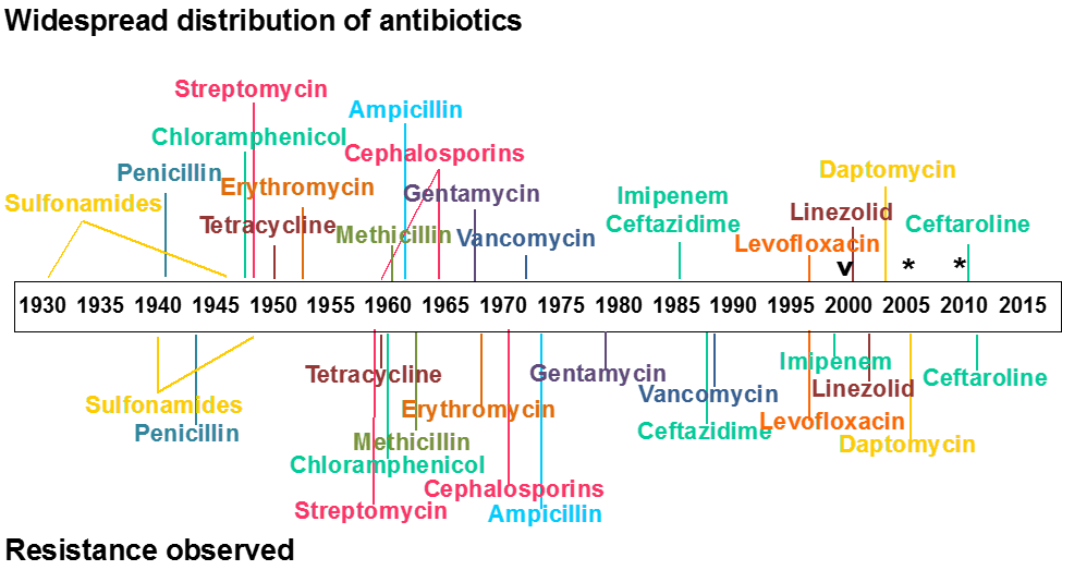

Figure 1.1. Timeline of the widespread distribution of antibiotics vs. resistance observed. (Adapted from [6]). **v** indicates observation of extensively drug-resistant organisms; ***** indicates observation of pan-drug-resistant organisms.

1.1.2. Antibiotic Resistance Mechanisms

Bacteria have an exceptional ability to evolve and overcome. Key examples include the multiple bacterial mechanisms of antibiotic resistance, such as decreased antibiotic permeability, alterations of target proteins, and modification of antibiotics to make them ineffective, and removal of antibiotics via efflux pumps [5, 7].

Modifications to antibiotic targets and importers reduce effectiveness of antibiotics. Mutations to OmpF, a non-specific porin, observed in *E. coli*, *K. pneumoniae*, and other Gram-negative bacteria resulted in a resistance to several β-lactams [8]. These modifications are not unique to OmpF. Mutations to the 30S or 50S subunit generate resistance to antibiotics such as chloramphenicol, macrolides, and aminoglycosides, which affect protein synthesis [9, 10]. Moreover, bacteria can produce enzymes that inactivate or destroy antibiotics. For example, β-

lactamases hydrolyze a substantial amount of β-lactams including penicillins, cephalosporins, monobactams, and carbapenems [5]. Aminoglycoside modifying enzymes reduce the binding affinity of antibiotics through molecule modifications [5].

Bacterial efflux pumps can remove both specific and a wide variety of antibiotics from the cell, decreasing intracellular concentrations [5]. Efflux pumps were first described in *E. coli* in the context of its resistance to tetracycline, and they have been widely observed since then. [11]. There are five major families of efflux pumps including the adenosine triphosphate-binding cassettes superfamily, resistance-nodulation-division family, small multidrug resistance family, major facilitator superfamily, and the multidrug and toxic compound extrusion family [11]. Thus, Gram-negative bacteria contain many diverse resistance mechanisms. Counting on the constant synthesis of new drugs to avoid these mechanisms does not appear to be a sustainable tactic. Therefore, novel approaches toward multidrug resistant bacteria is crucial.

1.2. Bacterial Survival

1.2.1. Evading Immune Response

Eukaryotic cells contain many effective means to deter infectious agents. Recognition of these various pathogens is accomplished by a wide field of pattern recognition receptors which detect pathogen-associated molecular patterns (PAMPs) and danger-associated molecular patterns (DAMPs) [12, 13]. PAMPs are structurally invariant features of pathogens that are recognized as a separate entity from the host cell [14]. Similar to PAMPs, DAMPs are recognized as danger signals to the host when found in abnormal cellular locations or molecular complexes under cellular stress [14]. Once recognized the host induces a diverse series of signaling pathways for the deterrence of potential infections. However, Gram-negative bacteria have many distinct mechanisms to evade the host immune response including modifications to the cell surface,

inhibiting host immune factors, and mimicking host molecules [15]. Bacterial lipopolysaccharides (LPS) are an example of a key PAMP associated with the Gram-negative bacteria cell wall [13]. The lipid region of LPSs, lipid A, is recognized by the Toll-like receptor 4:MD-2 complex, activating the host innate immune response [13]. A counter to this recognition is observed in *Y. pestis* as well as other bacterial species which deacylated lipid A, resulting in significantly lower recognition by immune systems [13, 15]. Another example of evasion includes the secretion of IgA proteases in *Neisserial* species which degrades IgA [15]. IgA is the most expressed immunoglobin that recognizes and binds infectious antigens, defending against many potentially harmful bacteria [16]. Despite such terrifyingly adept mechanisms of avoiding the immune response, ultimately bacterial survival is still dependent on their ability to acquire the appropriate nutrients for proliferation within the host.

1.2.2. Nutrient Acquisition

The ability to obtain and maintain vital nutrients in harsh conditions in crucial for bacterial survival. To do this, bacteria employ several techniques including passive diffusion through porins, changes in metabolism, and sequestering nutrients from host cells [17, 18]. Of the various important nutrients, iron is essential for cellular function and linked to cellular respiration, metabolism, and DNA replication [19]. Thus, numerous methods of obtaining iron from the environment is necessary. One interesting method includes stealing iron from host proteins via surface lipoproteins (SLPs). Many SLPs are present on the cell surface of Gram-negative bacteria, each exhibiting different functions including virulence, nutrient acquisition, and immune response evasion [20-22].The SLP, TbpB, is transcribed under iron-limiting conditions for binding of iron loaded transferrin [20]. Once bound, TbpB bound transferrin is handed off to its partner protein TbpA [23, 24]. TbpA, part of the TonB-dependent transporter/transducer (TBDT)

family, causes a conformational change in transferrin, destabilizing the transferrin bound iron for bacterial import [23]. Homologous SLPs, LbpB and HpuA, function in a similar manner through binding of lactoferrin and hemoglobin, respectively [23, 25].

Additionally, Gram-negative bacteria can utilize siderophores for iron chelation and uptake. Siderophores are low molecular weight molecules which bind iron with a high affinity [18]. Bacteria can utilize siderophore production for use as a virulence factor, as demonstrated in *E. coli* induced urinary tract infections, as well as for the scavenging of iron when bioavailability is low [18, 26]. For iron uptake, the iron loaded siderophore interacts with a TBDT for import into the cell with the aid of the TonB complex and the proton motive force (PMF) [27].

1.2.3. TonB-Dependent Iron Import

As previously mentioned, siderophore import initially involves binding to and travel through a TBDT [27]. TBDTs are widely distributed amongst Gram-negative bacteria and all have a homologous domain architecture composed of a 22-stranded β-barrel spanning the outer membrane and a plug domain filling the barrel (Figure 1.2) [1]. Siderophore interactions involve the extracellular side of the plug domain as well as the interior of the β-barrel domain and extracellular loops [1]. Individual binding sites are specific for each TBDT and binding of the unique siderophores. This is demonstrated by the aromatic binding residues of FhuA as compared to arginine residues found in FecA [1, 28-31]. Binding of the siderophore triggers a conformational change around the plug domain, leading to the extension of a short peptide region, termed the TonB box, into the periplasm (Figure 1.2) [1]. The TonB box is the site for interaction with TonB and coupling of the PMF through the TonB complex for siderophore import [1, 32].

The TonB complex is composed of the inner membrane anchored TonB, ExbB, and ExbD proteins [32, 33]. The exact stoichiometry of these proteins in the complex has yet to be fully established despite extensive structural investigations [34]. Additionally, the mechanism by which this complex utilizes the PMF is currently unknown. It seems that ExbB and ExbD work together and transfer this energy to TonB, applying a force to the TBDT and importing the ferric siderophore. Once in the periplasm, the siderophore may be reduced, releasing the iron [35, 36]. Released iron is bound by an ATP-binding cassette transporter for transport across the inner membrane [37]. Alternatively, ferric siderophores can bind ATP-binding cassette transporters for import into the cytoplasm and release of the iron [37, 38]. After translocation to the cytoplasm and reduction, iron can be incorporated into metalloproteins for use or storage [39].

Signaling and control of TBDT transcription is closely linked to siderophore transport. A feature unique to some TBDTs is the presence of a periplasmic N-terminal signaling domain (NTSD) (Figure 1.2). NTSDs are approximately 70-90 amino acids in length, containing a conserved βαβ-βαββ motif and a hydrophobic core [40-42]. Experimental studies of FecA indicate this domain is not essential for iron import [43, 44]. However, regulation of TBDT transcription is tightly associated with NTSD interactions with regulatory proteins in Gram-negative cell-surface signaling (CSS) pathways [44-46].

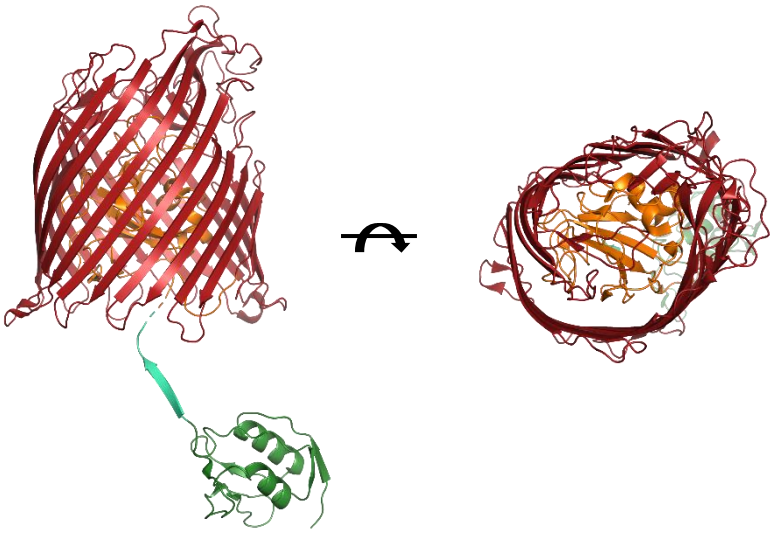

Figure 1.2. Structural domains of the TBDT from PDB 6I97. The N-terminal signaling domain (NTSD) (green), TonB box (cyan), plug domain (orange), and β-barrel domain (red) are represented in ribbons tracing the main chain. The β-barrel domain is located in the outer membrane with the plug domain blocking transport. The TonB box and NTSD extend into the periplasm for interaction with partner proteins.

1.3. TonB-Dependent Transducers and CSS

1.3.1. Cell-Surface Signaling

CSS is the process by which bacteria rapidly respond to extracellular stimuli via highly conserved pathways, transducing a signal to the cytoplasm. CSS pathways require three key proteins: an outer membrane TBDT, an inner membrane sigma regulator, and an extracytoplasmic (ECF) sigma factor (Figure 1.3) [1]. The TBDT senses extracellular signals and transmits them to the periplasm and imports extracellular signaling molecules. Once transduced to the periplasm, the sigma regulator transmits the signal into the cytoplasm. Leading to the release of the ECF sigma factor from the inner membrane. RNA polymerase is then recruited to specific promoter regions by the ECF sigma factor for upregulation of specific genes. Cellular activities including biofilm formation, intercellular interactions, release of virulence factors, and metabolite regulation are all regulated by various CSS pathways [45, 47]. Several CSS systems exist,

however, model systems such as the *E. coli* Fec system, *P. aeruginosa* Fpv system, and the *P. capeferrum* Pup system have paved the way for understanding signaling events for transcriptional upregulation.

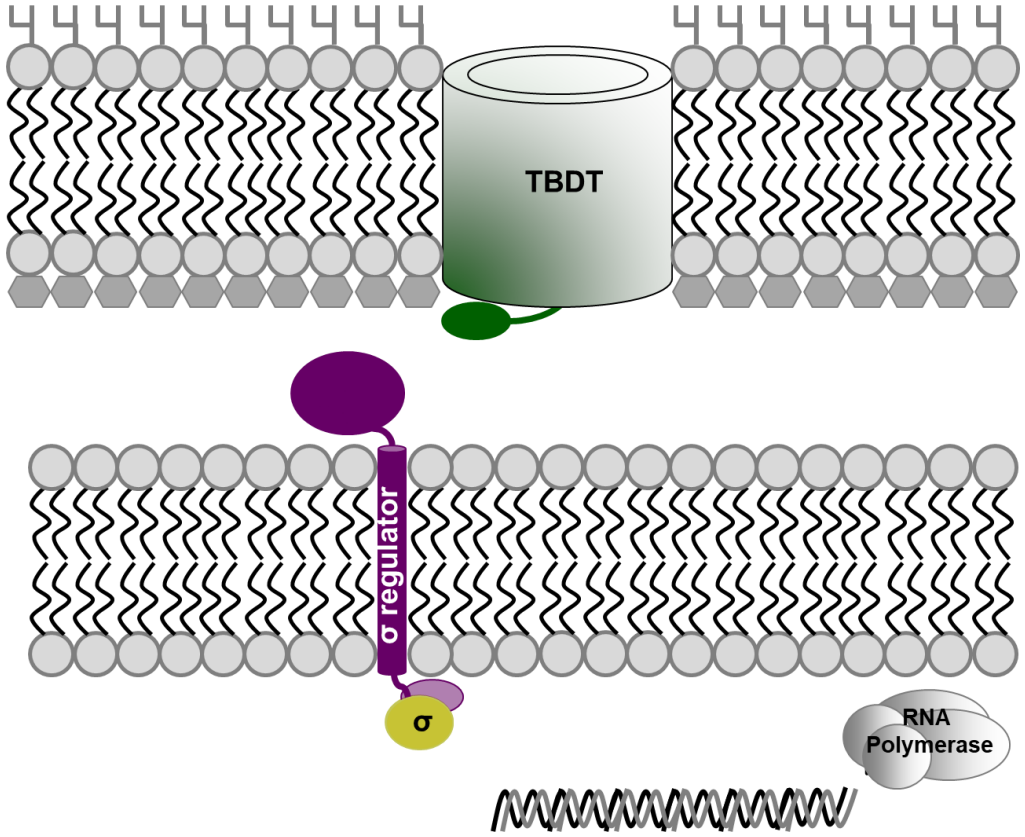

Figure 1.3. Key CSS proteins. Three key conserved cell-surface signaling proteins transduce an extracellular signal to the cytoplasm for release of the ECF sigma factor and transcriptional activation; the outer membrane TBDT (green), the inner membrane sigma regulator (purple), and the cytoplasmic ECF sigma factor (yellow) [1]. Release of the ECF sigma factor recruits RNA polymerase (grey) to the promoter region for transcriptional upregulation of specific genes [1].

1.3.2. Structure and Function of the TBDT

As previously stated, the TBDT contains an NTSD (in cases of CSS activity), a plug domain, and a conserved 22-stranded antiparallel β-barrel [1]. Additionally, all TBDTs contain an N-terminal signal peptide of approximately 13-50 residues which is cleaved following secretion and translocation [1]. The β-barrel domain spans the outer membrane allowing transport into the periplasm. Transport is initially blocked by the plug domain and the exact mechanism by which

the plug domain moves to allow transport is still unclear. It has been postulated that the plug undergoes a conformational change that either creates a pore between the plug domain and the inner wall of the β-barrel domain or the plug is completely removed from the barrel into the periplasm [31, 48-51]. The NTSD, composed of the conserved βαβ-βαββ motif, is stabilized by a hydrophobic core that likely remains folded throughout signaling and transport [40-42]. Previous studies hypothesized signal transduction was transduced to the periplasm through formation of the NTSD:sigma regulator complex. In contrast, our recent data suggests an alternative mechanism [45].

The short TonB box region between the plug domain and the NTSD of TBDTs is tucked into the β-barrel domain under non-signaling conditions [1, 52]. Upon binding of siderophore, conformational changes extend the TonB box into the periplasm, where, as indicated by its name, it interacts with the C-terminal domain (CTD) of TonB [1]. The interaction is mediated by a parallel β-strand with the antiparallel β-sheet of the TonB CTD [53-55]. Although Gram-negative bacteria need TBDTs, the number of TBDTs expressed is limited as they are also sites for bacteriocin binding as demonstrated by the Group B colicins [50]. Under iron limiting conditions, TBDT transcription can be upregulated by CSS via signal propagation to the inner membrane-anchored sigma regulator [47].

1.3.3. Structure and Function of the Sigma Regulator/Anti-Sigma Factor

CSS signal transduction is transmitted from the outer membrane TBDT to the inner membrane sigma regulator, or anti-sigma factor. The sigma regulator has 3 domains: the cytoplasmic N-terminal anti-sigma domain (ASD), the inner membrane transmembrane domain, and the periplasmic C-terminal cell-surface signaling domain (CCSSD) [56, 57]. CCSSDs are ~200

residue domains that extend into the periplasm. Interactions between the CCSSD and the TBDT NTSD facilitate signal transduction into the periplasm and across the inner membrane.

The sigma regulator ASD is anchored to the cytoplasmic side of the inner membrane. Sigma regulator ASDs are ~80-85 residues and primarily function to tether the ECF sigma factor to the inner membrane until signal transduction is activated. ASDs are usually composed of four helices, three of which form a three-helix bundle [57]. The fourth helix typically serves to block interaction of the sigma regulator and RNA polymerase as described by the ChrR, RseA, RskA, and RslA ASDs. In the Pup system, the PupR ASD lacks an ordered fourth helix in the absence of the ECF sigma factor [57]. Upon binding of the ECF sigma factor, the fourth helix may become ordered and inhibit ECF sigma factor association with the DNA promoter region [57]. Additionally, the PupR ASD exists as a symmetrical homodimer [57]. Functionally, homodimerization may be important for stabilization of the ASD or binding of a dimeric PupI [57]. However, this has yet to be fully elucidated.

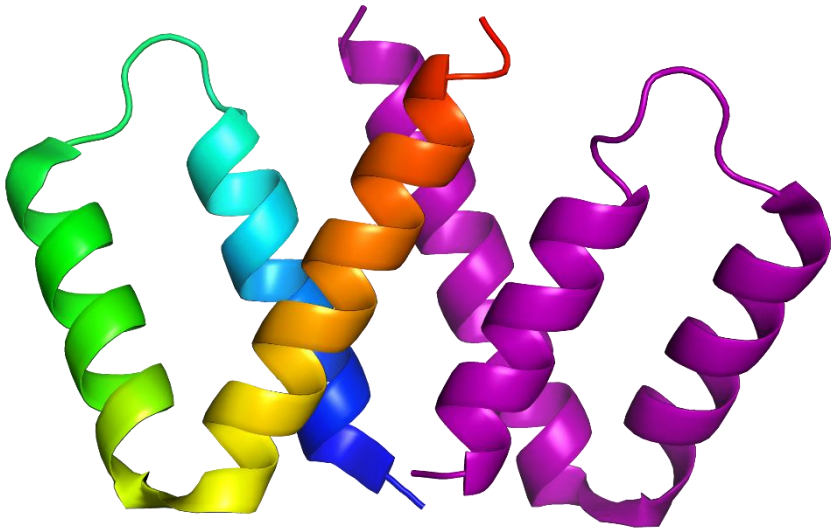

Figure 1.4. Structure and dimerization of the PupR ASD. The PupR ASD forms a symmetrical homodimer which may be functionally important for stabilization or binding of the cognate sigma factor PupI [57]. Monomer A is rendered in rainbow colors with blue at the N-terminus and red at the C-terminus. Monomer B is colored in purple.

Following the ASD is the transmembrane domain, which is a single pass helix composed primarily of nonpolar residues, with polar residues flanking on the cytoplasmic face and bulky hydrophobic residues on the periplasmic face. Typical sigma regulator transmembrane helices are ~15-20 residues [26]. Not only do the transmembrane domains anchor the sigma regulator to the inner membrane but transmit the extracellular signal across the inner membrane as well.

The CCSSD had previously not been structurally characterized. In *E. coli*, the Fec sigma regulator (FecR), residues 101-317, interacts with the FecA NTSD both *in vivo* and *in vitro* [56, 58]. A truncated FecR region, residues 237-317, was further demonstrated to be sufficient for interaction with the FecA NTSD [56, 58]. This region includes the STN subdomain and its relevance in NTSD interaction is discussed further below. Additionally, mutations to a conserved LLLV region of FecR reduced interactions with FecA [59]. As discussed later, this region forms the hydrophobic core of the Pup sigma regulator, PupR, and does not directly mediate interaction with the NTSD [45]. Rather, mutations to the LLLV region would disrupt STN folding and inhibit NTSD interaction.

1.3.4. Structure and Function of the ECF Sigma Factor

Transcription of general housekeeping genes is primarily accomplished by a central sigma factor in all bacteria. However, several alternative sigma factors also aid in transcription of specific genes. Two structurally distinct families of sigma factors, σ^{70} and σ^{54}, each demonstrate different promoter recognition methods [47, 60]. The σ^{70} family is further subdivided into four families and includes the diverse type IV subfamily of ECF sigma factors important for response to extracellular stimuli [47]. ECF sigma factors include several variations and are further split into 43 major groups and several minor groups [61]. The group IV ECF sigma factors of the Pup, Fec,

and Fpv pathways (PupI, FecI, and FpvI) are largely controlled by ASD containing sigma regulators [62-64].

ECF sigma factors are smaller than primary sigma factors at approximately 20-25 kDa and have a largely helical structure (Figure 1.6) [65]. Primary sigma factors are composed of three conserved domains, σ2, σ3, and σ4, whereas the ECF sigma factors contain only the σ2 and σ4 domains [65]. Typically, the σ2 domain of sigma factors are highly conserved and contains regions important for sequence specific interactions with the non-template strand downstream of the -10 promoter element, strong binding to RNA polymerase, and interactions with the -10 box of the promoter [47, 66, 67]. The σ4 domain interacts with the -35 promoter element [68].

Despite high conservation of σ2 in primary sigma factors, ECF sigma factors have a high degree of variation in σ2 and high conservation in σ4 domains [47, 65]. Variations in the σ2 domain may be responsible for the recognition of different promoter regions and gene specific upregulation.

ECF sigma factors are commonly co-transcribed with unique sigma regulators. The sigma regulators retain the ECF sigma factors at the cytoplasmic face of the inner membrane until signal transduction and upregulation of gene specific transcription [47]. Regulation of the release of ECF sigma factors and transcriptional activation is controlled at multiple levels. Two distinct mechanisms have been shown to result in the release of these sigma factors: the degradation of the ASD or loss of affinity between the ASD and ECF sigma factor. Proteolytic degradation of the RseA ASD releases its sigma factor whereas the ChrR loses affinity for its cognate sigma factor after the loss of a Zn^{2+} ion [69-71]. Interestingly, the FecR, FpvR, and likely the PupR ASDs remain associated with their individual ECF sigma factors during transcriptional activation [72-75].

The structure of this complex, and its implications for transcriptional activation, have yet to be determined.

1.3.5. Transcriptional Regulation by the Ferric Uptake Regulator

Transcription of supplemental signaling proteins is not completely dependent upon sigma factor liberation and binding to the promoter. In iron-rich conditions, many iron-dependent promoters are bound by a ferric uptake regulation (Fur) protein (47, 76, 77). Fur is a 17 kDa Fe2+ containing protein that binds to the iron-dependent promoter and acts as a transcriptional repressor (47, 76-78). The iron-dependent promoter, termed the iron box, is a 19 bp inverted repeat sequence that is widespread in bacterial genomes (79). When cellular Fe2+ levels drop due to iron minimal conditions, the Fe2+ cofactor is released and Fur is displaced from the iron-dependent promoter region (47, 76-78). This allows for upregulation of transcription by the associated sigma factor.

1.3.6. Cell-Surface Signaling Regulation

Regulation of sigma factor release plays a big role in transcriptional activation. Liberation of the sigma factor for transcriptional activation has been linked to the regulated intramembrane proteolysis (RIP) of the sigma regulator [76]. RIP is a sequential proteolytic cascade utilizing a site-1 and site-2 protease [76]. Recognition and cleavage by the site-1 protease modifies the substrate protein for recognition by the site-2 protease [76-78]. In *Pseudomonas* CSS systems, the site-1 protease, Prc (or Tsp), cleaves the periplasmic region of the sigma regulator via a hypothesized short ‘clipping’ mechanism [76, 78, 79]. Prc is a C-terminal processing serine endopeptidase with a catalytic serine-lysine catalytic dyad [79-81]. Following site-1 cleavage, the site-2 protease, RseP, cleaves the transmembrane domain of the sigma regulator [47, 82]. RseP is an

integral inner membrane zinc metalloprotease [47, 82]. Despite several studies, the initiation of RIP and substrate recognition by the proteases is not yet fully understood for all CSS pathways.

In the Fec and Fpv CSS pathways it is thought that upon siderophore binding, conformational changes of the NTSD induce conformational changes in the CCSSD, leading to activation of RIP [58, 76, 78, 83, 84]. Previous canonical views of CSS viewed this information and hypothesized that upon siderophore binding the NTSD and CCSSD interact, and this interaction leads to RIP and signal transduction.

1.4. Trojan Horse Antibiotics

With the emergence of drug resistant bacterial infections, the necessity for novel therapeutics grows by the day. One interesting approach is the smuggling of standard antimicrobials through TBDTs via conjugation to siderophores. This method, termed the "Trojan Horse" method, utilizes the presence of natural import mechanisms used for cell survival and nutrient acquisition against the bacteria by bypassing resistance mechanisms. Most of the efforts have been focused on the use of β-lactams conjugated to siderophores as the targets are in the periplasm and further translocation beyond the inner membrane is not necessary [85]. A few of the "Trojan Horse" antibiotics that have made it to clinical trials, such as the monobactam conjugates MC-1 and BAL30072, show great promise. Conjugation and translocation through TBDTs help evade the common antibiotic resistance mechanisms such as efflux pumps and bring about a new delivery method for antibiotics which currently have limited effectiveness. However, the low expression of TBDTs on the outer membrane makes this method of delivery inefficient. A comprehensive understanding of TBDT iron import and CSS transcriptional upregulation may allow for the hijacking of these pathways, to trigger excess TBDT expression, increasing the success rate of "Trojan Horse" antibiotics.

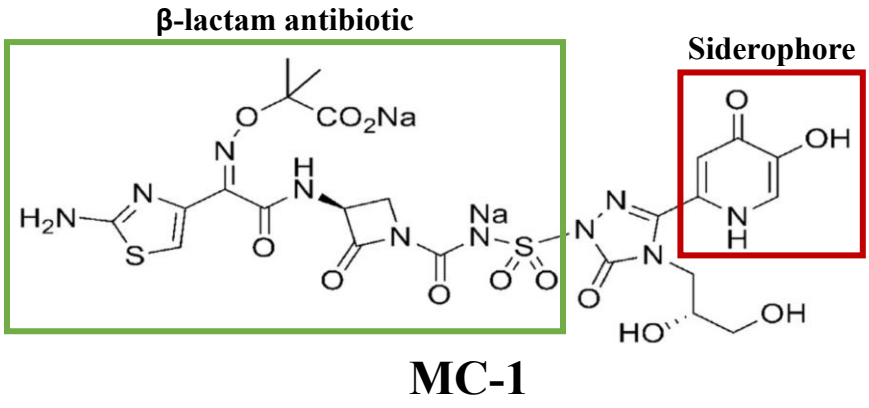

Figure 1.5. Chemical structure of the "Trojan Horse" MC-1 antibiotic. MC-1 is a siderophore conjugated monobactam with effectiveness against challenging Gram-negative bacterial infections [85]. The β-lactam antibiotic portion of MC-1 is boxed in green with the siderophore portion boxed in red.

1.5. Specific Aims

With the continued emergence of multidrug resistant Gram-negative bacteria, new efforts to thwart infections are important. To aid in this process a thorough understanding of TBDT iron import and CSS pathways is required. The goal of this work is to provide a structural understanding of CSS pathways and TBDT iron import by addressing the following specific aims:

1. To characterize and structurally validate the PupB NTSD:PupR CCSSD interaction and provide a rationale for complex formation in CSS.
2. To evaluate the FecA NTSD:FecR CCSSD structure and interactions for similarities with the *P. capeferrum* Pup pathway, in order to elucidate a universal CSS signal transduction mechanism.
3. To characterize the recognition and degradation of the PupR CCSSD, structurally and biophysically, by the site-1 protease Prc.
4. To assess the role of the PupB NTSD in shielding the PupR CCSSD from the site-1 protease prior to signal transduction.

5. To structurally validate the interaction of the TonB CTD with the PupB TBDT, and understand the series of events linking CSS signal transduction and iron import.

2. STRUCTURAL BASIS OF CELL-SURFACE SIGNALING BY A CONSERVED SIGMA REGULATOR IN GRAM-NEGATIVE BACTERIA[1]

2.1. Introduction

Cell-surface signaling (CSS) pathways allow Gram-negative bacteria to provide a rapid and effective response to environmental stimuli through transcriptional activation. Some iron import systems in Gram-negative bacteria involve such CSS pathways. The best characterized CSS iron import systems are the ferric citrate (*fec*) transport system from *Escherichia coli*, the ferric pyoverdine (*fpv*) import system from *Pseudomonas aeruginosa*, and the ferric pseudobactin BN7/BN8 (pup) system from *Pseudomonas capeferrum* (formerly *Pseudomonas putida WCS358*). Each of these homologous pathways involves 1) a TBDT, which transduces the extra-cytoplasmic signal to the periplasm and also imports extracellular metabolites; 2) an inner membrane sigma regulator, also known as an anti-sigma factor, which transfers the signal from the periplasm to the cytoplasm; and 3) an extra-cytoplasmic function sigma factor, that is released from the inner membrane to initiate expression of a target response gene (Table 2.1).

Sigma regulators are central to iron import CSS pathways. Sigma regulators (~325 amino acids) are proteins consisting of three domains, 1) an N-terminal anti-sigma domain, which regulates the sigma factor; 2) a single-pass transmembrane helix; and 3) a C-terminal periplasmic domain of 200 residues, responsible for interacting with the transducer[57, 58, 76, 86]. The periplasmic domain of the sigma regulator, FecR, has been shown to interact with the N-terminal signaling domain (NTSD) of its cognate transporter/transducer, FecA, and mutation of conserved

[1] The material in this chapter was co-authored by Dr. Jaime Jensen, Beau D. Jernberg, Dr. Sangita Sinha, and Dr. Christopher Colbert. Beau D. Jernberg performed protein expression and purifications, CD spectroscopy, thermal denaturation experiments, ITC, PupR CCSSD crystallization and data collection, and aided in manuscript preparation.

hydrophobic residues to proline within this periplasmic domain disrupted binding to the NTSD[58, 59]. The structure of the periplasmic domain of sigma regulators has not been previously described.

CSS has been determined to be activated by regulated intramembrane proteolysis (RIP) of the sigma regulator [76-78, 87, 88]. Siderophore binding/uptake triggers a signal, which presumably involves a protein interaction event between the transducer and the sigma regulator that results in cleavage of the sigma regulator by a site-1 protease, Prc, as shown for both FecR and FpvR, followed by intramembrane cleavage by a site-2 protease, RseP[76-78, 87, 88]. Prc, a site-1 serine protease, was shown to proteolyze the periplasmic sigma regulator domain in IutY from P. putida KT2440, although fragments of IutY are present in non-CSS conditions[78]. Alternatively, initial cleavage of the sigma regulator has also been proposed to include an autoproteolytic event via N-O acyl rearrangement through the nonconserved residues Gly191 and Thr192 of FoxR from P. aeruginosa, which are also found in the sequence of FecR [78, 89, 90]. However, the sequence of events that lead to initiation of RIP by Prc are still very unclear. Canonically, it has been viewed that siderophore binding triggers a protein:protein interaction between the sigma regulator and the TBDT that initiates RIP.

Here, we report the 1.56 Å resolution X-ray crystal structure of the periplasmic domain of the CSS sigma regulator, PupR, in complex with the NTSD of the transducer, PupB, solved by Dr. Jaime Jensen. This is the first report describing the structure of the periplasmic region of an iron import CSS sigma regulator. This structure of the periplasmic domain of PupR, hereafter referred to as the C-terminal cell-surface signaling domain (CCSSD), is comprised of two subdomains: residues 110–238, comprising the C-terminal juxta-membrane subdomain (CJM) and residues 250–324, comprising a Secretin/ TonB, short N-terminal subdomain (STN).

Additionally, affinity pulldown assays were utilized to indicate which subdomains are necessary to define the binding surface for the PupB NTSD. Furthermore, our biochemical and biophysical experiments were used to demonstrate PupR CCSSD stability in the presence and absence of PupB NTSD. Together, these results provide the structural rationale for how the CCSSD:TBDT NTSD interaction prevents RIP initiation of CSS prior to signal transduction.

Table 2.1. Protein components of the most well-studied CSS iron import systems from *P. capeferrum*, *E. coli*, and *P. aeruginosa*.

	TonB-dependent transducer	**Sigma regulator**	**Sigma factor**
P. capeferrum	PupB[a]	PupR[a]	PupI
E. coli	FecA	FecR	FecI
P. aeruginosa	FpvA	FpvR	FpvI, PvdS

[a] This study.

2.2. Materials and Methods

2.2.1. Cloning of PupR CCSSD Constructs

Potential PupR domains were delineated using secondary and tertiary structure predictions, including the N-terminal ASD (residues 1-82), a single-pass transmembrane helix (residues 86-104), and the periplasmic CCSSD (residues 110-324). Five expression constructs were made, comprising PupR residues 110–324, 110–238, 110–250, 238–324, or 250–324 cloned separately between NcoI and XhoI sites of the pMBP-Parallel1 vector [91].

2.2.2. Site-directed Mutagenesis of PupR CCSSD

Point mutations of WT PupR CCSSD (M251A, S286A, and T288A) were created by site directed mutagenesis from the expression vectors described above using a QuikChange II kit (Agilent). DNA sequencing verified the gene sequences of the mutant plasmids used for transformation.

2.2.3. Protein Expression and Purification of PupB NTSD

The *pupB NTSD* gene was initially cloned as previously described[92]. The *pupB NTSD* sequence was subsequently cloned into pET41, containing an N-terminal glutathione S-transferase (GST) tag and a TEV-protease recognition sequence (ENLYFQG) prior to the *pupb NTSD* coding sequence. PupB NTSD mutants (Q69K, H72D, & L74A) were generated by site-directed mutagenesis. DNA sequencing verified the gene sequences of the mutant plasmids used for transformation.

pET41-PupB NTSD constructs were used to transform chemically competent *E. coli* BL21 (DE3) pLysS cells for protein expression. 50 µL and 200 µL aliquots of the transformation mixture were used to inoculate two LB agar plates supplemented with 15 µg/ml kanamycin. Plates were inoculated overnight at 37 °C. A single colony was picked and added to a 70 mL culture of LB media supplemented with 15 µg/ml kanamycin and incubated at 37 °C overnight. For protein expression, 10 mL of overnight culture was added to 1 L of LB media supplemented with 15 µg/ml kanamycin. This culture was incubated at 37 °C with shaking at 200 rpm until it reached an OD_{600} of 0.7-0.9. Protein expression was induced with 0.5 mM isopropyl 1-thio-β-D-galactopyranoside (IPTG). Following induction, cells were grown overnight at 20 °C. Cells were then harvested at 4,000 x g by centrifugation, washed with 25 mM Tris HCl pH 7.8, 150 mM NaCl, 2 mM DTT, and stored at -80 °C.

Cell pellets were resuspended in 25 mM Tris HCl pH 7.8, 150 mM NaCl, 2 mM DTT and lysed with a Branson Sonifier 450 sonicator. Lysate was then clarified by centrifugation at 20,000 x g for 35 min and passed over Glutathione Sepharose 4B resin (Cytiva) equilibrated in lysis buffer. The column was washed with excess lysis buffer. Recombinant GST tobacco etch virus protease (GST-TEV) was applied to the column and incubated at 4 °C overnight to remove

the PupB NTSD GST tag. Lysis buffer was added to wash off the released PupB NTSD protein. The final purification step was size-exclusion chromatography over a Superdex 75 increase 10/300 GL column (Cytiva) using an isocratic elution gradient with 25 mM Tris HCl pH 7.8, 150 mM NaCl. Mutant PupB NTSD constructs were purified similarly. Pure PupB NTSD constructs were pooled, concentrated with a 3-kDa MWCO Amiconultra centrifugal filter unit (Millipore) to 10 – 20 mg/mL, flash frozen in liquid nitrogen, and stored at -80 °C. Protein purity was determined to be >95% by SDS-PAGE using a 4-20% TGX SDS-PAGE gel (Bio-Rad) and Coomassie Blue staining[93].

2.2.4. Protein Expression and Purification of MBP-tagged PupR CCSSD, and PupR CCSSD

Chemically-competent *E. coli* C41 (DE3) cells (Lucigen) were transformed using the pMBP-Parallel1-PupR CCSSD (PupR residues 110–324) plasmid for purification of MBP-tagged PupR CCSSD or PupR CCSSD. 50 µL and 200 µL aliquots of the transformation mixture were used to inoculate two LB agar plates supplemented with 100 µg/ml ampicillin. Plates were inoculated overnight at 37 °C. A single colony was picked and added to a 70 mL culture of LB media supplemented with 100 µg/ml ampicillin and incubated at 37 °C overnight. For protein expression, 10 mL of overnight culture was added to 1 L of LB media supplemented with 100 µg/ml ampicillin. This culture was incubated at 37 °C with shaking at 200 rpm until it reached an OD_{600} of 0.7-0.9. Protein expression was induced with 0.5 mM IPTG at 20 °C for 20 h. Cells were harvested by centrifugation, washed with 25 mM HEPES pH 7.5, 400 mM LiCl, 10% glycerol, and stored at -80 °C. At each subsequent stage of purification, protein purity was analyzed by SDS-PAGE and protein concentration determined by absorbance at 280 nm using

the molar extinction coefficient of 29,450 M^{-1} cm^{-1} and a theoretical molecular weight of 24,067 g/mol.

The cell pellet was thawed and resuspended in chilled lysis buffer (25 mM HEPES pH 7.5, 400 mM LiCl, 10% glycerol, 2 mM DTT), then lysed with a Nano DeBEE homogenizer (BEE International). The crude extract was clarified by centrifugation at 20,000 x g for 45 min. The clarified supernatant was loaded onto amylose affinity resin preequilibrated with lysis buffer. Once loaded, the column was washed with 30 column volumes (CV) of lysis buffer, and fusion protein eluted with lysis buffer containing 20 mM maltose. Elution fractions, one half CV each, were pooled and concentrated with a 30-kDa MWCO Amicon Ultra centrifugal filter unit (Millipore). The final step was SEC using a 16/60 Superdex 200 column (GE Lifesciences) equilibrated with lysis buffer without DTT. Fractions containing pure, homogeneous MBP-tagged PupR CCSSD eluted at 0.4 – 0.7 mL/min were pooled, concentrated to 18 mg/ml, flash frozen in liquid nitrogen in 20 – 50 µL aliquots, and stored at -80 °C. MBP-tagged PupR CJM, residues 110 – 238 or 110 – 250, and MBP-tagged PupR STN, residues 239 – 324 or 251 – 324, were purified in a manner similar to the MBP-tagged PupR CCSSD.

To purify the PupR CCSSD, MBP-tagged PupR CCSSD was first expressed and purified by amylose affinity chromatography. Instead of eluting, the bound fusion protein was subjected to on-column cleavage by addition of GST-TEV in a 1:10 mass ratio, followed by a 16-h incubation at 4 °C, which yielded a 219-residue product, comprising PupR residues 110–324, preceded by a 4-residue (GAMG) cloning artifact. Released PupR CCSSD was washed from the column and analyzed for the presence of contaminating MBP. Contaminating MBP was removed by a second pass over equilibrated amylose resin. The PupR CCSSD was concentrated using a 10-kDa MWCO Amicon Ultra centrifugal filter unit (Millipore) prior to SEC, which was

performed as described for MBP-tagged PupR CCSSD. The PupR CCSSD eluted in a single peak at 90.0 mL. Fractions containing PupR CCSSD were pooled, concentrated to 10 mg/ml, and stored at -80 °C. Final protein purity was estimated to be 90% by SDS-PAGE stained with Coomassie Blue as it had some MBP contamination [93].

2.2.5. Preparation of Selenomethionine-derivatized PupR CCSSD

Selenomethionine (SeMet)-derivatized PupR CCSSD was expressed using a modified protocol involving methionine synthesis suppression[94, 95]. *E. coli* C41 (DE3) cells transformed with pMBP-Parallel1-PupR CCSSD were grown at 37 °C to saturation in 3 ml of LB medium with 100 µg/ml of ampicillin, then transferred to pre-warmed M9 minimal medium containing 2 mM MgSO4, 0.1 mM CaCl2, 0.4% (w/v) glucose, and 100 µg/ml of ampicillin and incubated at 37 °C. Once the $OD_{600\ nm}$ reached 1.0, the medium was supplemented with SeMet (Acros Organincs), Lys, Thr, Phe, Leu, Ile, and Val; and the temperature lowered to 20 °C. Protein expression was induced with 0.5 mM IPTG for 18 h. Purification of SeMet PupR CCSSD was performed as described for native protein. The molecular mass of the final protein samples and SeMet incorporation were confirmed by electrospray ionization MS.

2.2.6. Co-expression and Affinity Pulldown Assays of PupR CCSSD:PupB NTSD Complexes

E. coli BL21 (DE3) pLysS cells were co-transformed with pMBP-Parallel1-PupR CCSSD and pET41-GST-PupB NTSD. Co-transformants were selected by growing on LB agar medium containing 100 µg/ml of ampicillin and 15 µg/ml of kanamycin. Co-expression followed the same purification procedure as for the individual proteins. Harvested cells were lysed and cell debris pelleted by centrifugation. The clarified supernatant was divided into two equal aliquots and combined with either 5 ml of amylose resin or 5 ml of Glutathione Sepharose 4B

resin. The columns were incubated for 30 min at 4 °C. Each column was washed with 10 column volumes of lysis buffer, then eluted with lysis buffer + 20 mM maltose or 15 mM reduced glutathione (GSH) (pH adjusted) as appropriate. Total protein content was determined by Bradford assay, and 20 µg of protein were loaded onto a 4–20% TGX SDS-PAGE gel (Bio-Rad). Gels were stained with Coomassie Blue and qualitatively analyzed for protein association. This protocol was repeated for all pulldown analyses. The identity of the proteins in the pulldown assays was confirmed by direct Western blotting, using commercially available anti-MBP-HRP (New England Biolabs) or anti-GST-HRP (GE Healthcare) antibodies.

2.2.7. CD Spectroscopy and Thermal Denaturation of PupR CCSSD, PupB NTSD, and PupR CCSSD:PupB NTSD

PupR CCSSD, PupB NTSD, or PupR CCSSD:PupB NTSD samples were dialyzed against 10 mM potassium phosphate pH 6.8, 100 mM $(NH_4)_2SO_4$ overnight at 4 °C and diluted to 50 µM (1.21, 0.405, and 1.61 mg/ml, respectively). Continuous scanning CD spectra were measured at 4 °C between 180 and 250 nm using a Jasco J-815 spectrometer with a PFD-425S Peltier cell holder and a 1-mm quartz cell. The spectra were buffer subtracted, and the secondary structure content estimated using CONTIN and CDSSTR, within the CDPro software suite[96].

CD melting and re-folding curves were recorded at 216 nm with 50 µM PupR CCSSD, PupB NTSD, or PupR CCSSD:PupB NTSD by increasing the temperature from 10 to 85 °C in 1 °C increments with a slope of 1 °C/min. Protein unfolding was monitored during both heating and cooling. Melting temperatures were determined by fitting a standard Boltzmann sigmoidal curve to the ellipticity in Origin 8 (OriginLab Corp., Northampton, MA). The final melting temperature was defined as the inflection point after fitting.

2.2.8. CD Spectroscopy and Thermal Denaturation of PupB NTSD Mutants

PupB NTSD mutant samples were dialyzed in 10 mM potassium phosphate pH 6.8, 100 mM $(NH_4)_2SO_4$ overnight at 4 °C and diluted to 25 µM. Continuous scanning CD spectra were measured at 20 °C from 190-250 nm using a Jasco J-815 spectrometer with a PFD-425S Peltier cell holder and a 1-mm quartz cell. Spectra were buffer subtracted and secondary structure contents estimated using CONTIN and CDSSTR within the CDPro software suite[96]. CD melting and re-folding curves were recorded at 217 nm with 25 µM PupB NTSD mutants by increasing temperature from 10-85 °C in 1 °C increments with a slope of 1 °C/min. Protein unfolding was monitored during both heating and cooling. Melting temperatures were determined by fitting a standard Boltzmann sigmoidal curve to the ellipticity in Origin 8 (OriginLab Corp., Northampton, MA). The melting temperature was defined as the inflection point after fitting.

2.2.9. ITC to Quantify the Thermodynamics of MBP-tagged PupR CCSSD Binding to PupB NTSD

ITC was performed using a Low Volume Nano ITC (TA Instruments). Purified proteins were loaded into separate dialysis cassettes, and co-dialyzed against 25 mM HEPES pH 7.5, 400 mM LiCl, 10% glycerol. All ITC experiments were performed at 15 °C, with 25 injections of 2 µl each. MBP-tagged PupR CCSSD, concentrated to 220–235 µM, was titrated into 27.5– 40 µM PupB NTSD. Titrations were repeated in triplicate. The values from a buffer-into-buffer titration were subtracted from the values of the protein-into-protein titration during analysis. Data were analyzed with either NanoAnalyze (TA Instruments) with an independent, single-site model, or NITPIC for data integration, followed by data processing with SEDPHAT and plotting of isotherms in GUSSI[97-101]. Processing included data refinement considering the local incompetent fraction as a function of the concentration compensation factor[102]. To control for possible

nonspecific interactions between MBP and PupB NTSD, 186–196 µM MBP was titrated into 45–57 µM PupB NTSD and analyzed.

Similar experiments were conducted with PupB NTSD mutants. Individual proteins were extensively dialyzed against 25 mM HEPES pH 7.5, 400 mM LiCl, 10% glycerol. at 15 °C with either 20 or 25 injections of 2.5 µl or 2 µl respectively. MBP-PupR CCSSD at 140 - 230 µM was titrated into individual PupB NTSD mutants at concentrations of 20 - 70 µM. Resulting data was integrated with NanoAnalyze (TA Instruments) using an independent, single-site model. All experiments were completed in triplicate.

2.2.10. PupR CCSSD:PupB NTSD Complex Crystallization, Data Collection, and Structure Solution

PupR CCSSD and PupB NTSD were combined in a 1:1 molar ratio. The MCSG crystallization suite (Anatrace) was used to identify initial crystallization conditions. Reproducible crystals were grown by sitting drop vapor diffusion in 200 mM sodium tartrate or Na-K tartrate, 20-25% (w/v) PEG 3350. Single crystals were cryoprotected with MiTeGen CryoOil and flash-frozen.

Diffraction data were collected at NE-CAT beamlines 24-ID-E and 24-ID-C at the APS under cryogenic conditions (~100 K). The native PupR CCSSD:PupB NTSD diffraction data set was processed using autoPROC with components POINTLESS for space group determination, MOSFLM for indexing, and XDS and SCALA for scaling[103-106]. Diffraction data from a single, orthorhombic crystal of Se-Met PupR CCSSD:PupB NTSD was processed with HKL2000[107]. The structure was determined to 1.6 Å by SAD phasing. Three of the four selenium sites per PupR CCSSD monomer were located, and initial phasing was performed using AutoSol in

PHENIX[108]. Initial electron density maps were interpreted by automated model building using AutoBuild[109].

Refinement was carried out in PHENIX with iterative model building in COOT[110, 111]. The Se-Met PupR CCSSD structure was used for molecular replacement (MR) against the native data set at 1.76 Å using Phaser-MR followed by AutoBuild[109, 112]. Automated TLS group determination and individual atomic B-factors were used during refinement in PHENIX for both the Se-Met and native structures[113]. The quality of the diffraction data and final refined structures are summarized in Table 2.2.

Model validation was performed using MolProbity and the PDB Validation Server (RRID: SCR_018135)[114]. Analyses of surface areas, protein interfaces, assemblies, and interactions were performed using the PISA server (RRID: SCR_015749)[115]. RMSD comparisons were carried out in PyMOL[116]. The DALI protein structure comparison server (RRID: SCR_013433) using DaliLite v.5 was used to identify the fold, family, and superfamily of each subdomain of the structure[117].

Table 2.2. X-ray data collection, phasing, and refinement statistics for the PupR CCSSD:PupB NTSD complex. Values in parenthesis pertain to the highest resolution shell.

	Native	**SeMet derivative**
Data collection		
Beamline	24-ID-E	24-ID-C
Wavelength (Å)	0.9792	0.9792
Space group	$P2_12_12_1$	$P2_12_12_1$
Unit-cell parameters (Å, °)	43.4, 44.6, 141.0 α,β,γ = 90	43.6, 44.7, 141.3 α,β,γ = 90
Resolution range (Å)	42.5-1.76 (1.767-1.761)	141.34-1.51 (1.53-1.51)
Total observations	190024 (1895)	258089 (2816)
Unique observations	27078 (2741)	43910 (1511)
Multiplicity	7.0 (6.9)	5.9 (1.9)
Completeness (%)	96.9 (99.3)	98.0 (70.2)
CC(1/2)	0.999 (0.966)	0.999 (0.765)
R_{merge}[a] (%)	5.6 (26.8)	5.2 (40.1)
R_{merge} (anom, %)	--	4.5 (42.9)
Mean $I/\sigma I$	25.2 (6.8)	18.9 (1.6)
Data processing program	autoPROC	HKL2000
Refinement		
Refinement program	PHENIX	PHENIX
Resolution range (Å)	42.5-1.76 (1.82-1.76)	42.6-1.60 (1.614-1.558)
Molecules per ASU	2	2
R_{work} (%)	14.9	15.3
R_{free} (%)	20.0	18.4
RMSD stereochemistry		
Bond lengths (Å)	0.014	0.018
Bond angles (°)	1.48	1.96
No. of atoms	2661	2787
PupR-CCSSD:PupB-NTSD	2325	2412
Ligands (tartrate)	20	20
Waters	316	355
Total average B (Å^2)	21.7	18.1
PupR-CCSSD	19.5	16.1
PupB-NTSD	23.9	18.6
Tartrate	25.3	20.0
Waters	29.7	27.4
Ramachandran plot (%)		
Preferred	98	98
Allowed	2	2
Outliers	0	0
PDB code	6OVK	6OVM

[a] $R_{merge} = \frac{\sum_{hkl}\sum_j |I_{hkl,j} - \langle I_{hkl}\rangle|}{\sum_{hkl}\sum_j I_{hkl,j}}$

2.2.11. PupR CCSSD Crystallization and Data Collection

Initial crystal hits were identified with the MCSG crystallization suite (Anatrace) at a concentration of 225-250 µM (5.4 – 6.0 mg/mL). Crystal hits were observed in multiple conditions throughout MCSG-1 (Table 2.3). Hits were reproduced and optimized around the 100 mM MES:NaOH pH 6.5, 600 mM NaCl, 20% PEG 4000 and 100 mM Bis-Tris HCl pH 5.5, 25% PEG 3350 buffer conditions via sitting drop vapor diffusion in 1:1 and 1:3 v/v mixture of protein solution to reservoir solution (2 µL total drop size) at 20°C (Fig. 2.1). Singular crystals were harvested and cryoprotected with MiTeGen CryoOil then flash-frozen in liquid nitrogen. Overlapping crystals were used in microseeding experiments to optimize singular crystal formation prior to harvesting.

Diffraction data was collected at NE-CAT beamline 24-ID-C at the Advanced Photon Source of Argonne National Laboratory under cryogenic conditions. The data was processed with XDS using the NE-CAT RAPD automated software suite. The data collection strategy program within RAPD, BEST, was used to formulate a collection strategy. Multiple data sets were taken, however, crystals either diffracted to poor resolution (Table 2.4, Data set 1) or succumbed to radiation damage before a complete data set could be collected (Table 2.4, Data set 2). Unfortunately, a data set usable for structure solution of the PupR CCSSD alone was unable to be collected despite testing 60 crystals for suitable diffraction.

Table 2.3. Crystal hit conditions identified for PupR CCSSD from the MCSG-1 crystal screen.

Screen ID	Well	Buffer	Salt	Precipitant
MCSG-1	B1	0.1 M MES: NaOH, pH 6.5	0.6 M NaCl	20% (w/v) PEG 4000
MCSG-1	C12	0.1 M Bis-Tris: HCl, pH 6.5	None	25 % (w/v) PEG 3350
MCSG-1	D4	None	0.2 M Sodium Thiocyanate, pH 6.9	20 % (w/v) PEG 3350
MCSG-1	D12	None	0.2 M Ammonium Chloride, pH 6.3	20 % (w/v) PEG 3350
MCSG-1	E7	None	0.2 M Ammonium Iodide	20 % (w/v) PEG 3350
MCSG-1	F2	0.2 M Ammonium Acetate	0.1 M Bis-Tris: HCl, pH 6.5	25 % (w/v) PEG 3350
MCSG-1	H9	0.1 M Bis-Tris: HCl, pH 5.5	None	25 % (w/v) PEG 3350

Table 2.4. X-ray data collection statistics for the PupR CCSSD.

Data Collection	Data Set 1	Data Set 2
Beamline	24-ID-C	24-ID-C
Wavelength (Å)	0.980540	0.980540
Space group	*I222*	*C121*
Mosaicity (°)	0.35	0.46
Unit-cell parameters (Å, °)	50.3, 53.0, 67.0 $\alpha,\beta,\gamma = 90$	86.37, 50.73, 52.92 90, 127.8, 90
Resolution range (Å)	41.6-4.95 (5.54-4.95)	41.8-2.86 (3.03-2.86)
Unique observations	416 (113)	1897 (295)
Multiplicity	3.0 (2.9)	1.9 (1.7)
Completeness (%)	92.1 (93.3)	45.4 (44.5)
CC(1/2)	0.850 (0.306)	0.944 (0.795)
R_{merge}	0.987 (1.366)	0.258 (1.148)
Mean $I/\sigma I$	1.2 (0.7)	1.7 (0.4)
Data processing program	XDS	XDS

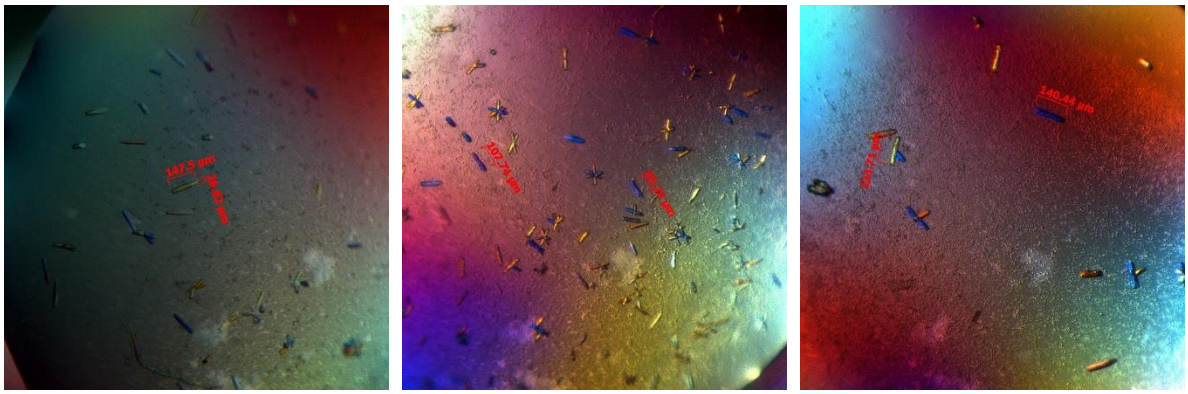
Figure 2.1. Singular and clustered crystals of PupR CCSSD.

2.2.12. Size Exclusion Chromatography Coupled to Small-angle X-ray Scattering (SEC-SAXS) Measurements and Analysis of PupR CCSSD and PupR CCSSD:PupB NTSD

SAXS data were recorded in tandem with SEC at BioCAT (beamline ID-18) at the Advanced Photon Source. Experimental details and structural parameters are summarized in Table 2.5. Prior to measurements, an inline Superdex 200 Increase 10/300 column was equilibrated with 25 mM HEPES, pH 7.5, 400 mM LiCl, 10% (v/v) glycerol. Purified PupB NTSD and PupR CCSSD were combined at a 1:1 molar ratio and incubated for 30 min at room temperature prior to loading. 800 µM complex or 400 µM PupR CCSSD alone were injected onto the SEC column with a flow rate of 0.6 ml/min, and scattering data recorded from a 1s exposure every 3 s at ambient temperature. Scattering data were collected at a wavelength of 1.03 Å (12 keV), covering a momentum transfer range (q) of 0.004– 0.36 $Å^{-1}$, using a Pilatus 3 1M detector at a distance of 3.5 m from the sample. Scattering data were normalized to the incident X-ray beam, and scattering from the SEC buffer was subtracted with Igor Pro and BioCAT beamline extension programs. SAXS data analyses were performed using the ATSAS suite [118]. PRIMUS was used for data merging, calculating the Rg with a Guinier approximation, and evaluating protein order by the Kratky plot [119]. The absence of protein aggregation was validated by examining the linearity of the Guinier region. The pair distribution function, P(r),

and maximum particle dimension, Dmax, were determined in GNOM [120]. Molecular weight was determined using the SAXS Molecular Weight webserver32 (RRID: SCR_018137) [121]. Theoretical scattering of the crystal structures was computed and fitted with the experimental data using CRYSOL [122]. To evaluate the flexibility of the PupR CCSSD linker, the HingeProt webserver (RRID: SCR_018136) was used to identify the optimal linker from the CCSSD structure [123]. It identified two possibilities, residues 239–250 or 232–250, which were input as flexible for multistate modeling with MultiFoXS [124]. The models with the lowest X^2 values and deviations from experimental data were identified. Additionally, EOM 2.0 was utilized to generate PupR CCSSD flexible conformers that align with the SAXS profile, using the two subdomains and full PupR CCSSD sequence as the input files [125]. Similarly, the CCSSD: NTSD SAXS scattering curve was evaluated using MultiFoXS, using various residues as being potentially disordered.

Table 2.5. SEC-SAXS data collection and structural parameters.

	PupR CCSSD				PupR CCSSD:PupB NTSD	
Data Collection Parameters						
Instrument	BioCAT ID-18				BioCAT ID-18	
Beam geometry (H µm x V µm)	5 x 3				5 x 3	
Detector distance (m)	3.5				3.5	
Detector	Pilatus 3 1M				Pilatus 3 1M	
Wavelength (Å)	1.03				1.03	
q range ($Å^{-1}$)[a]	0.004-0.36				0.004-0.36	
Exposure time (s/frame)	1				1	
Total number of frames	1100				1100	
Temperature (K)	298				298	
SEC Parameters						
SEC column	Superdex 200 Increase 10/300				Superdex 200 Increase 10/300	
Buffer	25 mM HEPES pH 7.5, 400 mM LiCl, 10% v/v glycerol				25 mM HEPES pH 7.5, 400 mM LiCl, 10% v/v glycerol	
Sample concentration (µM)	400				800	
Injection volume (µL)	500				500	
Flow rate (mL/min)	0.6				0.6	
Structural Parameters						
I(0) (cm^{-1}/absorbance) (from Guinier)	17.43 ± 0.06				45.53 ± 0.24	
Rg (Å) (from Guinier)	22.06 ± 0.99				26.21 ± 0.22	
R^2	0.9931				0.977	
I(0) (cm^{-1}/absorbance) [from P(r)]	17.45 ± 0.04				44.80 ± 0.18	
Rg (Å) [from P(r)]	22.31 ± 0.06				25.81 ± 0.14	
qRg range ($Å^{-1}$)	0.58 - 1.29				0.64 – 1.29	
Dmax (Å)	75.0				87.3	
χ^2 (total estimate from GNOM)	1.386 (0.835)				1.358 (0.895)	
Porod volume estimate ($Å^3$)	48580				55800	
SASBDB ID	SASDGA5				SASDGU5	
SAXS-Derived Molecular Mass						
From Porod volume (VPorod/1.7) (kDa)	28.6				32.8	
SAXSMoW2 (kDa)	23.3				40.0	
Molecular mass from sequence (kDa)	24.1				32.2	
Curve Fitting with Atomic Model	CCSSD Structure	Model 1	Model 2	Model 3	CCSSD Structure	Complex Structure
q range for modeling	0.026 - 0.300	0.026 - 0.300	0.026 - 0.300	0.026 - 0.300	0.024 – 0.300	0.024 – 0.300
X^2 , P-value	2.62, 0.00	2.16, 0.00	1.72, 0.00	2.01, 0.00	11.34, 0.00	2.45, 0.00
Predicted Rg (Å)	21.36	20.86	20.95	21.81	21.42	23.49
Dro ($e/Å^3$)[b]	0.075	0.045	0.075	0.018	0.075	0.075
Ra (Å)[c]	1.620	1.800	1.400	1.400	1.400	1.540
Vol (Å3)[d]	31631	30013	31597	34096	31631	42276
***Ab initio* Modeling**						
q max ($Å^{-1}$)	0.27				0.26	
Number of repetitions	20				20	
Normalized spatial discrepancy	0.598 ± 0.02				0.592 ± 0.02	

[a] $q = 4\pi\sin(\theta)/\lambda$, where 2θ is the scattering angle
[b] Contrast of hydration shell
[c] Atomic group radius
[d] Optimal excluded volume

2.3. Results

2.3.1. Expressions and Purifications of the PupB NTSD

The PupB NTSD and the individual PupB NTSD mutants (Q69K, H72D, and L74A) were purified by sequential GSH affinity chromatography with on-column TEV protease cleavage and SEC. The apparent molecular weights were 8.9, 8.8, 7.4, and 8.4 kDa for PupB NTSD WT, Q69K, H72D, and L74A respectively. These experimental molecular weights compare closely to the theoretical molecular weights of ~8.1 kDa based on the amino acid sequences. The single SEC peak and SDS-PAGE bands indicate the PupB NTSD constructs are pure and homogenous (Fig. 2.2 & 2.3).

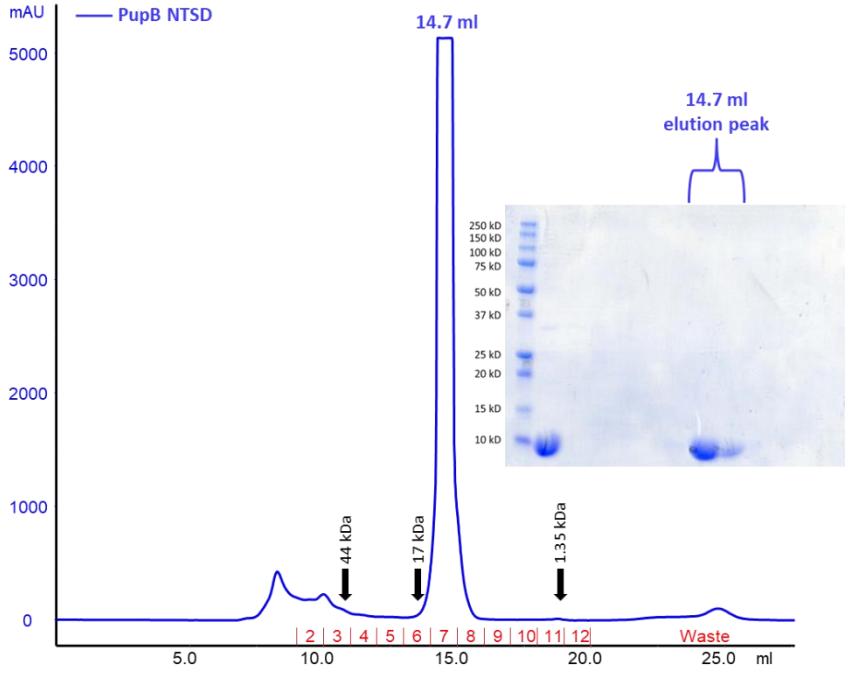

Figure 2.2. SEC chromatogram and related SDS-PAGE gel of PupB NTSD. Eluted positions of SEC standard are indicated by arrows. PupB NTSD eluted at a volume of 14.7 ml with a calculated molecular weight of ~8.9 kDa.

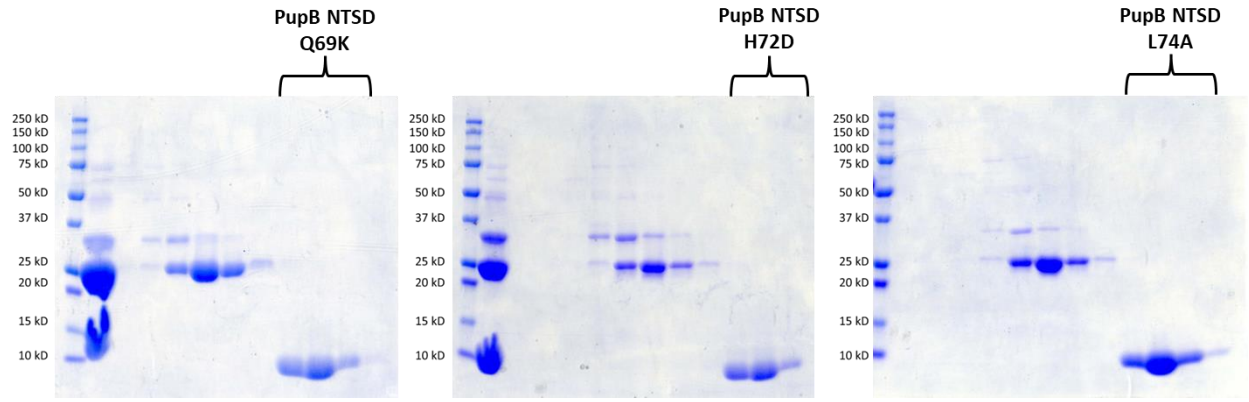

Figure 2.3. SDS-PAGE gels of PupB NTSD mutants Q69K, H72D, and L74A. Final pooled fractions from each purification is indicated by a bracket.

2.3.2. MBP-PupR CCSSD and PupR CCSSD Expression and Purification

MBP-PupR CCSSD was purified by sequential amylose affinity chromatography and SEC. The apparent molecular weight is 85.5 kDa based on the elution volume of the 78.0 ml SEC peak. This is approximately 1.27 times larger than the theoretical molecular weight of 67.4 kDa based on the amino acid sequence. The single SEC peak with a small shoulder and SDS-PAGE bands indicate the sample is mostly pure and homogenous MBP-PupR CCSSD with minimal contamination of free MBP (Fig. 2.4).

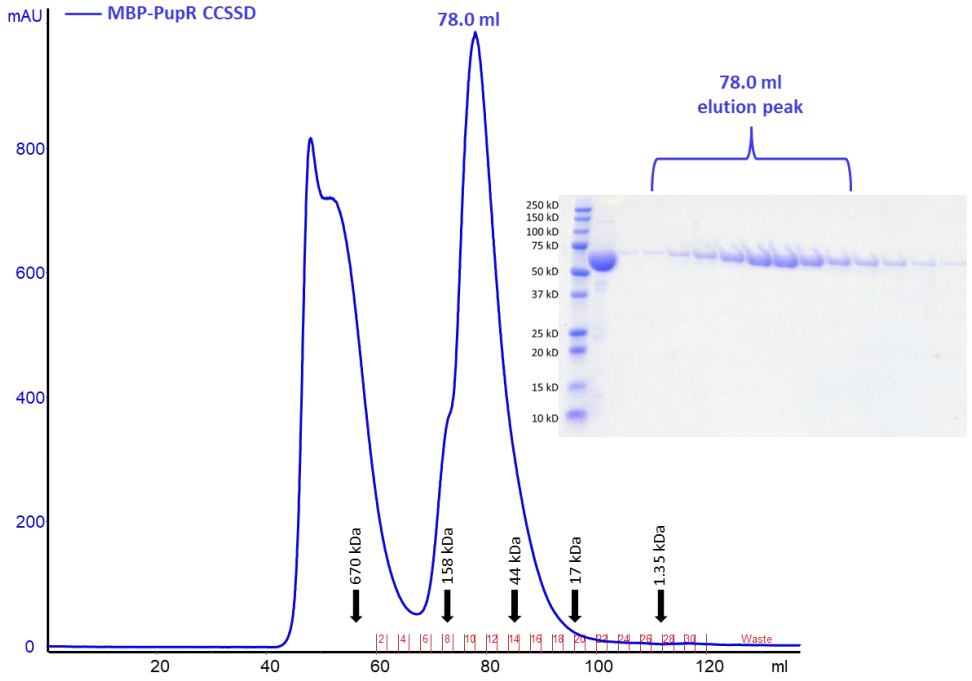

Figure 2.4. SEC chromatogram and related SDS-PAGE gel of MBP-PupR CCSSD. Positions of SEC standard elutions are indicated by arrows. MBP-PupR CCSSD eluted at a volume of 78.0 ml with a calculated molecular weight of ~85.5 kDa.

PupR CCSSD was purified by sequential amylose affinity chromatography with on-column TEV protease cleavage, followed by SEC. The apparent molecular weight is 22.2 kDa based on the elution volume of the 90.0 ml SEC peak. This is approximately 1.1 times smaller than the theoretical molecular weight of 24.1 kDa based on the amino acid sequence. The single SEC peak, has a small shoulder on the leading edge, but SDS-PAGE bands indicates the peak is mostly pure and homogenous PupR CCSSD with no contamination with free MBP (Fig. 2.5).

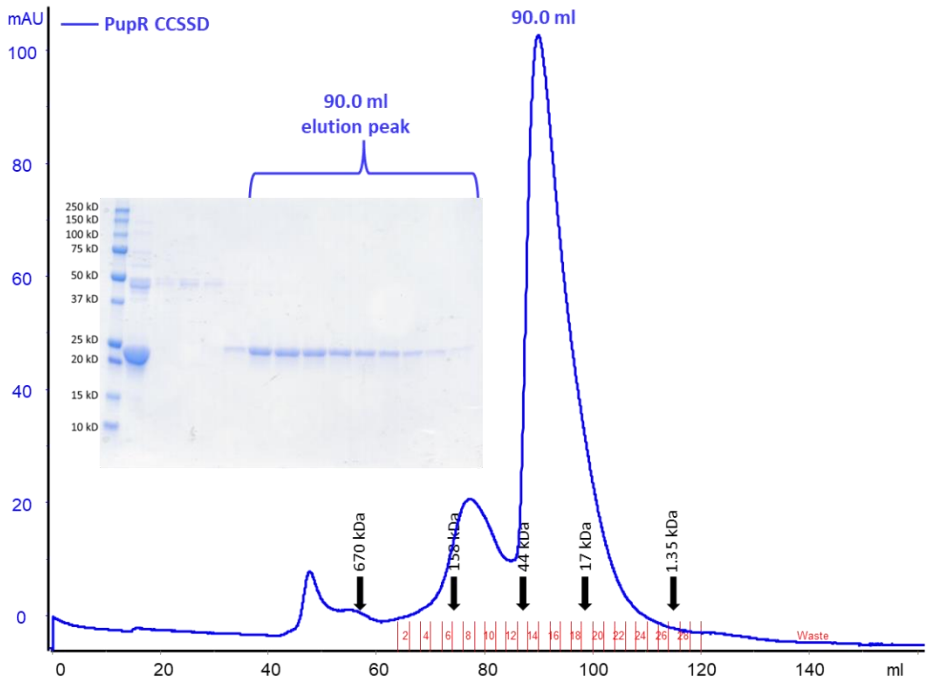

Figure 2.5. SEC chromatogram and related SDS-PAGE gel of PupR CCSSD. Positions of SEC standard elutions are indicated by arrows. PupR CCSSD eluted at a volume of 90.0 ml with a calculated molecular weight of ~22.2 kDa.

2.3.3. The PupR CCSSD Comprises Two Subdomains, Both of Which are Required for Binding the PupB NTSD

PupR domains delineated based on predictions of secondary structure using JPRED and transmembrane helix(ces) using HHMTOP, are: a cytoplasmic N-terminal anti-sigma domain (ASD), comprising residues 1– 82; a single-pass transmembrane helix, residues 86–104; and a periplasmic CCSSD, residues 110–324 (Fig. 2.6A) [57, 126, 127]. The CCSSD has two potential subdomains: residues 110–238, which constitute a subdomain named the CJM subdomain, and a second subdomain, comprising residues 250–324, that belongs to the STN domain family (SMART accession number SM00965) [128, 129]. However, when purified separately, these subdomains degrade rapidly and can only be individually purified as maltose-binding protein (MBP) fusion proteins, with the MBP-tagged STN still being very unstable.

PupB residues 45–130 comprise the NTSD (Fig. 2.6A) [92]. The role of each CCSSD subdomain in binding the NTSD was delineated by affinity pulldown assays using MBP-tagged CJM (PupR 110–238 or PupR 110–250) or STN (PupR 238–324 or PupR 250–324) subdomains and GSH S-transferase (GST)- tagged NTSD (PupB 49–128) fusion proteins. Although the complete CCSSD clearly binds to the NTSD (Fig. 2.6B), neither the isolated CJM nor STN subdomains associate with the NTSD (Fig. 2.6B). This indicates that individually, either the subdomains are insufficient for binding the NTSD, or that the subdomains are unfolded and binding-incompetent. Isothermal titration calorimetry (ITC) measurements indicate that the CCSSD and the NTSD bind in a 1:1 stoichiometry with an affinity (K_d) of 0.69 μM with a 68.3% confidence interval of [0.42, 1.11 μM] (values in square brackets indicate a 68.3% confidence interval (±1 standard deviation) for the mean value presented) (Fig. 2.7, Table 2.6). Our binding model includes a local incompetent fraction parameter during isotherm analysis due to CCSSD precipitation during ITC measurements and presence of residual MBP. The local incompetent fraction range was 0–12.8% among the triplicate experiments.

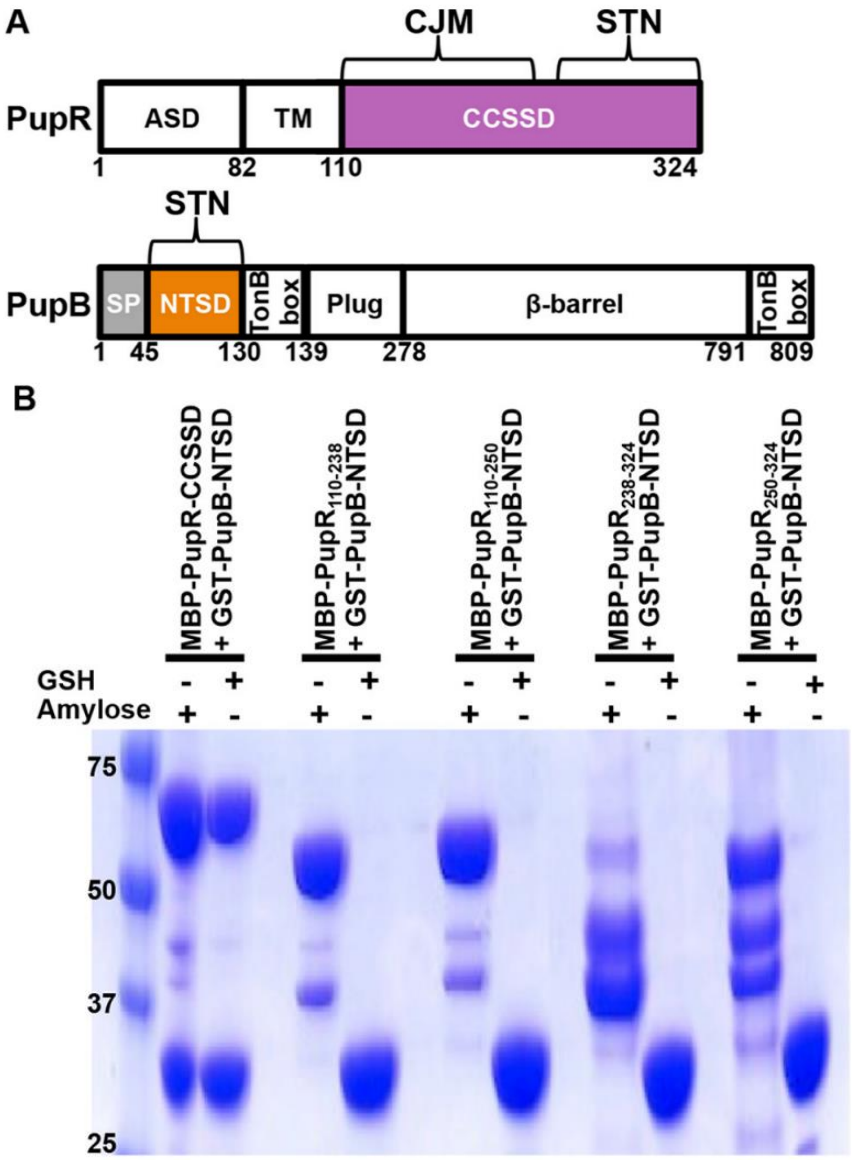

Figure 2.6. Interaction of PupR CCSSD truncations and PupB NTSD. A) domain organization of PupR (an ASD, transmembrane region (TM), and CCSSD)) and PupB (a signal peptide (SP), NTSD, TonB box (region that interacts with the TonB complex), plug, β-barrel, and C-terminal TonB box)). Regions included in the expression constructs are colored. B) affinity pulldown assays to detect interaction of GST-tagged PupB NTSD and different MBP-tagged PupR CCSSD fragments as indicated. Equivalent aliquots of the clarified lysate from a co-expression of the two component proteins were applied to either amylose affinity agarose or GSH-Sepharose resins. Each resin was washed, then protein was eluted and analyzed by Coomassie-stained SDS-PAGE. The + sign above each lane indicates which resin was used for each experiment. The masses (kDa) of molecular weight markers are indicated in the first lane.

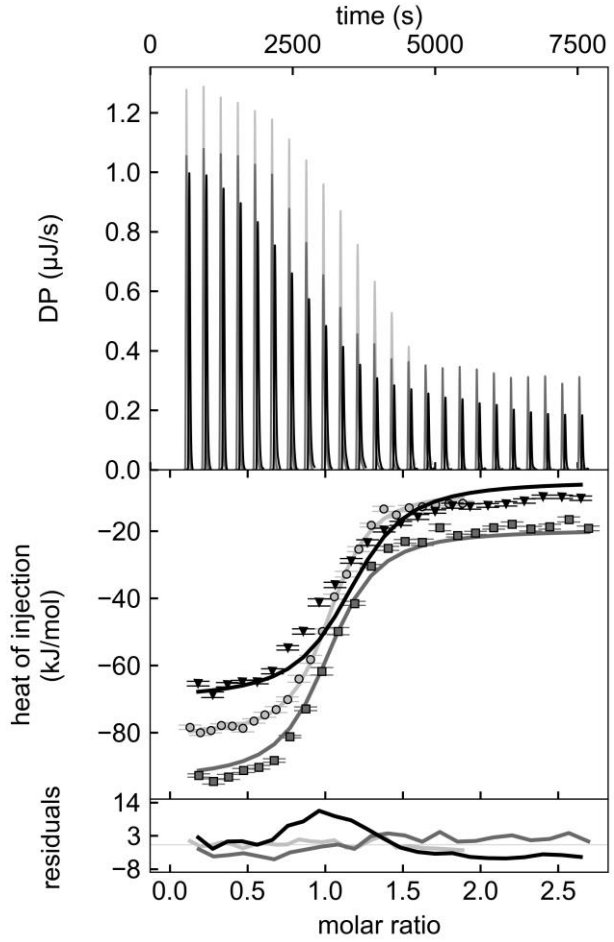

Figure 2.7. Global analysis of ITC isotherms for PupR CCSSD titrated into PupB NTSD. The hears of binding (top panel), the isotherms with the curves for the global model (middle panel), and residuals of the global model fit (bottom panel) for the triplicate experiments are shown in black, gray, and light gray.

Table 2.6. Thermodynamic parameters of the CCSSD:NTSD interaction as determined from ITC data using a global analysis in SEDPHAT. Mean values were determined from a global fit to a set of three ITC experiments.

	NTSD (µM)	**CCSSD (µM)**	**LIF[a]**	**K_d**	**ΔH (kJ/mol)**	**ΔS (J/mol·K)**	**ΔG (kJ/mol)**
Set 1 (3 runs)	28	220	0.128	0.69 [0.42, 1.11]	-73.99 [-80.99, -68.27]	-138.83 [-158.94, -122.93]	-33.990 [-35.196, -32.843]
	27.5	220	0.00				
	42	235	0.051				

[a] Local incompetent fraction (LIF).
[b] Values in square brackets indicate a 68.3% confidence interval (±1 S.D.) for the mean value presented.

2.3.4. Interaction of the PupR CCSSD with the PupB NTSD Stabilizes the Sigma Regulator

Analyses of the circular dichroism (CD) spectra of the isolated CCSSD reveal it has significant secondary structure (Table 2.7, Fig. 2.8A). The secondary structure content estimated from the CD spectra of the CCSSD:NTSD complex is comparable with the sum of secondary structure content estimated from the CCSSD and NTSD separately, suggesting that these domains do not undergo substantial secondary structure transitions upon binding (Table 2.7). The thermal denaturation CD curve of the CCSSD, recorded at the spectral minima of 216 nm, indicates it has a melting temperature (Tm) of 40.2 °C (Fig. 2.8B); however, the CCSSD precipitates during cooling renaturation. The thermal denaturation CD curves of the NTSD indicate it has a Tm of 52.8 (heating) and 62 °C (cooling) (Fig. 2.8C) and its thermal denaturation is reversible. Strikingly, when the CCSSD is complexed with the NTSD, thermal denaturation of the whole complex is reversible and the Tm of the complex increases to 51.4 or 52.9 °C for heating or cooling, respectively (Fig. 2.8D), demonstrating that binding of the NTSD stabilizes the CCSSD.

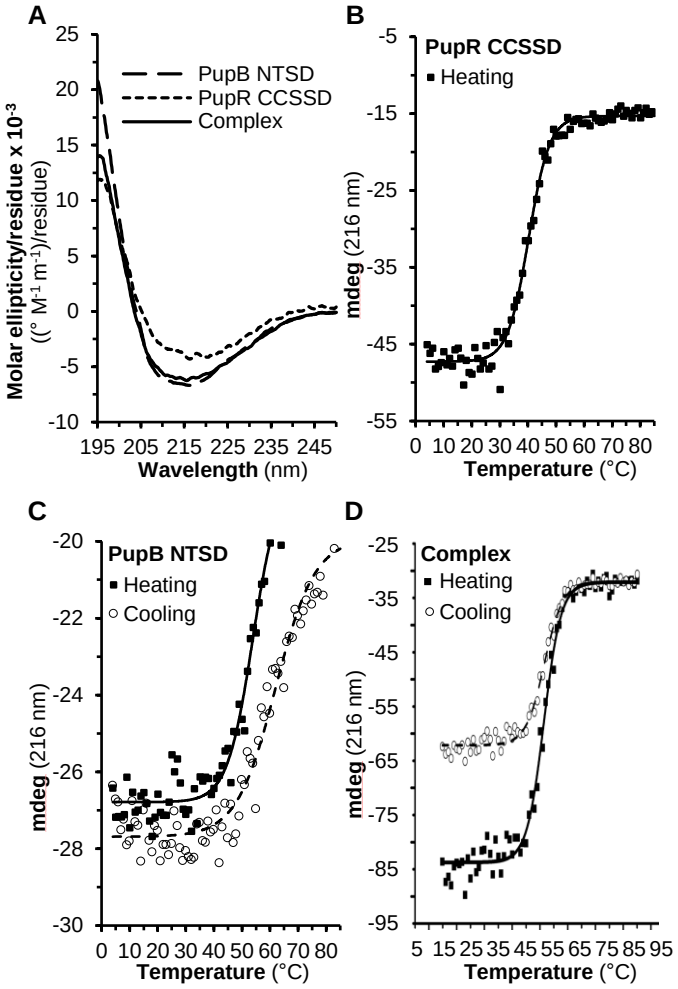

Figure 2.8. CD spectra and melting curves. A) CD spectra of PupB NTSD (dashes), PupR CCSSD (dots), and the complex (solid) B) PupR CCSSD melting curve C) PupB NTSD melting curve D) the complex melting curve. Unfolding (heating; black squares) and refolding (cooling; open circles) data points are shown. The Boltzmann fits to the melting curves are shown.

Table 2.7. Comparison of secondary structure content estimated from CD spectra analyses using CDPro and from DSSP assignments within PyMOL of the X-ray crystal structure.

	CD Analyses (N_{res})				X-ray Structure (N_{res})			
Protein	**Helix**	**Strand**	**Coil + Turn**	**Total**	**Helix**	**Strand**	**Coil + Turn**	**Total[a]**
CCSSD	16	89	113	218	31	112	76	219
NTSD	16	30	36	82	25	24	33	82
Complex	55	100	145	300	56	136	109	301

[a] Total number of residues indicates the full expressed protein, including any additional residues remaining after cleavage of affinity tags.

2.3.5. The X-ray Crystal Structure of the PupR CCSSD:PupB NTSD Reveals a Unique Fold and Topological Arrangement of Subdomains within the PupR CCSSD

A high-quality electron-density map of the CCSSD:NTSD complex was obtained by single-wavelength anomalous diffraction (SAD) phasing using selenium atoms incorporated into the CCSSD. Refinement of the final atomic model was completed at 1.56 Å resolution with Rwork = 15.0% and Rfree = 18.3% (Table 2.2). The final Se-Met and native models include residues 111– 323 of PupR, residues 49–128 PupB, 20 tartrate molecules, and 355 or 319 water molecules, respectively. The Se-Met and native proteins have practically identical structures, although there are some differences in interacting residues at the complex interface.

The two subdomains are clearly delineated in the CCSSD structure (Fig. 2.9).

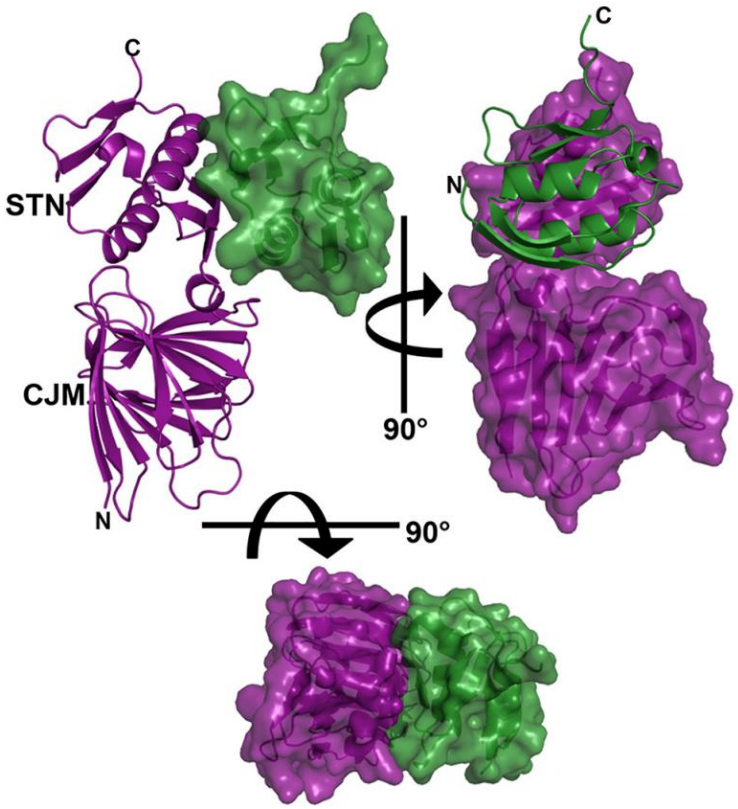

Figure 2.9. The X-ray crystal structure of the PupR CCSSD:PupB NTSD complex. Ribbon and transparent surface representations are colored purple for the PupR CCSSD and green for the PupB NTSD. The two CCSSD subdomains, the CJM and STN, are indicated.

The first subdomain, the CJM, comprising residues 110–238, has a novel all-β-fold that can be described as a twisted β-solenoid–like motif. A search through the PDB using DALI did not reveal any structure with a Z-score >5.6 that has been previously described in literature [117]. The CJM is comprised of two 7-stranded β-sheets linked by loops or β-arches: strands β2, β3, β6, β9, β10, β13, and β14 form an anti-parallel sheet, whereas strands β1, β4, β5, β7, β8, β11, and β12 form a mixed -sheet (Fig. 2.10A). The hydrophobic packing of the side chains from the two β-sheets stabilizes the core of the CJM subdomain. As expected from sequence analyses, the second subdomain, comprising residues 250–324, belongs to the STN domain family [128, 129]. It shares a common-fold, including two βαβ-repeat structural motifs, with the PupB NTSD (Fig. 2.10, B and C).

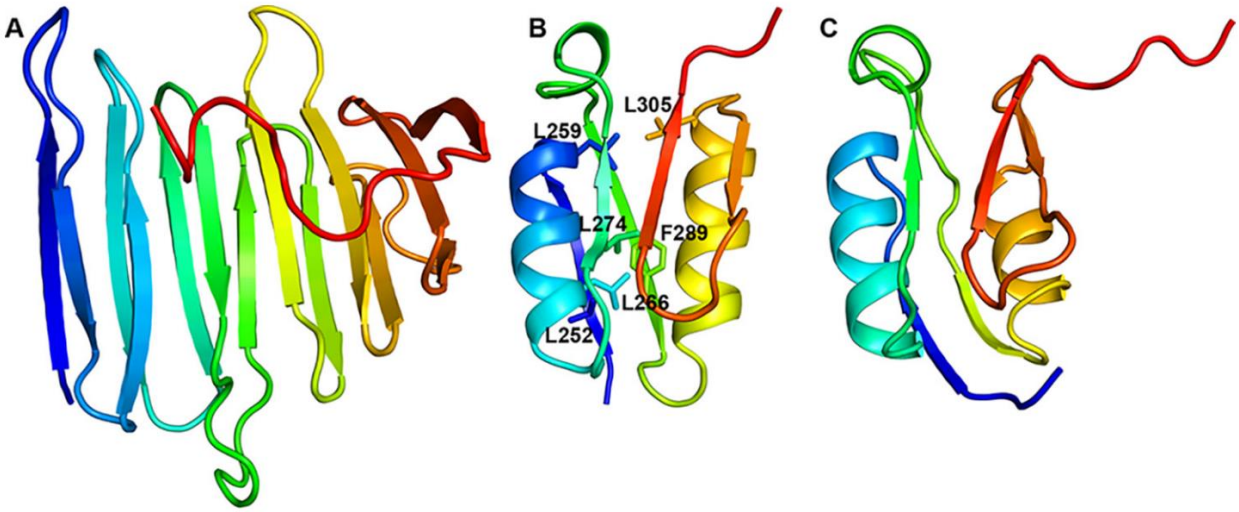

Figure 2.10. Unique structural features of the PupR CCSSD. All structures are displayed in ribbon, rainbow color-ramped from blue at the N terminus to red at the C terminus. A) the CJM subdomain has a novel all-β-fold. B) the STN subdomain of the CCSSD is shown with the conserved residues L252, L259, L274, L266, L305, and F289 from the "LLLV" region in stick. C) the PupB NTSD, displayed in a superimposable orientation to the STN subdomain in B.

A search of the SMART nonredundant database identifies over 8,000 proteins with STN domains, yet surprisingly, all these STN domains are arranged N-terminal to other domains within their respective proteins. Thus, the presence of an STN at the extreme C terminus of PupR

(Figs. 2.6A and 2.10) represents a new architectural arrangement of this domain type. Sequence conservation suggests that the CCSSD-fold is common among periplasmic sigma regulator proteins (Fig. 2.11).

The CJM and STN are connected via an 11-residue linker that is primarily unstructured, apart from a single helical turn. The total buried surface area between the two subdomains is 821.9 Å^2 with the interface stabilized by salt bridges between residues STN Arg268 and Asp265 to CJM Arg192 and Glu159, respectively (Fig. 2.12), and includes several partly or fully buried residues (Table 2.8).

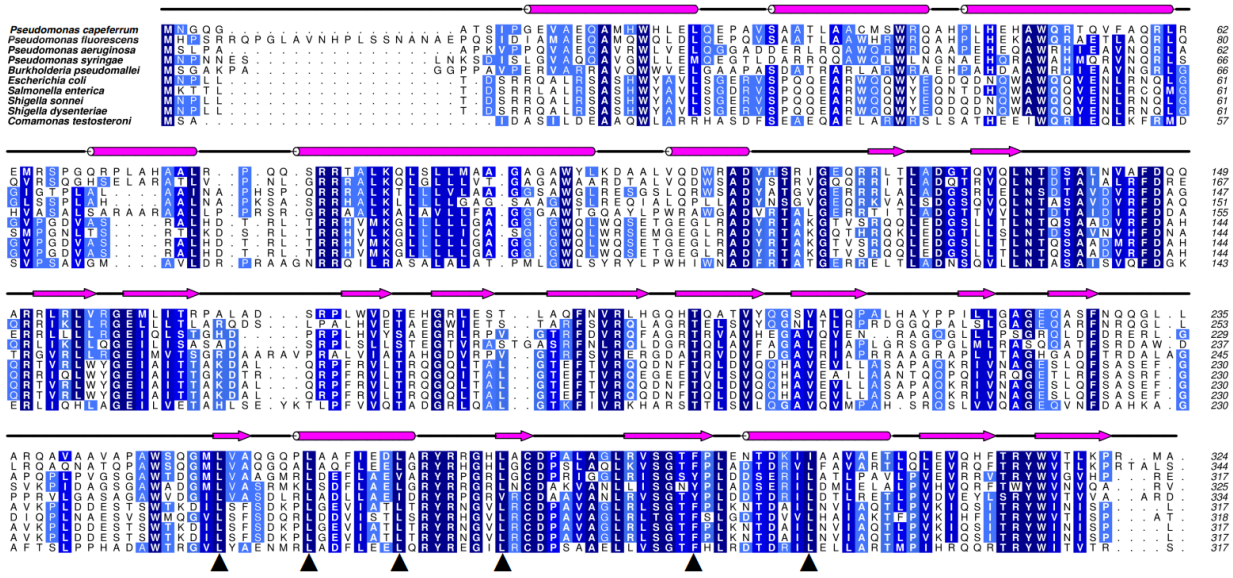

Figure 2.11. Sequence alignment and consensus secondary structure prediction of sigma regulator proteins from various proteobacteria with putative iron transport TBDTs. PupR (Uniprot ID Q52209, *Pseudomonas capeferrum*) was aligned with PupR (Q4KDP8, *Pseudomonas fluorescens*), FpvR (Q91192, *Pseudomonas aeruginosa*), FecR/PupR (Q48ML1, *Pseudomonas syringae*), FecR (Q63LI7, *Burkholderia pseudomallei*), FecR (P23485, *Escherichia coli*), FecR (A0A3V6D9V0, *Salmonella enterica*), FecR (Q3YU71, *Shigella sonnei*), FecR (B3WZ95, *Shigella dysenteriae*), and FecR (H1RKR8, *Comamonas testosteroni*). Invariant residues are highlighted in navy blue, and conserved residues in varying lighter shades of blue, with the lightest shade corresponding to the least conserved residues. Predicted secondary structure is displayed above the primary sequence, with cylinders, arrows and lines denoting helices, β-strands and coils, respectively. Conserved residues that stabilize the core of the PupR CCSSD STN and have previously been called the "LLLV" region are indicated (black triangles).

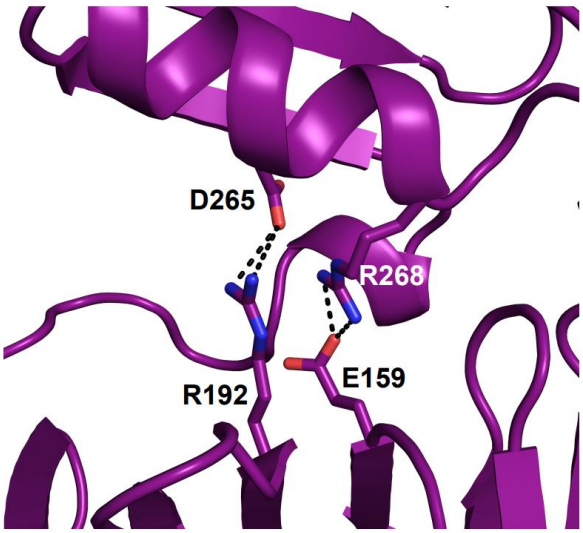

Figure 2.12. Salt bridges stabilizing the interface between the CJM and STN subdomains. Residues involved in salt bridges are shown in stick.

Table 2.8. Buried surface area per residue at the CCSSD CJM:STN interface.

CJM residue	**% buried**
I120	39.4
G122	30.4
Q123	19.2
N137	100.0
T138	97.0
D139	10.8
G158	23.7
E159	62.2
R192	64.1
H194	6.6
Linker	
A246	64.0
W247	65.9
Q249	9.4
G250	81.8
STN residue	
M251	57.7
L252	24.0
V253	21.7
E264	10.3
D265	42.5
R268	69.5
Y269	81.5
L291	52.1

2.3.6. The PupR CCSSD:PupB NTSD Interaction Interface

The PupB NTSD shares 37.1% sequence identity with the PupA NTSD, 30.5% sequence identity with the FecA NTSD, and 28.4% sequence identity with the FpvA NTSD. As expected, the PupB NTSD structure in the CCSSD:NTSD complex is similar to the *P. capeferrum* PupA NTSD and *E. coli* FecA NTSD structures, determined using NMR, and found in the structures of the complete *P. aeruginosa* FpvA transducer [41, 130-132]. These NTSDs superimpose with root-mean-square deviations (RMSD) ranging from 1.29 to 2.58 Å over 72– 80 Cα atoms.

The interface between the CCSSD and the NTSD has a substantial buried surface area of ~1438.6 $Å^2$ and involves residues from the linker, β17 and α2 of the CCSSD and α1 and β2 of the NTSD (Fig. 2.9). The interface is stabilized by salt bridges between NTSD His72 and Glu83 to CCSSD Glu292 and Arg284, respectively (Fig. 2.13, A and B), as well as an extensive hydrogen bonding network (Fig. 2.13, C–E, Table 2.9). Hydrophobic interactions at the interface include two extensively buried residues, NTSD Leu74 (84% buried) and CCSSD Met251 (98% buried) (Fig. 2.13, F and G).

Previously, residues 247–268 within the periplasmic domain of the homologous sigma regulator, FecR, were named the LLLV region as this region includes conserved leucine and valine residues (Fig. 2.11) [59]. Mutation of these conserved hydrophobic residues to proline was shown to abrogate binding to the FecA NTSD [59]. Our structure shows that this LLLV region corresponds to the hydrophobic core of the PupR STN subdomain (Fig. 2.10B) and does not directly mediate the interaction with the NTSD. Rather, our structure indicates that these residues are essential for the structural integrity of the STN and that mutation of these residues to proline likely disrupts secondary structure and causes unfolding of the subdomain, preventing it from binding to the NTSD.

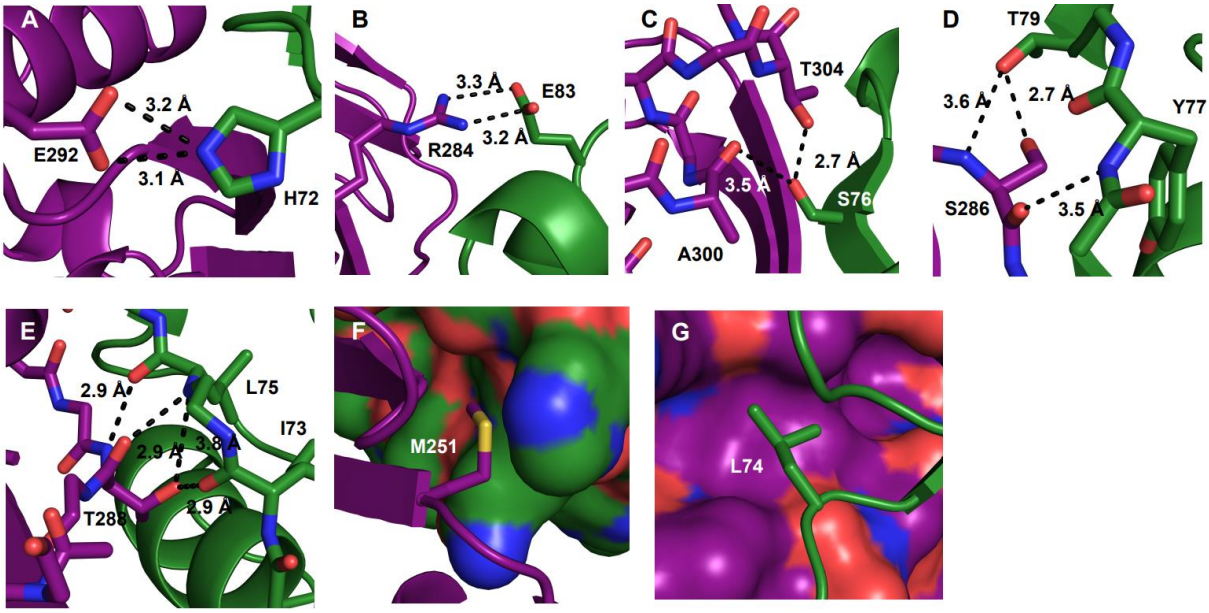

Figure 2.13. Interactions stabilizing the PupR CCSSD:PupB NTSD interface. Salt bridges between (A) NTSD H72 and CCSSD E292, (B) NTSD E83 and CCSSD R284; hydrogen bonding between (C) NTSD S76 and the CCSSD, (D) CCSSD S286 and the NTSD, (E) CCSSD T288 and the NTSD; and hydrophobic packing between (F) CCSSD M251 and the NTSD and (G) NTSD L74 and the CCSSD. Residues are shown in stick. Hydrogen bonds or salt bridges are denoted by dashes.

Table 2.9. Summary of hydrogen bonds stabilizing the PupB NTSD:PupR CCSSD interaction.

PupB NTSD	H-bond Length (Å)	PupR CCSSD
L75-N	2.9	T288-O
L75-N	3.8	T288-OG
L75-O	2.9	T288-N
I73-O	2.9	T288-OG
S76-OG	3.5	A300-O
S76-OG	2.7	T304-OG
T77-N	3.5	S286-OG
T79-OG	2.7	S286-OG
T79-OG	3.6	S286-N

2.3.7. Small Angle X-ray Scattering Coupled to Size Exclusion Chromatography (SEC-SAXS) Indicates the PupR CCSSD is Partially Flexible

SEC-SAXS was used to determine and compare low-resolution structure and solution properties such as molecular mass and oligomeric states of the CCSSD and CCSSD:NTSD

complex (Fig. 2.14, Table 2.5), and were performed concurrently with crystallographic experiments. Given the instability of the CCSSD alone in solution and secondary structure estimates from CD analysis, we hypothesized that the CCSSD is conformationally heterogeneous with multiple orientations between the subdomains when not bound to the NTSD. Linearity of the Guinier plot in the $0 < q < 0.003$ Å verifies the absence of aggregation in the samples (Fig. 2.14A, Fig. 2.15). The radius of gyration (Rg), calculated from the Guinier region (Fig. 2.14A), is 22 Å for the CCSSD and 26 Å for the CCSSD:NTSD complex, whereas the distance distribution function, P(r), indicates a Dmax of 75 Å for the CCSSD and 87 Å for the complex (Fig. 6B). These values agree with the theoretical Rg calculated from a CCSSD-only model, and for the CCSSD:NTSD complex crystal structure. The Kratky plots indicate that both samples are partially flexible in solution (Fig. 2.14, C and D). The molecular mass of the CCSSD, estimated from the SAXS data is 23–29 kDa (theoretical mass = 24 kDa), indicating that the CCSSD is monomeric in solution (Fig. 2.14E, Table 2.5). The molecular mass of the CCSSD:NTSD complex, estimated from the SAXS data is 33– 40 kDa (theoretical mass = 32.3 kDa), suggesting that the primary species in solution is a 1:1 complex (Fig. 2.14F, Table 2.5), consistent with the crystal structure and ITC data.

SAXS is also useful for evaluating the internal flexibility of multidomain proteins. The experimental SAXS curve of the CCSSD exhibited weak agreement with the theoretical curve calculated from the CCSSD crystal structure alone (Fig. 2.14E). The possibility of conformational heterogeneity of the PupR CCSSD in solution was explored using MultiFoxS to generate 10,000 conformers, maintaining the CJM and STN subdomains of the CCSSD as rigid bodies and defining residues 232–250 as a flexible linker. The experimental data best fit a two-state model, wherein the predominant conformation has a Rg of 21.7 Å and comprises 87% of

the solution state, and the secondary species has a Rg of 18.7 Å and is sampled in 13% of conformations. The predominant species of the best-fitting conformers from each model improved the χ value to 1.24, and significantly improved the goodness of fit around q = 0.2 $Å^{-1}$, indicating structural flexibility between the two subdomains of the CCSSD (Fig. 2.16). Similarly, whereas the scattering curve calculated from the complex fits better than that for the CCSSD alone, the fit of the complex is not perfect (Fig. 2.17), suggesting50 there could be inter-subdomain or inter-protein flexibility not accounted for by the crystal structure (Fig. 2.14F). MultiFoxS was used to assess various regions of potential flexibility and only marginally improved the fit (χ = 1.2–1.8).

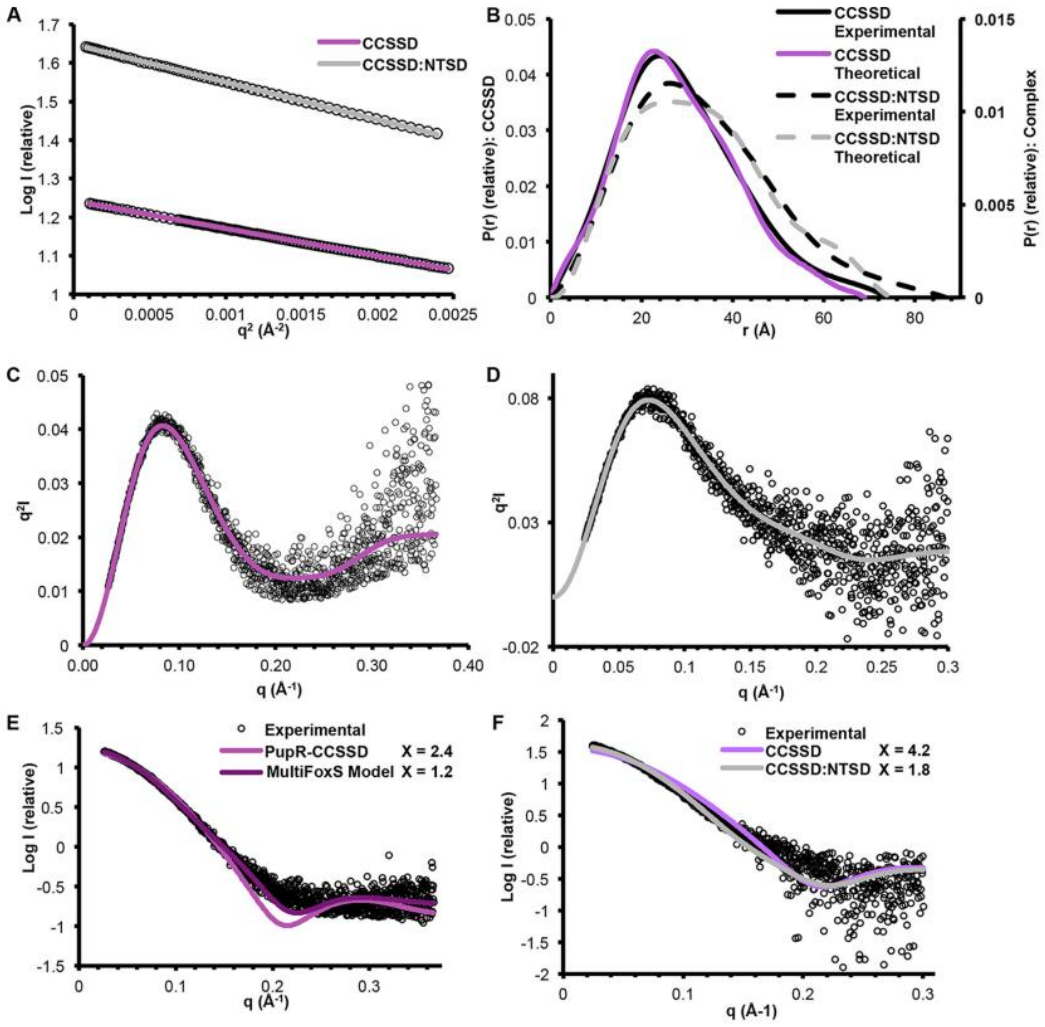

Figure 2.14. SEC-SAXS analysis of the CCSSD and CCSSD:NTSD complex. A) Guinier plot of the low q region. B) distance distribution P(r) for the experimental data (black lines), the theoretical curve calculated from the CCSSD crystal structure (purple line), and the CCSSD:NTSD complex (gray dashed line). Kratky plots of the (C) CCSSD and (D) the CCSSD:NTSD complex are shown. E) experimental scattering profile for the CCSSD, fit with the theoretical scattering profiles calculated from the rigid crystal structure of the CCSSD only (purple) and the flexible model derived from MultiFoxS, generated by structural conformation sampling (dark purple). F) experimental scattering profile for the complex, fit with the theoretical scattering profiles calculated from crystals structures of the CCSSD only (purple) and the CCSSD:NTSD complex (gray). χ values for each fit are indicated.

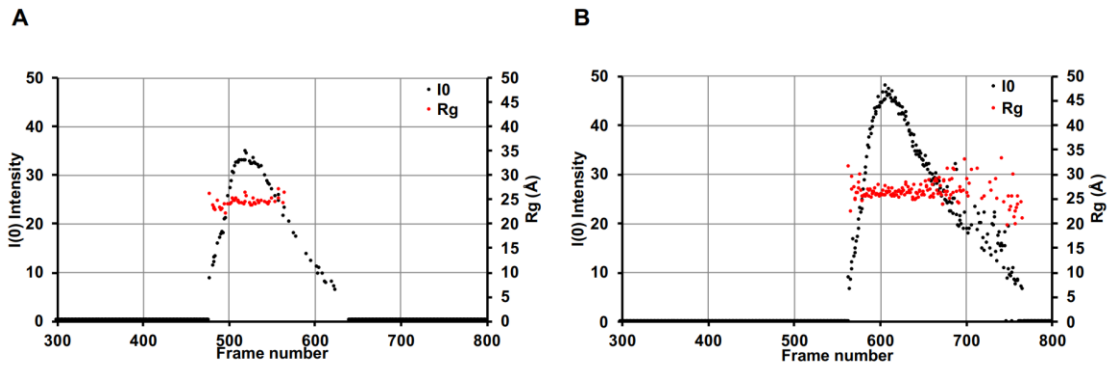

Figure 2.15. SEC-SAXS analysis of the concentration dependence of Rg for the (A) CCSSD and the (B) CCSSD:NTSD complex. Rg (red) and I(0) (black) plotted by frame number. For each, the Rg remains consistent with changing protein concentrations.

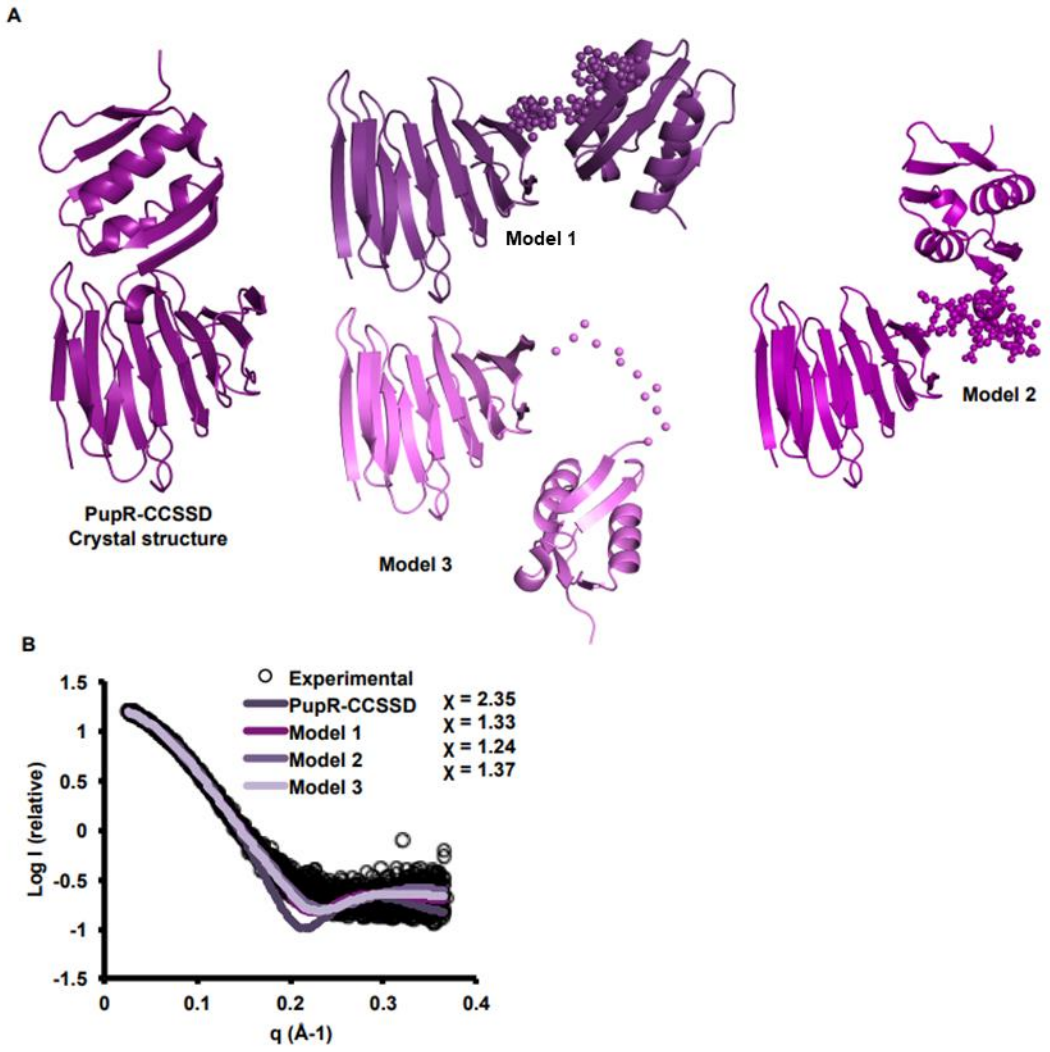

Figure 2.16. Conformational heterogeneity of the PupR CCSSD in solution. (A) Three PupR CCSSD models were assessed and compared with the CCSSD crystal structure: Model 1, which defined the linker region as residues 239-250; Model 2, which defined the linker region as residues 232- 250; and Model 3, the EOM output. The CJM domain of each model is shown in a superimposable orientation with that of the PupR CCSSD crystal structure. The two subdomains of the CCSSD are shown in shades of purple ribbon, with linker regions of Models 1, 2, and 3 displayed as non-bonded spheres. B) Experimental scattering profile of the CCSSD (black circles), fit with theoretical scattering profiles calculated from the CCSSD crystal structure, and Models 1-3, generated by structural conformation sampling. χ values for each fit are indicated.

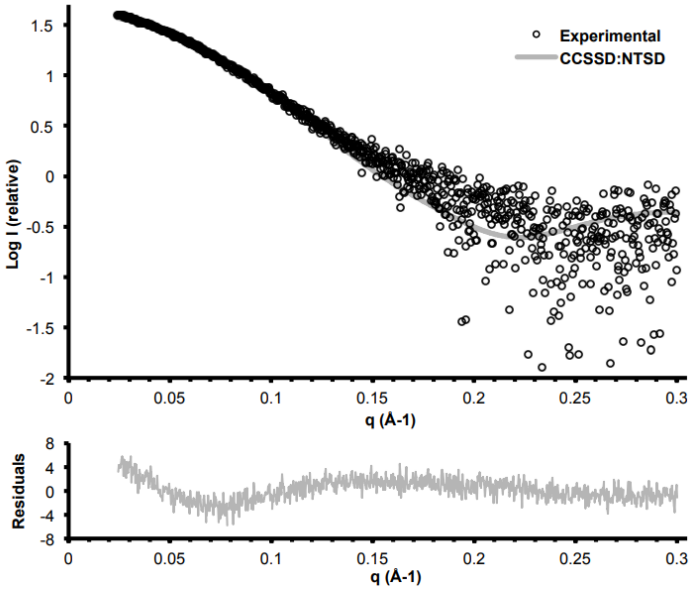

Figure 2.17. Experimental scattering profile of the CCSSD:NTSD complex and the fit to the theoretical scattering curve of the CCSSD:NTSD crystal structure. Top panel shows the experimental scattering profile (black circles) and the fit of the theoretical scattering profile calculated from the CCSSD:NTSD crystal structure (gray line). Bottom panel shows the plot of the residuals of the fit (gray) to the experimental scattering curve.

2.3.8. Confirmation of the PupR CCSSD:PupB NTSD Interaction Interface

The importance of key residues at the complex interface identified from the structure was qualitatively assessed by generating the following point mutations: NTSD residues Q69K, H72D (Fig. 2.13A), and L74A (Fig. 2.13G), and CCSSD residues M251A (Fig. 2.13F), S286A (Fig. 2.13D), and T288A (Fig. 2.13E). Residues Gln69 and His72 were mutated to the corresponding residues of the homologous, but signaling incompetent, PupA NTSD. The pulldown assays show that the H72D, L74A, and M251A mutations completely disrupt or significantly weaken the CCSSD:NTSD interaction, whereas S286A and T288A appear to limit, but not completely abrogate, the interaction (Fig. 2.18).

Consistent with the pulldown assay results, ITC results showed the complete disruption of the PupR CCSSD:PupB NTSD interaction with the L74A mutation and ~22-fold weakening of the interaction with the H72D mutation (Table 2.10). The PupB NTSD Q69K mutation did not

significantly alter the interaction affinity (Table 2.10). The PupR CCSSD T288A mutation decreased the binding affinity by ~10-fold (2.10). The S286A and M251A mutations proved too unstable to monitor interactions with the PupB NTSD further. Analysis of the Q69K, H72D, and L74A mutants depict a minor decrease in helicity for Q69K and H72D point mutants (Table 2.11, Fig. 2.19). However, melting and renaturation temperatures determined by thermal denaturation appear to vary little from the wild type PupB NTSD indicating the mutants do not undergo a major conformation change (Table 2.12, Fig. 2.20).

Interestingly, a polar interaction linking NTSD His72 and CCSSD Glu292 is critical for interaction between the two proteins, but the atoms involved are variable. In the native crystal structure, the Nε2 of the His72 imidazole ring forms a salt bridge with Glu292 Oε1 and Oε2 (Fig. 2.15). However, in the Se-Met– derivative crystals, the interaction is indirect, with the Glu292 side chain being replaced by a bridging water molecule that links the Nε2 of the His72 imidazole ring to the backbone amide of Leu291, the backbone amide of Glu292, and the backbone carbonyl of Gly250. The Glu292 side chain adopts a different conformer with the closest atom, Oε2, shifting 4.7 Å from His72. These results suggest that in addition to the complementary surfaces, a polar interaction at this position is critical to the interaction.

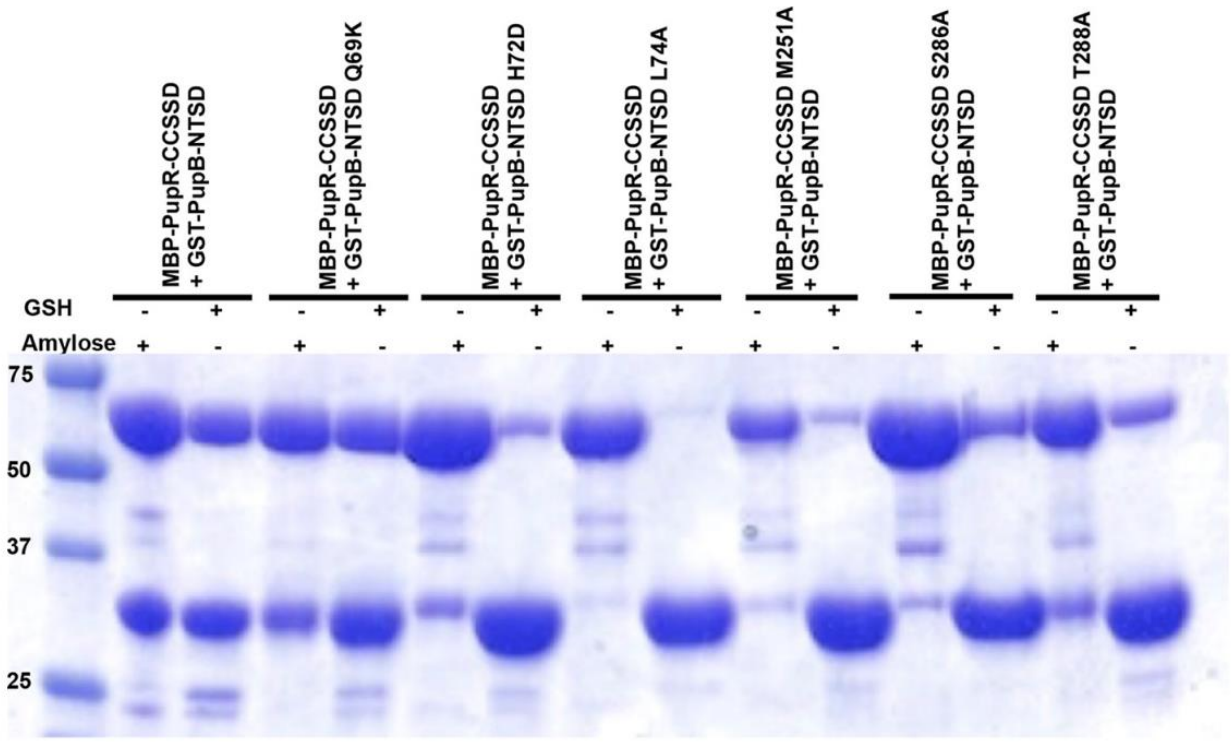

Figure 2.18. Affinity pulldown assays to detect interaction between different GST-tagged PupB NTSD and MBP-PupR CCSSD mutants. Wild-type interaction between the PupR CCSSD and the PupB NTSD (second and third lanes). Residues stabilizing the PupR CCSSD:PupB NTSD interface were mutated as follows PupB Q69K (fourth and fifth lanes), PupB H72D (sixth and seventh lanes), PupB L74A (eighth and ninth lanes), PupR M251A (10th and 11th lanes), PupR S286A (12th and 13th lanes), and PupR T288A (14th and 15th lanes). The Coomassie-stained SDS-PAGE gel is shown. The + sign above each lane indicates which affinity resin was used for each experiment, as in Fig. 1. The masses of molecular weight markers are indicated in the first lane.

Table 2.10. Binding affinity comparison for the CCSSD:NTSD mutants as determined by ITC. Data analyzed by NanoAnalyze.

NTSD	CCSSD	NTSD (μM)	CCSSD (μM)	K_d
WT	WT	27.5-42	220-235	0.79 ± 0.14
WT	T288A	22-41	155-232	8.09 ± 2.20
Q69K	WT	20-30	186-230	0.88 ± 0.27
H72D	WT	35-42	160-180	17.70 ± 0.27
L74A	WT	No Interaction Detected		

Table 2.11. Comparison of secondary structure content estimated from CD spectra analyses using CDPro.

	CD Analyses (Nres)			
Protein	**Helix**	**Strand**	**Coil + Turn**	**Total**
WT	16	30	36	82
Q69K	10	31	41	82
H72D	9	31	42	82
L74A	17	30	35	82

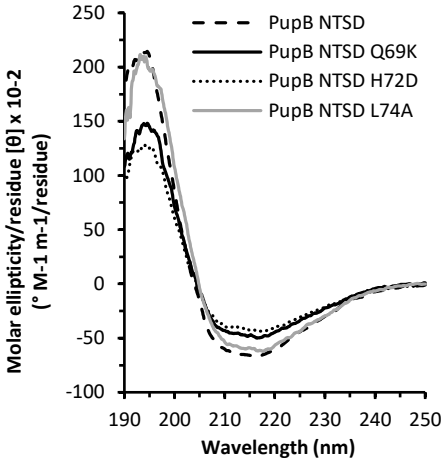

Figure 2.19. CD comparisons of PupB NTSD and PupB NTSD mutants. PupB NTSD (dashes), PupB NTSD Q69K (solid black), PupB NTSD H72D (dots), and PupB NTSD L74A (solid grey) are depicted.

Table 2.12. CD thermal denaturation comparison of PupB NTSD WT and point mutants.

Protein	**Tm (melting)**	**Tm (cooling)**
WT	52.8	62.0
Q69K	56.5	57.1
H72D	51.3	51.2
L74A	53.4	55.4

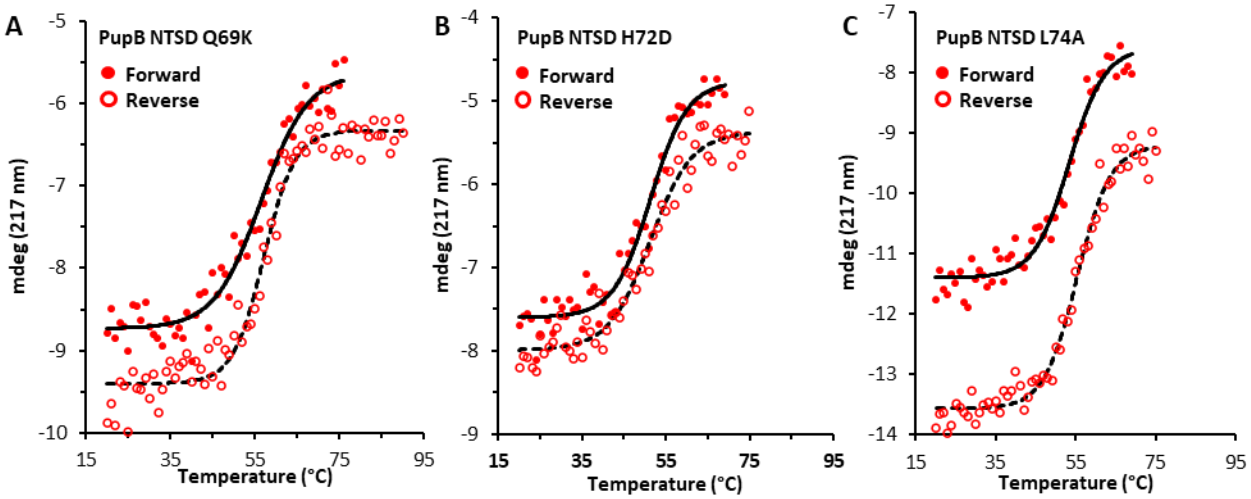

Figure 2.20. CD thermal denaturation comparisons of PupB NTSD point mutants; A) PupB NTSD Q69K B) PupB NTSD H72D C) PupB NTSD L74A.

2.4. Discussion and Conclusions

Our structure of the CCSSD:NTSD complex and our biophysical data answer several outstanding questions about the mechanism of CSS and help resolve conflicting hypotheses for the interaction between a sigma regulator and a TonB-dependent transducer. Our results reveal the CCSSD is comprised of two structured subdomains, the CJM and STN, which are linked by an 11-residue, conformationally flexible linker. Furthermore, our structure and pulldown assays using various PupR CCSSD truncations indicate that the CJM and STN are both required for binding the PupB NTSD *in vitro*. Notably, PupR STN residues analogous to the FecR LLLV region, comprising residues 247–268, that were previously reported to be critical for binding to the FecA NTSD, correspond to the PupR STN subdomain hydrophobic core essential for structure integrity (Fig. 2.10) and do not directly mediate the interaction with the NTSD [59].

In contrast to the information provided here, a recent NMR study investigating the interaction of the C-terminal domain (CTD) of sigma regulator HasS with the NTSD of its cognate transducer HasR, members of the heme acquisition system (Has) of *Serratia marcescens*, suggests that the HasS CTD is partially disordered and contains a region that may

interact with the inner membrane [42]. However, the HasS CTD is analogous to the structured STN subdomain defined here. Our studies show that the STN subdomain is unstable in the absence of the CJM, and when not bound to the NTSD. Consistent with our observations, purification of the HasS CTD involved refolding of protein expressed into inclusion bodies. In the same study, chemical shift changes on the HasR NTSD were thought to indicate a "disordered wrapping mode" brought about by interaction with a partially disordered region of HasS [42]. Our CD and SAXS data both indicate that whereas the PupR CCSSD in solution displays some flexibility in the 11-residue linker between the CJM and STN subdomains, the domain is largely folded even in the absence of NTSD binding. CD analyses of the isolated CCSSD in solution indicates the secondary structure content estimated is comparable with that of the CCSSD crystallized in complex with the NTSD. Indeed, comparison of secondary structure content of the isolated CCSSD and NTSD estimated via CD to that of the CCSSD:NTSD crystal content confirms that there are no dramatic changes in secondary structure upon complex formation. Last, α2 of the STN subdomain of the CCSSD packs against the NTSD. Hence, it is unlikely this region interacts with the inner membrane. Thus, our data appears to preclude the proposed disordered wrapping mode for association, and instead demonstrates that both the CCSSD and NTSD are ordered and identifies the specific structural elements of each domain responsible for the interaction.

NTSD residues involved in the interaction are on a surface defined by α2 and β2 (PupB residues 60– 80). Our site-directed mutagenesis of residues in this region, particularly His72 and Leu74, confirm the role of this region in binding. Analysis of mutant secondary structure and melting temperatures confirmed a folded NTSD and weakened binding affinities measured by ITC were due to changes at the interaction interface and not an unfolding event. This is in

contrast to previous studies with homologous NTSDs that suggest a region defined by the C terminus of α1 and the β3-α2 loop, which does not map to the CCSSD:NTSD interface in our crystal structure, is involved in interaction with the sigma regulator [40, 58, 133].

Finally, data showing activation of CSS by regulated intramembrane proteolysis indicate fragments of sigma regulators are present even under nonsignaling conditions [76, 78]. Our research on the PupR sigma regulator provides a rationale for this phenomenon. It demonstrates that the CCSSD alone is highly dynamic and consequently, sensitive to proteolysis, but is stable when in complex with the NTSD. Therefore, until a transducer is located and bound, and the CCSSD stabilized, it may be nonspecifically proteolyzed. Together, our data leads us to propose a new model for the mechanism of the sigma regulator in CSS: this CSS system may be "primed" for activation, meaning the CCSSD must be stabilized by interacting with the NTSD so that it cannot be nonspecifically degraded [76, 78]. Binding of siderophore to PupB induces conformational changes in the CCSSD:NTSD complex, causing the CCSSD to be recognized by a site-1 protease such as Prc, leading to initiation of regulated intramembrane proteolysis and subsequent cleavage by a site-2 protease (RseP) to release the ASD:sigma factor complex.

3. BIOPHYSICAL ANALYSIS OF CELL-SURFACE SIGNALING IN THE MODEL FERRIC CITRATE, FEC, PATHWAY

3.1. Introduction

Gram-negative CSS pathways contain three key components including the outer membrane TonB-dependent transducer (TBDT), the inner membrane sigma regulator, and the extra-cytoplasmic function (ECF) sigma factor [1, 47]. Mechanisms for signal transduction across the inner membrane of these highly conserved pathways have been disputed. However, the consensus is that a change in interactions between the sigma regulator and N-terminal signaling domain (NTSD) of the outer membrane TBDT induces the RIP of the sigma regulator [76-78, 87, 88]. This RIP leads to the release of the ECF sigma factor and upregulation of transcription.

Originally, it was thought that upon signal activation the sigma regulator interacted with the TBDT NTSD, propagating a signal across the inner membrane for transcriptional upregulation [47]. However, this is not supported by our recent studies of the *Pseudomonas capeferrum* Pup CSS pathway. As shown in the previous chapter, the PupR periplasmic domain, termed the C-terminal CSS Domain or CCSSD is sigma regulator, PupR, is unstable on its own and prone to proteolytic degradation [45]. Complex formation with the Pup TBDT, PupB, stabilizes the PupR CCSSD [45]. This suggests a CSS mechanism in which the PupR CCSSD complexes with the PupB NTSD prior to signal activation in a 'primed' state and signal activation would cause dissociation of the PupR:PupB complex, facilitating RIP of the CCSSD, and release of the ECF sigma factor.

However, this 'primed' mechanism has yet to be demonstrated in homologous CSS pathways. Notably, there are important differences between diverse sigma factors. For example, in the *P. putida* Iut system, the sigma regulator and ECF sigma factor are a single protein, IutY

[46, 78]. IutY is composed of a cytoplasmic N-terminal sigma factor domain linked by a transmembrane helix to a periplasmic anti-sigma C-terminal domain, like that of the PupR CCSSD [78]. In contrast, the more commonly known *P. aeruginosa* ferripyoverdine (Fpv) pathway contains a sigma regulator, FpvR, that is architecturally similar PupR, but interacts with multiple ECF sigma factors [26, 47, 134]. Additionally, FpvR contains non-conserved autoproteolytic Gly-Thr residues within the FpvR CCSSD, as seen in FoxR [89, 90]. Finally, one of the most well-known CSS pathway, the *Escherichia coli* ferric citrate or Fec CSS pathway, closely resembles that of the Pup pathway. The Fec sigma regulator, FecR, is architecturally similar to PupR, and interacts with only one ECF sigma factor [135, 136]. However, like the Fpv and Fox sigma regulators, FecR contains the non-conserved Gly^{181}-Thr^{182} residues which induces the autoproteolysis of the FecR CCSSD [89, 90].

Therefore, to truly understand CSS mechanisms of signal transduction, multiple homologous systems should be investigated. Here we assess the binding of the FecR CCSSD to the FecA NTSD with the wildtype and with a non-autoproteolytic T182A mutant using pulldown assays and ITC. Additionally, we characterize the low-resolution structural data of the FecA NTSD, FecR CCSSD, and FecA NTSD:FecR CCSSD T182A with the use of SEC-SAXS. Finally, we quantify the thermal stability of the FecR CCSSD T182A in the presence of the FecA NTSD by CD thermal denaturation. Together, these early insights into FecR CCSSD interaction with FecA NTSD suggest a similar ‘primed’ signaling method as observed in the Pup system and a potential universal mechanism for Gram-negative CSS.

3.2. Materials and Methods

3.2.1. Cloning, Expression, and Purification of FecA NTSD

The FecA NTSD construct was designed based on a FecA NTSD construct used to determine its NMR solution structure as well as secondary structure predictions using JPred and homologous NTSD domains [40, 126]. The gene sequence encoding the *fecA NTSD* was amplified from *E. coli* K12 genomic DNA, using primers 5'-CTG TAT TTT CAG GGC GGA TCC GCA CAG GTT AAT ATC GCA CCG-3' and 5'-GTG GTG GTG GTG GTG GTG GTG CTC GAG TCA CTT TTG GTG CGG GCG CGG-3', and subsequently cloned into pET41. The expression construct, pET41-FecA NTSD, contains an N-terminal GST tag followed by a TEV-protease recognition sequence (ENLYFQG) and the inserted FecA NTSD.

The pET41-FecA NTSD construct was used to transform chemically competent *E. coli* BL21 (DE3) pLysS cells for protein expression. 50 µL and 200 µL aliquots of the transformation mixture were used to inoculate two LB agar plates supplemented with 15 µg/ml kanamycin. Plates were inoculated overnight at 37 °C. A single colony was picked and added to a 70 mL culture of LB media supplemented with 15 µg/ml kanamycin and incubated at 37 °C overnight. For protein expression, 10 mL of overnight culture was added to 1 L of LB media supplemented with 15 µg/ml kanamycin. This culture was incubated at 37 °C with shaking at 200 rpm until it reached an OD_{600} of 0.7-0.9. Cultures were then induced with 0.5 mM IPTG and incubated overnight at 20 °C. Following incubation, cells were harvested by centrifugation at 4,000 x g, washed with 25 mM Tris HCl pH 7.8, 150 mM NaCl, 2 mM DTT, and stored at -80 °C.

Cell pellets were resuspended in 25 mM Tris HCl pH 7.8, 150 mM NaCl, 2 mM DTT and lysed by sonication with a Branson Sonifier 450 sonicator. Lysate was clarified by centrifugation at 20,000 x g for 35 min and passed over Glutathione Sepharose 4B resin (Cytiva) equilibrated in

lysis buffer. The column was washed with excess lysis buffer. Recombinant GST-TEV protease was applied to the column and incubated at 4 °C overnight to release the FecA NTSD. Lysis buffer was added to wash free cleaved FecA NTSD from the column. The FecA NTSD was further purified by SEC over a Superdex 75 increase 10/300 GL column (Cytiva) using an isocratic gradient consisting of 25 mM Tris HCl pH 7.8, 150 mM NaCl. Pure FecA NTSD was concentrated to 14.8 mg/ml, and flash frozen in 20 – 50 µl aliquots in liquid nitrogen prior to storage at -80 °C. Protein purity was determined to be >95% by SDS-PAGE using a 4-20% TGX SDS-PAGE gel (Bio-Rad) and Coomassie Blue staining [93].

3.2.2. Cloning, Expression, and Purification of WT MBP-FecR CCSSD

The FecR CCSSD construct was designed based on our PupR CCSSD construct and secondary structure predictions using JPred to adjust potential domain boundaries [45, 126]. The *fecR CCSSD* gene was amplified with primers 5'-TTT TCA GGG CGC CAT GGA TCC AGA AGG TCT GCG GGC AGA TTA C-3' and 5'-GCC AAG CTT GGT ACC GCA TGC CTC GAG TTA CAG TGG TGA AAT GTT TAT-3', from *E. coli* K12 genomic DNA and subsequently cloned into pMBP-parallel1 via Gibson assembly between the restriction sites BamHI and XhoI [91]. The expression construct, pMBP-FecR CCSSD, contains an N-terminal MBP fusion tag followed by a TEV-protease recognition sequence (ENLYFQG) and the inserted FecR CCSSD coding sequence.

The pMBP-FecR CCSSD construct was used to transform chemically competent *E. coli* C41 cells for protein expression. 50 µL and 200 µL aliquots of the transformation mixture were used to inoculate two LB agar plates supplemented with 100 µg/ml ampicillin. Plates were inoculated overnight at 37 °C. A single colony was picked and added to a 70 mL culture of LB media supplemented with 100 µg/ml ampicillin and incubated at 37 °C overnight. For protein

expression, 10 mL of overnight culture was added to 1 L of LB media supplemented with 100 µg/ml ampicillin. This culture was incubated at 37 °C with shaking at 200 rpm until it reached an OD_{600} of 0.7-0.9. Cultures were then induced with 0.5 mM IPTG and incubated overnight at 20 °C. Following overnight incubation, the cells were harvested by centrifugation at 4,000 x g, washed with 25 mM HEPES pH 7.0 400 mM LiCl, 10% glycerol, and stored at -80 °C.

Cell pellets were resuspended in 25 mM HEPES pH 7.0 400 mM LiCl, 10% glycerol and lysed by sonication with a Branson Sonifier 450 sonicator. The resulting lysate was clarified by centrifugation at 20,000 x g for 35 min and passed over 10 ml amylose resin preequilibrated in lysis buffer. Excess lysis buffer was used to wash the column. Following 20+ column volumes of washing, the MBP-FecR CCSSD was eluted from the column by addition of lysis buffer + 20 mM maltose. Following affinity chromatography, SEC was used to further purify the MBP-FecR CCSSD. A volume of 1.1 mL of MBP-FecR CCSSD at 12-14 mg/mL was loaded onto a HiLoad 16/60 Superdex 200 column (Cytiva) and eluted using an isocratic gradient of 25 mM HEPES pH 7.0, 400 mM LiCl, 10% glycerol. Pure MBP-FecR CCSSD was concentrated, and flash frozen in 20 – 50 µL aliquots in liquid nitrogen prior to storage at -80 °C. Protein purity was determined by SDS-PAGE with a 4-20% TGX SDS-PAGE gel (BioRad) and Coomassie Blue staining [93].

3.2.3. Cloning, Expression, and Purification of FecR CCSSD T182A and MBP-FecR CCSSD T182A

The FecR CCSSD contains the autoproteolytic residues, Gly^{181} and Thr^{182}, that leads to self-cleavage during purification. To prevent this, mutagenesis of pMBP-FecR CCSSD using the primers 5’ – GTC AGG GCC AGC TCA CTG CTT TAG GGG CGG AAT TTA CCG TCC GCC AGC AGG ATA AT – 3’ and 5’ – ATT ATC CTG CTG GCG GAC GGT AAA TTC CGC

CCC TAA AGC AGT GAG CTG GCC CTG AC – 3' was utilized to mutate threonine 182 to alanine (T182A) to prevent autoproteolysis of the CCSSD during purification. The expression construct, pMBP-FecR CCSSD T182A, contains an N-terminal MBP fusion tag followed by a TEV-protease recognition sequence (ENLYFQG) and the inserted FecR CCSSD T182A coding sequence.

pMBP-FecR CCSSD T182A construct was used to transform chemically competent *E. coli* C41 cells for protein expression. 50 µL and 200 µL aliquots of the transformation mixture were used to inoculate two LB agar plates supplemented with 100 µg/ml ampicillin. Plates were inoculated overnight at 37 °C. A single colony was picked and added to a 70 mL culture of LB media supplemented with 100 µg/ml ampicillin and incubated at 37 °C overnight. For protein expression, 10 mL of overnight culture was added to 1 L of LB media supplemented with 100 µg/ml ampicillin. This culture was incubated at 37 °C with shaking at 200 rpm until it reached an OD_{600} of 0.7-0.9. Cultures were then induced with 0.5 mM IPTG and incubated overnight at 20 °C. Following overnight incubation, the cells were harvested by centrifugation at 4,000 x g, washed with 25 mM HEPES pH 7.0 400 mM LiCl, 10% glycerol, and stored at -80 °C.

The cell pellets, containing the expressed MBP-FecR CCSSD T182A, were resuspended in 25 mM HEPES pH 7.0, 400 mM LiCl, 10% glycerol and lysed by sonication with a Branson Sonifier 450 sonicator. The resulting lysate was clarified by centrifugation at 20,000 x g for 35 min and passed over ~15 mL amylose resin preequilibrated in lysis buffer. Lysis buffer (~20 column volumes) was used to wash the column and remove non-specifically bound proteins. The MBP-FecR CCSSD T182A protein was eluted from the column with lysis buffer + 2mM DTT and 20 mM maltose. Following affinity chromatography, recombinant GST tagged TEV protease was added to the pooled elution fractions and incubated overnight at 4 °C. To remove MBP from

the released FecR CCSSD T182A, cation exchange chromatography was performed. The resulting sample was diluted 2.7-fold with 25 mM HEPES pH 7.0, 10% glycerol and loaded onto an 8 ml MonoS cation exchange column (Cytiva) equilibrated in the same buffer. Bound FecR CCSSD T182A was separated from free MBP and contaminants via a 15% Buffer B wash, followed by a 50% Buffer B bump elution (Buffer A: 25 mM HEPES pH 7.0, 10% glycerol, Buffer B: 25 mM HEPES pH 7.0, 1M LiCl, 10% glycerol). Elutions containing FecR CCSSD T182A were pooled and concentrated for further purification by SEC with a Superdex 200 increase 10/300 GL (Cytiva) equilibrated in 25 mM HEPES pH 7.0, 400 mM LiCl, 10% glycerol. Protein purity was determined to be >95% by SDS-PAGE with a 4-20% TGX SDS-PAGE gel (BioRad) and Coomassie Blue staining [93].

Expression and purification of MBP-FecR CCSSD T182A was performed using the same strategy as the MBP-FecR CCSSD described previously. Protein purity was determined to be ~90% by SDS-PAGE with a 4-20% TGX SDS-PAGE gel (BioRad) and Coomassie Blue staining [93].

3.2.4. Expression and Purification of the FecR CCSSD T182A:FecA NTSD Complex

Chemically competent *E. coli* BL21 (DE3) pLysS cells were transformed with the pMBP- FecR CCSSD T182A and pET41-FecA NTSD constructs. 50 µL and 200 µL aliquots of the transformation mixture were used to inoculate two LB agar plates supplemented with 100 µg/mL ampicillin and 15 µg/ml kanamycin. Plates were inoculated overnight at 37 °C. A single colony was picked and added to a 70 mL culture of LB media supplemented with 100 µg/mL ampicillin and 15 µg/ml kanamycin and incubated at 37 °C overnight. For protein expression, 10 mL of overnight culture was added to 1 L of LB media supplemented with 100 µg/mL ampicillin and 15 µg/ml kanamycin. This culture was incubated at 37 °C with shaking at 200 rpm until it

reached an OD_{600} of 0.7-0.9. Cultures were then induced with 0.5 mM IPTG and incubated overnight at 20 °C. Following overnight incubation, the cells were harvested by centrifugation at 4,000 x g, washed with 25 mM HEPES pH 7.0, 400 mM LiCl, 10% glycerol, and stored at -80 °C.

Harvested cell pellets containing expressed MBP-FecR CCSSD T182A and GST-FecA NTSD were resuspended in 25 mM HEPES pH 7.0, 400 mM LiCl, 10% glycerol and lysed by sonication with a Branson Sonifier 450 sonicator. The lysate was clarified by centrifugation at 20,000 x g for 35 min and passed over ~10 mL of Glutathione Sepharose 4B resin (Cytiva) preequilibrated in lysis buffer. The column was washed with lysis buffer (~20 column volumes) to remove non-specifically bound proteins. Recombinant GST-TEV protease was applied to the column and incubated overnight at 4 °C to remove the FecR CCSSD T182A MBP tag as well as the FecA NTSD GST tag. Lysis buffer was added to wash off the cleaved FecR CCSSD T182A FecA NTSD complex. The collected fractions were loaded over ~15 mL of amylose resin preequilibrated in lysis buffer to bind and remove any remaining free MBP or MBP-FecR CCSSD T182A. The amylose column flowthrough was concentrated and further purified by SEC with a Superdex 200 10/300 GL column (Cytiva) using 25 mM HEPES pH 7.0, 400 mM LiCl, 10% glycerol. Pure FecR CCSSD T182A FecA NTSD complex was concentrated, and flash frozen in 20 – 50 µL aliquots in liquid nitrogen prior to storage at -80 °C. Protein purity was determined to be >95% using a 4-20% TGX SDS-PAGE gel (Bio-Rad) and Coomassie Blue staining [93].

3.2.5. FecR CCSSD T182A Protein Complexing with FecA NTSD

Individually purified FecR CCSSD and FecA NTSD were mixed in a 1:1 molar ratio and incubated at 4 °C for 1 hr. Protein complex was frozen in liquid nitrogen and stored at -80 °C.

Complex formation was assessed by the thawing of frozen protein and SEC using a Superdex 200 10/300 GL column (Cytiva). Individual FecR CCSSD T182A and FecA NTSD were run as well for SEC peak comparison.

3.2.6. Affinity Pulldown Assays between the FecA NTSD and FecR CCSSD WT or T182A

BL21 (DE3) pLysS cells were co-transformed with pMBP-FecR CCSSD and pET41-FecA NTSD. Cells were co-expressed following the same protocol outlined for the purification of the FecR CCSSD T182A:FecA NTSD complex. The harvested cells were lysed by sonication with a Branson Sonifier 450 sonicator. The lysate was clarified by centrifugation at 20,000 x g. The clarified supernatant was split into two aliquots and loaded onto either amylose or Glutathione Sepharose 4B resin (Cytiva) equilibrated in lysis buffer (25 mM HEPES pH 7.0, 400 mM LiCl, 10% glycerol). Each column was washed with lysis buffer to remove unbound protein from the resin. Protein was eluted from the respective columns with lysis buffer + 20 mM maltose or 15 mM reduced GSH (pH adjusted). The presence of protein complexes was assessed by SDS-PAGE using a 4-20% TGX SDS-PAGE gel (Bio-Rad) followed by Coomassie blue staining [93]. This was repeated with the co-expressed MBP-FecR CCSSD T182A FecA NTSD proteins.

3.2.7. ITC to Quantify Affinity of MBP-FecR CCSSD T182A Binding to FecA NTSD

ITC was performed using a Low Volume Nano ITC (TA Instruments). Purified proteins were loaded into separate dialysis cassettes, and co-dialyzed against 2 L of 25 mM HEPES pH 7.0, 400 mM LiCl, and 10% glycerol. ITC experimentation was setup at 20 °C, with 20 injections of 2.5 µl each. In contrast to the PupR CCSSD:PupB NTSD ITC experiment, the FecA NTSD (302 µM) was titrated into 75 µM MBP-tagged FecR CCSSD T182A. Data was analyzed using NanoAnalyze (TA Instruments) with an independent, single-site model.

3.2.8. SEC-SAXS Analysis of FecR CCSSD T182A, FecA NTSD, and FecR CCSSD T182A:FecA NTSD Complex

SEC-SAXS was performed at BioCAT (beamline 18ID at the Advanced Photon Source, Chicago). Individual samples of the FecR CCSSD T182A (300 µL at 5.5 mg/mL), FecA NTSD (250 µL at 14.8 mg/mL), or FecR CCSSD:FecA NTSD complex (130 µL at 6 mg/mL) were loaded onto a Superdex 200 Increase 10/300 GL column (Cytiva) running at 0.6 ml/min on an AKTA Pure FPLC (GE). Eluate was passed through the UV monitor and subsequent SAXS flow cell. The flow cell consists of a 1.0 mm ID quartz capillary with ~20 µm walls. A coflowing sheath buffer was used to separate sample from the capillary walls and preventing radiation damage[137]. Scattering intensity was recorded using a Pilatus3 X 1M (Dectris) detector, which was placed at 3.66 m from the sample allowing access to a q-range of 0.003 $Å^{-1}$ to 0.35 $Å^{-1}$. Exposures of 0.5 s were acquired every 1 s during elution and data was reduced using BioXTAS RAW 2.1.1[138]. Buffer blanks were created by averaging regions flanking the elution peak and subtracting from exposures selected from the elution peak to create the I(q) vs q curves used for subsequent analysis. Protein structures were superimposed to the SEC-SAXS protein envelopes with SUPCOMB from the ATSAS suite [139].

Table 3.1. SEC-SAXS data collection parameters and details.

SAS data collection parameter	
Instrument	BioCAT facility at the Advanced Photon Source beamline 18ID with Pilatus3 X 1M (Dectris detector
Wavelength (Å)	1.033
Beam size (μm²)	150 (h) x 25 (v) focused at the detector
Camera length (m)	3.66
q-measurement range ($Å^{-1}$)	0.003-0.35
Absolute scaling method	Glassy Carbon, NIST SRM 3600
Basis for normalization to constant counts	Transmitted intensity by beam-stop counter
Method for monitoring radiation damage	Automated frame-by-frame comparison of relevant regions using CORMAP[140] implemented in BioXTAS RAW
Exposure time, number of exposures	0.5 s exposure time with a 1 s total exposure period (0.5 s on, 0.5 s off) of entire SEC elution
Sample configuration	SEC-SAXS with sheath-flow cell[137], effective path length 0.542 mm. Size seperation by an AKTA Pure with a Superdex 200 Increase 10/300 GL column
Sample temperature (°C)	23
Software employed for SAS data reduction, analysis, and interpretation	
SAXS data reduction	Radial averaging; frame comparison, averaging, and subtraction done using BioXTAS RAW 2.1.1[138]
Basic analysis: Guinier, M.W., P(r)	Guinier fit and M.W. using BioXTAS RAW, P(r) function using GNOM[141]. RAW uses MoW and Vc M.W. methods[142].

3.2.9. CD and Thermal Denaturation of FecR CCSSD T182A, FecA NTSD, and FecR CCSSD T182A:FecA NTSD

FecR CCSSD T182A, FecA NTSD, and FecR CCSSD T182A:FecA NTSD (1:1 molar mixture of individually purified proteins) were dialyzed in 10 mM Potassium Phosphate pH 7.5, 100 mM $(NH_4)_2SO_4$ overnight at 4 °C and diluted to 7 μM, 20 μM, and 5 μM, respectively. Continuous scanning CD spectra were measured at 20 °C from 190-250 nm using a Jasco J-715 spectrometer with a PTC-423S/15 Peltier cell holder and a 1 mm quartz cell. Spectra were buffer subtracted and secondary structure contents estimated using CONTIN and CDSSTR within the CDPro software suite [96]. CD melting and re-folding curves were recorded at 217 nm for all

proteins at the concentrations given above by increasing temperature from 20-90 °C in 1 °C increments with a slope of 1 °C/min. The wavelength, 217 nm, was chosen for measuring β-strand content similar to that of the Pup data (Figure 2.8) and obtaining high signal data. Protein unfolding was monitored during both heating and cooling. Melting temperatures were determined by fitting a standard or double Boltzmann sigmoidal curve to the ellipticity in Origin 8 (OriginLab Corp., Northampton, MA). The melting temperature was defined as the inflection point after fitting.

3.3. Results

3.3.1. FecA NTSD Expression and Purification

FecA NTSD was purified by sequential GSH affinity chromatography with on-column TEV protease cleavage followed by SEC. The apparent molecular weight was 9.1 kDa as determined by calculating K_{avg} using an elution volume (v_e) of 14.8 ml for the SEC peak. This is in good agreement with the theoretical molecular weight of 9.8 kDa based on the amino acid sequence. The single SEC peak and SDS-PAGE bands indicate that the sample is pure and homogenous FecA NTSD (Fig. 3.1).

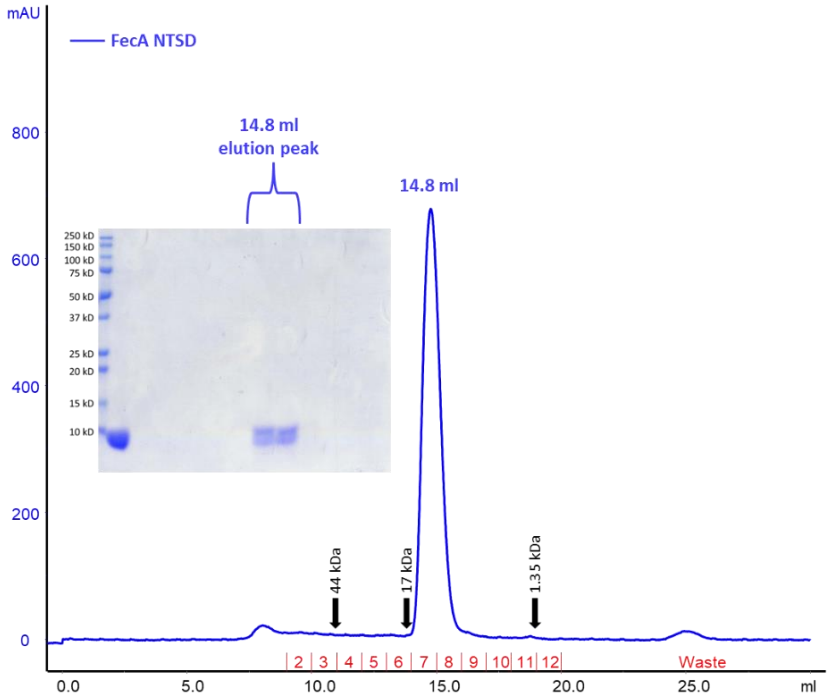

Figure 3.1. SEC chromatogram and related SDS-PAGE gel of FecA NTSD. Elution positions of SEC standards are indicated by arrows. FecA NTSD eluted at a volume of 14.8 ml with a calculated molecular weight of 9.1 kDa.

3.3.2. MBP-FecR CCSSD Expression and Purification

MBP-FecR CCSSD was purified by sequential amylose affinity chromatography and SEC. The apparent molecular weight of MBP-FecR CCSSD calculated from K_{avg} using a v_e = 81.2 ml is ~59.7 kDa. This is in good agreement with the theoretical molecular weight of 67.3 kDa based on the amino acid sequence. Despite the single SEC peak, SDS-PAGE indicates that the sample is only ~90% pure, and there are multiple fragments from the autoproteolysis of the FecR CCSSD (Fig. 3.2).

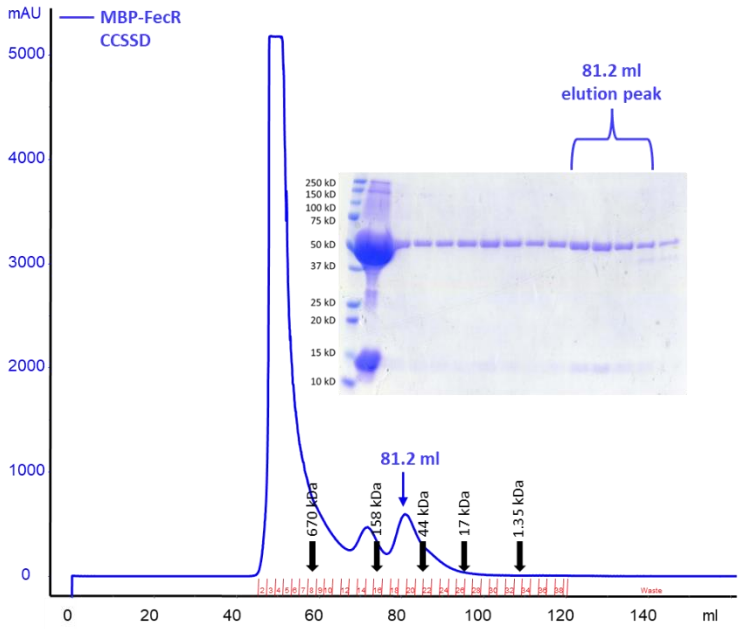

Figure 3.2. SEC chromatogram and related SDS-PAGE gel of MBP-FecR CCSSD. Elution positions of SEC standards are indicated by arrows. MBP-FecR CCSSD eluted at a volume of 81.2 ml with a calculated molecular weight of ~59.7 kDa

3.3.3. MBP-FecR CCSSD T182A and FecR CCSSD T182A Expression and Purification

MBP-FecR CCSSD T182A was purified by sequential amylose affinity chromatography and SEC. The apparent molecular weight of MBP-FecR CCSSD T182A calculated from K_{avg} using a v_e = 81.7 ml is ~56.4 kDa. This is approximately 1.2 times smaller than the theoretical molecular weight of 67.3 kDa based on the MBP-FecR CCSSD T182A amino acid sequence. The existing contaminants are largely separated from the MBP-FecR CCSSD T182A SEC peak, and the SDS-PAGE band associated with the 81.7 mL SEC peak indicate the MBP-FecR CCSSD T182A is mostly pure and homogenous (Fig. 3.3).

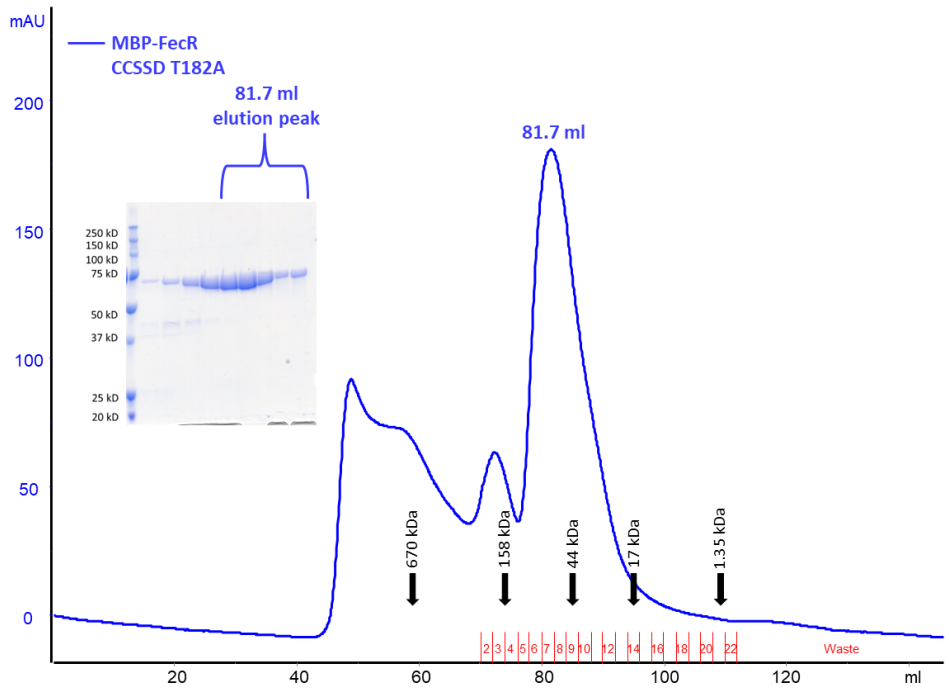

Figure 3.3. SEC chromatogram and related SDS-PAGE gel of MBP-FecR CCSSD T182A. Elution positions of SEC standards are indicated by arrows. MBP-FecR CCSSD T182A eluted at a volume 81.7 ml with a calculated molecular weight of ~56.4 kDa.

FecR CCSSD T182A was purified by Amylose affinity chromatography with on-column TEV protease cleavage, followed by cation exchange chromatography, and SEC. The apparent molecular weight of FecR CCSSD T182A calculated from K_{avg} using v_e = 16.8 ml ~11.4 kDa. This is approximately 2.1 times smaller than the theoretical molecular weight of 24 kDa based on the FecR CCSSD T182A amino acid sequence. The single SEC peak and SDS-PAGE band indicate the FecR CCSSD T182A is pure and homogenous (Fig. 3.4).

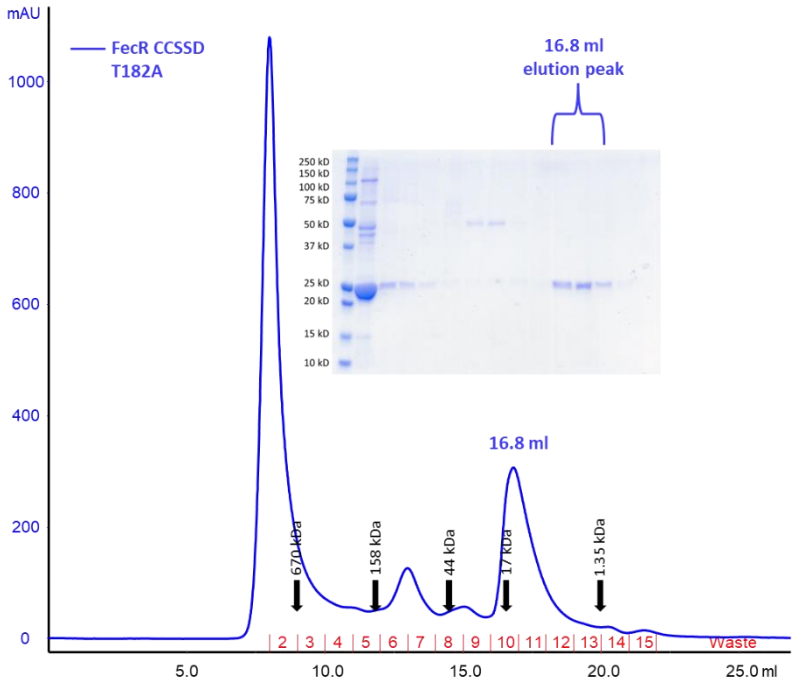

Figure 3.4. SEC chromatogram and related SDS-PAGE gel of FecR CCSSD T182A. Elution positions of SEC standards are indicated by arrows. FecR CCSSD T182A eluted at a volume 16.8 ml with a calculated molecular weight of ~11.4 kDa.

3.3.4. FecR CCSSD T182A:FecA NTSD Expression and Purification

Co-expressed FecR CCSSD T182A:FecA NTSD complex was purified by Glutathione Sepharose 4B resin (Cytiva) affinity chromatography with on-column TEV protease cleavage, followed by amylose affinity chromatography and SEC. The apparent molecular weight of FecR CCSSD T182A:FecA NTSD calculated from K_{avg} using a v_e = 17.5 ml is ~11.6 kDa. This is approximately 2.9 times smaller than the theoretical molecular weight of 33.8 kDa based on the FecR CCSSD T182A:FecA NTSD amino acid sequence. The single SEC peak together with only two bands upon SDS-PAGE corresponding to the molecular mass of the FecR CCSSD and the FecA NTSD indicate that the FecR CCSSD T182A:FecA NTSD complex is pure and homogenous (Fig. 3.5). FecR CCSSD T182A:FecA NTSD complex purification yields were low and variable between purifications.

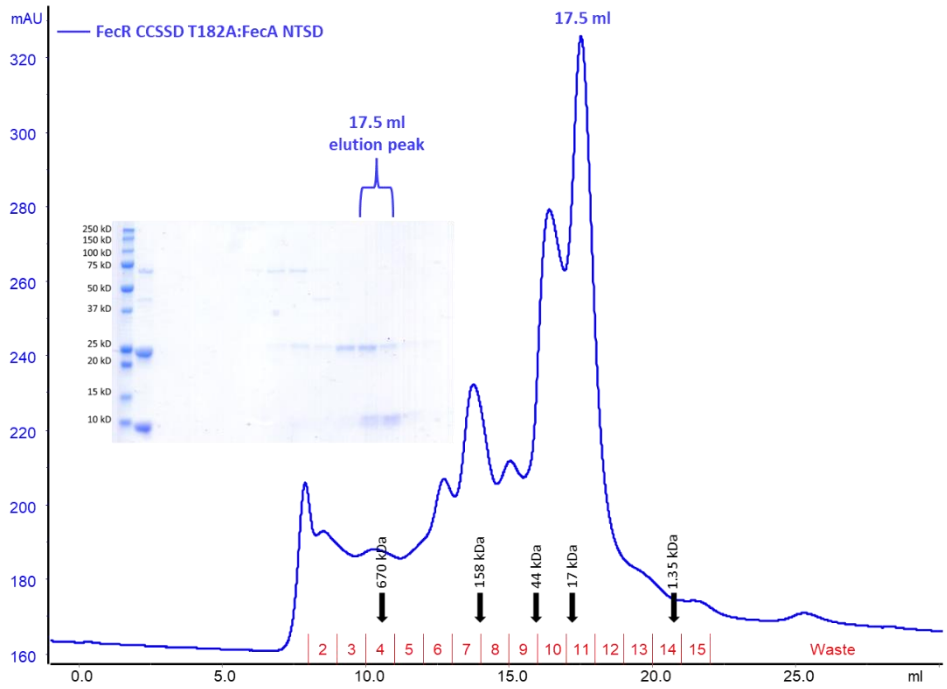

Figure 3.5. SEC chromatogram and related SDS-PAGE gel of FecR CCSSD T182A:FecA NTSD. Positions of SEC standard elutions are indicated by arrows. FecR CCSSD T182A:FecA NTSD eluted at a volume 17.5 ml with a calculated molecular weight of ~11.6 kDa.

3.3.5. FecR CCSSD T182A Complexing with FecA NTSD

To address low purification yields of the co-expressed FecR CCSSD T18A:FecA NTSD, individually purified FecR CCSSD T182A and FecA NTSD were mixed in a 1:1 molar ratio. SEC peak shifts of freeze-thawed proteins were used to assess complex formation. The FecR CCSSD T182A SEC peak elutes at a volume of 17.3 ml and the FecA NTSD elutes at a volume of 18 ml. The SEC peak for the FecR CCSSD T18A:FecA NTSD complex elutes at a volume of 17.0 ml. The left shift of the SEC elution peak for the complex relative to the SEC peaks for the individual proteins, indicates that the eluted protein is larger than the individual proteins, i.e. a complex is formed. The apparent molecular weight of the complex calculated from K_{avg} using a v_e = 17.0 mL SEC peak is ~27.7 kDa. This is approximately 1.2 times smaller than the theoretical molecular weight of 33.7 kDa based on the combined amino acid sequences of the

FecR CCSSD T18A and FecA NTSD. The single SEC peak suggests that the complex is pure and homogenous (Fig. 3.6).

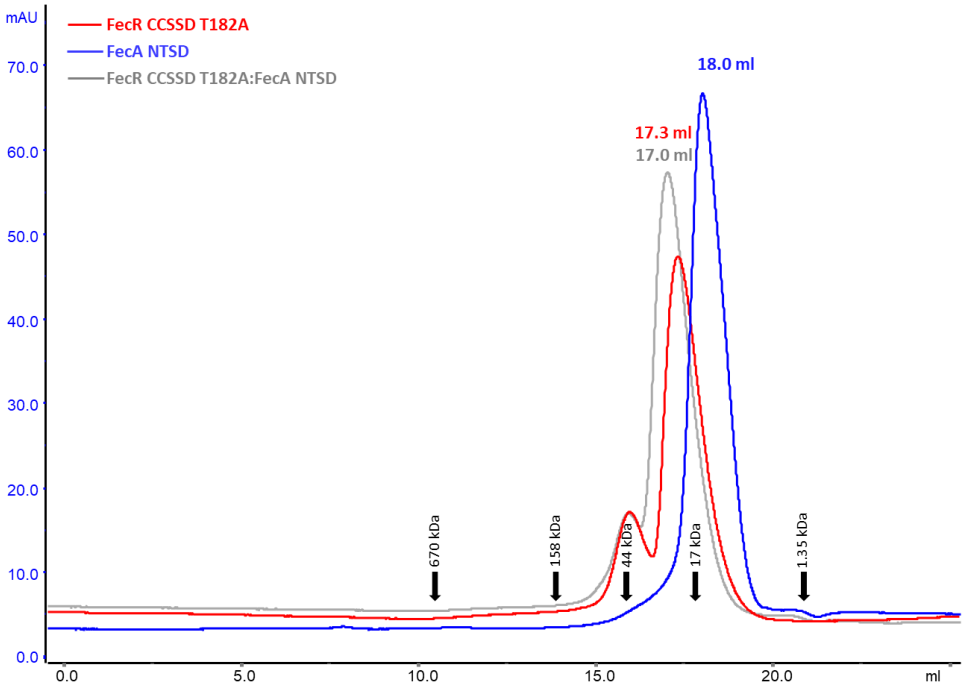

Figure 3.6. SEC peak shifts of FecR CCSSD T182A, FecA NTSD, and FecR CCSSD T182A:FecA NTSD. Individual proteins and the protein complex were freeze-thawed and run on a Superdex 200 10/300 column (Cytiva). FecR CCSSD T182A (red), FecA NTSD (blue), and FecR CCSSD T182A:FecA NTSD (grey) SEC curves are displayed. Position of SEC standards elutions are indicated by arrows.

3.3.6. The FecR CCSSD Autoproteolysis Mutant, T182A, Interacts with the FecA NTSD

Initial pulldown assays indicate that WT MBP-FecR and GST-FecA NTSD did not appear to form a stable complex (data not shown), despite previous reports of WT FecR interaction with FecA [56, 58]. However, following the T182A mutation, a stable complex was observed in both the amylose and GSH resin pulldown assays (Fig. 3.7). ITC measurements indicate that the FecA NTSD binds to MBP-FecR CCSSD T182A with an affinity (K_d) of ~2.1 µM (Table 3.2 & Fig. 3.8). Qualitative pulldown results suggest a 1:1 stoichiometric relationship between FecR and FecA, despite the inconclusive results from ITC. This is also supported by the

stoichiometry of binding of the homologous PupR CCSSD and PupB NTSD proteins as discussed in chapter 2 of this dissertation.

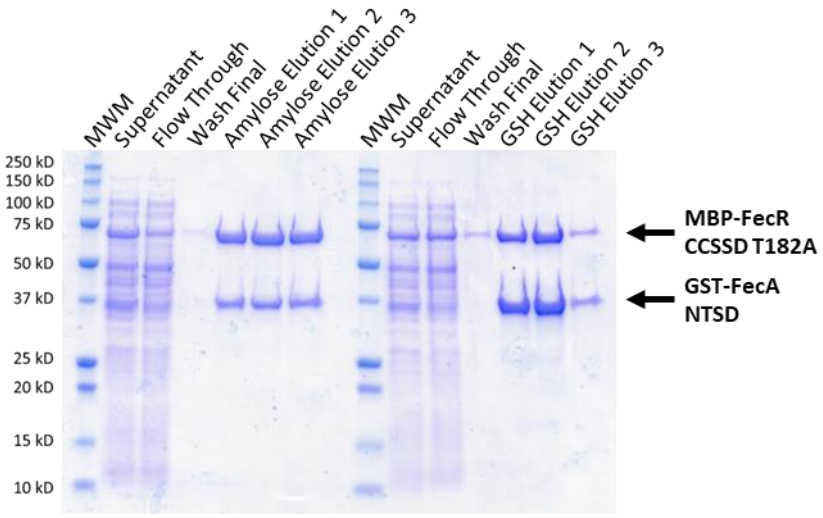

Figure 3.7. SDS-PAGE analysis of pulldown assays assessing interaction of the MBP-FecR CCSSD T182A and GST-FecA NTSD. Equivalent aliquots of clarified lysate were applied to either amylose or GSH resin. Each resin was washed, eluted, and analyzed by Coomassie-stained SDS-PAGE. Arrows indicate the location of each protein in elution fractions.

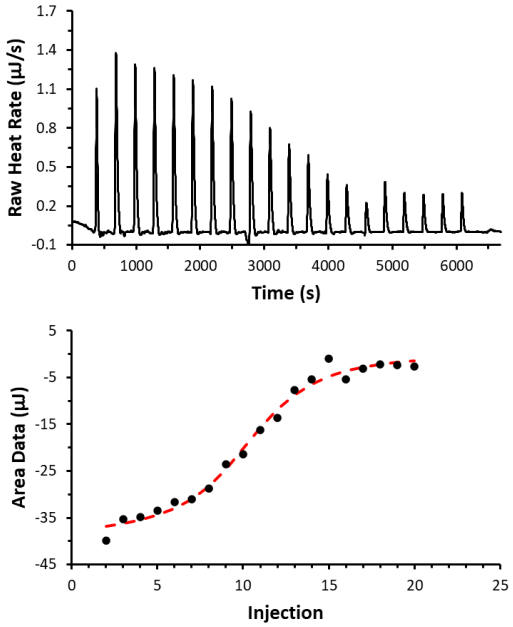

Figure 3.8. ITC profile of FecA NTSD titrated into MBP-FecR CCSSD T182A.

Table 3.2. Thermodynamic parameters of the MBP-FecR CCSSD T182A:FecA NTSD interaction as determined by ITC.

NTSD (μM)	CCSSD (μM)	K_d (μM)	ΔH (kJ/mol)	ΔS (J/mol·K)	ΔG (kJ/mol)	n
302	75	2.1	-51.7	-67.7	-31.9	0.64

[a] Stoichiometry of protein complex (n)

3.3.7. Low-Resolution Structural Features of the FecR CCSSD T182A, FecA NTSD, and FecR CCSSD T182A:FecA NTSD Analyzed by SEC-SAXS

Based on the results of our pulldown assays and given the previous structural data on homologous sigma regulators, including the PupR CCSSD:PupB NTSD interaction discussed in Chapter 2, we hypothesized that the FecR CCSSD T182A and the FecA NTSD form a 1:1 complex. To assess complex formation and stoichiometry in the absence of definitive ITC results, we used SEC-SAXS to evaluate the low-resolution structure and solution properties of FecR CCSSD T182A, FecA NTSD, and the FecR CCSSD T182A:FecA NTSD complex. All SEC-SAXS data was reduced and analyzed from BioXTAS RAW [138]. Following buffer subtraction, the auto calculated R_g distribution across the sample regions were linear for FecA NTSD and FecR CCSSD T182A:FecA NTSD samples indicating homogenous scattering particles; whereas the FecR CCSSD T182A failed to auto calculate the R_g distribution due to low intensity (Fig. 3.9A, 3.10A, 3.11A). Guinier plots are linear in the low *q* region, implying the samples are monodisperse. The FecR CCSSD T182A and FecA NTSD have R_g values of 19.0 and 13.2 Å, respectively, whereas the protein complex has an R_g value of 20.5 Å (Fig. 3.9B, 3.10B, 3.11B). *P(r)* distribution curves suggest the FecA NTSD is a compact globular protein with a D_{max} of 40.2 Å, the FecR CCSSD T182A is a slightly elongated molecule with a D_{max} of 62.0 Å, and the protein complex is again an elongated molecule with a D_{max} of 71.0 Å (Fig. 3.9C, 3.10C, 3.11C). Similarly, the Kratky plots indicate that the FecA NTSD as well-folded, whereas the FecR CCSS T182A and the complex are partially-folded (Fig. 3.9D, 3.10D, 3.11D). The

molecular weight estimations from the SEC-SAXS analyses are 8.4, 17.9, and 19.2 kDa for the FecA NTSD, FecR CCSSD T182A, and FecR CCSSD T182A:FecA NTSD. These values vary slightly from the theoretic values of 8.3, 24.0, and 32.3 kDa.

Individual samples fit reasonably to experimental protein envelopes (Fig. 3.9E, 3.10E, 3.11E). When comparing experimental values of the FecR CCSSD T182A and complex the R_g values increase from 19.0 to 20.5 Å, D_{max} values increase from 62.0 to 71.0 Å, and the experimental molecular weight estimates increase from 17.9 to 19.2 kDa. The experimental R_g, D_{max}, and molecular weight estimate, and protein envelopes suggest a 1:1 stoichiometric complex. Further analysis by X-ray crystallography or SEC-MALS would definitively address this deduction.

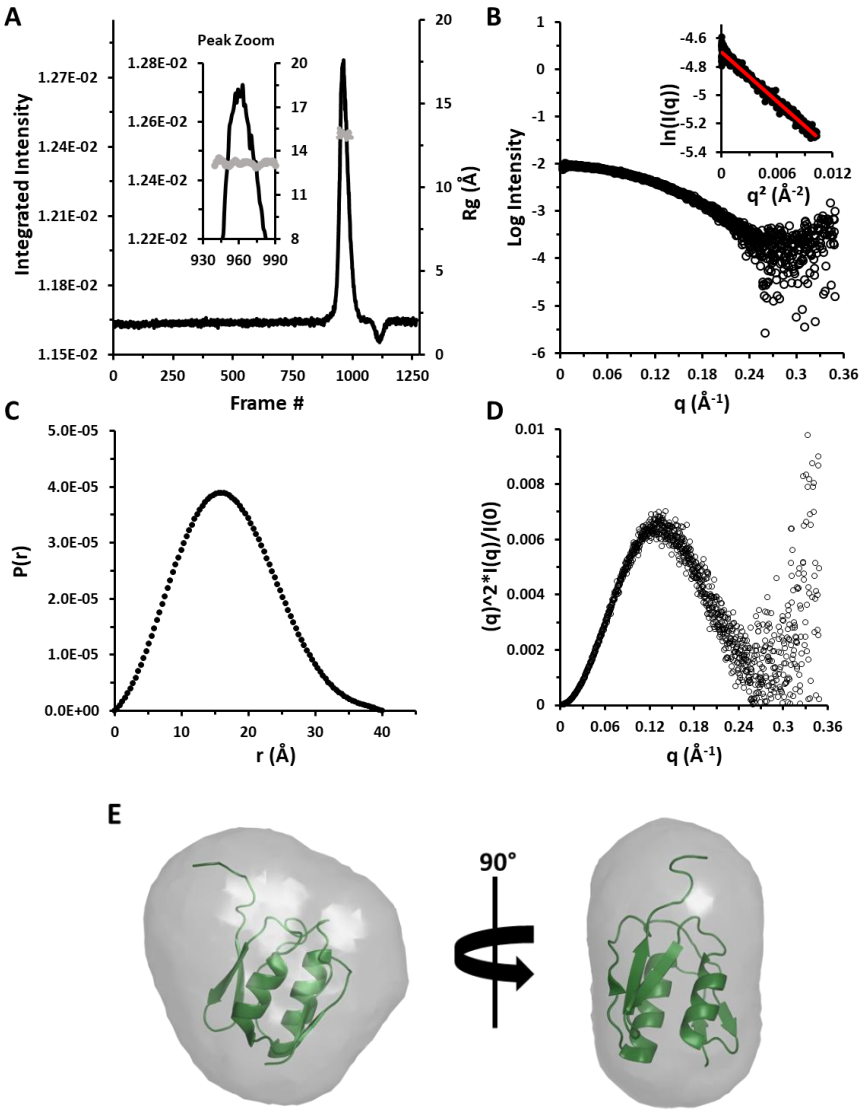

Figure 3.9. SEC-SAXS analysis of the FecA NTSD. A) Buffer subtracted scattering plot (black) with Rg distribution (grey) across the peak of interest (Inset: zoomed in view of the scattering plot peak and R_g distribution). B) Experimental scattering profile and inset Guinier plot of the low q region. C) Distance distribution P(r) plot. D) Kratky plot. E) Experimental protein envelope superimposed on the structure of FecA NTSD (1ZZV).

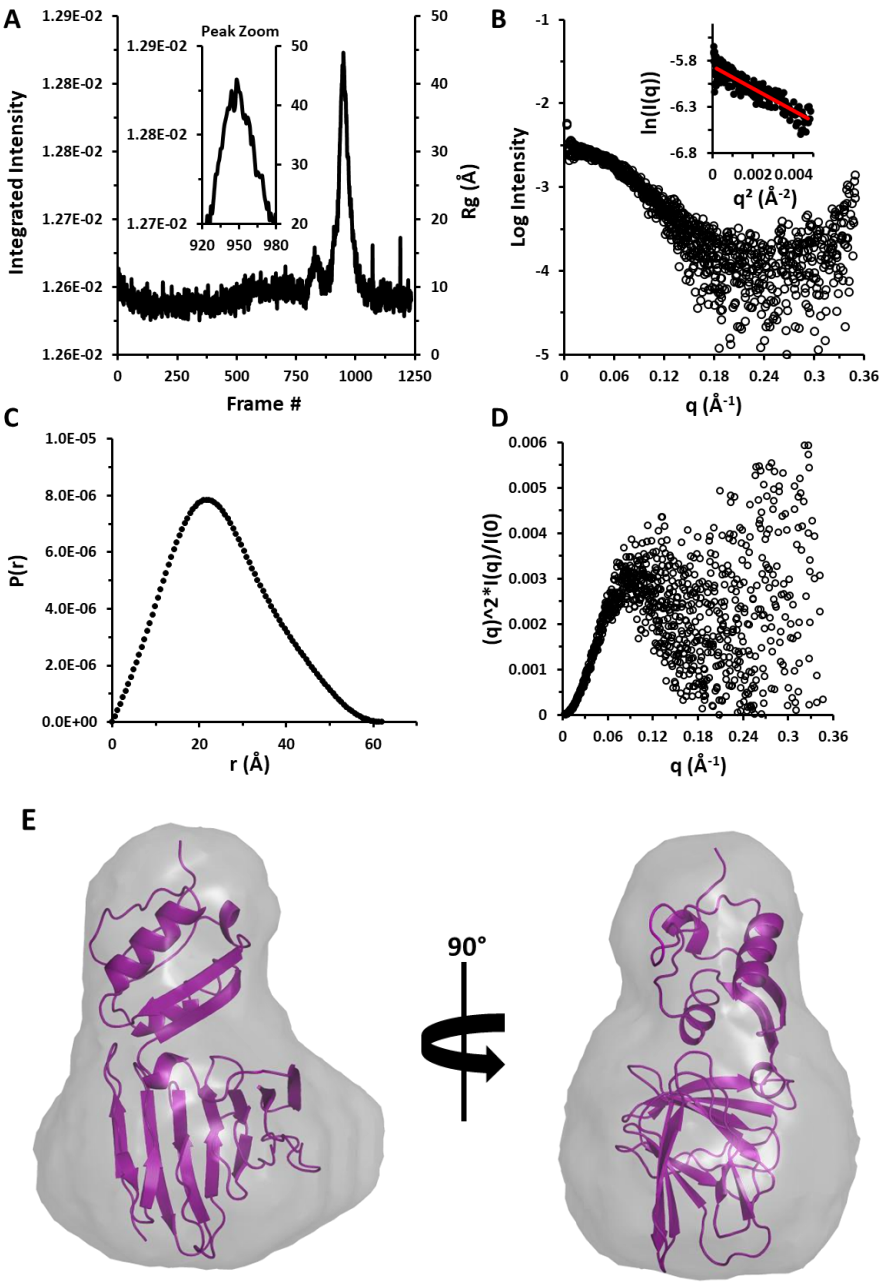

Figure 3.10. SEC-SAXS analysis of the FecR CCSSD T182A. A) Buffer subtracted scattering plot (black) with Rg distribution (grey) across the peak of interest (Inset: zoomed in view of the scattering plot peak and R_g distribution). B) Experimental scattering profile and inset Guinier plot of the low q region. C) Distance distribution P(r) plot. D) Kratky plot. E) Experimental protein envelope superimposed on the structure of PupR CCSSD (6OVK without the PupB NTSD).

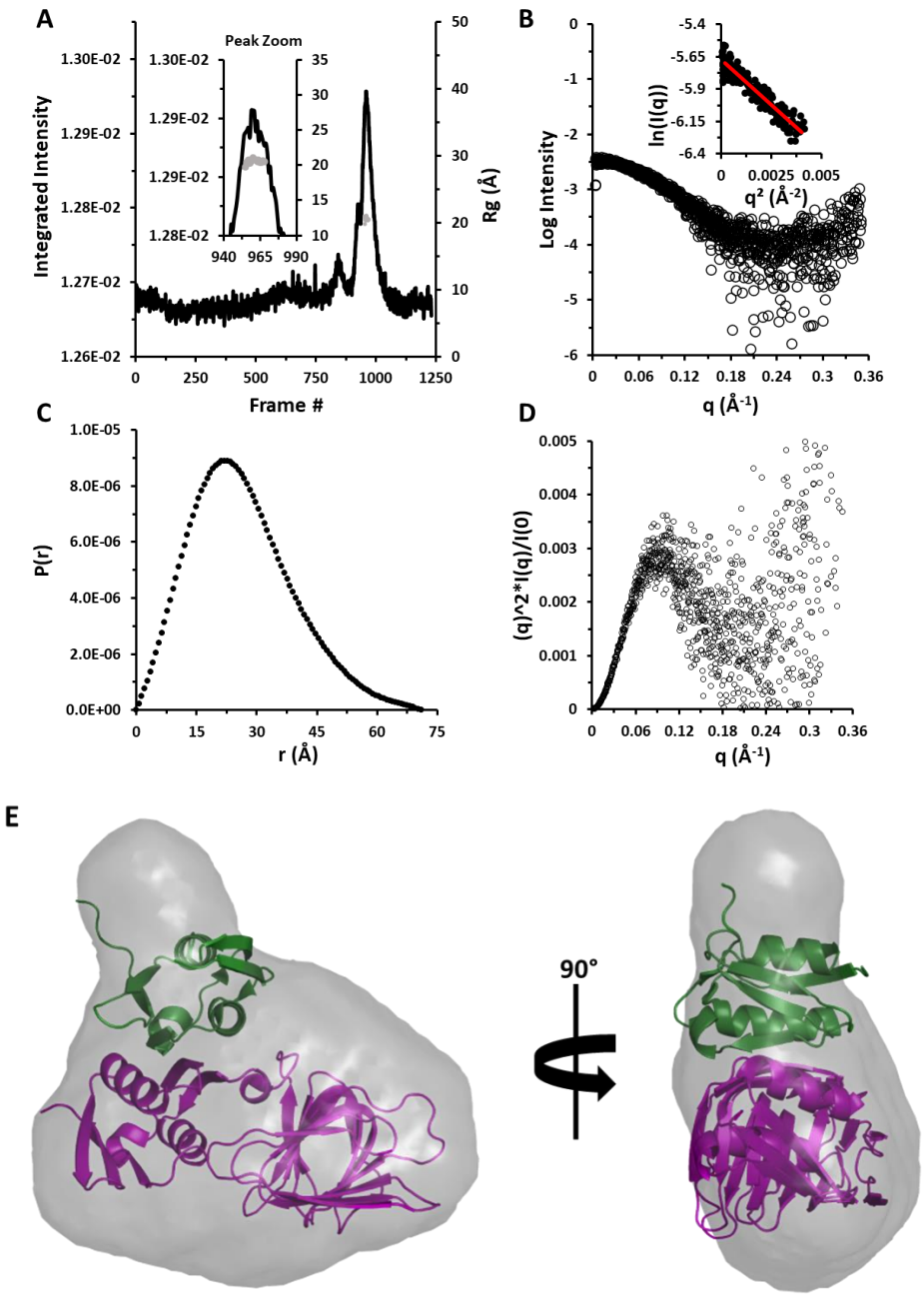

Figure 3.11. SEC-SAXS analysis of the FecR CCSSD T182A:FecA NTSD. A) Buffer subtracted scattering plot (black) with Rg distribution (grey) across the peak of interest (Inset: zoomed in view of the scattering plot peak and R_g distribution). B) Experimental scattering profile and inset Guinier plot of the low q region. C) Distance distribution P(r) plot. D) Kratky plot. E) Experimental protein envelope aligned with the structure of PupR CCSSD:PupB NTSD (6OVK).

3.3.8. The FecA NTSD Stabilizes the Fec Sigma Regulator

CD spectra of the individually isolated FecR CCSSD T182A and FecA NTSD reveal each has significant secondary structure (Fig. 3.12A, Table 3.3). The secondary structure content

of the FecR CCSSD T182A:FecA NTSD complex is consistent with the sum of residues estimated to be in each secondary structure for FecR CCSSD T182A and FecA NTSD separately (Fig. 3.12A, Table 3.3). This indicates a lack of substantial secondary structures changes from either domain upon binding of the two proteins. The CD thermal denaturation curve of the FecR CCSSD T182A, recorded at 217 nm, indicates a Tm of 52.7 °C (Fig. 3.12B). However, the FecR CCSSD T182A appears to precipitate during cooling, and a reverse CD thermal denaturation curve could not be recorded. CD thermal denaturation of the FecA NTSD indicates a Tm of 49.0 °C during heating and 45.4 °C during cooling (Fig. 3.12C). Interestingly, formation of the FecR CCSSD T182A:FecA NTSD complex increases the Tm for heating to 56.4 °C, suggesting that binding of the FecA NTSD stabilizes the FecR CCSSD T182A (Fig. 3.12D). However, the FecR CCSSD T182A:FecA NTSD complex Tm for cooling is 47.0 °C (Fig. 3.12D). It is likely that the CCSSD precipitates at high temperatures and the renaturation curve recorded likely corresponds to the refolding of the FecA NTSD alone.

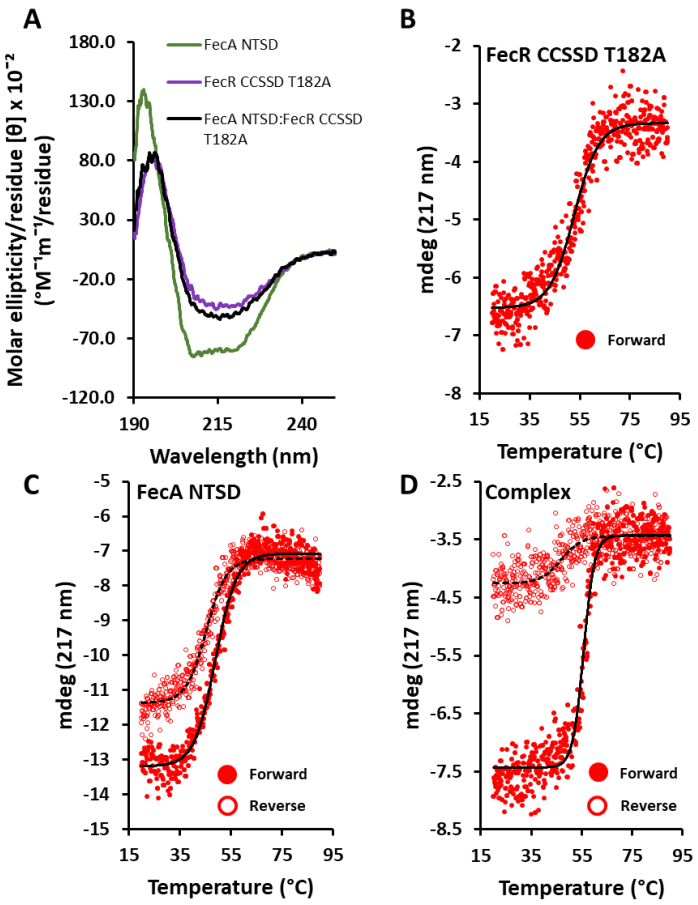

Figure 3.12. CD spectra and melting curves. A) CD spectra of FecA NTSD (green), FecR CCSSD T182A (purple), and the complex (black). B) FecR CCSSD T182A melting curve. C) FecA NTSD melting curves. D) FecR CCSSD T182A:FecA NTSD melting curves. Unfolding (heating; solid dots) and refolding (cooling; open circles) data points are shown. Boltzmann fits to the melting curves are shown.

Table 3.3. Secondary structure content estimated from CD spectra analyzed using CDPro.

	Estimated Secondary Structure Content in % (N_{res})			
Protein (# of residues)	**Helix**	**Strand**	**Coil + Turn**	**Total**
FecA NTSD (81)	22.2% (18)	27.2% (22)	50.6% (41)	100% (81)
FecR CCSSD T182A (217)	10.6% (23)	34.6% (75)	54.8% (119)	100% (217)
FecR CCSSD T182A:FecA NTSD (299)	15.4% (46)	32.6% (97)	52.0% (155)	100% (298)

3.4. Discussion and Conclusions

Our current pulldown assay conditions do not show interaction between the WT FecR CCSSD 105-317 and the FecA NTSD. However, mutating the FecR CCSSD threonine-182 to alanine, prevents autoproteolytic cleavage, and allows formation of the complex. The FecR CCSSD and FecA NTSD bind with an affinity of ~2.1 μM, similar to the PupR PupB interaction [45]. Interestingly, previous studies using a bacterial two-hybrid system, as well as a modified Ni-NTA pulldown assay using full length WT His_{10}-FecR solubilized from inclusion bodies, showed that FecR residues 101-317 interact with the NTSD [58]. Further, the bacterial two-hybrid system was used to show that FecR CCSSD residues 237-317 are required for interaction with the NTSD [56]. FecR residues 237-317 correspond to the PupR CCSSD STN subdomain (PupR residues 250-324), which forms an extensive hydrogen bonding network with the PupB NTSD [45]. However, the PupR STN subdomain of the PupR CCSSD is unstable and degrades rapidly during purification, and is therefore insufficient for binding to PupB NTSD [45]. Thus, it is likely that the WT FecR CCSSD auto-proteolyzes and therefore does not bind to the FecA NTSD.

Mutagenesis experiments indicate that within the FecR 237-317 region, residues 247-268, termed the 'LLLV' region, were critical for interaction with FecA [56]. However, the 'LLLV' region forms the hydrophobic core for the STN subdomain in the homologous PupR structure as well as in the AlphaFold structure of FecR (Fig. 3.13) which superimposes on the PupR CCSSD structure with an RMSD of 1.36 Å over 208 Cα atoms [45]. Therefore, it is likely that mutation of these hydrophobic residues disrupts the subdomain structure rather than directly interfering with binding to FecA (Fig. 3.14). Unfortunately, this study did not monitor whether these mutations impact the fold of the protein.

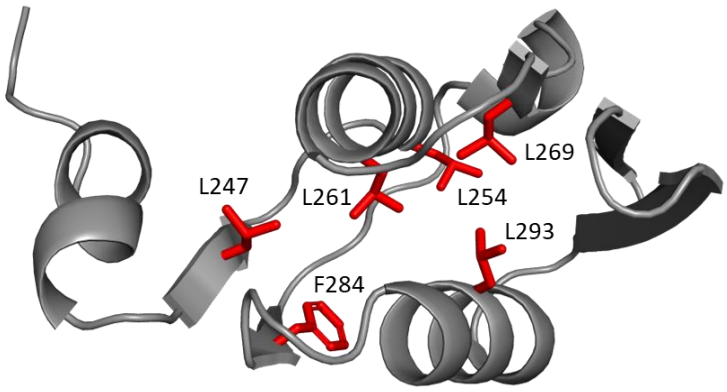

Figure 3.13. AlphaFold model of the FecR CCSSD STN subdomain and conserved 'LLLV' region. The AlphaFold model of the FecR CCSSD STN subdomain (grey) is shown with the conserved hydrophobic core residues, termed the 'LLLV' region, shown in stick (red).

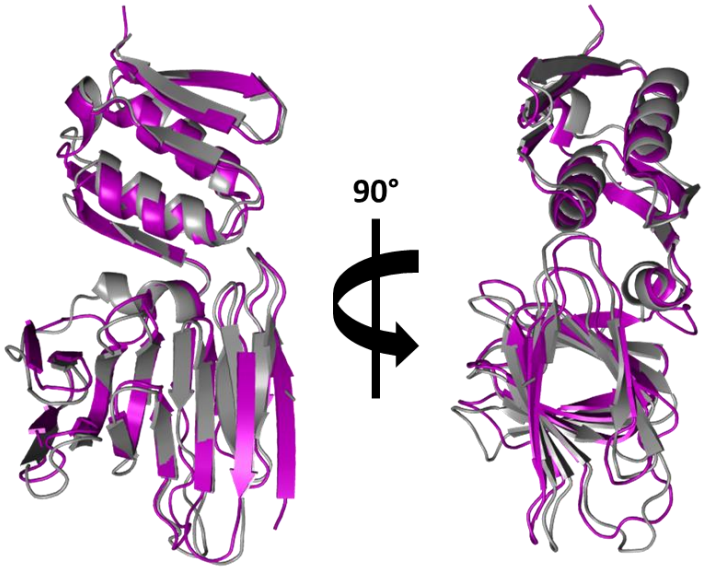

Figure 3.14. Structure alignment of the PupR CCSSD (6OVK) and the FecR CCSSD AlphaFold model. The FecR CCSSD AlphaFold model (grey) was fit to the PupR CCSSD (purple) with an RMSD of 1.36 over 208 Cα atoms.

We used SEC-SAXS to assess and compare the solution low-resolution structural properties of each individual protein, FecR CCSSD T182A and FecA NTSD, as well as of the complex. These studies indicate that the FecR CCSSD T18A:FecA NTSD has increased R_g and D_{max} compared to either the FecR CCSSD T182A or the FecA NTSD alone, indicating that a complex is formed. The AlphaFoldDB model indicates that similar to the PupR CCSSD, the

FecR CCSSD contains an STN and a CJM subdomain separated by a short linker region, and likely exists in a flexible state similar to the PupR CCSSD (Fig 3.15) [45]. However, the low intensity SEC-SAXS data could not resolve this information.

Our CD analyses indicates that formation of the FecR CCSSD T182A:FecA NTSD complex does not significantly alter the secondary structure content of the individual proteins. However, binding of the NTSD to the CCSSD stabilizes the CCSSD. In the context of CSS, this NTSD stabilization of the CCSSD supports the new 'primed' mechanism that we have proposed based on our studies of the PupR CCSSD:PupB NTSD interactions. It is likely that in the absence of interaction with the FecA NTSD, the FecR CCSSD is prone to proteolytic degradation, leading to transcriptional upregulation. It is possible in this model, binding of FecA to FecR would disrupt autoproteolysis, until siderophore-binding triggers dissociation of the complex. Along with autoproteolysis, the site-1 protease Prc likely acts as a house-keeping protease for the degradation of the remaining STN subdomain or further cleavage of the remaining CJM subdomain as described by Braun, V., *et al* [143]. Following the autocleavage/site-1 cleavage, RseP would further proteolyze FecR, release its cytoplasmic region and the cognate ECF sigma factor, FecI, as previously described [144]. In our studies, we have used the T182A mutation to limit the autoproteolytic cleavage of the FecR CCSSD, thereby stabilizing it enough to allow *in vitro* studies.

Together, the results of our research on the PupR and FecR CCSSDs support our new CSS paradigm, wherein prior to signal transduction, the CCSSDs reside in a 'primed' state which is disrupted and cleaved by RIP to release the ECF sigma factor.

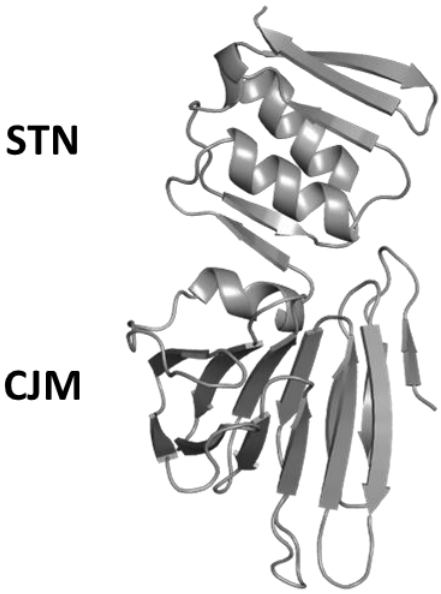

Figure 3.15. AlphaFold structural prediction of the FecR CCSSD. The model of the FecR CCSSD (grey) includes the STN and CJM subdomains connected by a short linker region.

This research provides a start to understanding a universal CSS mechanism, yet many details remain to be elucidated. Further analysis of the FecR CCSSD degradation products and roles of the RIP proteases in this process will help us validate the new CSS paradigm and elucidate variations if any exist.

4. THE ROLE OF THE PUPB N-TERMINAL SIGNALING DOMAIN IN BLOCKING SITE-1 PROTEASE ACTIVITY IN GRAM-NEGATIVE CELL SURFACE SIGNALING

4.1. Introduction

Our model CSS system, the *Pseudomonas capeferrum* pseudobactin BN7/8 (Pup) import system, is composed of three key conserved components; a TBDT, PupB, that senses an extracellular signal and imports metabolites, a periplasmic membrane spanning sigma regulator, PupR, that transduces a signal from the periplasm to the cytoplasm, and an extracytoplasmic function (ECF) sigma factor, PupI, which activates transcription of target genes. Activation of the Pup CSS pathway leads to the upregulation of transcription of the outer membrane spanning TBDT, PupB [75].

CSS signal transduction is activated by the RIP of the inner membrane sigma regulator [76-78, 88]. RIP is a sequential proteolytic cascade utilizing a site-1 protease which modifies the substrate for recognition and cleavage by a site-2 protease [76-78, 88]. Previous research indicates Prc (or Tsp) is the site-1 protease in *Pseudomonas* CSS, followed by the site-2 protease RseP [78]. Prc is a C-terminal processing serine endopeptidase implicated in the proteolytic degradation of many periplasmic proteins involved in cell wall expansion, alginate production, iron import, and more [78, 79, 81, 145]. RseP is an inner membrane localized metalloprotease that cleaves the transmembrane regions of substrate proteins [82, 146]. During iron import, Prc is hypothesized to proteolyze C-terminal region of CSS substrate proteins, such as PupR or IutY, by continual short 'clipping' [78, 79, 146, 147]. Despite several studies focused on Prc, little is known about its recognition of substrates and role in RIP of CSS pathways.

Previous views of Gram-negative CSS pathways suggested an interaction between the outer membrane TBDT N-terminal signaling domain (NTSD) and periplasmic sigma regulator

C-terminal CSS domain (CCSSD) was formed following siderophore binding. This interaction would then induce a signaling cascade and RIP for the release of the ECF sigma factor and upregulation of transcription. However, this does not appear to be the case for the Pup import pathway. As shown in Chapter 2, the PupR CCSSD is unstable in the absence of the PupB NTSD, and unlikely to exist alone prior to signal activation [45]. Additionally, the C-terminal secretin/TonB short N-terminal subdomain (STN) of PupR CCSSD forms significant contacts with the PupB NTSD, likely to occlude Prc interaction [45]. This suggests a revised CSS model in which the NTSD of the outer membrane TBDT interacts with and shields the sigma regulator CCSSD from proteolysis prior to signaling. Signal activation then leads to dissociation of the NTSD from the CCSSD, facilitating interaction with the site-1 protease, Prc, leading to RIP of the sigma regulator.

Here we use pulldown assays to investigate whether binding of the PupB NTSD to the PupR CCSSD, prevents binding of Prc and use ITC to compare binding affinities of the PupR CCSSD to the PupB NTSD and Prc. Additionally, we utilize protease assays and mass spectrometry to study the PupR CCSSD proteolysis by Prc and discern the proteolytic fragments of PupR CCSSD following degradation by Prc. Furthermore, we present the 2.01 Å and 2.16 Å X-ray crystallographic structures of Prc-His_6 S485A and Prc-His_6 K510A:PupR CCSSD 242-254, respectively, to analyze the conformational changes of Prc during substrate binding. We utilize SEC-SAXS to characterize the conformational flexibility of Prc in solution and create a model for binding of the PupR CCSSD to Prc. Jointly, this data supports a revised CSS model and new structural insights into RIP and CSS activation.

4.2. Materials and Methods

4.2.1. Cloning and Mutagenesis

The *P. capeferrum prc* DNA sequence was identified via a tblastn search (https://blast.ncbi.nlm.nih.gov/), using the *E. coli* Prc protein sequence (Uniprot Accession ID: P23865) against the *P. capeferrum* WCS358 genome (taxid:1495066). The DNA sequence was amplified from *P. capeferrum* with the forward primer, 5'- CAT CAT CAT CAT CAT CAC GTC GCG GAT CCA ATG CGT GAT -3' and reverse primer, 5'- CTC AGT GGT GGT GGT GGT GGT GCT CGA GGT GCT TGG CCA CCT GCG AGC -3' Then cloned into pET28a between the BamHI and XhoI restriction sites. The final construct encoded a C-terminal His_6-tag used for affinity purification. Prc mutants (S485A and K510A) were generated by site-directed mutagenesis using a QuikChange II kit (Agilent). DNA sequencing (MCLab) verified appropriate gene sequences. The PupR CCSSD expression construct was designed as previously described [45].

4.2.2. Protein Expression and Purification

PupR CCSSD and PupB NTSD constructs were expressed/purified as previously described[45]. Recombinant Prc-His_6 and mutant constructs (Prc-His_6 S485A and Prc-His_6 K510A) were used to transform chemically competent *E. coli* BL21 (DE3) cells for protein expression. 50 µL and 200 µL aliquots of the transformation mixture were used to inoculate two LB agar plates supplemented with 15 µg/ml kanamycin. Plates were inoculated overnight at 37 °C. A single colony was picked and added to a 70 mL culture of LB media supplemented with 15 µg/ml kanamycin and incubated at 37 °C overnight. For protein expression, 10 mL of overnight culture was added to 1 L of LB media supplemented with 15 µg/ml kanamycin. This culture was incubated at 37 °C with shaking at 200 rpm until it reached an OD_{600} of 0.7-0.9. Protein

expression was induced with 0.5 mM IPTG. Following induction, cells were grown overnight at 20 °C. Cells were then harvested at 4,000 x g by centrifugation, washed with 50 mM Tris-HCl pH 8.0, 500 mM NaCl, and stored at -80 °C.

Cell pellets were resuspended in 50 mM Tris-HCl pH 8.0, 500 mM NaCl, 25 mM imidazole and lysed with a Branson Sonifier 450 sonicator. Crude lysate was clarified by centrifugation at 20,000 x g for 35 min at 4°C. The clarified supernatant was loaded onto 5 – 10 mL of nickel-nitrilotriacetic acid agarose (Thermo Scientific) resin preequilibrated with lysis buffer. The column was then washed with 30 CV of lysis buffer. Protein was eluted with the addition of lysis buffer + 250 mM imidazole. Elution fractions (1 CV) were collected. The protein eluted in the first 5 - 10 CV as determined by SDS-PAGE and OD_{280} measurements. Fractions were pooled and concentrated with a 30-kDa MWCO Amicon Ultra centrifugal filter unit (Millipore). The wildtype Prc fractions were pooled, flash frozen in liquid nitrogen, and stored at -80 °C. No concentrating of the sample was required.

Prc-His_6 mutant constructs were further purified by SEC over a Superdex 200 10/300 increase column (Cytiva) equilibrated in 25 mM Tris-HCl pH 8.0, 100 mM NaCl. Proteins were eluted using an isocratic gradient. Fractions of pure, homogenous Prc-His_6 constructs were pooled, concentrated (20 mg/ml), flash frozen in liquid nitrogen, and stored at -80 °C. Protein purity was determined to be >95% by SDS-PAGE with a 4-20% TGX SDS-PAGE gel (Bio-Rad) and Coomassie Blue staining[93]. Prc-His_6 K510A:PupR CCSSD complex was formed by mixing individually purified proteins in a 1:1 molar ratio. Wildtype Prc-His_6 was purified as described above but stopped prior to SEC to limit degradation.

4.2.3. Binary MBP-PupR CCSSD:Prc-His_6 S485A/K510A Affinity Pulldown Assays

Purified MBP-PupR CCSSD and Prc-His_6 S485A or K510A were thawed and mixed in a 1:1 molar ratio at a concentration of 200 – 250 µM each. Proteins were incubated overnight at 4 °C. Protein mixtures were loaded onto 0.5 mL of Ni-NTA agarose resin in equilibration buffer (25 mM HEPES pH 7.5, 400 mM LiCl, 10% glycerol, and 25 mM imidazole). Columns were then washed with 30 CV of equilibration buffer to remove unbound protein and eluted with equilibration buffer + 250 mM imidazole. Samples were analyzed by SDS-PAGE on a 4-20% TGX SDS-PAGE gel (Bio-Rad) followed Coomassie Blue staining[93].

4.2.4. Tertiary MBP-PupR CCSSD:PupB NTSD:Prc-His_6 S485A/K510A Pulldown Assays

Purified MBP-PupR CCSSD and PupB NTSD were thawed and mixed in a 1:10 molar ratio, respectively. The concentrations for MBP-PupR CCSSD and PupB NTSD were ~250 µM and 2.5 mM, respectively. The MBP-PupR CCSSD:PupB NTSD complex mixture was incubated at 4 °C for 3 hrs. Following initial incubation, Prc-His_6 S485A or K510A was added in a 1:1 molar ratio to that of MBP-PupR CCSSD. The tertiary complex was then incubated at 4 °C overnight and loaded onto 0.5 mL of Ni-NTA agarose resin equilibrated with 25 mM HEPES pH 7.5, 400 mM LiCl, 10% glycerol, and 25 mM imidazole. The columns were washed with 30 CV of equilibration buffer and eluted in equilibration buffer + 250 mM imidazole. All samples were run on a 4-20% SDS-PAGE gel (Bio-Rad) and stained with Coomassie Blue stain[93]. Similar experiments were implemented using PupB NTSD mutant constructs (PupB NTSD Q69K, H72D, and L74A) described previously to evaluate complex formation under weakened PupB NTSD:PupR CCSSD interactions.

4.2.5. Quantifying the MBP-PupR CCSSD Interaction with Prc-His_6 K510A by ITC

ITC of MBP-PupR CCSSD titrated into Prc-His_6 K510A was performed using a Low Volume Nano ITC (TA Instruments). Individual proteins (~0.5 – 1.0 mL) were extensively dialyzed against 2 L of 25 mM HEPES pH 7.5, 400 mM LiCl, 10% glycerol. Experiments were completed at 15 °C with 25 injections of 2 µl. MBP-PupR CCSSD at 190 - 200 µM was titrated into Prc-His_6 K510A at concentrations of 34 - 40 µM. Resulting data was integrated with NanoAnalyze (TA Instruments) using an independent, single-site model. All experiments were completed in triplicate. Similar experiments were performed using the Prc-His_6 S485A mutant construct, however, no interaction was detected.

4.2.6. Prc Protease Assay

Protease activity was determined by mixing 0.625 µM Prc-His_6 with 12.5 µM MBP-PupR CCSSD in 25 mM HEPES pH 7.5, 400 mM LiCl, and 10% glycerol. Protein mixtures were incubated at 20 °C. The time course of the reaction was monitored by taking aliquots of the mixture at specific time points (0, 5, 15, 60, 120, and 240 min) and quenching the protease reaction. Reactions were quenched immediately at each time point by the addition of an SDS loading buffer and boiling for 1 min. Cleavage products were visualized by SDS-PAGE followed by Coomassie blue staining[93]. Control experiments with only Prc-His_6 (0.625 µM) or MBP-PupR CCSSD (12.5 µM) were performed to monitor for nonspecific protein degradation.

The protease activity was repeated in the presence of the PupB NTSD. First, 125 µM PupB NTSD was combined with 12.5 µM MBP-PupR CCSSD in 25 mM HEPES pH 7.5, 400 mM LiCl, and 10% glycerol. Proteins were incubated at 4 °C for 2 hrs then 20 °C for 15 min. Following the incubation at 20 °C, 0.625 µM Prc-His_6 was added to the mixture and the protease assay monitored for 240 min. Samples were collected and analyzed as described above.

4.2.7. Mass Spectrometry Analyses of Protease Assay Fragments

All mass spectrometry experiments were performed using a Waters SYNAPT MS system controlled by MassLynx 4.2 Software. An ACQUITY I-class UPLC System equipped with 2.1 x 100 mm BEH300 1.7 μm Peptide Separation Technology C18 column was used for the separation. Mobile phase A was 0.1% FA in water, the mobile phase B was 0.1% FA in acetonitrile. The flow rate was 0.2 mL/min, and the column temperature was 65 °C. An auxiliary pump delivered a lockmass solution (100 fmol/μL (GLu1)-fibrinopeptide B in 50:50 acetonitrile/water containing 0.1% FA) for mass accuracy reference. The sample was injected and separated using a 1 min non-gradient flow at initial conditions (3% B) followed by a 20 min gradient (3 to 37 %B).

Initially, the sample (5 μL at 0.1 mg/mL) was injected into the mass spectrometer using an ESI source. The instrument was operated in the positive ion V-mode. An alternating low collision energy (5 V) and elevated collision energy (ramping from 17 to 40 V) acquisition was used to acquire peptide precursor (MS) and fragmentation (MSE) data. Scan time was 0.5 sec (1 sec total duty cycle). The capillary voltage was 3.0 kV, source temperature 110 °C, cone voltage 30 V, cone gas flow 10 L/h, scan mass range 50 to 2000 Da. Sampling of the lock spray channel was performed every 1 min. A second injection (10 μL at 0.1 mg/mL) was injected to obtain information about the lower abundance peptides.

The acquired data were processed with IdentityE Software of ProteinLynx Global SERVER 3.0.3. The processed data were searched against manual database consisting of the PupR CCSSD sequence. Primary Digest Reagent was selected as non-specific, while Cysteine (C) carbamidomethylation, and methionine (M) oxidation were allowed as optional

modifications in this search. The average mass of intact protein was determined by the MaxEnt1 function of the Mass Lynx software.

4.2.8. PupR CCSSD Experimental Peptides

PupR CCSSD proteolytic peptide fragments identified from protease assays as described in section 4.2.7, were assessed for future experimentation. 819 peptides were identified, however, only 60 peptides were of high confidence. Of the 60 high confidence peptides, five peptides of varying length (9-25 amino acids), covering N-terminal, middle, and C-terminal regions of the STN subdomain were chosen (Table 4.1). These peptides were chosen to provide insight into binding at multiple regions of the PupR CCSSD as well as varying peptide lengths. The chosen identified peptides were synthesized by EZBiolab with a purity of >95%. Solubilization of lyophilized peptides was accomplished using 25 mM Tris HCl pH 7.5, 100 mM NaCl and pH adjusted with the addition of NaOH.

Table 4.1. PupR CCSSD peptides chosen for downstream experimentation.

Peptide	Sequence
PupR CCSSD 242-254	AVAPAWSQGMLVA
PupR CCSSD W+300-313	WAVAETLQLEVQHF
PupR CCSSD 300-324	AVAETLQLEVQHFTRYWVTLKPRMA
PupR CCSSD 314-324	RYWVTLKPRMA
PupR CCSSD 316-324	WVTLKPRMA

4.2.9. Microscale Thermophoresis of Prc-His_6 K510A and PupR CCSSD Peptides

Prc-His_6 K510A was fluorescently labeled using the Nanotemper RED-NHS 2nd generation labeling kit according to the manufacturer's instructions. The final assay buffer consisted of 25 mM HEPES pH 7.5, 400 mM LiCl, and 10% glycerol. The final degree of labeling (DOL) was determined from the ratio of absorbance at 280 nm and 650 nm, using the Prc-His_6 K510A extinction coefficient of e280 = 65,780 $M^{-1}cm^{-1}$. Microscale thermophoresis (MST) experiments were performed with a Nanotemper Monolith Pico Red/Blue (Nanotemper

Technologies GmbH). RED-NHS labeled Prc-His_6 K510A was diluted to 20 nM with assay buffer in the presence of serial diluted PupR CCSSD peptide ligands (0.0045 - 258 µM) and mixed in a 96-well plate. Samples were incubated together at room temperature for ~20 minutes prior to loading in Monolith premium capillaries (Nanotemper Technologies GmbH). Measurements were taken at 25 °C and MST traces collected with an excitation power of 80-100% and MST power of 40%. Interaction affinity and dissociation constant (K_d) was analyzed by the M.O. Control Analysis software (Nanotemper Technologies GmbH) using the K_d fit model.

4.2.10. Crystallization, Data Collection, and Structure Solution of Prc-His_6 S485A

Purified Prc-His_6 S485A was subjected to sparse matrix crystallization at 20 mg/mL (250 µM) in volume ratios of 3:1, 1:1, and 1:3 protein:buffer. Initial Prc-His_6 S485A crystallization conditions were determined by the MCSG crystallization suite (Anatrace). Optimized crystals were grown by sitting drop vapor diffusion in 100 mM HEPES:NaOH pH 7.5, 200 mM $(NH_4)_2SO_4$, 25% PEG 3350 at 20 °C. Needle-shaped crystals suitable for diffraction experiments grew to approximately 100-500 µm x 50 µm x 30 µm after 2-4 days. Crystals were cryoprotected in MiTeGen CryoOil and flash-frozen in liquid nitrogen prior to data collection.

Single crystal diffraction data were collected at the NE-CAT beamline 24-ID-C at the Advanced Photon Source under cryogenic conditions. Individual data sets were processed using XDS within the NE-CAT RAPD automated software suite [148]. The space group was determined with POINTLESS and data scaled using AIMLESS [104, 149]. Multiple data sets were merged within SCALA for the reported data set [104].

The structure was solved by molecular replacement (MR), using Phaser-MR and the *E. coli* Prc structure (6IQR) [112]. Initial electron density maps were interpreted by automated model

building using AutoBuild [109]. Phenix was utilized for refinement and combined with iterative model building in COOT [110, 111]. Diffraction data collection statistics and the final refined model statistics are found in Table 4.5. Model validation was performed with MolProbity and PDBredo [114, 150]. RMSD comparisons of the *E. coli* model and our model were calculated using Pymol [116].

4.2.11. Crystallization and Data Collection of Prc-His$_6$ K510A:PupR CCSSD 242-254

Prc-His$_6$ K510A and PupR CCSSD 242-254 were thawed and mixed in equimolar aliquots. The Prc-His$_6$ K510A:PupR CCSSD 242-254 complex was subjected to sparse matrix crystallization at 20 mg/ml (276 μM), in volume ratios of 3:1, 1:1, and 1:3 protein:buffer. Initial crystallization conditions were determined by the MSCG crystallization suite (Anatrace). Optimized crystals were grown by sitting drop vapor diffusion in 50 mM sodium citrate: citric acid pH 5.5, 16% PEG 3000 at 20 °C with a 2 μL drop at a protein:buffer ratio of 3:1. Long, needle shaped crystals appeared overnight and continued to grow for a minimum of 3 days to maximum dimensions of 500 μm x 50 μm x 50 μm before they were cryoprotected in MiTeGen CryoOil and flash-frozen in liquid nitrogen prior to data collection.

Single crystal diffraction data was collected at the GM/CA beamline 23-ID-B at the Advanced Photon Source under cryogenic conditions. Data sets were processed with XDS within the gmcaproc pipeline [148]. POINTLESS was utilized to determine the space group [104]. Data was scaled with XSCALE and statistics recalculated with a resolution cutoff using AIMLESS [148, 149]. The *E. coli* Prc structure 5WQL was used for molecular replacement (MR) against the native data set using Phaser-MR [112]. Initial electron density maps were interpreted by automated model building using AutoBuild [109]. Refinement and iterative model building were performed with Phenix and COOT, respectively [110, 111]. Diffraction data collection statistics and the final refined model statistics are found in Table 4.5. Model validation was performed with MolProbity and

PDBredo [114, 150]. RMSD comparisons of the *E. coli* model and our model were calculated using Pymol [116].

4.2.12. SEC-SAXS Analysis of Prc S485A, Prc K510A, and the Prc:PupR CCSSD Complex

SAXS data collection was performed at BioCAT (beamline 18ID at the Advanced Photon Source, Chicago) with in-line size exclusion chromatography. Experiment details are summarized in Table 4.2. Samples were loaded onto a Superdex 200 Increase 10/300 GL column (Cytiva) equilibrated with a buffer consisting of 25 mM HEPES pH 7.5, 400 mM LiCl, and 10% glycerol. Prc-His_6 K510A and PupR CCSSD were mixed in a 1:1 molar ratio (250 µM each) and complexed prior to injection. All samples, Prc-His_6 S485A, Prc-His_6 K510A, and the Prc-His_6 K510A:PupR CCSSD complex were run at 0.6 ml/min by an AKTA Pure FPLC (GE) following injection. The eluate then passed through the SAXS flow cell consisting of a 1.0 mm ID quartz capillary with ~20 µm walls. A coflowing buffer sheath was used to separate sample from capillary walls, helping prevent radiation damage [137]. Scattering intensity was recorded using a Pilatus3 X 1M (Dectris) detector placed at 3.7 m for access to a q-range of 0.003 – 0.35 $Å^{-1}$. 0.5 s exposures were acquired every 1 s during elution and data was reduced using BioXTAS RAW 2.1.1 [138]. Buffer blanks were created by averaging regions preceding the elution peak and subtracted from exposures selected from the elution peaks to create the I(q) vs q curves. Evolving factor analysis was used to separate overlapping species into individual scattering curves when necessary [151]. These curves were subsequently used for data analysis. Theoretical scattering data from crystal structures of Prc-His_6 S485A and Prc-His_6 K510A:PupR CCSSD 242-254 as well as a Prc-His_6 K510A:PupR CCSSD model was computed and fit to the experimental data using Crysol [122]. Fits with the lowest X^2 as well as the use of OLIGOMER were used in validation of protein conformations in solution [119].

Table 4.2. SAXS data parameters used for low-resolution structural analysis of Prc and its interaction with the PupR CCSSD.

SAS data collection parameter	
Instrument	BioCAT facility at the Advanced Photon Source beamline 18ID with Pilatus3 X 1M (Dectris detector
Wavelength (Å)	1.033
Beam size (μm²)	150 (h) x 25 (v) focused at the detector
Camera length (m)	3.7
q-measurement range ($Å^{-1}$)	0.003-0.35
Absolute scaling method	Glassy Carbon, NIST SRM 3600
Basis for normalization to constant counts	To transmitted intensity by beam-stop counter
Method for monitoring radiation damage	Automated frame-by-frame comparison of relevant regions using CORMAP [140] implemented in BioXTAS RAW
Exposure time, number of exposures	0.5 s exposure time with a 1 s total exposure preiod (0.5 s on, 0.5 s off) of entire SEC elution
Sample configuration	SEC-SAXS with sheath-flow cell [137], effective path length 0.542 mm. Size seperation by an AKTA Pure with a Superdex 200 Increase 10/300 GL column
Sample temperature (°C)	23
Software employed for SAS data reduction, analysis, and interpretation	
SAXS data reduction	Radial averaging; frame comparison, averaging, and subtraction done using BioXTAS RAW 2.1.1 [138]
Basic analysis: Guinier, M.W., P(r)	Guinier fit and M.W. using BioXTAS RAW, P(r) function using GNOM [141]. RAW uses MoW and Vc M.W. methods [142].

4.2.13. CD Spectroscopy of the Prc-His$_6$ S485A and K510A Mutants

Prc-His$_6$ S485A and Prc-His$_6$ K510A were dialyzed against 2 L of 10 mM potassium phosphate pH 7.5, 100 mM $(NH_4)_2SO_4$ overnight at 4 °C and diluted to 2 μM. Continuous scanning CD spectra were measured at 20 °C between 190 and 250 nm using a Jasco J-715 spectrometer with a PTC-423S/15 Peltier cell holder and a 1-mm quartz cell. The secondary structure content was estimated using CONTIN and CDSSTR within the CDPro software suite [96].

4.2.14. Structural Prediction and Modeling of the Prc:PupR CCSSD Complex

Initial structural predictions of the Prc:PupR CCSSD complex were performed using AlphaFold-Multimer in the AlphaFold v2.0 pipeline [152, 153]. Subsequently, the X-ray crystallographic structures of Prc-His_6 K510A:PupR CCSSD 242-254 and the PupR CCSSD (PDBID: 6OVK, chain R) were aligned to the predicted structure. PupR CCSSD peptide fragments 302-313 and 314-324 were excised from the PupR CCSSD crystal structure and used to determine an approximate distance from the interior of the PDZ domain to the exterior of the proteolytic groove. The modeled PupR CCSSD was then truncated after residue 301 to represent the remaining portion of the CCSSD being fed through the proteolytic groove to the carboxylate binding loop of the PDZ domain.

4.3. Results

4.3.1. Expression and Purification of Prc-His_6 S485A and Prc-His_6 K510A

Both Prc-His_6 S485A and Prc-His_6 K510A mutants were purified by sequential Ni-NTA affinity chromatography and SEC. Prc-His_6 S485A has a single, symmetric SEC peak and single SDS-PAGE bands indicating it is pure and homogenous (Fig 4.1). The apparent molecular weight of Prc-His_6 S485A calculated from K_{avg} using a v_e = 14.1 mL is 50.6 kDa, which is approximately 1.6 times smaller than the theoretical molecular weight of 80.0 kDa based on the amino acid sequence. However, the Prc-His_6 K510A SEC profile contains a significant leading shoulder indicating there could be some heterogeneity within the sample although the right side of the elution peak is symmetric in support of the sample being homogenous. SDS-PAGE bands indicate the sample is pure (Fig. 4.2). The apparent molecular weight of Prc-His_6 K510A

calculated from K_{avg} using a v_e = 13.9 mL is 56.5 kDa. This is approximately 1.4 times smaller than the theoretical molecular weight of 80.0 kDa based on the amino acid sequence.

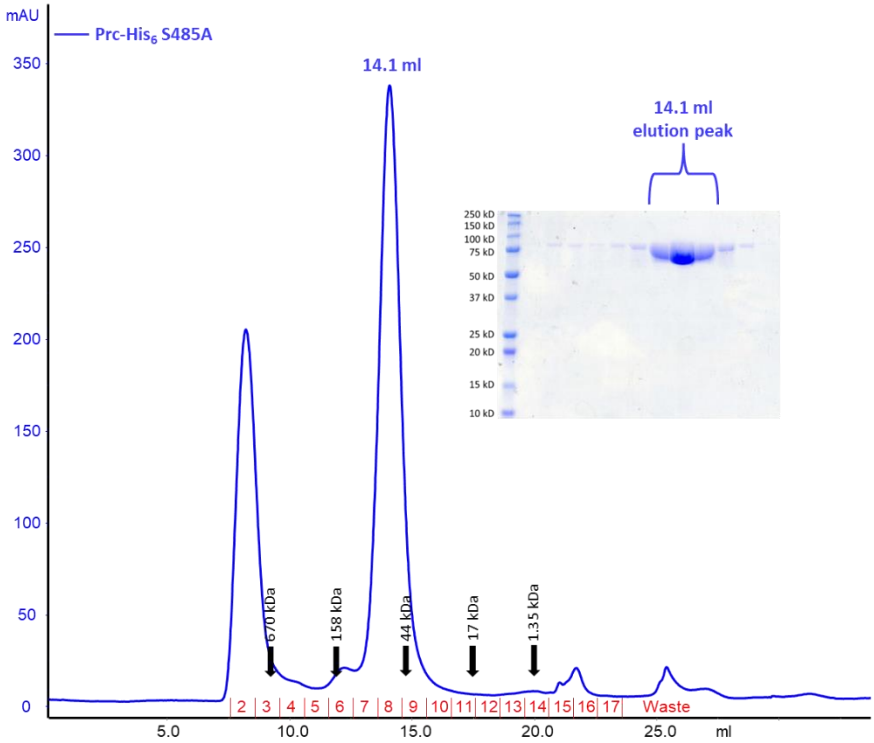

Figure 4.1. SEC chromatogram and related SDS-PAGE gel of Prc-His_6 S485A. Positions of SEC standard elutions are indicated by arrows.

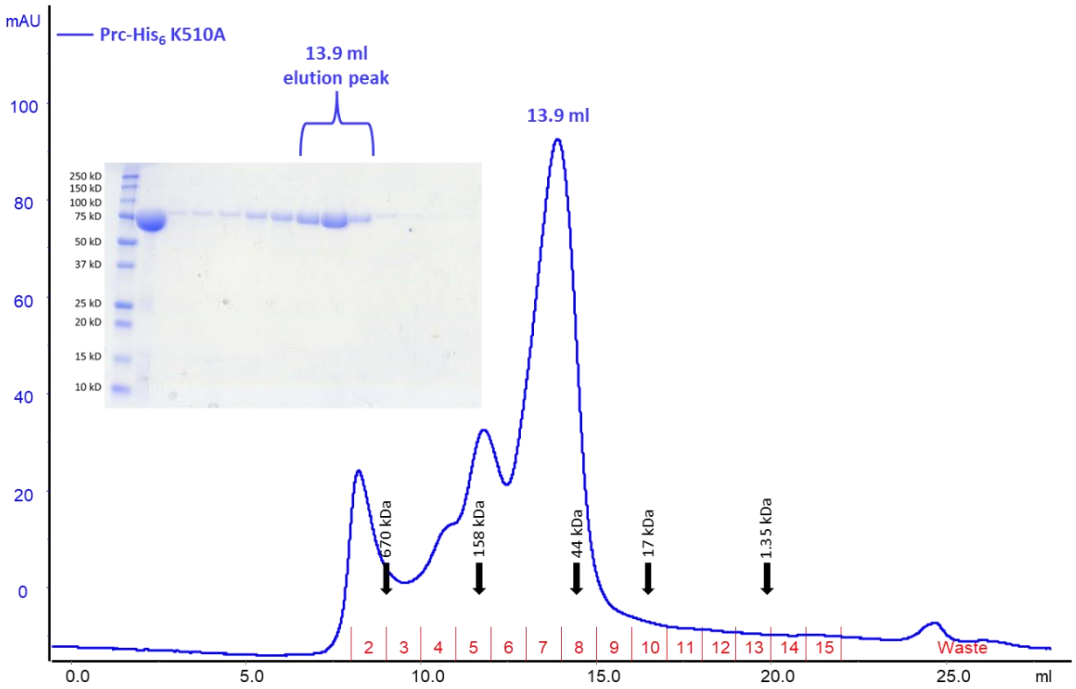

Figure 4.2. SEC chromatogram and related SDS-PAGE gel of Prc-His_6 K510A. Positions of SEC standard elutions are indicated by arrows.

4.3.2. PupB NTSD shields the PupR CCSSD from interaction with the site-1 protease, Prc

Ni-NTA pulldown assays clearly indicate that Prc-His_6 S485A and Prc-His_6 K510A bind MBP-PupR CCSSD (Fig. 4.3). Relative to Prc-His_6 S485A, the K510A mutant appears to bind better, resulting in a 1:1 stoichiometry of binding (Fig. 4.3A and B, lanes CP elution). However, pre-incubation of the PupR CCSSD with the PupB NTSD prevents Prc from binding to the PupR CCSSD (Fig. 4.3A & B). This indicates that the PupB NTSD not only stabilizes the PupR CCSSD prior to CSS, as was previously shown, but also shields it from recognition by the site-1 protease, Prc [45].

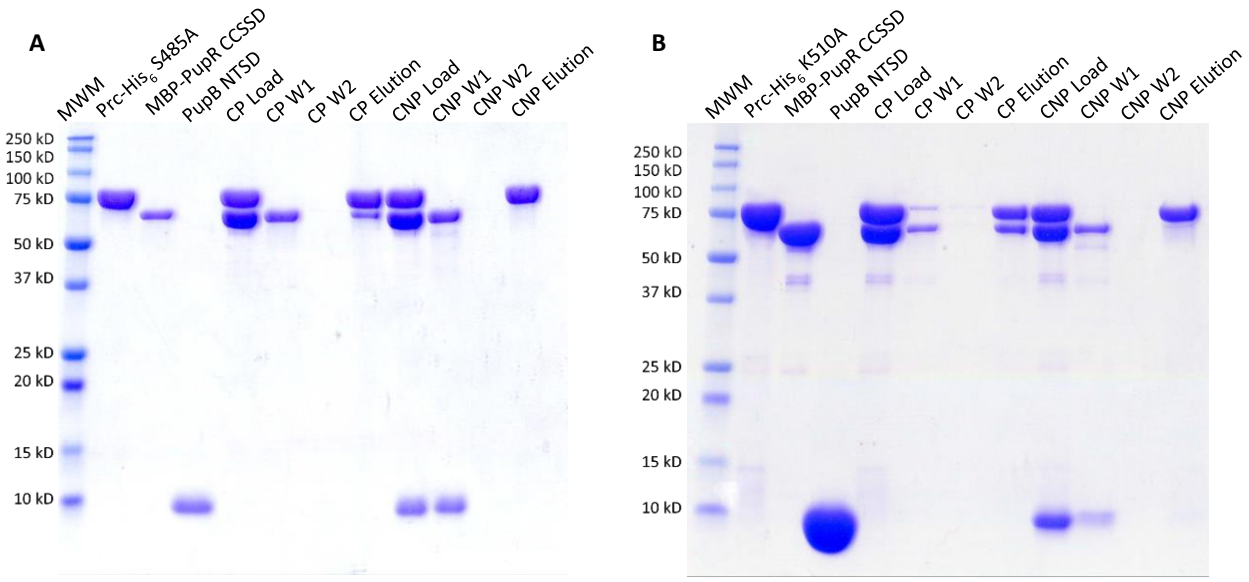

Figure 4.3. Affinity pulldown assays showing Prc interaction with PupR CCSSD and shielding of this interaction by PupB NTSD. A) Samples labeled CP include MBP-PupR CCSSD (C) and Prc-His6 S485A (P). CNP pulldown samples include MBP-PupR CCSSD (C), PupB NTSD (N), and Prc-His6 S485A (P). B) Samples labeled CP include MBP-PupR CCSSD (C) and Prc-His6 K510A (P). CNP pulldown samples include MBP-PupR CCSSD (C), PupB NTSD (N), and Prc-His6 K510A (P).

ITC was used to quantify the dissociation constant and stoichiometry of binding between Prc and the PupR CCSSD. Prc-His_6 K510A binds to the MBP-PupR CCSSD in a 1:1 stoichiometric manner with a binding affinity of 2.29 ± 0.33 µM (Fig. 4.4 & Table 4.3). However, no heats of interaction were detected between Prc-His_6 S485A and the MBP-PupR CCSSD despite the pulldown assay showing an interaction. Our previous research has shown that the PupB NTSD also interacts with the PupR CCSSD in a 1:1 stoichiometry with a K_d of 0.69 µM [45, 153]. This agrees with our pulldown results in that the PupB NTSD shields the PupR CCSSD from Prc, due to a tighter binding affinity.

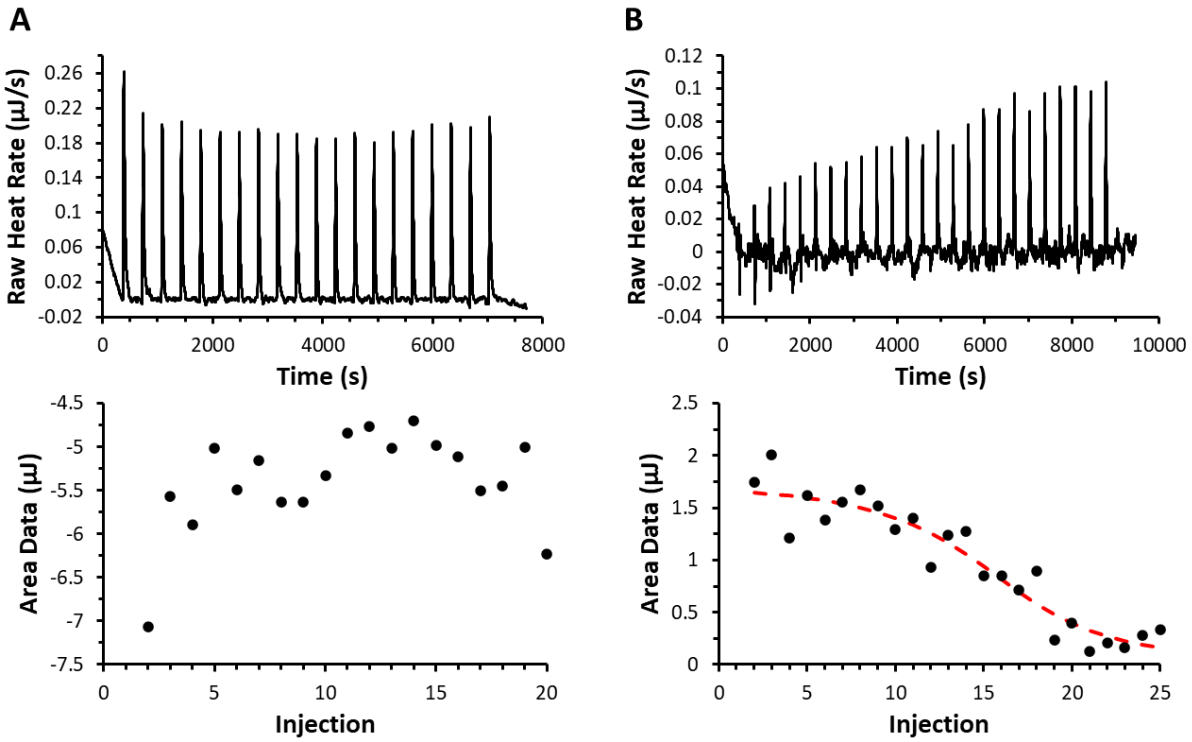

Figure 4.4. ITC profiles of MBP-PupR CCSSD titrated into Prc. A) ITC profile of MBP-PupR CCSSD titrated into Prc-His_6 S485A. B)ITC profile of MBP-PupR CCSSD titrated into Prc-His_6 K510A.

Table 4.3. Thermodynamic properties of the interaction between MBP-PupR CCSSD and Prc-His_6 K510A as determined by ITC.

MBP-PupR CCSSD (µM)	**Prc-His6 K510A (µM)**	**K_d (µM)**	**ΔH (kJ/mol)**	**ΔS (J/mol·K)**	**ΔG (kJ/mol)**
190 – 200	34 – 40	2.29 ± 0.33	5.20 ± 0.38	126.10 ± 1.18	-31.11

4.3.3. Prc Degrades the STN subdomain of PupR CCSSD in the Absence of the PupB NTSD

We incubated active Prc with the PupR CCSSD in the presence and absence of the PupB NTSD to analyze whether the NTSD protected the PupR CCSSD from degradation. SDS-PAGE analysis of the PupR CCSSD protease assay using WT Prc clearly shows the appearance of a protein band at ~58 kDa just below the 67.4 kDa MBP-PupR CCSSD band, indicating the CCSSD is proteolyzed (Fig. 4.5A). Importantly, the intensity of this 58 kDa band increases over

the course of the 240 min experiment. The final intensity of this band is appears greater than that of the 80 kDa Prc-His_6 added in this assay. This suggests the band corresponds to a large N-terminal fragment of the MBP-PupR CCSSD, likely cleaved at the C-terminus, as Prc is a C-terminal processing protease. There is no visible secondary band observable on the SDS-PAGE gel to indicate a single cleavage event. Control experiments containing only Prc-His_6 or MBP-PupR CCSSD under our assay conditions do not contain the protein degradation band, ruling out non-specific degradation (Fig. 4.5B & C).

Further, the inclusion of the Pup NTSD during the protease assay shows that the presence of the NTSD prevents degradation. SDS-PAGE analysis shows the NTSD completely prevents the formation of the 58.2 kDa MBP-PupR CCSSD protein band (Fig. 4.5 D). This further supports our hypothesis that the PupB NTSD stabilizes and protects the PupR CCSSD from Prc proteolysis.

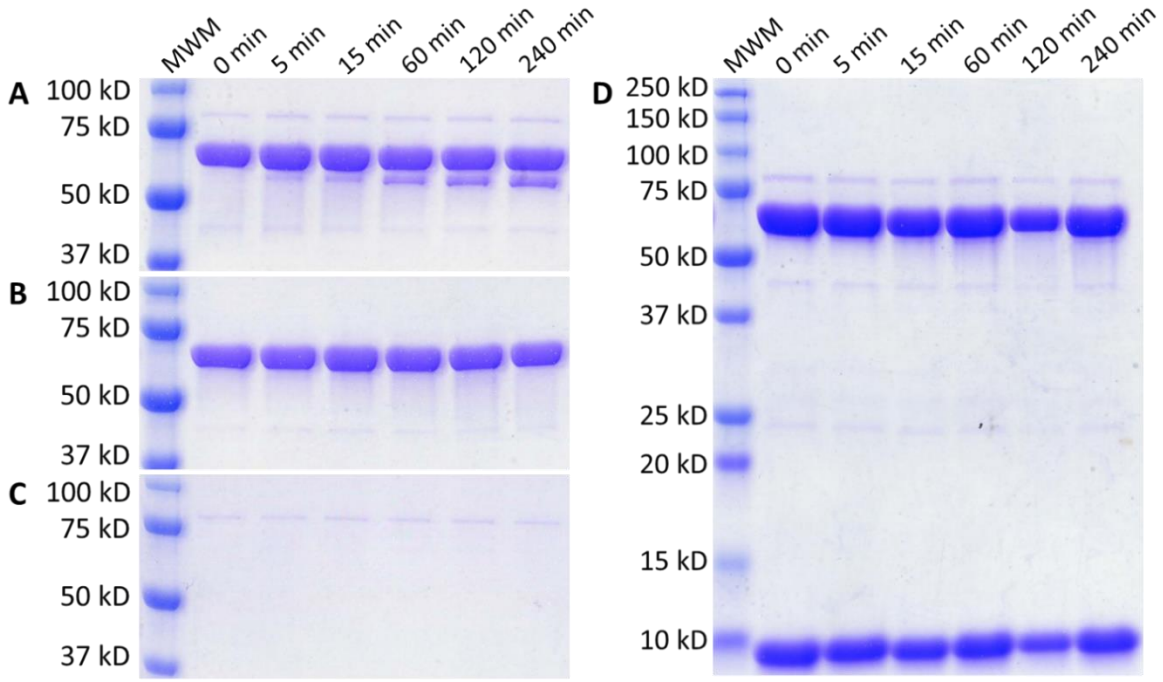

Figure 4.5. Protease assay showing Prc degrades the STN subdomain of PupR CCSSD in the absence of the PupB NTSD. Proteolysis was monitored at the time points indicated. A) Protease assay monitoring proteolysis of the MBP-PupR CCSSD by Prc-His6. The intensity of the degradation band increased with time. B) Protease assay control incubating only the MBP-PupR CCSSD. No degradation band is observed. C) Protease assay control incubating only Prc-His6. No degradation band is observed. D) Protease assay monitoring proteolysis of the MBP-PupR CCSSD:PupB NTSD complex by Prc-His_6. No degradation band is observed.

4.3.4. Mass Spectrometry Reveals that Prc Sequentially Degrades the STN Subdomain of the PupR CCSSD

Mass spectrometry analysis of the protease assay reaction products revealed two significant large protein masses one at 67,344.8 Da and the second at 58242.8 Da (Fig. 4.6). The 67.3 kDa experimental mass agrees with the full-length MBP-PupR CCSSD (residues 110-324) theoretical MW of 67,358 Da determined from the sequence. The 58.2 mass compares well to a remnant containing MBP-PupR CCSSD 110-240, which has a theoretical MW of 58,257 Da. A proteolytic remnant with a mass associated with PupR CCSSD residues 241-324 was not identified. However, several small peptides are present. Further analysis of the peptide fragments

found in the protease reaction identified them as being derived from the proteolysis of PupR CCSSD residues 242-324. The peptides ranged from 6-25 residues in length and were sequenced using MS MS (Table 4.4). Mapping of the peptides onto the sequence of PupR indicated these peptides derived from the PupR CCSSD residues 242-324. Thus, the processed C-terminal residues include the entire PupR CCSSD STN subdomain and part of the subdomain linker responsible for forming the PupR CCSSD:PupB NTSD complex. Together these data indicate Prc degrades the C-terminal residues of PupR CCSSD via many short "clips" until it stops at residue 240, rather than one cleavage of the entire region (Fig. 4.7).

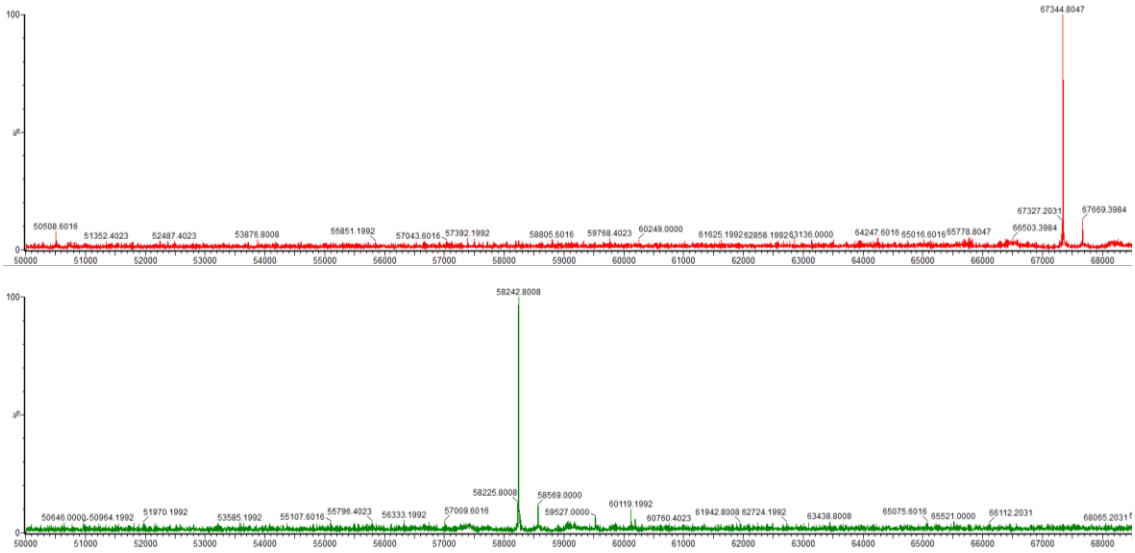

Figure 4.6. Protein masses detected by mass spectrometry upon completion of the protease assay (Fig. 4.5A). Masses of 67,344.8 Da (red) and 58,242.8 Da (green) were detected.

Table 4.4. Peptides identified in the reaction mixture after 240 minutes of the PupR CCSSD protease. Only peptides identified with high confidence are included in the table. Identified peptides cover amino acids 242-267 and 287-324 of the PupR CCSSD. Peptides indicated with an asterisk were selected for peptide synthesis for use in binding co-crystallization experiments.

PupR CCSSD Residues	Sequence	
242-253	AVAPAWSQGMLV	
242-254	AVAPAWSQGMLVA	*
242-261	AVAPAWSQGMLVAQGQPLAA	
243-254	VAPAWSQGMLVA	
245-254	PAWSQGMLVA	
248-254	SQGMLVA	
255-260	QGQPLA	
255-261	QGQPLAA	
255-267	QGQPLAAFIEDLA	
261-267	AFIEDLA	
262-267	FIEDLA	
287-299	GTFPLENTDKIIA	
300-312	AVAETLQLEVQHF	
300-313	AVAETLQLEVQHFT	*
300-317	AVAETLQLEVQHFTRYWV	
300-318	AVAETLQLEVQHFTRYWVT	
300-324	AVAETLQLEVQHFTRYWVTLKPRMA	*
302-313	AETLQLEVQHFT	
303-313	ETLQLEVQHFT	
303-317	ETLQLEVQHFTRYWV	
314-324	RYWVTLKPRMA	*
315-324	YWVTLKPRMA	
316-324	WVTLKPRMA	*

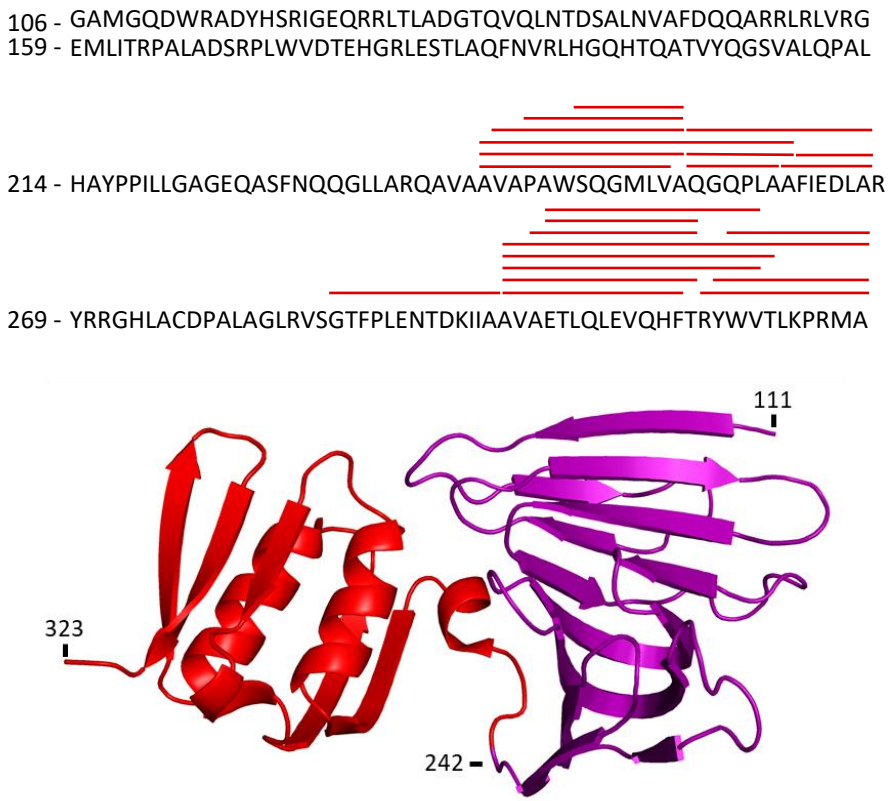

Figure 4.7. Cleavage map of the peptides released upon proteolysis of the PupR CCSSD by Prc. The peptides listed in Table 4.4 are represented by the red lines above the CCSSD amino acid sequence. Lower confidence peptides for the missing 268-286 residues were observed, however these were excluded to only show high confidence fragments. Prc-mediated proteolysis products are mapped on the PupR CCSSD structure. The 57.2 kDa peak corresponds to the CJM subdomain (purple), while the red region corresponds to the STN and linker regions that are proteolyzed into small fragments.

4.3.5. PupR CCSSD Peptide Binding to Prc

As described previously, Prc degrades the PupR CCSSD STN and the linker region into short peptides. MST was used to determine the binding affinity of PupR CCSSD peptides to Prc as well as the best candidate for complexing with Prc for crystallization trials. MST validated the binding of three PupR CCSSD peptides to Prc-His6 K510A. PupR CCSSD 242-254, W+300-313, and 314-324 bind to Prc-His6 K510A with a K_d and 95% confidence interval of 3.25 [2.77-3.80], 11.55 [0.34-39.5], and 15.84 [0.58-43.1] µM, respectively (Table 4.5 & Fig. 4.8). Due to

its tightest binding affinity to Prc-His6 K510A, PupR CCSSD 242-254 was used in crystallization trials.

Table 4.5. PupR CCSSD binding to Prc-His_6 K510A determined by MST. Binding affinities in μM are reported with the 95% confidence interval in brackets.

Target	**Ligand**	**K_d (μM)**
Prc-His_6 K510A	PupR CCSSD 242-254	3.25 [2.77 - 3.80]
Prc-His_6 K510A	PupR CCSSD W+300-313	11.55 [0.34 - 39.5]
Prc-His_6 K510A	PupR CCSSD 300-324	-
Prc-His_6 K510A	PupR CCSSD 314-324	15.84 [0.58 - 43.1]
Prc-His_6 K510A	PupR CCSSD 316-324	-

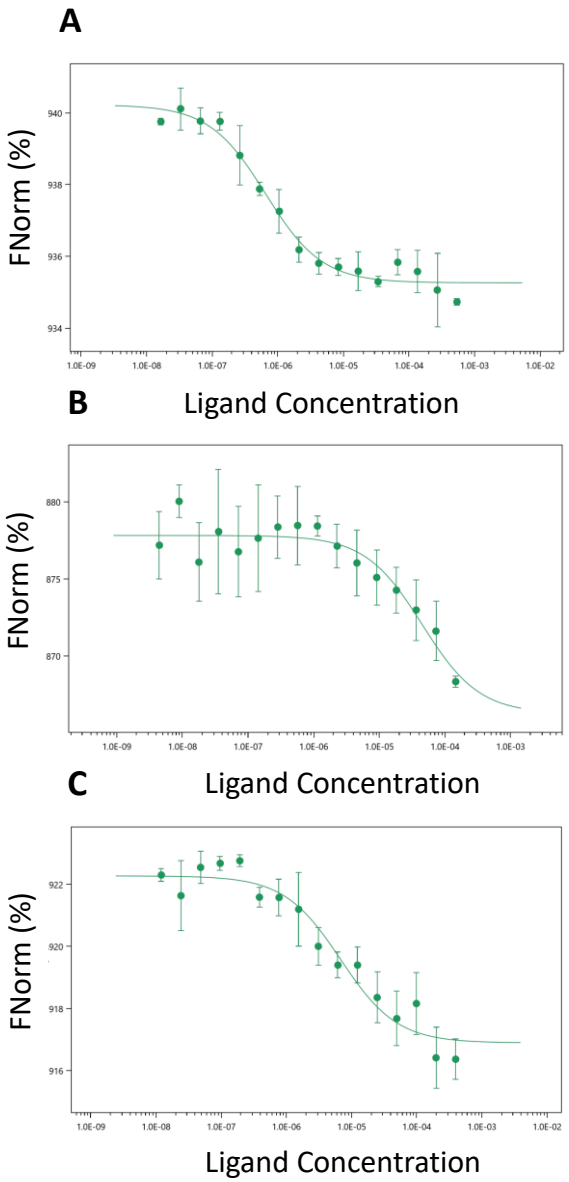

Figure 4.8. MST binding curves and fits for PupR CCSSD binding to Prc-His_6 K510A. A) Data points, curve fits, and data point errors plotted as FNorm (%) vs ligand concentration for PupR CCSSD 242-254:Prc-His_6 K510A. B) Data points, curve fits, and data point errors plotted as FNorm (%) vs ligand concentration for PupR CCSSD W+300-313:Prc-His_6 K510A. C) Data points, curve fits, and data point errors plotted as FNorm (%) vs ligand concentration for PupR CCSSD 314-324:Prc-His_6 K510A.

4.3.6. Prc Structure and Conformational Transitions

Structures of Prc in complex with the PupR CCSSD or peptides derived from the CCSSD should provide substantial information regarding the mechanism of Prc in CSS. We first

attempted to determine the unliganded structure of Prc. We were unable to crystallize the WT Prc or the Prc-His_6 K510A mutant, however, we were able to obtain and optimize crystals of Prc-His_6 S485A. The Prc-His_6 S485A crystals belong to the space group $P2_12_12_1$, with 1 molecule per asymmetric unit. The data collection statistics show that high quality diffraction data were collected to 2.0 Å (Table 4.6). The structure of Prc-His_6 S485A was solved by molecular replacement (MR) using the *E. coli* Prc structure (PDB 6IQR) as a search model. Final model was refined at 2.01 Å resolution with an R_{work} = 0.209 and R_{free} = 0.249. Refinement statistics indicate the model is of high quality (Table 4.6). Electron density is present for Prc residues 40-244, 255-658- and 677-705. Prc is composed of a N-terminal helical domain (NHD), a vault domain which provides corridor for substrate peptide binding, a platform domain which contains the catalytic residues and the base for the vault domain, a PDZ domain and a C-terminal helical domain (CHD) (Figure 4.9). It has overall dimensions of 86 Å x 57 Å x 37 Å. In its "closed" state, the NHD, vault domain, platform and CHD form a bowl that encompasses the PDZ domain, with an approximate PDZ domain buried surface area of 1,231 Å (Fig. 4.9).

Table 4.6. X-ray data collection, phasing, and refinement statistics for Prc-His_6 S485A and Prc-His_6 K510A:PupR CCSSD 242-254. Values in parenthesis indicate the highest resolution shell.

c	**Prc-His_6 S485A**	**Prc-His_6 K510A:PupR CCSSD 242-254**
Beamline	24-ID-C	23-ID-B
Wavelength (Å)	0.98054	1.03317
Space group	$P2_12_12_1$	$P6_122$
Unit-cell parameters (Å, deg)	80.0, 101.6, 101.8 αβγ = 90	143.6, 143.6, 145.8 αβ=90 γ = 120
Resolution range (Å)	101.84-2.01 (2.12-2.01)	124.4-2.16 (2.20-2.16)
Total observations	760928 (72675)	965966 (46874)
Unique observations	55905 (8071)	47960 (2356)
Multiplicity	13.6 (9.0)	20.1 (19.9)
Completeness (%)	99.9 (100.0)	100.0 (100.0)
CC(1/2)	0.998 (0.800)	0.999 (0.357)
R_{merge}	0.146 (1.255)	0.191 (4.769)
Mean $I/\sigma I$	19.9 (1.9)	10.3 (0.8)
Refinement		
Resolution range (Å)	71.9-2.01 (2.04-2.01)	47.31-2.16 (2.63-2.16)
R_{work} (%)	21.33	20.59
R_{free} (%)	24.88	23.90
RMSD sterochemistry		
Bond lengths (Å)	0.017	0.008
Bond angles (deg)	1.578	0.919
No. of atoms	5255	5265
Prc-His_6 S485A	5065	4908
Ligand	-	122
Waters	190	181
Ramachandran plot (%)		
Preferred	96.7	97.8
Allowed	3.3	2.2
Outliers	0	0

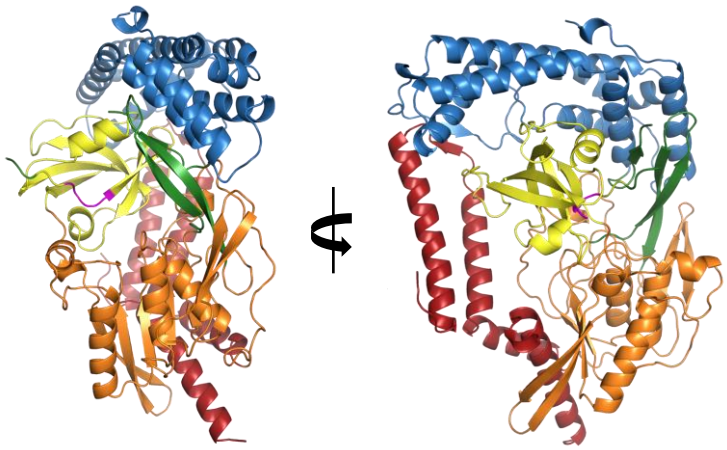

Figure 4.9. An X-ray crystal structure of Prc-His_6 S485A. Prc is composed of 5 domains, depicted in different colors as indicated. The the NHD (blue), vault domain (green), platform domain (orange), and CHD (red) form a bowl-like structure that encompass the PDZ domain (yellow). The PDZ domain carboxylate binding loop, highlighted in magenta, faces inward towards the distorted proteolytic groove.

The NHD and CHD interact via two anti-parallel β-strands to form a large portion of the bowl. The vault domain and platform domain finish the bowl, creating the proteolytic groove. Residues 245-254 of the vault domain are lacking electron density and are likely disordered. The missing region is a key component in forming the proteolytic groove. The catalytic dyad residues serine 485 (mutated to an alanine in this model) and lysine 510 are found at the base of the presumptive proteolytic groove on the platform domain.

The PDZ domain consists of a canonical β-sandwich bordered by two α-helices [154, 155]. The highly conserved carboxylate binding loop, G260-I261-G262-A263, faces inward near the distorted proteolytic groove (Fig. 4.10). Similarly, the conserved R321 sits above the carboxylate binding loop, stabilizing the substrate C-termini (Fig. 4.10). However, the hinge regions that connect the PDZ domain to the vault domain and platform domain and contain the conserved substrate-sensing leucine residues (L258 and L356) are disordered.

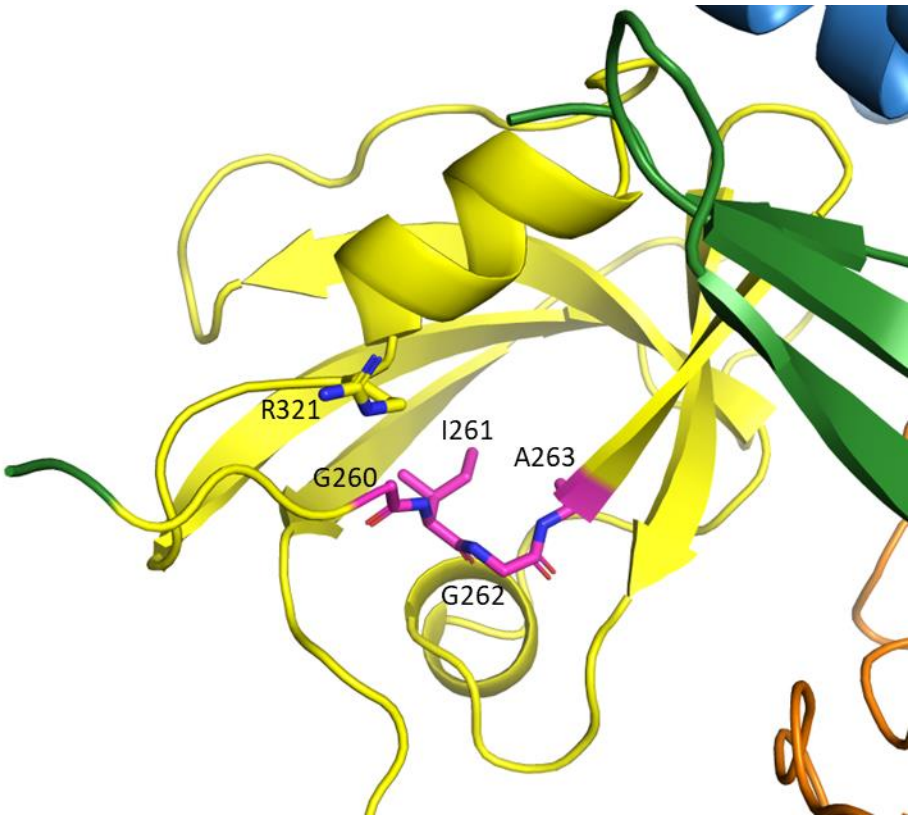

Figure 4.10. The carboxylate binding loop and R321 interact with the substrate C-termini. In the resting state, the carboxylate binding loop (magenta) of the PDZ domain (yellow) faces in toward the distorted vault domain (green). The backbone amides of the carboxylate binding loop, residues G260-I261-G262-A263, interact with the C-termini of substrate proteins. Similarly, the side chain of R321 aids in stabilization of the substrate C-termini.

P. capeferrum Prc shares 44% sequence identity to the *E. coli* Prc, and the closed conformation structures of the two proteins superimpose with a root-mean-square deviation (RMSD) of 1.67 Å over 504 Cα atoms. The missing electron density for the vault domain residues 245-254 aligns with the *E. coli* 6IQR structure in which the vault domain helix is displaced and partially unfolded in the closed state [147]. Additionally, the 6IQR substrate-sensing hinge region containing the conserved leucine residues is unfolded into two coils, like our structure [81, 147].

Subsequently, we were able to obtain crystals for the Prc-His_6 K510A mutant in complex with a peptide consisting of PupR CCSSD residues 242-254. The Prc-His_6 K510A:PupR CCSSD

242-254 crystal belongs to the space group $P6_122$ with 1 molecule per asymmetric unit. The data collection statistics show that high quality diffraction data were collected to 2.2 Å resolution (Table 4.6). Phases for the initial electron density map of Prc-His_6 K510A:PupR CCSSD 242-254 was obtained using molecular replacement (MR) with the *E. coli* Prc structure (PDB 5WQL). Final refinement was accomplished at 2.16 Å with an R_{work} = 0.206 and R_{free} = 0.239 (Table 4.6). Refinement statistics indicate the model is of high quality (Table 4.6). Prc electron density is present for residues 39-636 and 680-700 with overall dimensions of 82 Å x 55 Å x 47 Å. Interestingly, electron density was found for the entirety of the vault domain. Unexpectedly, electron density for a second peptide was found bound to the PDZ domain. This density agreed well with the sequence of the five C-terminal residues of the PupR CCSSD 242-254 peptide and was modeled as GMLVA.

Prc-His_6 K510A:PupR CCSSD 242-254 shares a similar bowl-like structure composed of the NHD, vault domain, platform domain, and CHD. However, the Prc-His_6 K510A structure is in "open" conformation in which the PDZ domain is extended ~17 Å away from the bowl, in relation to the Prc-His_6 S485A structure (Fig. 4.11 & 4.12). Additionally, the vault domain of Prc-His_6 K510A vault domain is fully folded, unlike in the Prc-His_6 S485A. The catalytic dyad residues are now within hydrogen-bonding distances, and the hinge regions connecting the PDZ domain are ordered with the sidechains of the conserved substrate-sensing L258 and L356 residues facing the PDZ bound peptide.

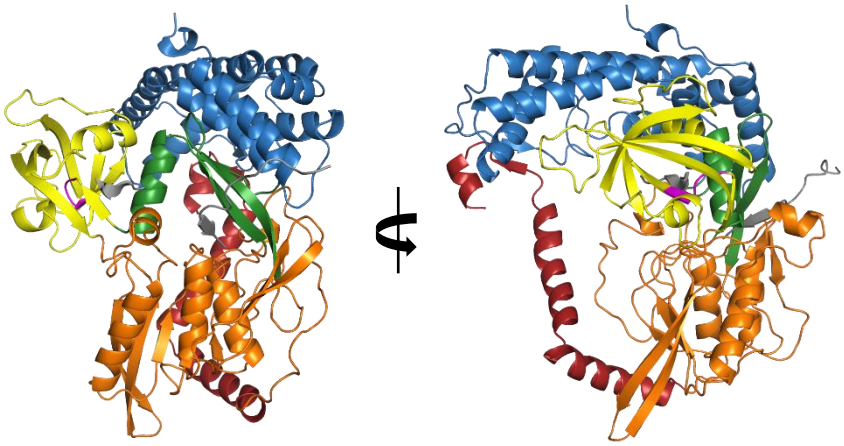

Figure 4.11. An X-ray crystal structure of the Prc-His6 K510A:PupR CCSSD 242-254 complex. Domains are depicted in different colors as indicated. The bowl-like structure of the NHD (blue), vault domain (green), platform domain (orange), CHD (red) and extended PDZ domain (yellow). The PDZ domain carboxylate binding loop, in magenta, faces toward the core of the protein and ordered proteolytic groove. The bound peptides to the proteolytic groove and PDZ domain are represented in grey.

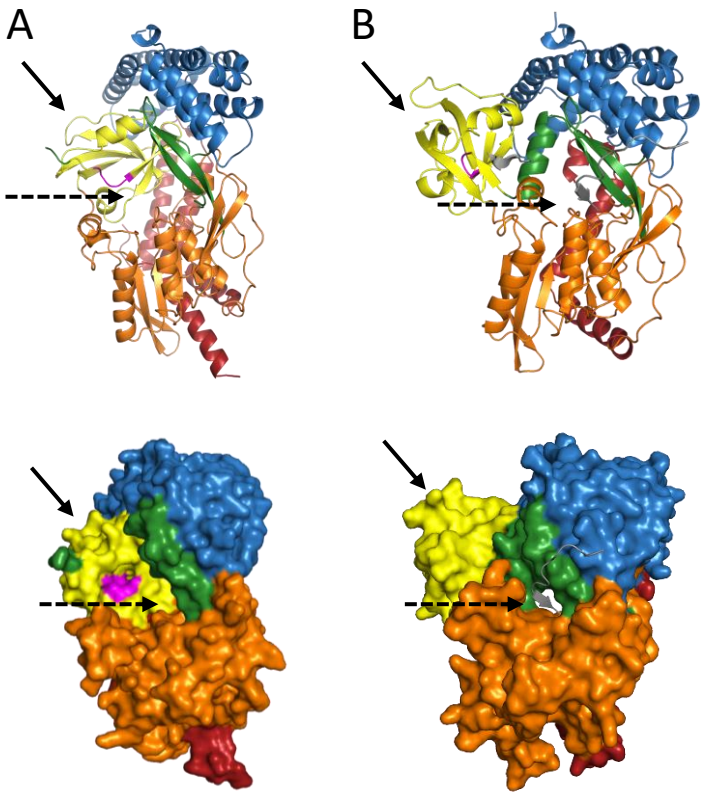

Figure 4.12. Conformational changes from resting to active between the Prc-His6 S485A and Prc-His6 K510A:PupR CCSSD242-254 structures. Upon binding to substrate, Prc undergoes a conformational change discernable by the outward extension of the PDZ domain (indicated by the solid arrow) and ordering of the proteolytic groove formed by the vault domain and platform domain (indicated by the dashed arrow). A) Inactive Prc-His6 S485A represented in cartoon and surface view. B) Active Prc-His6 K510A:PupR CCSSD 242-254 represented in cartoon and surface view.

The Prc-His_6 K510A:PupR CCSSD 242-254 structure superimposes well with the "open" conformation of *E. coli*, PDB 5WQL, with an RMSD of 1.32 Å over 560 Cα atoms. The "open" conformations of Prc-His_6 K510A and the *E. coli* Prc show similar conformational transitions relative to their "closed" conformations: i.e. outward movement of the PDZ domain, ordering of the vault domain, and movement of the catalytic dyad residues closer to hydrogen bonding distance [81, 147]. Interestingly, the *E. coli* Prc structure also contains two short peptides bound to the active site as well as to the PDZ domain [81]. However, the origin of the peptides is unknown

whereas the covalently linked PupR CCSSD 242-254 provides insights into binding of a specific substrate as well as a trapped cleavage intermediate.

4.3.7. Peptide Binding to the Prc Active Site and PDZ Domain

As discussed previously, the Prc-His_6 K510A:PupR CCSSD 242-254 structure contains two bound peptides. MST validated the binding of three PupR CCSSD peptides to Prc-His_6 K510A. Electron density is visible for the entire PupR 242-254 peptide, extending outward from the catalytic Ser (S485) in the active site. Notably, the C-terminus of this bound peptide appears to be covalently linked to the catalytic S485 of Prc, representing an acyl-enzyme intermediate (Fig. 4.13).

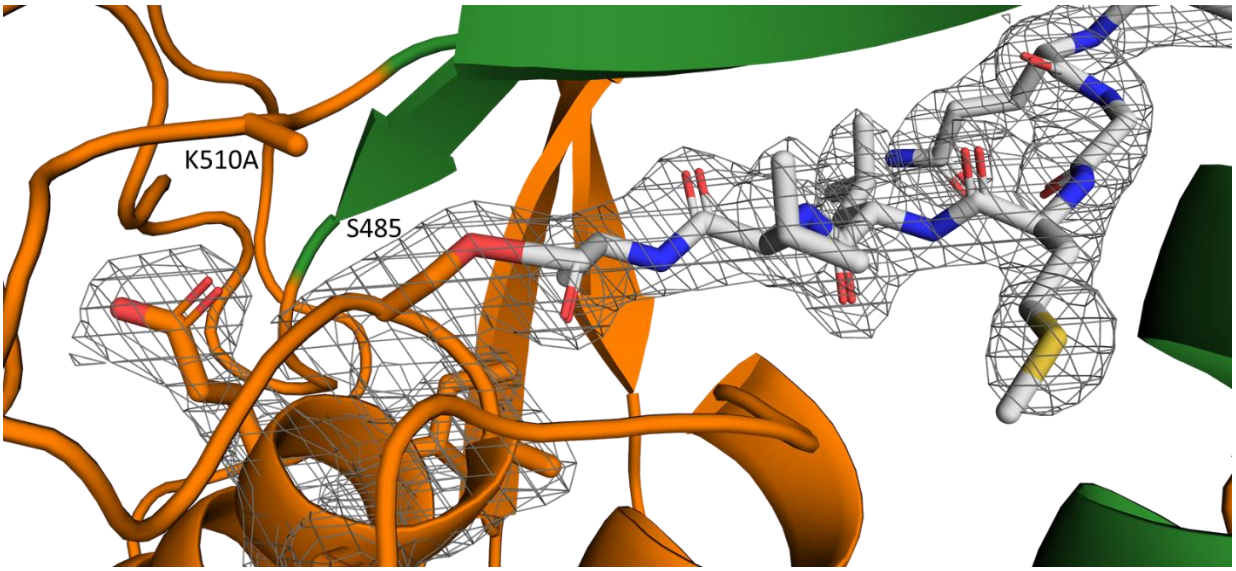

Figure 4.13. Covalent linkage of the PupR 242-254 C-terminal alanine to the Prc catalytic serine sidechain. The Prc vault domain (green) and platform domain (orange) are depicted in cartoon with the catalytic S485 and K510A shown in stick. The PupR 242-255 peptide is represented in stick (carbon atoms in grey, nitrogen atoms in blue, oxygen atoms in red, and sulfur atoms in yellow). Electron density contoured at 1.0 sigma, surrounding PupR 242-255 and the residues around Prc S485 is shown.

Electron density was also observed for a five-residue peptide bound to the PDZ domain of Prc (Fig. 4.14). The exact amino acid sequence of the peptide is unknown. However, the PupR residues 250-254, GMLVA, fit reasonably to this density and were used to model substrate

binding, but we cannot unambiguously verify the exact amino acid sequence of this peptide. Final refinements indicate that the C-termini of the PDZ-bound peptide is stabilized by the backbone amides of the carboxylate binding loop. Additionally, the substrate-sensing leucine sidechains appear to stabilize the hydrophobic PupR CCSSD V254 sidechain. Furthermore, R321 stabilizes the PDZ bound peptide through electrostatic interactions with the backbone of the penultimate peptide residue.

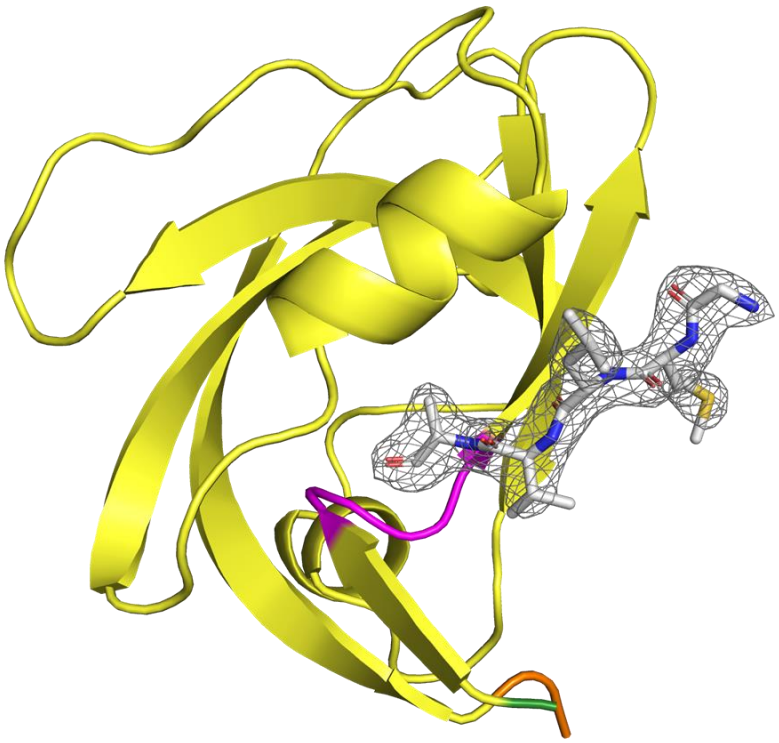

Figure 4.14. Peptide bound to the carboxylate binding loop of the Prc PDZ domain. The unknown peptide modeled as the five C-terminal residues of PupR CCSSD 242-255 are represented in stick (carbon atoms in grey, nitrogen atoms in blue, oxygen atoms in red, and sulfur atoms in yellow) bound to the carboxylate binding loop (magenta) of the Prc PDZ domain (yellow). The electron density surrounding the peptide is contoured at 1.0 sigma.

4.3.8. SEC-SAXS Analysis of Prc-His_6 S485A and K510A Solution Conformations

SEC-SAXS was used to determine and compare low-resolution conformation and solution properties such as molecular mass and oligomeric states of Prc-His_6 S485A and Prc-His_6

K510A. Following buffer subtraction, the auto calculated Rg distribution across the sample region for Prc-His_6 S485A is linear, indicating homogenous scattering particles (Fig. 4.15A). The sample Guinier plot is linear in the low q region, implying the sample is monodisperse with an Rg value of 30.0 Å (Fig. 4.15B). The P(r) distribution curve suggests Prc-His_6 S485A is a mostly compact molecule with an elongated region giving rise to a Dmax value of 110 Å (Fig. 4.15C). Additionally, the Kratky plot describes a partially-folded molecule (Fig. 4.15D). The Kratky plots agree with CD results in which ~50% of secondary structure exists in coil and turn (Fig. 4.16 and Table 4.7). The Vp molecular weight estimate from the SEC-SAXS analysis is 84.5 kDa; agreeing well with the theoretical molecular weight of ~80 kDa based on the amino acid sequence.

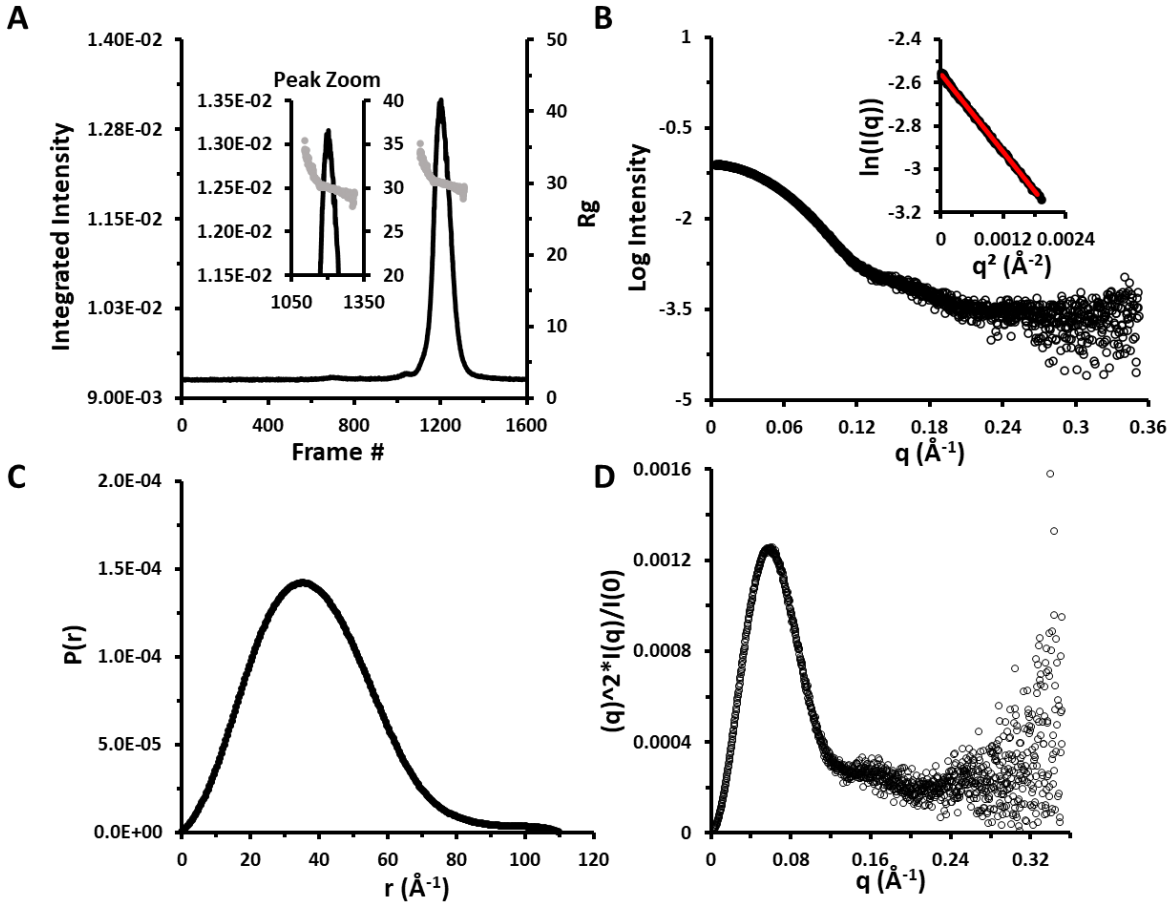

Figure 4.15. SEC-SAXS analysis of Prc-His_6 S485A. A) Subtracted scattering plot (black) with Rg distribution (grey) across the peak of interest. B) Experimental scattering profile and Guinier plot of the low q region. C) Distance distribution P(r) plot. D) Kratky plot.

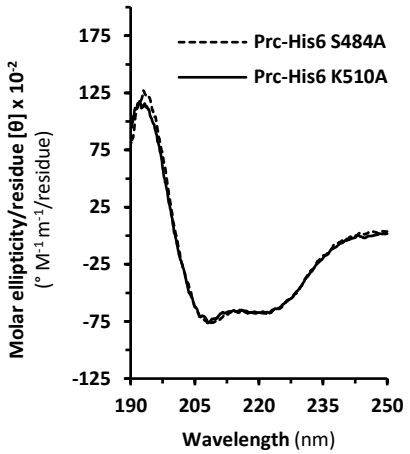

Figure 4.16. CD spectra of Prc-His_6 S485A and K510A. CD spectra of Prc-His_6 S485A (dots) and Prc-His_6 K510A (line).

Table 4.7. Comparison of secondary structure content estimated from CD spectra analyses using CDPro [96].

	CD analyses (N_{res})			
Protein	**Helix**	**Strand**	**Coil + Turn**	**Total**
Prc-His_6 S485A	265.2 ± 3.9	92.2 ± 3.2	352.4 ± 9.3	709.9
Prc-His_6 K510A	242.4 ± 2.5	111.8 ± 6.4	356.7 ± 10.0	711

For Prc-His_6 K510A, following buffer subtraction, the auto calculated R_g distribution across the sample region for Prc-His_6 K510A is linear, indicating homogenous scattering particles (Fig. 4.17A). The sample Guinier plot is linear in the low *q* region, implying the sample is monodisperse with an R_g value of 30.2 Å (Fig. 4.17B). The *P(r)* distribution curve suggests Prc-His_6 K510A is a mostly compact molecule with an elongated region giving rise to a D_{max} value of 108 Å (Fig. 4.17C). Additionally, the Kratky plot describes a partially folded molecule (Fig. 4.17D). The Kratky plots agree with the CD results in which ~50% of secondary structure exists in coil and turn (Fig. 4.16 and Table 4.7). The Vp molecular weight estimate from the SEC-SAXS analysis is 85.5 kDa; agreeing well with the theoretical molecular weight of ~80 kDa based on the amino acid sequence.

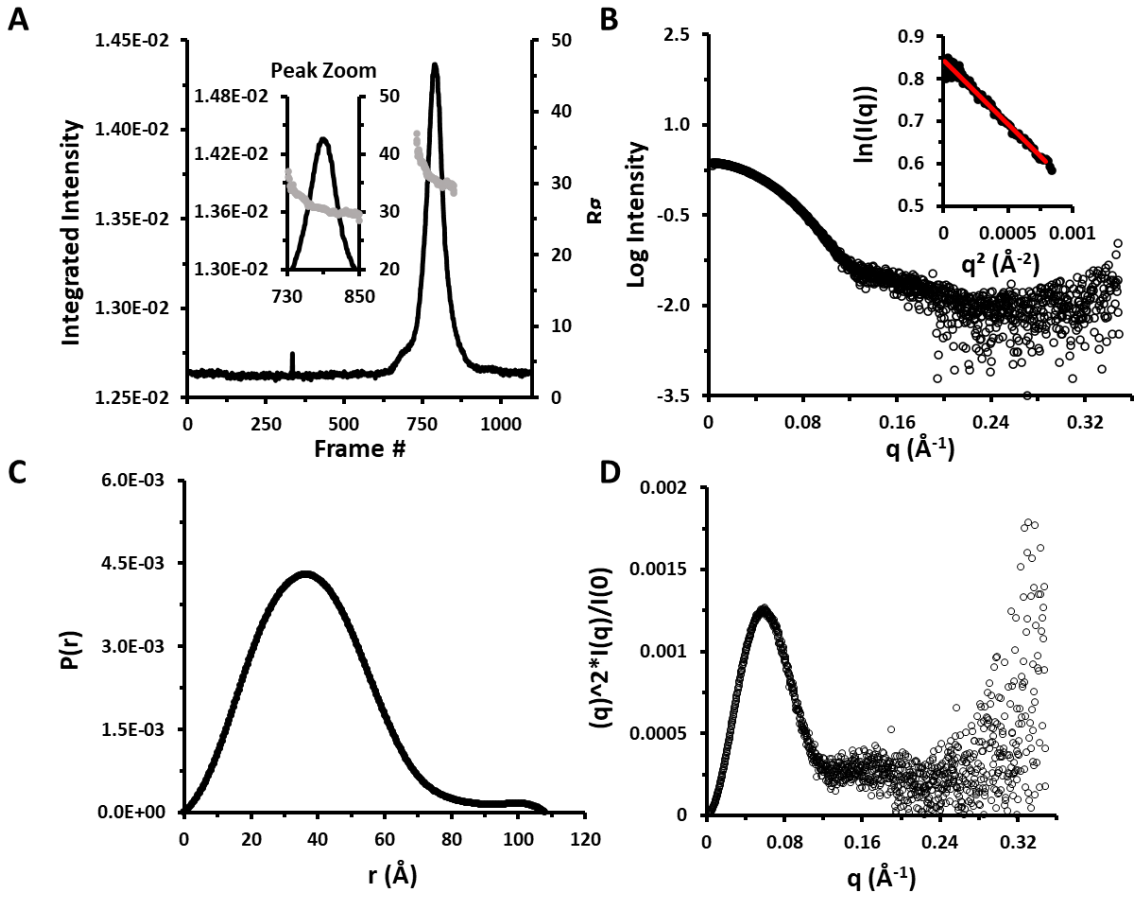

Figure 4.17. SEC-SAXS analysis of Prc-His$_6$ K510A. A) Subtracted scattering plot (black) with Rg distribution (grey) across the peak of interest. B) Experimental scattering profile and Guinier plot of the low q region. C) Distance distribution *P(r)* plot. D) Kratky plot.

To assess individual molecule conformations in solution, the theoretical scattering curves of Prc-His$_6$ S485A and Prc-His$_6$ K510A:PupR CCSSD 242-254 were aligned to the scattering curves of Prc-His$_6$ S485A and K510A using CRYSOL from the ATSAS suite (Fig. 4.18A & 4.19A) [122]. The Prc-His$_6$ S485A experimental data fit with chi^2 values of 1.94 and 5.49 to theoretical scattering curves of Prc-His$_6$ S485A and Prc-His$_6$ K510A:PupR CCSSD 242-254 respectively; indicating the Prc-His$_6$ S485A likely exists in a resting conformation in solution. Similarly, the Prc-His$_6$ K510A experimental data fit with chi^2 values of 2.36 and 3.15 to theoretical scattering curves of Prc-His$_6$ S485A and Prc-His$_6$ K510A:PupR CCSSD 242-254

respectively. To determine if a mixture of conformations exist in solution, OLIGOMER from the ATSAS suite was utilized [119]. Interestingly, OLIGOMER suggests 61.0 ± 1.1% of the represented species in the Prc-His_6 S485A experimental data exists in a "closed" conformation and 39.0 ± 1.1% in the "open" conformation. Additionally, contrary to the chi^2 values, only 5.6 ± 1.9% of the represented species in the Prc-His_6 K510A experimental data are in the "closed" conformation and 94.4 ± 1.8% exist in the "open" conformation. This suggests the Prc-His_6 S485A construct favors the "closed" conformation whereas the Prc-His_6 K510A construct favors the "open" state and may support observations in pulldowns that the K510A mutant more readily forms a 1:1 complex with PupR CCSSD. OLIGOMER results were further utilized for superimposition of the Prc-His_6 S485A structure ("closed" conformation) to the Prc-His_6 S485A SEC-SAXS protein envelope and the Prc-His_6 K510A:PupR CCSSD 242-254 ("open" conformation) to the Prc-His_6 K510A SEC-SAXS protein envelope with SUPCOMB from the ATSAS suite (Fig. 4.18B & 4.19B) [139].

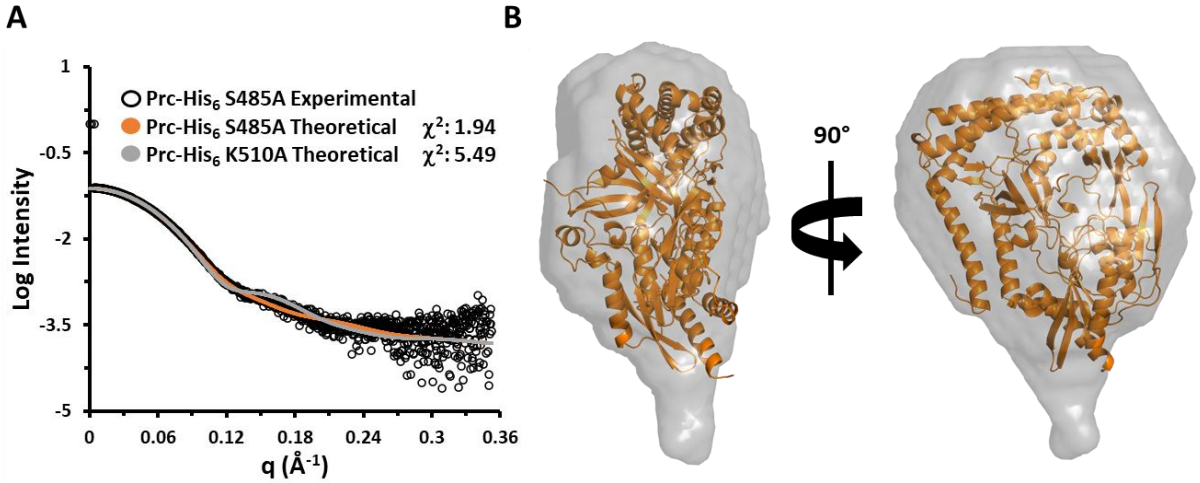

Figure 4.18. SEC-SAXS alignments and analysis of Prc-His6 S485A. A) Theoretical scattering curves of Prc-His_6 S485A and Prc-His_6 K510A fit to the experimental scattering curve of Prc-His_6 S485A using Crysol. B) Experimental protein envelope aligned with the structure of Prc-His_6 S485A using SUPCOMB [139].

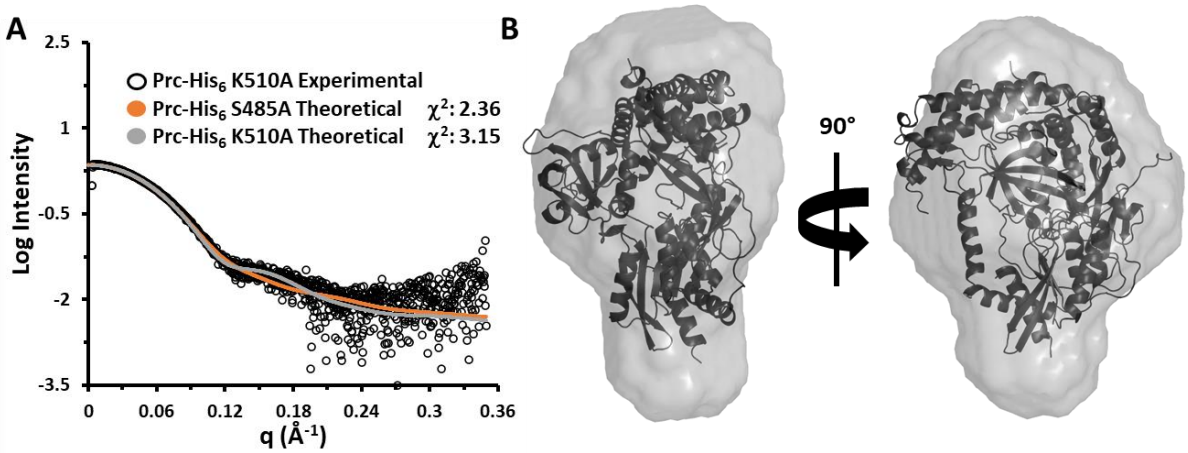

Figure 4.19. SEC-SAXS alignments and analysis of Prc-His$_6$ K510A. A) Theoretical scattering curves of Prc-His$_6$ S485A and Prc-His$_6$ K510A fit to the experimental scattering curve of Prc-His$_6$ K510A using Crysol. B) Experimental protein envelope aligned with the structure of Prc-His6 K510A:PupR CCSSD 242-254 using SUPCOMB [139].

4.3.9. SEC-SAXS Analysis of Prc-His$_6$ K510A:PupR CCSSD Complex

To evaluate the low-resolution structural and solution characteristics of the Prc-His$_6$ K510A:PupR CCSSD complex we utilized SEC-SAXS with a data reduction from BioXTAS Raw [138]. After buffer subtraction, the auto calculated R_g distribution across the sample region appeared to contain multiple species (Fig. 4.20A). Evolving factor analysis (EFA) was used to separate individual scattering components [151]. Two distinct components were identified; one of which matched well to the Prc-His$_6$ K510A scattering and a second is believed to be the Prc-His$_6$ K510A:PupR CCSSD complex. For the protein complex, the Guinier plot is linear in the low q region, indicating a monodisperse sample with an R_g of 35.7 Å (Fig. 4.20B). The *P(r)* distribution curve suggests an extended molecule with a D_{max} value of 138 Å (Fig. 4.20C). Furthermore, the Kratky plot describes a partially folded molecule (Fig. 4.20D). Vc molecular weight estimates from the SEC-SAXS analysis suggest a 98.2 kDa molecule. The molecular weight estimate matches closely to the theoretical molecular weight of 104 kDa based on the amino acid sequence.

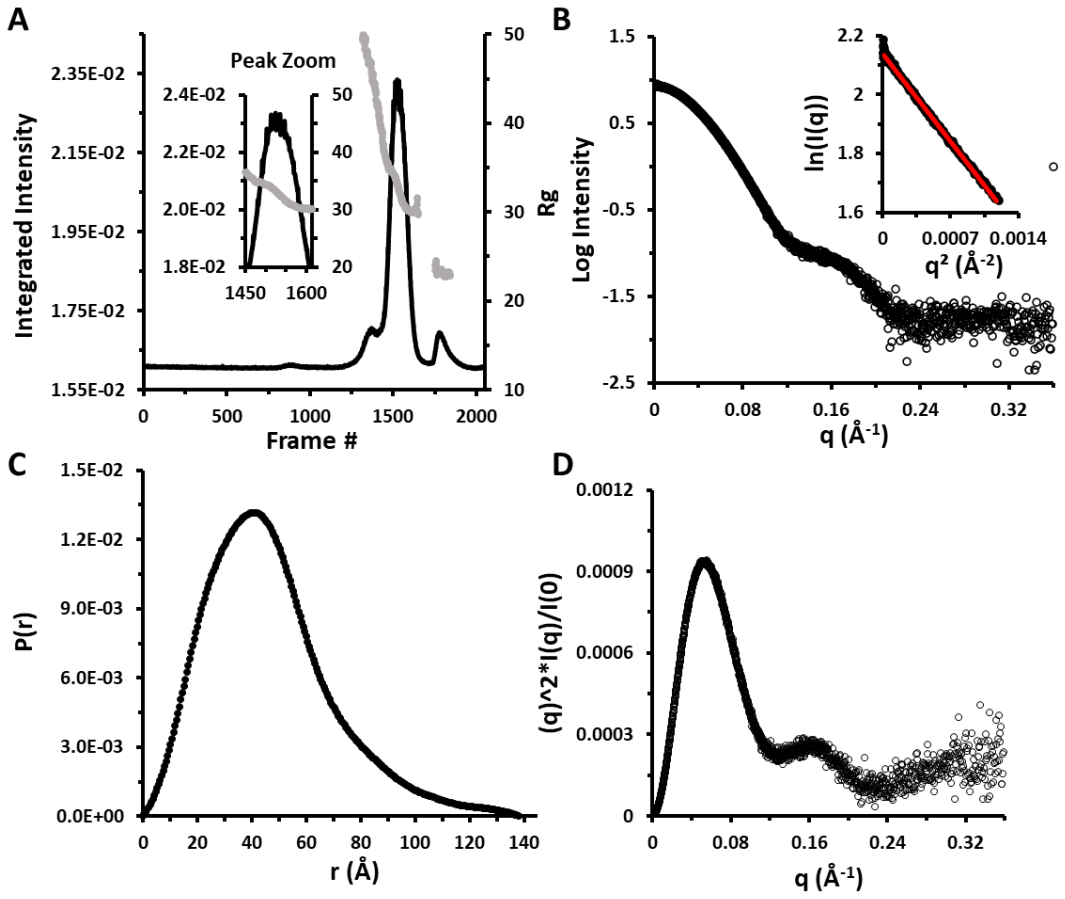

Figure 4.20. SEC-SAXS analysis of Prc-His$_6$ K510A:PupR CCSSD. A) Subtracted scattering plot (black) with R_g distribution (grey) across the peak of interest. B) Experimental scattering profile and Guinier plot of the low *q* region. C) Distance distribution *P(r)* plot. D) Kratky plot.

Theoretical scattering curves from the structures of Prc-His$_6$ S485A and Prc-His$_6$ K510A:PupR CCSSD 242-254 as well as the modeled complex of the Prc-His$_6$ K510A:PupR CCSSD were aligned to the experimental scattering curve using Crysol (Fig. 4.21A) [122]. Theoretical curves of Prc-His$_6$ S485A and Prc-His$_6$ K510A fit the scattering data with chi^2 values of 163.9 and 193.7 respectively. Alternatively, the modeled complex fit with a chi^2 value of 5.33. Non-ideal fitting of the modeled complex may be due to unmodeled flexibility associated with the unfolding of the PupR CCSSD STN subdomain during complex formation and feeding of the C-terminal region through the proteolytic groove of Prc. The modeled complex was fit to the

SEC-SAXS protein envelope with Crysol, agreeing well to an extended PupR CCSSD away from proteolytic region of Prc (Fig. 4.21B) [122].

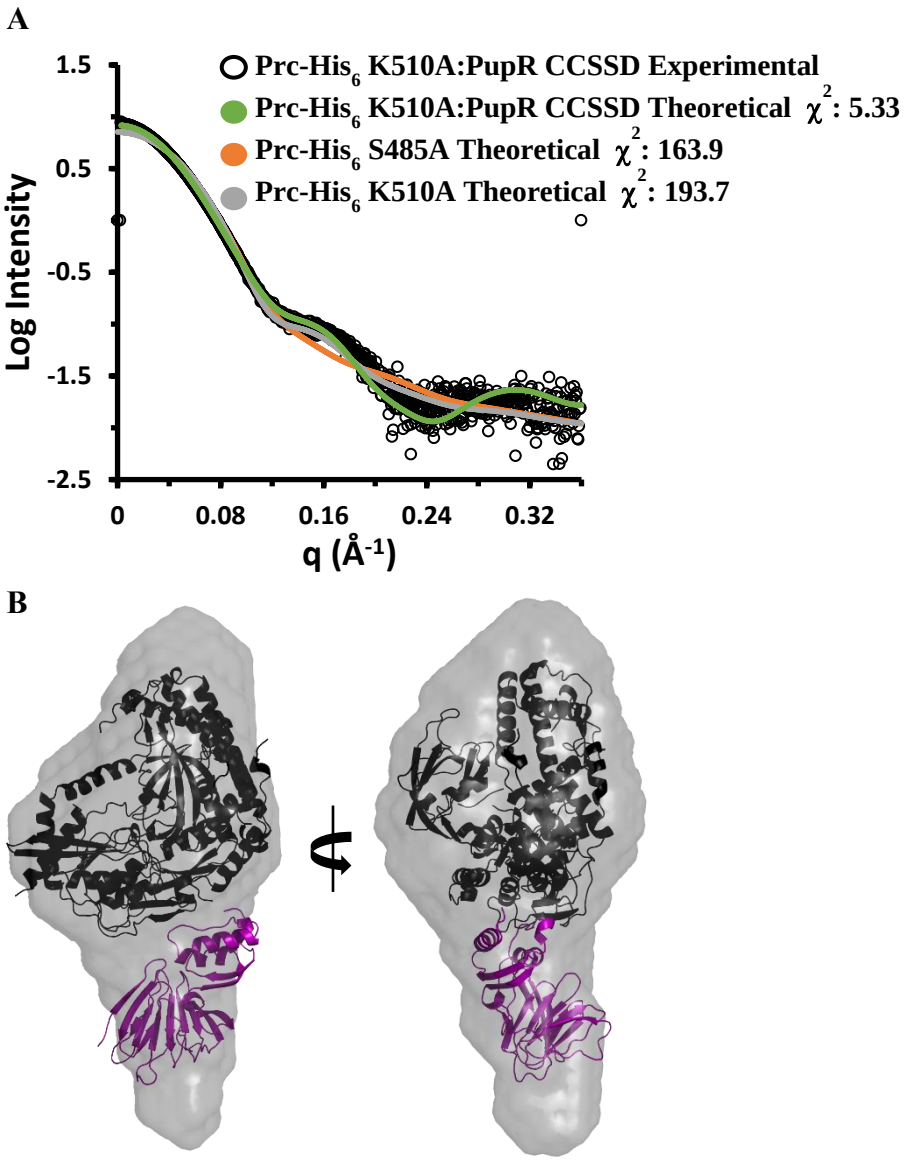

Figure 4.21. SEC-SAXS alignments and analysis of Prc-His_6 K510A:PupR CCSSD. A) Theoretical scattering curves of Prc-His_6 K510A:PupR CCSSD, Prc-His_6 S485A, and Prc-His_6 K510A fit to the experimental scattering curve of Prc-His_6 K510A:PupR CCSSD using Crysol. B) Experimental protein envelope aligned with the model of Prc-His_6 K510A:PupR CCSSD using SUPCOMB [139].

4.4. Discussion

Our structural and biophysical data investigate a critical step in CSS and the RIP of the PupR sigma regulator. The PupB NTSD was previously determined to stabilize the PupR CCSSD under non-signaling conditions in a 'primed' state [45]. Here we demonstrate for the first time that the PupB NTSD serves a dual role in CSS, stabilizing the CCSSD and shielding it from RIP under non-signaling conditions. The extensive interaction interface between the NTSD:CCSSD complex likely limits availability of the CCSSD C-termini and recognition by the site-1 protease. Further, our pulldown assays and ITC results indicate that the PupB NTSD outcompetes Prc interaction due to its tighter binding affinity for the CCSSD. Additionally, our protease assays show that the PupB NTSD shields the PupR CCSSD from Prc-mediated proteolysis. Prc was previously determined to recognize C-termini with a preference for hydrophobic unfolded substrates [79, 80]. Consistent with that preference, in the absence of the PupB NTSD, Prc proteolyzes the entire STN subdomain of the CCSSD into short peptides, as seen in the *Pseudomonas putida* Iut CSS system [46, 78].

Structurally, Prc is distinct from other C-terminal processing proteases like the *Scenedesmus obliquus* D1P, *Bacillus subtilis* CtpB, and *Pseudomonas aeruginosa* CtpA, despite sharing 23.6-34.7% sequence identity with these proteases [156-158]. Prc is a monomer comprised of a NHD, vault domain, platform domain, and CHD, forming a bowl-like structure into which the PDZ domain nestles. Our protein structures and SEC-SAXS data describe a conformational change from a "closed" to "open" state involving the extension of the PDZ domain, ordering of the vault domain, and movement of the catalytic dyad. Interactions at the carboxylate binding loop and conserved residues around the PDZ domain appear to thread the unfolded substrate into the interior of the protease. Ordering of the vault domain creates a narrow proteolytic groove

which allows entry of single peptides such as the PupR CCSSD 242-254 seen in our structure of the Prc-His_6 K510A:PupR CCSSD 242-254. Thus, a likely proteolytic mechanism would involve alternating between the "closed" state, which would allow substrate binding by the PDZ domain, transitioning to the "open" state, which would pull the substrate polypeptide chain through the active sites allowing nucleophilic attack and substrate cleavage. Prc would then reset to the "closed" conformation allowing the cycle to repeat, which explains the multiple fragments of the STN subdomain we observe. In agreement with our analyses, recent work on the *E. coli* Prc described a thorough structural transition from "closed" to "open" conformation, which is presented as representing the resting and active states, respectively [81, 147]. However, Prc from *E. coli* interacts with a lipoprotein, NlpI, increasing Prc activity towards the substrate MepS and localizing the site-1 protease to the outer membrane [81]. A homologous lipoprotein from *P. capeferrum* has yet to be identified.

Despite this, our structures, SEC-SAXS, and modeled complex detail a probable complex formation upon CSS signal activation. Following the dissociation of the PupB NTSD, Prc recognizes the destabilized PupR CCSSD, forming an elongated complex. The orientation of the Prc:PupR CCSSD complex would allow for the recognition of the CCSSD C-termini while the CCSSD remains localized in the inner membrane. The mechanism behind the dissociation of the NTSD:CCSSD complex has yet to be determined. However, a potential cause could be related to conformational changes upon binding of the TonB C-terminal domain (CTD) to the TonB box of PupB and iron import. Although, binding of the TonB CTD to the TonB-dependent transducer FoxA under non-signaling conditions has been demonstrated [55]. Additionally, AlphaFold Multimer modeling of the PupB:PupR CCSSD:TonB CTD ternary complex indicates that the ternary complex could exist in non-signaling conditions.

In summary, this study provides new insights into the role of the NTSD in regulating CSS by regulating the recognition and degradation of the sigma regulator by the site-1 protease. Under non-signaling conditions the NTSD not only stabilizes the sigma regulator CCSSD but also shields it from RIP. Upon signaling and the dissociation of the NTSD:CCSSD complex, the site-1 protease ‘clips’ the entire STN subdomain. The remaining ‘clipped’ sigma regulator would then be free for processing by the site-2 protease and release of the sigma factor for transcriptional activation.

5. TONB AND ITS ROLE IN IRON UPTAKE THROUGH THE COUPLED TONB-DEPENDENT TRANSDUCER, PUPB

5.1. Introduction

Import of most small molecules into Gram-negative bacteria is accomplished by passive diffusion through outer membrane (OM) porins such as the *E. coli* OmpF, OmpC, and PhoE [159-161]. However, the transport of larger substrates present at low concentrations in the environment requires specialized transport. Key amongst these transporters are the TonB-dependent transporters (TBDTs), which import ferric siderophores >600 Da, as well as other diverse molecules such as Vitamin B12, carbohydrates, and heme into the periplasm [1]. This is an energy dependent transport system that concentrates iron against its gradient. Energy input is accomplished through utilization of the proton motive force via the coupled TonB-ExbB-ExbD (Ton) complex [1, 32].

The Ton complex formation and mechanism of interaction with TBDTs has yet to be fully elucidated despite an abundance of structural analysis. All Ton complex proteins are anchored to the inner membrane by at least one transmembrane (TM) helix [32, 33]. TonB and ExbD each contain a small N-terminal cytoplasmic domain, one TM helix, and a periplasmic C-terminal domain connected to the TM helix by a flexible linker [32-34]. ExbB on the other hand contains a small N-terminal periplasmic domain, three TM helices, and a large cytoplasmic domain [32-34]. Currently, the stoichiometry of the Ton complex is unclear, despite extensive structural and biochemical research, as results have indicated possible ExbB:ExbD pairings of 4:2, 5:2, 6:3, 6:1, and 5:1 and ExbB:ExbD:TonB pairings of 4:2:1 and 7:2:1 [34]. Additionally, the mechanism of how the Ton complex utilizes the proton motive force is not understood. It appears

that the ExbB:ExbD complex captures this energy and transmits it to TonB, which subsequently transfers energy to the TBDT [1, 32].

TonB and the TBDT interact via the C-terminal domain (CTD) of TonB and a region of the TBDT termed the TonB box. Similar interactions likely exist in *P. capeferrum* as TonB is highly conserved across Gram-negative bacteria, with sequence identities ranging between 24.0 – 97.9% across the Gram-negative bacteria selected (Fig. 5.1) [162-165]. TonB CTDs, whose structures have been determined using soluble domain constructs, consists of an α/β structure, including a 3-4 β-stranded antiparallel β-sheet and two α-helices organized into a cylinder-like shape (Fig. 5.2) [162-165]. Both monomeric and dimeric structures have been observed, however, it appears that the monomeric structure is more likely to interact with TBDTs. Several structures of different TBDT and TonB CTD complexes have been solved, including those of *P. aeruginosa* FoxA, *E. coli* BtuB, and *E. coli* FhuA (Fig. 5.3 A-C). In each case, the TonB box of the TBDT forms a β-strand that hydrogen bonds to, and extends, the TonB CTD antiparallel β-sheet (Fig. 5.3 A-C) [53-55]. However, in these various structures the TonB CTD has differing spatial arrangements relative to the TBDT, and therefore interacts differently with the β-barrel and plug domains of the TBDT [53-55]. The significance of these variations is not yet completely understood.

Here we describe the cloning, expression, and purification of the TBDT PupB and the TonB CTD from *P. capeferrum* used to obtain pure protein. Similarly, pulldown assays of purified proteins were utilized to investigate the potential interaction of the TonB CTD with PupB. Furthermore, we characterized the solution state of the TonB CTD by SEC-SAXS to determine the oligomeric state of our *P. capeferrum* TonB CTD construct as well as the general folded state. Together this data will provide early insights into *P. capeferrum* TonB CTD structure, and interactions between the TonB CTD and the PupB.

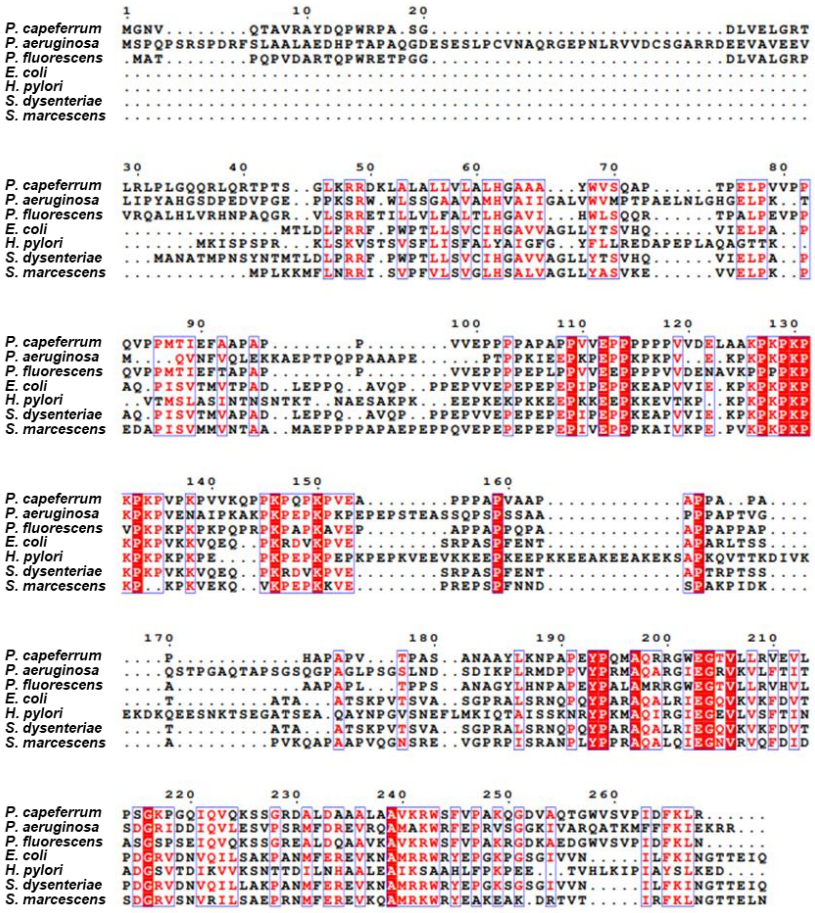

Figure 5.1. Sequence alignment of TonB proteins from different Gram-negative bacteria. Sequences were aligned using Clustal Omega and prepared with ESPript 3.0 [166, 167]. Columns with red text surrounded by blue squares indicate conserved residues. Residues highlighted in red with white text surrounded by blue squares indicate invariant residues. The percent sequence identity between the selected TonB proteins ranges from 24.0 – 97.9%.

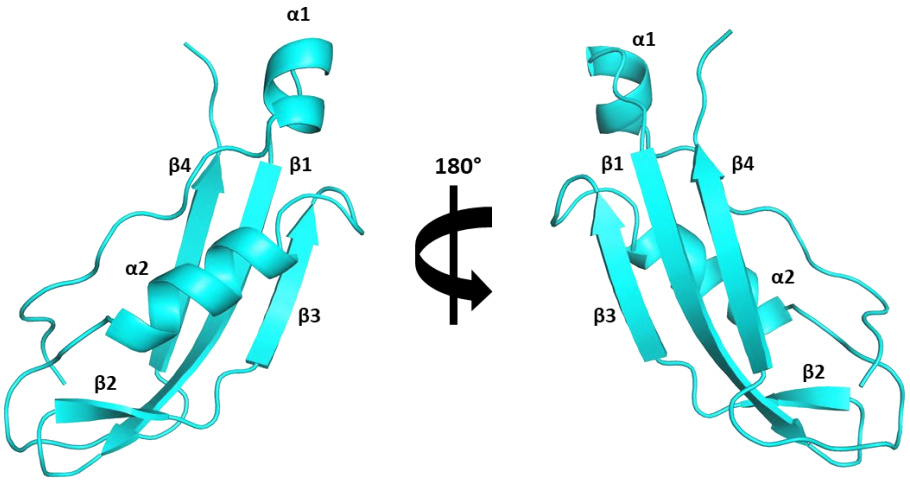

Figure 5.2. Cartoon representation of TonB CTD from *E. coli* (2GSK) with labeled secondary structure elements.

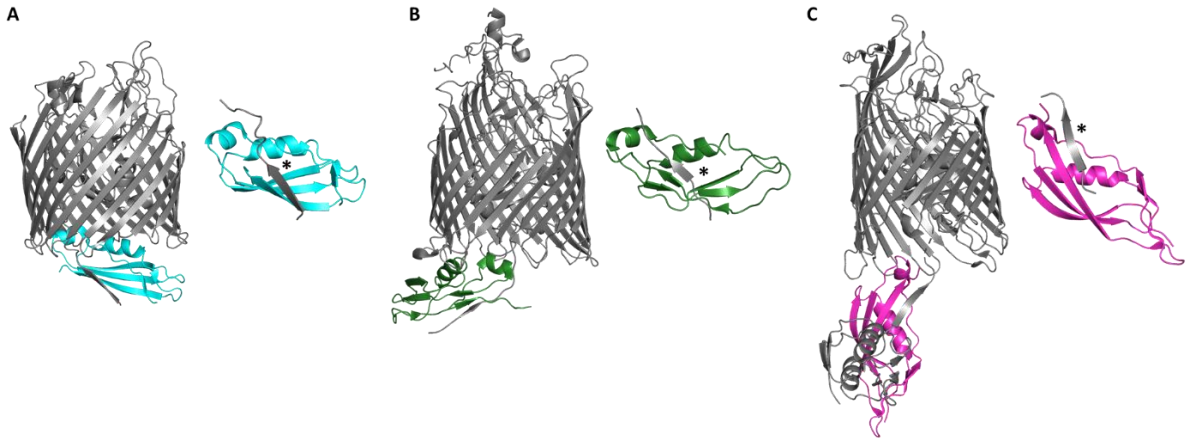

Figure 5.3. Structures of TBDT:TonB CTD complexes. The main chain of the TBDTs is shown in grey ribbon while that of the TonB CTD is in different colors. The TonB box of the TBDT, indicated by an asterisk, forms a parallel β-strand with the TonB CTD antiparallel β-sheet. A) The *E. coli* BtuB:TonB CTD (2GSK). Inset: A different view of the TonB box:TonB CTD that better shows the interaction between the TonB box alignment and the TonB CTD. B) The *E. coli* FhuA:TonB CTD (2GRX). Inset: A different view of the TonB box:TonB CTD that better shows the interaction between the TonB box alignment and the TonB CTD. C) The *P. aeruginosa* FoxA:TonB CTD (6I97). A different view of the TonB box:TonB CTD that better shows the interaction between the TonB box alignment and the TonB CTD.

5.2. Materials and Methods

5.2.1. Cloning, Expression, and Purification of the *P. capeferrum* WCS358 TonB CTD Construct

The TonB CTD construct was modeled after the homologous *E. coli* protein structures, 2GSK and 6I97, and secondary structure predictions from Jpred 3[126]. PCR was used to amplify the *tonB* gene region, encoding amino acids 177-268, from *P. capeferrum* WCS358 genomic DNA with primers 5' – AAC CTG TAT TTT CAG GGC GGA TCC ACG CCG GCT TCG GCC AAC – 3' and 5' – GTG GTG GTG GTG GTG GTG CTC GAG TTA TCG AAG CTT GAA GTC – 3'. The PCR product was subsequently cloned into pET41 via Gibson assembly between the restriction sites BamHI and XhoI. The final construct encodes an N-terminal GST tag, followed by a TEV-protease recognition sequence (ENLYFQG), fused to the TonB CTD. This plasmid was designated pET41-TonB CTD.

pET41-TonB CTD was used to transform chemically competent *E. coli* BL21 (DE3) cells for protein expression. 50 µL and 200 µL aliquots of the transformation mixture were used to inoculate two LB agar plates supplemented with 15 µg/ml kanamycin. Plates were inoculated overnight at 37 °C. A single colony was picked and added to a 70 mL culture of LB media supplemented with 15 µg/ml kanamycin and incubated at 37 °C overnight. For protein expression, 10 mL of overnight culture was added to 1 L of LB media supplemented with 15 µg/ml kanamycin. This culture was incubated at 37 °C with shaking at 200 rpm until it reached an OD_{600} of 0.7-0.9. Protein expression was induced with 0.5 mM IPTG. Following induction, cells were grown overnight at 20 °C. Cells were then harvested at 4,000 x g by centrifugation, washed with 25 mM Tris HCl pH 8.0 and 100 mM NaCl, and stored at -80 °C.

Cell pellets were resuspended in lysis buffer, 25 mM Tris HCl pH 8.0, 100 mM NaCl, and 2 mM DTT and lysed via a Branson Sonifier 450 sonicator. The lysate was then clarified by centrifugation at 20,000 x g and loaded onto Glutathione Sepharose 4B resin (Cytiva) equilibrated in lysis buffer. The column was subsequently washed with lysis buffer until unbound proteins were completely removed (~30- CV). Recombinant GST-TEV protease was added to the column and incubated at 4 °C overnight to release the TonB CTD from the GST tag. Lysis buffer was used to wash released the TonB CTD from the column. The TonB CTD was further purified by size-exclusion chromatography on a Superdex 75 increase 10/300 GL column (Cytiva) with an isocratic gradient buffer consisting of 25 mM Tris HCl pH 8.0 and 100 mM NaCl. Pure TonB CTD was concentrated to ~20 mg/mL, and flash frozen in liquid nitrogen prior to storage at -80 °C. Protein purity was determined to be >95% by SDS-PAGE with a 4-20% TGX SDS-PAGE gel (Bio-Rad) and Coomassie Blue staining[93].

5.2.2. Expression and Purification of the PupB Transporter

The following expression and purification protocols for PupB were originally designed by Dr. Jaime Jensen and Dr. Chris Colbert. Cloning of the pET17b-PupB was accomplished by Dr. Jaime Jensen.

The pET17b-PupB construct was transformed into *E. coli* BL21 (DE3) pLysS for protein expression. 50 µL and 200 µL aliquots of the transformation mixture were used to inoculate two LB agar plates supplemented with 100 µg/ml ampicillin. Plates were inoculated overnight at 37 °C. A single colony was picked and added to a 70 mL culture of LB media supplemented with 100 µg/ml ampicillin and incubated at 37 °C overnight. For protein expression, 10 mL of overnight culture was added to 1 L of LB media supplemented with 100 µg/ml ampicillin. This culture was incubated at 37 °C with shaking at 200 rpm until it reached an OD_{600} of 0.7-0.9.

Protein expression was induced with 0.5 mM IPTG. Following induction, cells were grown overnight at 20 °C. Cells were then harvested at 4,000 x g by centrifugation, washed with 25 mM HEPES pH 7.5 and 150 mM NaCl, and stored at -80 °C.

Cell pellets containing expressed PupB were resuspended in lysis buffer (25 mM HEPES pH 7.5 and 150 mM NaCl) and lysed by emulsification. The crude lysate was clarified by ultracentrifugation at 30,000 rpm (120,744 x g) for 45 min in a Beckman L8-70M ultracentrifuge using a F40L-8x100 Fiberlite rotor (Thermo Scientific). The pellet containing cell membranes was separated from the supernatant and hand homogenized in lysis buffer + 25 mM imidazole. Homogenized membranes were solubilized by the addition of 1% w/v FC-13 and gentle stirring at 4 °C for ~1 hr. The solubilized sample was clarified a second time by ultracentrifugation at 30,000 rpm (120,744 x g) for 45 min to remove remaining cellular debris. The supernatant containing solubilized PupB was loaded onto a 5 ml HisTrap column (Cytiva) equilibrated in 25 mM HEPES pH 7.5, 150 mM NaCl, 25 mM imidazole, 0.1% FC-13. The column was washed with equilibration buffer until absorbance at 280 nm was baselined. The bound PupB was eluted from the column with the addition of equilibration buffer + 250 mM imidazole (25 mM HEPES pH 7.5, 150 mM NaCl, 250 mM imidazole, 0.1% FC-13). Fractions containing PupB were further purified by size-exclusion chromatography on a Superose 6 10/300 GL column (Cytiva) with 25 mM HEPES pH 7.5, 150 mM NaCl, 0.05% FC-13. Pure His_6-PupB was concentrated, and flash frozen in liquid nitrogen prior to storage at -80 °C. Protein purity was determined to be ~95% by SDS-PAGE with a 4-20% TGX SDS-PAGE gel (Bio-Rad) and Coomassie Blue staining [93].

5.2.3. Interaction Detection by Pulldown Assay of the TonB CTD and TBDT PupB

Purified PupB and TonB CTD were thawed, diluted to 40 µM each in binding buffer (25 mM HEPES pH 7.5, 150 mM NaCl, 0.05% FC-13, and 25 mM imidazole), and mixed in a 1:1 molar ratio. Proteins were then incubated overnight at 4 °C. The mixture was loaded onto 0.5 mL Ni-NTA agarose resin preequilibrated in binding buffer. The column was washed with 30 CV of binding buffer to remove unbound proteins and eluted with binding buffer + 250 mM imidazole. Samples were analyzed by SDS-PAGE using a 4-20% TGX SDS-PAGE gel (Bio-Rad) followed by Coomassie Blue staining [93]. Similarly, pulldown assays were completed with the addition of pseudobactin BN7/BN8 siderophore (kindly provided by Dr. Jaime Jensen) added to the overnight incubation mixture.

5.2.4. Secondary Structure Determination of TonB CTD by CD Spectroscopy

The TonB CTD was diluted 100-fold to 7 µM in 5 mM Potassium phosphate pH 7.5, 100 mM $(NH_4)_2SO_4$ at 4 °C. Continuous scanning CD spectra were measured at 20 °C from 190-250 nm using a Jasco J-715 spectrometer with a PTC-423S/15 Peltier cell holder and a 1-mm quartz cell. Spectra were buffer subtracted and secondary structure contents estimated using CONTIN and CDSSTR within the CDPro software suite [96]. A similar experiment was performed in 5 mM Potassium phosphate pH 7.5, 100 mM $(NH_4)_2SO_4$, 0.05% w/v FC-13 to evaluate detergent effects on TonB CTD secondary structure.

5.2.5. SEC-SAXS Analysis of the TonB CTD

SAXS was performed at BioCAT (beamline 18ID at the Advanced Photon Source, Chicago) with in-line size-exclusion chromatography (SEC-SAXS) similar to section 4.2.12. Sample was loaded onto a Superdex 200 Increase 10/300 GL column (Cytiva) running at 0.7 ml/min on an AKTA Pure FPLC (GE). Eluate was passed through the UV monitor and

subsequent SAXS flow cell. The flow cell consists of a 1.0 mm ID quartz capillary with ~20 µm walls. A coflowing sheath buffer was used to separate sample from the capillary walls and preventing radiation damage [137]. Scattering intensity was recorded using a Pilatus3 X 1M (Dectris) detector placed at 3.6 m from the sample allowing access to a q-range of 0.005 $Å^{-1}$ to 0.35 $Å^{-1}$. Exposures of 0.5 s were acquired every 1 s during elution and data was reduced using BioXTAS RAW 2.1.1 [138]. Buffer blanks were created by averaging regions flanking the elution peak and subtracting from exposures selected from the elution peak to create the I(q) vs q curves used for subsequent analysis. Theoretical scattering curves were calculated from PDBs 2GSK, 2GRX, 6I97, 1XX3, 5LW8, 6FIP, 1IHR, and 1QXX and fit to the experimental data using Crysol and FoxS [122, 168]. Fits with the lowest X^2 values were used in validation of protein conformations in solution. Similarly, structures were superimposed to the SEX-SAXS protein envelope with SUPCOMB from the ATSAS suite[139].

Table 5.1. SEC-SAXS data collection parameters.

SAS data collection parameter	
Instrument	BioCAT facility at the Advanced Photon Source beamline 18ID with Pilatus3 X 1M (Dectris detector
Wavelength (Å)	1.033
Beam size (μm²)	150 (h) x 25 (v) focused at the detector
Camera length (m)	3.6
q-measurement range ($Å^{-1}$)	0.004-0.352
Absolute scaling method	Glassy Carbon, NIST SRM 3600
Basis for normalization to constant counts	To transmitted intensity by beam-stop counter
Method for monitoring radiation damage	Automated frame-by-frame comparison of relevant regions using CORMAP [140] implemented in BioXTAS RAW
Exposure time, number of exposures	0.5 s exposure time with a 1 s total exposure preiod (o.5 s on, 0.5 s off) of entire SEC elution
Sample configuration	SEC-SAXS with sheath-flow cell [137], effective path length 0.542 mm. Size seperation by an AKTA Pure with a Superdex 200 Increase 10/300 GL column
Sample temperature (°C)	23
Software employed for SAS data reduction, analysis and interpretation	
SAXS data reduction	Radial averaging; frame comparison, averaging, and subtraction done using BioXTAS RAW 2.1.1 [138]
Basic analysis: Guinier, M.W., P(r)	Guinier fit and M.W. using BioXTAS RAW, P(r) function using GNOM[141]. RAW uses MoW and Vc M.W. methods [142].

5.3. Results

5.3.1. TonB CTD Expression and Purification

TonB CTD was purified by sequential GSH affinity chromatography with on-column TEV protease cleavage followed by SEC. It elutes as a single symmetric peak with a v_e = 15.4 mL indicating it is homogenous (Fig. 5.4) Thus, the apparent molecular weight of TonB CTD determined by K_{avg} is ~7 kDa. This is approximately 1.4 times smaller than the theoretical molecular weight of 10.1 kDa based on its amino acid sequence. The typical yield from one liter of expression culture was ~4 mg. SDS-PAGE confirmed the purity of the TonB CTD to be >95% pure by Coomassie Blue staining (Fig. 5.4).

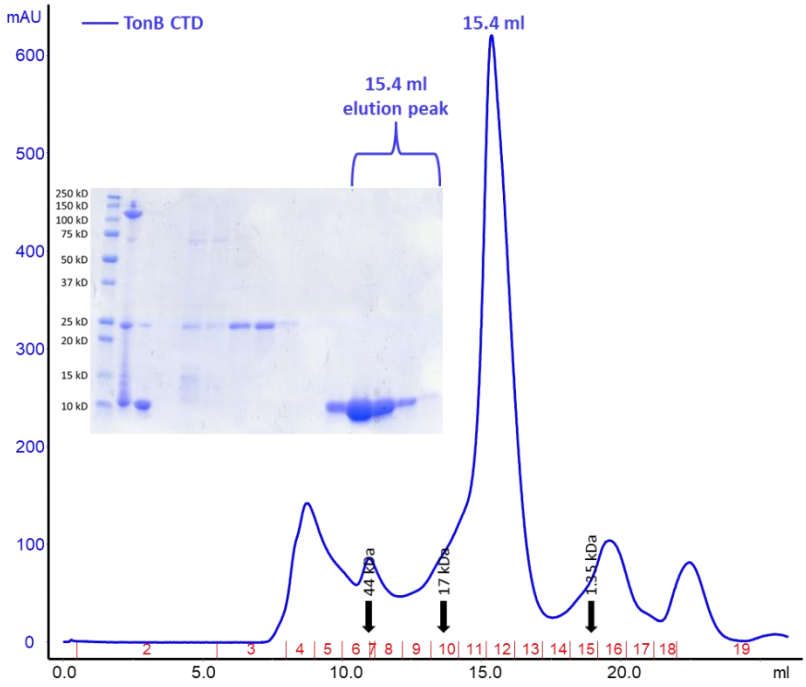

Figure 5.4. SEC chromatogram and SDS-PAGE gel of final purified TonB CTD. Positions of SEC standard elutions are indicated by arrows.

5.3.2. His_6-PupB Expression and Purification

His_6-tagged, full-length PupB was purified by Ni-affinity chromatography followed by SEC. PupB eluted at 15 mL from a Superose 6 10/300 column. The apparent molecular weight of His_6-PupB determined by K_{avg} using a v_e = 15.0 mL was ~280 kDa. This is approximately 3.3 times larger than the theoretical molecular weight of 84 kDa based on the amino acid sequence of His_6-PupB, but does not account for the FC-13 detergent micelle, which is surrounding the protein. An FC-13 micelle has a theoretical MW of ~32 kDa. There are multiple shoulders on the PupB SEC peak indicating the protein is heterogenous given the lack of extra protein bands on the SDS-PAGE gel (Fig. 5.5) The final yield from one liter of expression culture was ~1 mg.

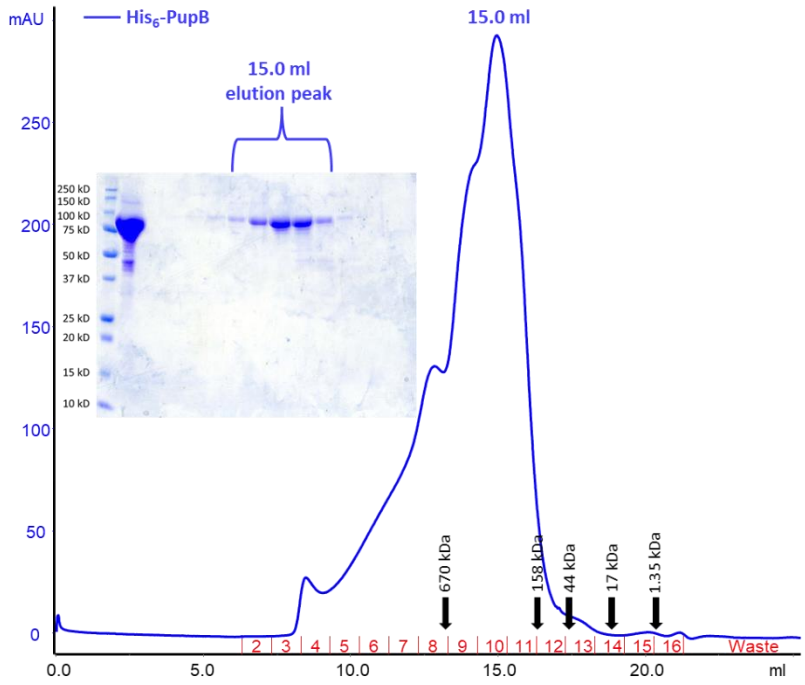

Figure 5.5. SEC chromatogram and related SDS-PAGE gel of His_6-PupB. Positions of SEC standard elutions are indicated by arrows.

5.3.3. Interaction of the TonB CTD and PupB Assessed by Pulldown Assay

Initial pulldown assay results do not show clear binding between PupB and TonB CTD in the absence and presence of the siderophore pseudobactin BN7/BN8 (Fig. 5.6). In both cases, the PupB is observed in the elution fractions with an absence of the loaded TonB CTD. This suggests our TonB CTD construct does not directly interact with the TBDT PupB despite this interaction being observed in homologous systems [53-55]. However, it can't be ruled out that the chaotropic detergent, FC-13, at 0.05% w/v interferes with the formation of hydrophobic interaction surfaces. Additionally, the folding states of PupB or the TonB CTD hasn't been verified. Either protein could be misfolded and therefore unable to interact with its binding partner.

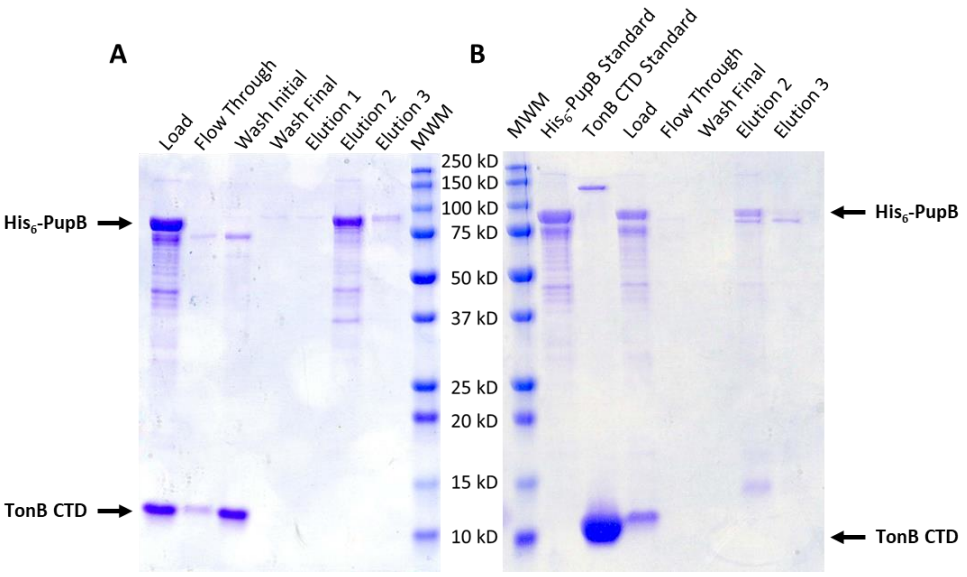

Figure 5.6. Pulldown assays analyzed by SDS-PAGE assessing interaction of His_6-PupB and the TonB CTD. A) Pulldown assay in the absence of siderophore. No interaction was observed. B) Pulldown assay in the presence of siderophore. No interaction was observed.

5.3.4. Assessment of the Folding State of the TonB CTD by CD Spectroscopy

The secondary structure of the purified TonB CTD was assessed by CD spectroscopy. Under standard conditions (5 mM Potassium phosphate pH 7.5, 100 mM $(NH_4)_2SO_4$ at 4 °C), the TonB CTD is composed of ~6% helix, ~32% β-strand and ~62% coil/turn (Fig. 5.7 & Table 5.2). Similar values were observed from homologous X-ray crystal structures when assessed by PDBsum, suggesting our construct does not contain substantially different secondary structure content than previous models [169]. As we tested the TonB CTD interaction with His_6-PupB in the presence of detergent, we measured the secondary structure content of the TonB CTD in the presence of 0.05% w/v FC-13. The addition of 0.05% FC-13, which is equal to that used in the pulldown assays, had virtually no effect on the secondary structure content of the TonB CTD **(**Fig. 5.7 & Table 5.2**)**. Thus, it does not appear that FC-13 altered or disrupted the structure of the TonB CTD. Currently, it appears likely that FC-13 is the cause of the observed absence of TonB CTD:PupB interaction.

Table 5.2. Secondary structure content of the TonB CTD in CD buffer and CD buffer supplemented with 0.05% FC-13.

	Estimated # Residues (Estimated Secondary Structure %)			
Protein	Helix	Strand	Coil + Turn	Total
TonB CTD	5.4 ± 0.9 (5.7)	30.7 ± 0.1 (32.3)	58.7 ± 1.1 (61.8)	94.8
TonB CTD + 0.05% FC-13	5.5 ± 0.6 (5.8)	31.5 ± 0.2 (33.2)	58.1 ± 0.5 (61.2)	95.2

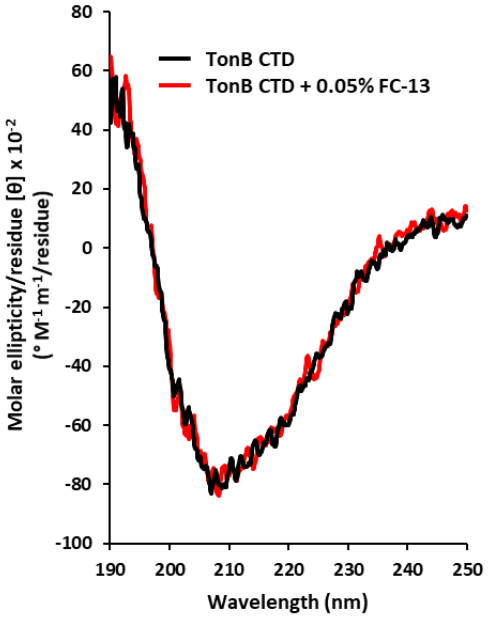

Figure 5.7. CD Spectra of TonB CTD and the effects of FC-13 on secondary structure content. The TonB CTD in CD buffer (black) and CD buffer supplemented with 0.05% FC-13 (Red) are depicted.

5.3.5. Solution Properties and Low-Resolution Molecular Envelope of the TonB CTD Determined by SEC-SAXS

The solution properties, including oligomeric state, and low-resolution structure of the TonB CTD were assessed by SEC-SAXS. Following buffer subtraction, the auto-calculated radius of gyration (R_g) across the sample region was constant indicating homogenous scattering particles (Fig. 5.8A). The Guinier plot in the low q region is linear, implying the sample is monodisperse with an R_g of 15.1 Å (Fig. 5.8B). The $P(r)$ distribution curve suggests a slightly extended globular protein with a D_{max} of 50 Å (Fig. 5.8C). Similarly, the Kratky plot describes a partially folded TonB CTD in solution (Fig. 5.8D). CD spectroscopy agrees with the Kratky plot

analysis of the TonB CTD folded state with 61.8% modeled as coil (Fig. 5.7 & Table 5.2). However, the molecular weight estimated from the SAXS is 8.8 kDa; which is in better agreement with the theoretical molecular weight of 10.1 kDa compared to the 7 kDa molecular weight determined by SEC.

Theoretical scattering curves and R_g values were calculated for a series of TonB CTD structures deposited in the PDB: PDB IDs 2GSK, 2GRX, 6I97, 1XX3, 5LW8, 6FIP, 1IHR, and 1QXX, using both Crysol and FoxS[122, 124, 168]. PDB IDs 2GSK, 2GRX, and 6I97 represent monomeric TonB CTD structures extracted from co-crystallized structures in complex with TBDTs. PDBs 1XX3, 5LW8, and 6FIP include monomeric TonB CTD structures solved by nuclear magnetic resonance (NMR). PDBs 1IHR and 1QXX are dimeric TonB CTD crystal structures. Theoretical scattering curves calculated for each structure were each fit to the experimental TonB CTD scattering profile, goodness of fit ranging between chi^2 values of 1.02 – 1.77 from Crysol (Fig. 5.9 A-H) and 1.02 – 1.33 from FoxS (Fig. 5.10 A-H).

The theoretical scattering curves calculated from the monomeric TonB CTD molecules, especially those from TBDT co-crystal structures, fit with a lower chi^2 to the experimental data. There is a small difference in the chi^2 values for monomeric vs dimeric fits, calculated using FoxS. However, the monomeric TonB CTD theoretical scattering curves generally fit better than dimeric TonB CTD curves. Additionally, the R_g values calculated from monomeric TonB CTD structures agreed better with the experimental R_g value of 15.1 Å determined from both programs, Crysol and FoxS. Further analysis was conducted by automated superimposition of the TonB CTD structures and the experimental TonB CTD SEC-SAXS envelope with SUPCOMB[139] (Fig. 5.11 A-H). Monomeric TonB CTD structures fit nominally better to the experimental

SAXS envelope. Together, our SEC-SAXS analyses suggest that our TonB CTD is a homogenous and partially folded sample that likely exists in a monomeric state in solution.

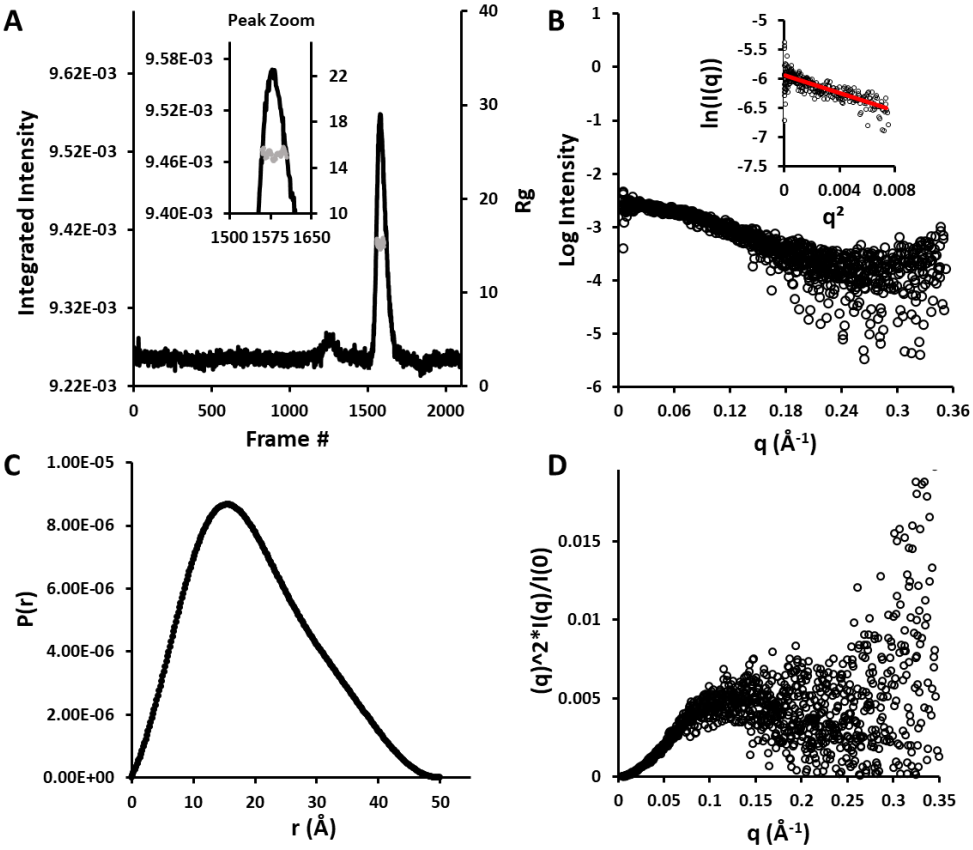

Figure 5.8. SEC-SAXS analysis of TonB CTD. A) Subtracted scattering plot (black) with R_g distribution (grey) across the peak of interest (Inset). B) Experimental scattering profile and Guinier plot of the low *q* region (Inset). C) Distance distribution *P(r)* plot. D) Kratky plot.

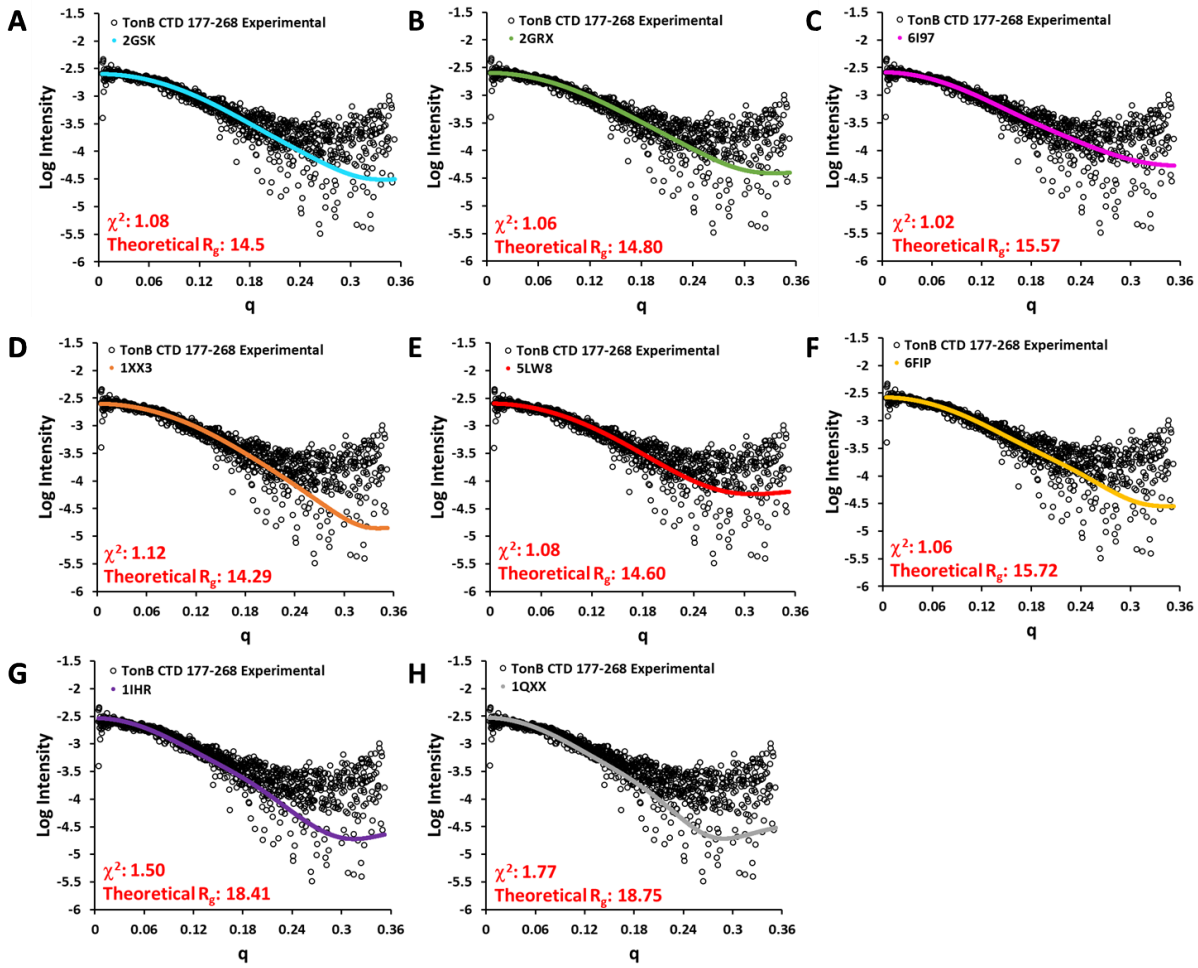

Figure 5.9. Comparison of the *P. capeferrum* TonB CTD SEC-SAXS experimental scattering data to theoretical scattering profiles of homologous TonB CTD molecules using Crysol [122]. Experimental scattering profile (open circles) fit with the theoretical scattering profile of A) monomeric *E. coli* TonB CTD extracted from the TBDT complex crystal structure (cyan). B) the monomeric *E. coli* TonB CTD extracted from the TBDT complex crystal structure (green). C) the monomeric *P. aeruginosa* TonB CTD extracted from the TBDT complex crystal structure (magenta). D) the monomeric *E. coli* TonB CTD solved by NMR (orange). E) the monomeric *H. pylori* TonB CTD solved by NMR (red). F) the monomeric *P. aeruginosa* TonB CTD solved by NMR (yellow). G) the dimeric *E. coli* TonB CTD solved by X-ray crystallography (purple). H) the dimeric *E. coli* TonB CTD solved by X-ray crystallography (gray).

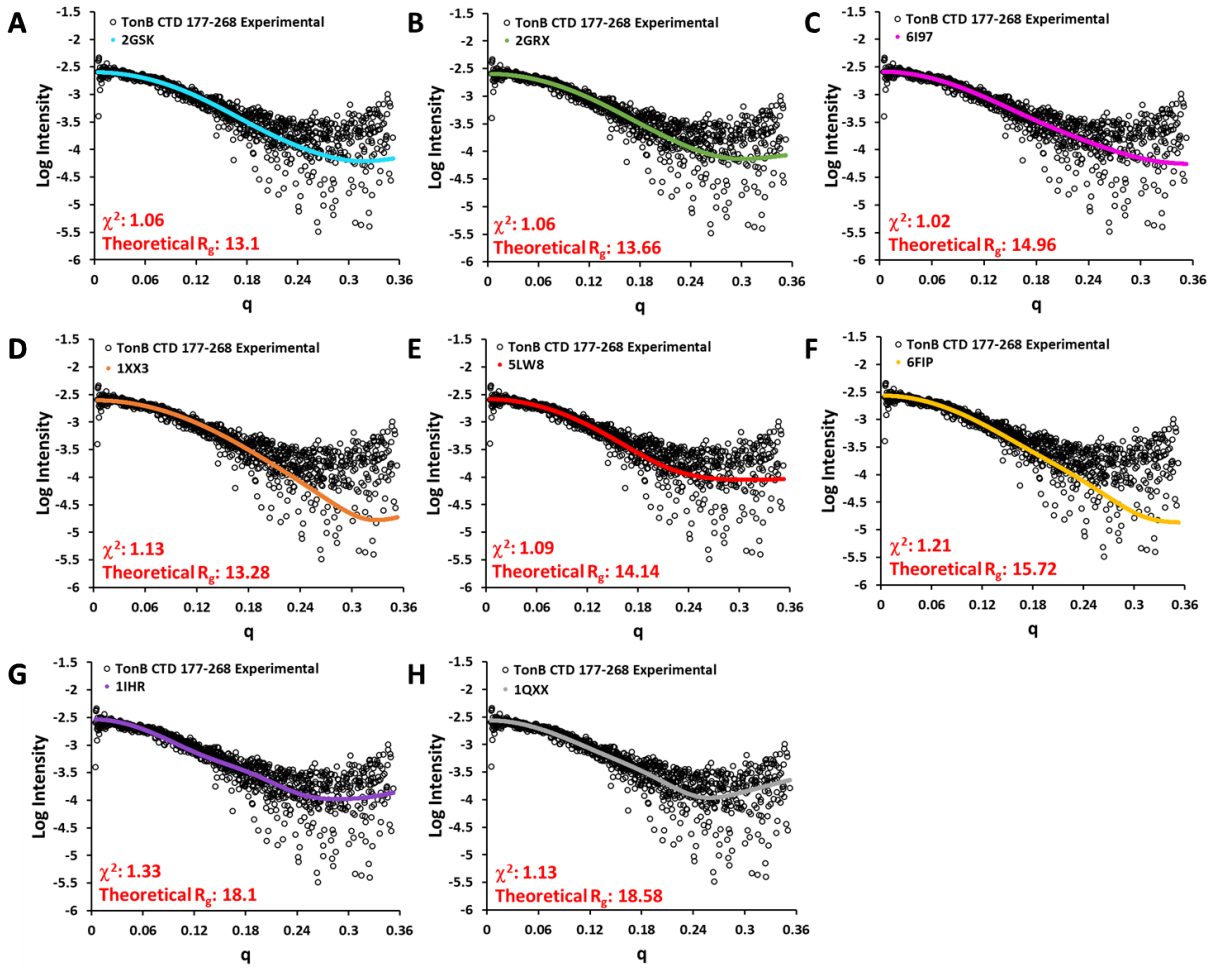

Figure 5.10. Comparison of *P. capeferrum* TonB CTD SEC-SAXS experimental scattering data to theoretical scattering profiles of homologous TonB CTD molecules using FoxS[124]. Experimental scattering profile (open circles) fit with the theoretical scattering profile A) monomeric *E. coli* TonB CTD extracted from the TBDT complex crystal structure (cyan). B) the monomeric *E. coli* TonB CTD extracted from the TBDT complex crystal structure (green). C) the monomeric *P. aeruginosa* TonB CTD extracted from the TBDT complex crystal structure (magenta). D) the monomeric *E. coli* TonB CTD solved by NMR (orange). E) the monomeric *H. pylori* TonB CTD solved by NMR (red). F) the monomeric *P. aeruginosa* TonB CTD solved by NMR (yellow). G) the dimeric *E. coli* TonB CTD solved by X-ray crystallography (purple). H) the dimeric *E. coli* TonB CTD solved by X-ray crystallography (gray).

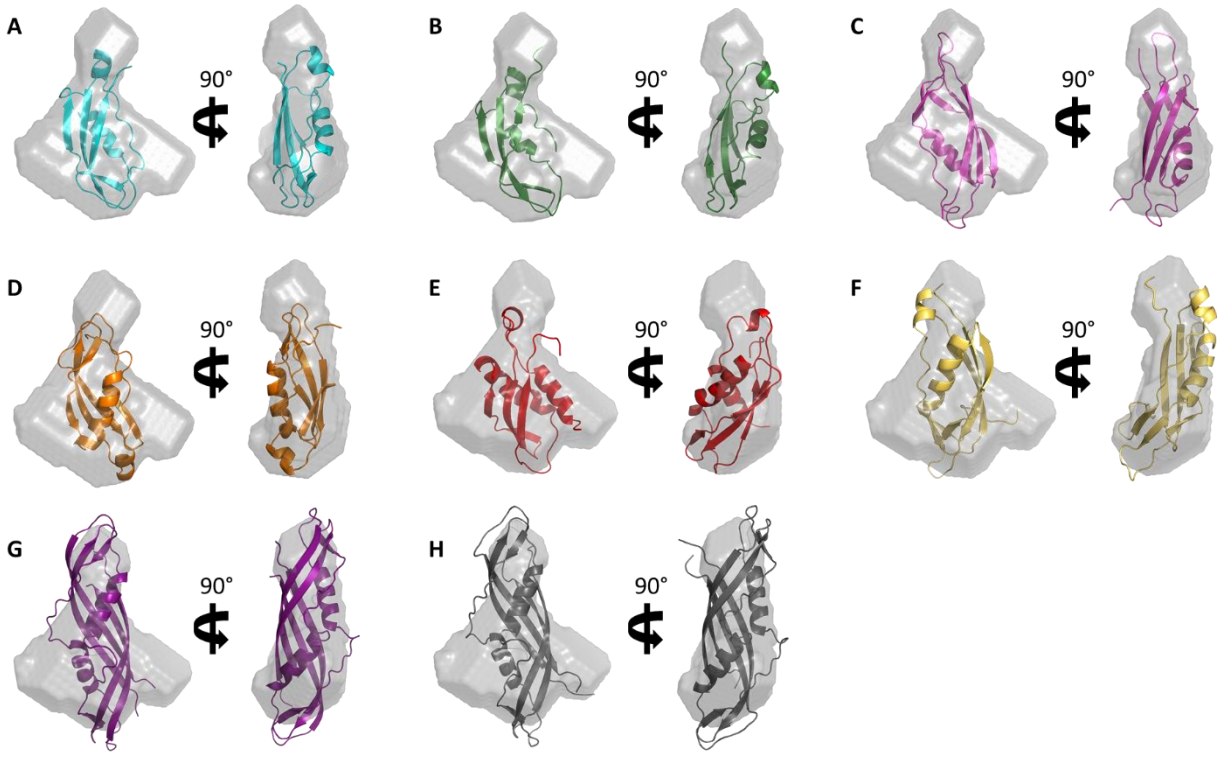

Figure 5.11. The SEC-SAXS envelope (light grey) of the *P. capeferrum* TonB CTD fit to homologous TonB CTD structures [139]. A) Monomeric *E. coli* TonB CTD (cyan) extracted from the TBDT complex crystal structure (2GSK). B) Monomeric *E. coli* TonB CTD (green) extracted from the TBDT complex crystal structure (2GRX). C) Monomeric *P. aeruginosa* TonB CTD (magenta) extracted from the TBDT complex crystal structure (6I97). D) Monomeric *E. coli* TonB CTD (orange) solved by NMR (1XX3). E) Monomeric *H. pylori* TonB CTD (red) solved by NMR (5LW8). F) Monomeric *P. aeruginosa* TonB CTD (yellow) solved by NMR (6FIP). G) Dimeric *E. coli* TonB CTD (purple) solved by X-ray crystallography (1IHR). H) Dimeric *E. coli* TonB CTD (grey) solved by X-ray crystallography (1QXX).

5.4. Discussion and Conclusions

Our biophysical and biochemical data of PupB and the TonB CTD offers early insights into *P. capeferrum* TonB function as well as directions for future exploration. Under current pulldown assay conditions PupB does not appear to interact with the TonB CTD. In contrast to our findings, multiple TBDTs have been shown to interact with TonB CTDs. Notable structures include BtuB:TonB CTD, FhuA:TonB CTD, and FoxA:TonB CTD. In each case, the TonB box of the TBDT forms a parallel β-strand with the antiparallel β-sheet of the TonB CTD [53-55]. Additionally, the use of fluorescence anisotropy found TonB CTD interacts tightly (26 – 64 nM)

with both BtuB and FhuA but did not show interaction with the *E. coli* FecA [170]. In contrast to BtuB and FhuA, PupB contains an NTSD, which may explain the difficulty in observing interaction. However, structural studies of FoxA:TonB CTD distinctly show TonB CTD interaction despite the presence of an NTSD [55]. Apo FoxA:TonB CTD has a K_d of 111 ± 6.5 nM whereas ferrioxamine B-FoxA:TonB CTD has a K_d of 6.6 ± 1.2 nM, both comparable to BtuB/FhuA TonB CTD interactions [55].

An additional reason for the observed lack of binding could be the conditions used for the pulldown assays. The solubilization and purification of the outer membrane PupB requires the use of FOS-Choline-13 (FC-13). FOS-Choline (FC) based detergents are commonly used for the isolation of membrane proteins and have been proven to maintain structure and function. However, FC based detergents are fairly chaotropic and may serve to interfere with binding. Surface plasmon resonance studies on the chemokine receptor CCR5 showed little to no ligand binding in the presence of FC-12, although other detergents did not hinder interactions [171]. Further analysis by CD spectroscopy and NMR suggest that the CCR5 ligand, RANTES, undergoes significant structural changes with a complete loss of β-content and a large disruption of α-content in the presence of FC-12 [172]. Structural perturbations like this would completely abrogate TonB CTD interaction with PupB, however, our CD spectroscopy data indicates that the secondary structure of the TonB CTD does not change significantly in the presence of FC-13. We cannot however, rule out the possibility that hydrogen bonds may be disrupted by FC-13 addition, thereby inhibiting the TonB box from forming the parallel β-strand alongside the antiparallel β-sheet of the TonB CTD, which is required for PupB:TonB CTD interaction [34, 53-55].

Although the interaction of the TonB CTD with PupB was not observed, we were able to obtain some low-resolution structural insights and a prediction of the oligomeric state of our

TonB CTD construct. SEC-SAXS results show a homogenous sample as the R_g distribution across our scattering peak was uniform and the Guinier plot of the low *q* region is linear. The slightly extended bell curve of the *P(r)* distribution plot points to a somewhat extended, partially unfolded, globular protein as observed for many TonB CTD structures. This agrees with secondary structure content estimated by CD spectroscopy and quantification of secondary structure elements from solved structures by PDBsum [169].

Data analysis suggests the *P. capeferrum* TonB CTD is monomeric in solution. Comparisons of the monomeric and dimeric TonB CTD structures to the experimental scattering curve using FoxS, Crysol, and SUPCOMB indicate a monomeric TonB CTD [122, 124, 139]. Since all isolated TBDTs thus far are monomeric, it is most likely the *P. capeferrum* TonB CTD also interacts as a monomer [55, 170]. As previously described, the TonB CTD co-structures with BtuB, FhuA, and FoxA each contain a monomeric TonB CTD [53-55]. Additional structures solved by both NMR and X-ray crystallography depict monomeric and dimeric TonB CTD molecules. Monomeric TonB CTD molecules extracted from TBDT co-structures and NMR structures fit with a lower chi^2 to our data. Whereas dimeric structures fit with moderate chi^2 values. This agrees with our assumption that the complex between the TonB CTD and a TBDT is between individual monomers. Our construct was modeled after the TonB CTD structure of BtuB:TonB CTD and NMR monomer structures. These molecules encompass much of the structural data available. However, a 92-residue *E. coli* TonB CTD X-ray crystal structure contained a dimeric assembly in the asymmetric unit even though it was isolated as a monomer in solution [173].

In conclusion, interactions between TonB CTD and TBDTs have been documented. However, under current assay conditions *P. capeferrum* His_6-PupB does not interact with the *P. capeferrum* TonB CTD. This is likely because of the presence of a very chaotropic detergent,

which is known to interfer with other interactions. Our TonB CTD construct is homogenous and likely well folded as determined by SEC, CD spectroscopy, and SEC-SAXS. Therefore, it appears TonB CTD is structurally intact and pulldown assay optimizations are the next critical step in evaluating the relationship between PupB and TonB.

6. CONCLUSIONS, PERSPECTIVES, AND FUTURE DIRECTIONS

CSS is a highly conserved signal transduction system in Gram-negative bacteria for sensing of extracellular stimuli leading to transcriptional upregulation. Our research has focused on the CSS pathways involved in iron import. These CSS pathways are composed of three distinct proteins including an outer membrane transducer, which transmits the extracellular signal to the periplasm, an inner membrane sigma regulator, which propagates the signal across the inner membrane, and an ECF sigma factor, which recruits RNA polymerase and upregulates transcription of specific iron import genes. In iron import CSS the outer membrane transducers serve a dual purpose of transmitting signal and transporting specific iron-laden siderophores into the periplasm. This plays a vital role in the import of the limited nutrient, iron. Iron bound siderophores serve not only as a tool for scavenging iron from the environment, but also the initial signaling stimuli for CSS activation. However, intercellular iron levels are under the control of the master ferric uptake regulator that inhibits iron import until iron limiting conditions are met, therefore CSS is only effective under iron limiting conditions.

Iron import CSS signal transduction is tightly regulated. RIP is a key mechanism in the activation of CSS. RIP is a sequential proteolytic cascade that leads to the degradation of specific substrates. In iron import CSS, the substrate is the sigma regulator. The sigma regulator is initially degraded by a site-1 protease followed by a site-2 protease cleavage. For our iron import model of the *P. capeferrum* Pup system, site-1 cleavage likely occurs by the C-terminal processing serine endopeptidase, Prc. Subsequently, the site-2 protease, RseP, further degrades the sigma regulator for release of the ECF sigma factor.

The structure of the PupB NTSD:PupR CCSSD solved at 1.6 Å revealed multiple unique features. Interestingly, the CCSSD is composed of two subdomains, the CJM and the STN. The

CJM contains a novel β-solenoid-like motif. The STN, contains the same βαβ-repeat motif similar to the NTSD domain, but at the C-terminus, which is a unique architectural arrangement of this subdomain.

Further, the NTSD significantly stabilizes the CCSSD as determined by CD spectroscopy. Stabilization of the CCSSD likely reduces non-specific degradation of the domain and unintentional signal activation. Existence of this 'primed' state between the NTSD and CCSSD has not been validated outside of the Pup CSS pathway. Additionally, pulldown assay and ITC analysis of the FecA NTSD:FecR CCSSD T182A complex coupled with CD spectroscopy points to a similar mechanism in the Fec CSS pathway. Characterization of the Fec complex will likely elucidate similar results and confirm a conserved characteristic in CSS pathways.

Due to the stabilization of the CCSSD by the NTSD, we hypothesized that the NTSD would prevent the CCSSD from degradation. Pulldown assays confirmed and ITC validated that the NTSD prevents recognition of the PupR CCSSD by Prc. However, in the absence of the NTSD, the site-1 protease, Prc, recognizes and cleaves the CCSSD STN subdomain into short peptides. Prc cleavage is accomplished by several conformational transitions that reorganize the proteolytic groove and extends the PDZ domain for threading of the substrate protein into the protease, resulting in 'open' and 'closed' conformations. Observation of the 'closed' to 'open' conformational change was evaluated by the structure solution of the Prc-His_6 S485A and the Prc-His_6 K510A:PupR CCSSD 242-254. Surprisingly, capturing the 'open' conformation in the presence of the PupR CCSSD 242-254 fragment yielded a covalently linked peptide to the catalytic serine 485 as well as a PDZ bound peptide.

Whether CSS can occur independent of iron import or as a result of iron import is up to debate. To evaluate this step in CSS, the *P. capeferrum* TonB CTD was purified and structural characterized by SEC-SAXS. The TonB CTD exists as a monomer in solution, conducive to binding the TonB box of PupB. Despite this, interaction of the two has yet to be shown. Further, modifications of pulldown assay conditions are needed to show this interaction. Once interaction has been observed, structural characterization of the complex and assessment of a possible tertiary complex between PupB, PupR CCSSD, and the TonB CTD would shed light on iron import versus CSS.

Our data show the series of events leading to RIP signal activation appear to be linked to the dissociation of the NTSD from the CCSSD followed by site-1 protease, Prc, recognition and cleavage. However, the cause of dissociation between the NTSD:CCSSD complex has yet to be evaluated. Further work is required to decipher this mechanism. However, we have provided a strong foundation for understanding the initial steps in CSS activation and provided a plausible universal CSS mechanism.

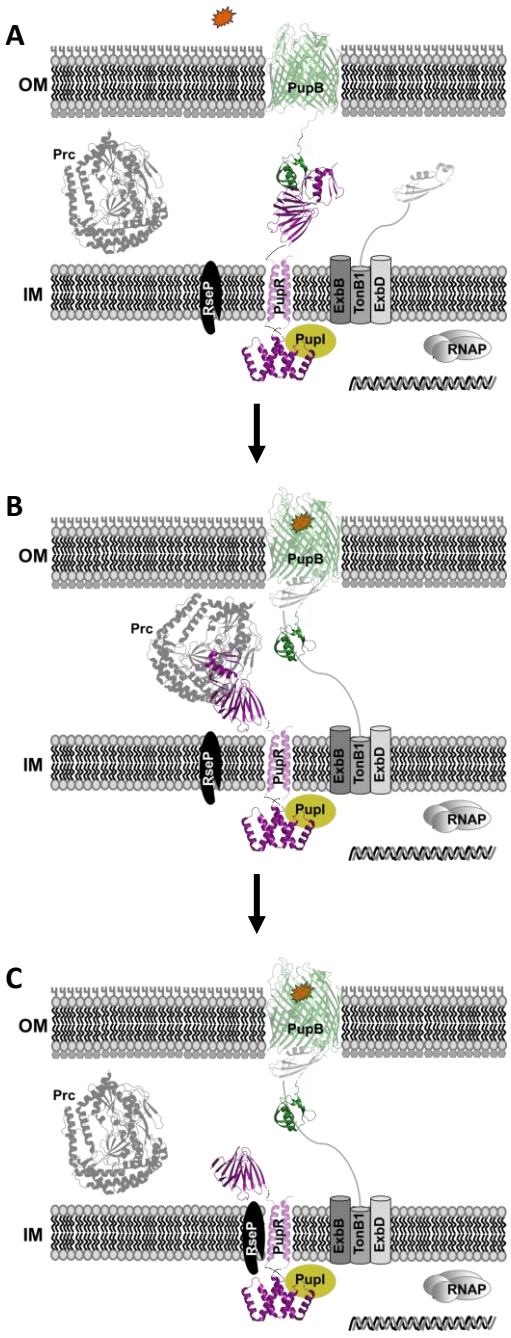

Figure 6.1 The proposed universal mechanism of CSS signal activation as delineated from research on the pseudobactin uptake system from *P. capeferrum*. A) CSS resting state in which the PupB NTSD is complexed with the PupR CCSSD in a primed state. B) Dissociation of the PupB NTSD:PupR CCSSD complex allows recognition of the PupR CCSSD by the site-1 protease, Prc. C) Prc degrades the STN subdomain of the PupR CCSSD, relinquishing a shortened sigma regulator for recognition by the site-2 protease, RseP, which cleaves and releases the PupR ASD:PupI complex and recruits RNA polymerase to the *pupB* promoter.

REFERENCES

(1) Noinaj, N.; Guillier, M.; Travis J. Barnard; Buchanan, S. K. TonB-Dependent Transporters: Regulation, Structure, and Function. *Annual Review of Microbiology* **2010**, *64*, 43-60, review-article. DOI: 10.1146/annurev.micro.112408.134247.

(2) Glatter, K.; Finkelman, P. History of the Plague: An Ancient Pandemic for the Age of COVID-19. *The American journal of medicine* **2021**, *134* (2). DOI: 10.1016/j.amjmed.2020.08.019.

(3) Ali, M.; Nelson, A. R.; Lopez, A. L.; Sack, D. A. Updated global burden of cholera in endemic countries. *PLoS neglected tropical diseases* **2015**, *9* (6). DOI: 10.1371/journal.pntd.0003832.

(4) Scott H, P. Pneumonia before Antibiotics: Therapeutic Evolution and Evaluation in Twentieth-Century America. *Social History of Medicine* **2007**, *20* (3), 612-613. DOI: 10.1093/shm/hkm082.

(5) Kapoor, G.; Saigal, S.; Elongavan, A. Action and resistance mechanisms of antibiotics: A guide for clinicians. *Journal of anaesthesiology, clinical pharmacology* **2017**, *33* (3). DOI: 10.4103/joacp.JOACP_349_15.

(6) CDC. *Antibiotic Resistance Threats in the United States, 2013*; Center for Disease Control, 2013.

(7) Munita, J. M.; Arias, C. A. Mechanisms of Antibiotic Resistance. *Microbiology spectrum* **2016**, *4* (2). DOI: 10.1128/microbiolspec.VMBF-0016-2015.

(8) Choi, U.; Lee, C. R. Distinct Roles of Outer Membrane Porins in Antibiotic Resistance and Membrane Integrity in Escherichia coli. *Frontiers in microbiology* **2019**, *10*. DOI: 10.3389/fmicb.2019.00953.

(9) Lambert, P. A. Mechanisms of antibiotic resistance in Pseudomonas aeruginosa. *Journal of the Royal Society of Medicine* **2002**, *95 Suppl 41* (Suppl 41).

(10) Tenover, F. C. Mechanisms of antimicrobial resistance in bacteria. *The American journal of medicine* **2006**, *119* (6 Suppl 1). DOI: 10.1016/j.amjmed.2006.03.011.

(11) Blanco, P.; Hernando-Amado, S.; Reales-Calderon, J. A.; Corona, F.; Lira, F.; Alcalde-Rico, M.; Bernardini, A.; Sanchez, M. B.; Martinez, J. L. Bacterial Multidrug Efflux Pumps: Much More Than Antibiotic Resistance Determinants. *Microorganisms* **2016**, *4* (1). DOI: 10.3390/microorganisms4010014.

(12) Reddick, L. E.; Alto, N. M. Bacteria fighting back: how pathogens target and subvert the host innate immune system. *Molecular cell* **2014**, *54* (2). DOI: 10.1016/j.molcel.2014.03.010.

(13) Matsuura, M. Structural Modifications of Bacterial Lipopolysaccharide that Facilitate Gram-Negative Bacteria Evasion of Host Innate Immunity. *Frontiers in immunology* **2013**, *4*. DOI: 10.3389/fimmu.2013.00109.

(14) Kumar, H.; Kawai, T.; Akira, S. Pathogen recognition by the innate immune system. *International reviews of immunology* **2011**, *30* (1). DOI: 10.3109/08830185.2010.529976.

(15) Finlay, B. B.; McFadden, G. Anti-immunology: evasion of the host immune system by bacterial and viral pathogens. *Cell* **2006**, *124* (4). DOI: 10.1016/j.cell.2006.01.034.

(16) Sousa-Pereira, P.; Woof, J. M. IgA: Structure, Function, and Developability. *Antibodies (Basel, Switzerland)* **2019**, *8* (4). DOI: 10.3390/antib8040057.

(17) Fatima, U.; Senthil-Kumar, M. Plant and pathogen nutrient acquisition strategies. *Frontiers in plant science* **2015**, *6*. DOI: 10.3389/fpls.2015.00750.

(18) Khasheii, B.; Mahmoodi, P.; Mohammadzadeh, A. Siderophores: Importance in bacterial pathogenesis and applications in medicine and industry. *Microbiological research* **2021**, *250*. DOI: 10.1016/j.micres.2021.126790.

(19) Caza, M.; Kronstad, J. W. Shared and distinct mechanisms of iron acquisition by bacterial and fungal pathogens of humans. *Frontiers in cellular and infection microbiology* **2013**, *3*. DOI: 10.3389/fcimb.2013.00080.

(20) Hooda, Y.; Shin, H. E.; Bateman, T. J.; Moraes, T. F. Neisserial surface lipoproteins: structure, function and biogenesis. *Pathogens and Disease* **2017**, *75* (2). DOI: 10.1093/femspd/ftx010.

(21) Hooda, Y.; Lai, C. C. L.; Moraes, T. F. Identification of a Large Family of Slam-Dependent Surface Lipoproteins in Gram-Negative Bacteria. *Frontiers in cellular and infection microbiology* **2017**, *7*, 207-207. DOI: 10.3389/fcimb.2017.00207 PubMed.

(22) Tommassen, J.; Arenas, J. Biological Functions of the Secretome of *Neisseria meningitidis*. *Frontiers in Cellular and Infection Microbiology* **2017**, *7*. DOI: 10.3389/fcimb.2017.00256.

(23) Noinaj, N.; Easley, N. C.; Oke, M.; Mizuno, N.; Gumbart, J.; Boura, E.; Steere, A. N.; Zak, O.; Aisen, P.; Tajkhorshid, E.; et al. Structural basis for iron piracy by pathogenic Neisseria. *Nature* **2012**, *483* (7387), 53-58, OriginalPaper. DOI: doi:10.1038/nature10823.

(24) Calmettes, C.; Alcantara, J.; Yu, R.-H.; Schryvers, A. B.; Moraes, T. F. The structural basis of transferrin sequestration by transferrin-binding protein B. *Nature structural & molecular biology* **2012**, *19* (3), 358-360. DOI: 10.1038/nsmb.2251 PubMed.

(25) Cole, G. B.; Bateman, T. J.; Moraes, T. F. The surface lipoproteins of gram-negative bacteria: Protectors and foragers in harsh environments. *The Journal of biological chemistry* **2021**, *296*. DOI: 10.1074/jbc.REV120.008745.

(26) Lamont, I. L.; Beare, P. A.; Ochsner, U.; Vasil, A. I.; Vasil, M. L. Siderophore-mediated signaling regulates virulence factor production in Pseudomonasaeruginosa. *Proceedings of the National Academy of Sciences of the United States of America* **2002**, *99* (10). DOI: 10.1073/pnas.092016999.

(27) Page, M. G. P. The Role of Iron and Siderophores in Infection, and the Development of Siderophore Antibiotics. *Clinical infectious diseases : an official publication of the Infectious Diseases Society of America* **2019**, *69* (Suppl 7). DOI: 10.1093/cid/ciz825.

(28) Yue, W. W.; Grizot, S.; Buchanan, S. K. Structural evidence for iron-free citrate and ferric citrate binding to the TonB-dependent outer membrane transporter FecA. *Journal of molecular biology* **2003**, *332* (2). DOI: 10.1016/s0022-2836(03)00855-6.

(29) Ferguson, A. D.; Chakraborty, R.; Smith, B. S.; Esser, L.; van der Helm, D.; Deisenhofer, J. Structural basis of gating by the outer membrane transporter FecA. *Science (New York, N.Y.)* **2002**, *295* (5560). DOI: 10.1126/science.1067313.

(30) Ferguson, A. D.; Breed, J.; Diederichs, K.; Welte, W.; Coulton, J. W. An internal affinity-tag for purification and crystallization of the siderophore receptor FhuA, integral outer membrane protein from Escherichia coli K-12. *Protein science : a publication of the Protein Society* **1998**, *7* (7). DOI: 10.1002/pro.5560070719.

(31) Locher, K. P.; Rees, B.; Koebnik, R.; Mitschler, A.; Moulinier, L.; Rosenbusch, J. P.; Moras, D. Transmembrane signaling across the ligand-gated FhuA receptor: crystal structures of free and ferrichrome-bound states reveal allosteric changes. *Cell* **1998**, *95* (6). DOI: 10.1016/s0092-8674(00)81700-6.

(32) Ollis, A. A.; Manning, M.; Held, K. G.; Postle, K. Cytoplasmic membrane protonmotive force energizes periplasmic interactions between ExbD and TonB. *Molecular microbiology* **2009**, *73* (3). DOI: 10.1111/j.1365-2958.2009.06785.x.

(33) Celia, H.; Botos, I.; Ni, X.; Fox, T.; De Val, N.; Lloubes, R.; Jiang, J.; Buchanan, S. K. Cryo-EM structure of the bacterial Ton motor subcomplex ExbB–ExbD provides information on structure and stoichiometry. *Communications Biology* **2019**, *2* (1), 1-6, OriginalPaper. DOI: doi:10.1038/s42003-019-0604-2.

(34) Celia, H.; Noinaj, N.; Buchanan, S. K. Structure and Stoichiometry of the Ton Molecular Motor. *International Journal of Molecular Sciences* **2020**, *21* (2), 375, Review. DOI: 10.3390/ijms21020375.

(35) Yeterian, E.; Martin, L. W.; Lamont, I. L.; Schalk, I. J. An efflux pump is required for siderophore recycling by Pseudomonas aeruginosa. *Environmental microbiology reports* **2010**, *2* (3). DOI: 10.1111/j.1758-2229.2009.00115.x.

(36) Greenwald, J.; Hoegy, F.; Nader, M.; Journet, L.; Mislin, G. L.; Graumann, P. L.; Schalk, I. J. Real time fluorescent resonance energy transfer visualization of ferric pyoverdine uptake in Pseudomonas aeruginosa. A role for ferrous iron. *The Journal of biological chemistry* **2007**, *282* (5). DOI: 10.1074/jbc.M609238200.

(37) Delepelaire, P. Bacterial ABC transporters of iron containing compounds. *Research in microbiology* **2019**, *170* (8). DOI: 10.1016/j.resmic.2019.10.008.

(38) Hvorup, R. N.; Goetz, B. A.; Niederer, M.; Hollenstein, K.; Perozo, E.; Locher, K. P. Asymmetry in the structure of the ABC transporter-binding protein complex BtuCD-BtuF. *Science (New York, N.Y.)* **2007**, *317* (5843). DOI: 10.1126/science.1145950.

(39) Schalk, I. J.; Guillon, L. Fate of ferrisiderophores after import across bacterial outer membranes: different iron release strategies are observed in the cytoplasm or periplasm depending on the siderophore pathways. *Amino acids* **2013**, *44* (5). DOI: 10.1007/s00726-013-1468-2.

(40) Ferguson, A. D.; Amezcua, C. A.; Halabi, N. M.; Deisenhofer, J. Signal transduction pathway of TonB-dependent transporters. *Proceedings of the National Academy of Sciences of the USA* **2007**, *104*, 513-518.

(41) Garcia-Herrero, A.; Vogel, H. J. Nuclear magnetic resonance solution structure of the periplasmic signalling domain of the TonB-dependent outer membrane transporter FecA from Escherichia coli. *Molecular microbiology* **2005**, *58* (5). DOI: 10.1111/j.1365-2958.2005.04889.x.

(42) Malki, I.; Simenel, C.; Wojtowicz, H.; de Amorim, G. C.; Prochnicka-Chalufour, A.; Hoos, S.; Raynal, B.; England, P.; Chaffotte, A.; Delepierre, M.; et al. Interaction of a partially disordered antisigma factor with its partner, the signaling domain of the TonB-dependent transporter HasR. *PloS one* **2014**, *9* (4). DOI: 10.1371/journal.pone.0089502.

(43) Mahren, S.; Schnell, H.; Braun, V. Occurrence and regulation of the ferric citrate transport system in Escherichia coli B, Klebsiella pneumoniae, Enterobacter aerogenes, and Photorhabdus luminescens. *Archives of microbiology* **2005**, *184* (3). DOI: 10.1007/s00203-005-0035-y.

(44) Kim, I.; Stiefel, A.; Plantör, S.; Angerer, A.; Braun, V. Transcription induction of the ferric citrate transport genes via the N-terminus of the FecA outer membrane protein, the Ton system and the electrochemical potential of the cytoplasmic membrane. *Molecular microbiology* **1997**, *23* (2). DOI: 10.1046/j.1365-2958.1997.2401593.x.

(45) Jensen, J. L.; Jernberg, B. D.; Sinha, S.; Colbert, C. L. Structural basis of cell surface signaling by a conserved sigma regulator in Gram-negative bacteria. *Journal of Biological Chemistry* **2020**, *295* (17), 5795-5806. DOI: 10.1074/jbc.RA119.010697.

(46) Bastiaansen, K. C.; Civantos, C.; Bitter, W.; Llamas, M. A. New Insights into the Regulation of Cell-Surface Signaling Activity Acquired from a Mutagenesis Screen of

the Pseudomonas putida IutY Sigma/Anti-Sigma Factor. *Frontiers in microbiology* **2017**, *8*. DOI: 10.3389/fmicb.2017.00747.

(47) Llamas, M. A.; Imperi, F.; Visca, P.; Lamont, I. L. Cell-surface signaling in Pseudomonas: stress responses, iron transport, and pathogenicity. *FEMS Microbiology Reviews* **2014**, *38* (4), 569-597. DOI: 10.1111/1574-6976.12078.

(48) Buchanan, S. K.; Smith, B. S.; Venkatramani, L.; Xia, D.; Esser, L.; Palnitkar, M.; Chakraborty, R.; van der Helm, D.; Deisenhofer, J. Crystal structure of the outer membrane active transporter FepA from Escherichia coli. *Nature structural biology* **1999**, *6* (1). DOI: 10.1038/4931.

(49) Ferguson, A. D.; Hofmann, E.; Coulton, J. W.; Diederichs, K.; Welte, W. Siderophore-mediated iron transport: crystal structure of FhuA with bound lipopolysaccharide. *Science (New York, N.Y.)* **1998**, *282* (5397). DOI: 10.1126/science.282.5397.2215.

(50) Buchanan, S. K.; Lukacik, P.; Grizot, S.; Ghirlando, R.; Ali, M. M.; Barnard, T. J.; Jakes, K. S.; Kienker, P. K.; Esser, L. Structure of colicin I receptor bound to the R-domain of colicin Ia: implications for protein import. *The EMBO journal* **2007**, *26* (10). DOI: 10.1038/sj.emboj.7601693.

(51) Chimento, D. P.; Kadner, R. J.; Wiener, M. C. Comparative structural analysis of TonB-dependent outer membrane transporters: implications for the transport cycle. *Proteins* **2005**, *59* (2). DOI: 10.1002/prot.20416.

(52) Llamas, M. A.; Bitter, W. Iron gate: the translocation system. *Journal of bacteriology* **2006**, *188* (9). DOI: 10.1128/JB.188.9.3172-3174.2006.

(53) Shultis, D. D.; Purdy, M. D.; Banchs, C. N.; Wiener, M. C. Outer membrane active transport: structure of the BtuB:TonB complex. *Science (New York, N.Y.)* **2006**, *312* (5778). DOI: 10.1126/science.1127694.

(54) Pawelek, P. D.; Croteau, N.; Ng-Thow-Hing, C.; Khursigara, C. M.; Moiseeva, N.; Allaire, M.; Coulton, J. W. Structure of TonB in complex with FhuA, E. coli outer membrane receptor. *Science (New York, N.Y.)* **2006**, *312* (5778). DOI: 10.1126/science.1128057.

(55) Josts, I.; Veith, K.; Tidow, H. Ternary structure of the outer membrane transporter FoxA with resolved signalling domain provides insights into TonB-mediated siderophore uptake. *eLife* **2019**, *8*. DOI: 10.7554/eLife.48528.

(56) Enz, S.; Brand, H.; Orellana, C.; Mahren, S.; Braun, V. Sites of Interaction between the FecA and FecR Signal Transduction Proteins of Ferric Citrate Transport in Escherichia coli K-12. *Journal of Bacteriology* **2003**, *185*, 3745-3752, research-article. DOI: 10.1128/JB.185.13.3745-3752.2003.

(57) Jensen, J. L.; Balbo, A.; Neau, D. B.; Chakravarthy, S.; Zhao, H.; Sinha, S. C.; Colbert, C. L. Mechanistic Implications of the Unique Structural Features and Dimerization of the

Cytoplasmic Domain of the Pseudomonas Sigma Regulator, PupR. *Biochemistry* **2015**, *54*, 5867-5877, research-article. DOI: 10.1021/acs.biochem.5b00826.

(58) Enz, S.; Mahren, S.; Stroeher, U. H.; Braun, V. Surface signaling in ferric citrate transport gene induction: interaction of the FecA, FecR, and FecI regulatory proteins. *Journal of bacteriology* **2000**, *182* (3). DOI: 10.1128/JB.182.3.637-646.2000.

(59) Enz, S.; Mahren, S.; Menzel, C.; Braun, V. Analysis of the ferric citrate transport gene promoter of Escherichia coli. *Journal of bacteriology* **2003**, *185* (7). DOI: 10.1128/JB.185.7.2387-2391.2003.

(60) Merrick, M. J. In a class of its own--the RNA polymerase sigma factor sigma 54 (sigma N). *Molecular microbiology* **1993**, *10* (5). DOI: 10.1111/j.1365-2958.1993.tb00961.x.

(61) Staroń, A.; Sofia, H. J.; Dietrich, S.; Ulrich, L. E.; Liesegang, H.; Mascher, T. The third pillar of bacterial signal transduction: classification of the extracytoplasmic function (ECF) sigma factor protein family. *Molecular microbiology* **2009**, *74* (3). DOI: 10.1111/j.1365-2958.2009.06870.x.

(62) Campbell, E. A.; Greenwell, R.; Anthony, J. R.; Wang, S.; Lim, L.; Das, K.; Sofia, H. J.; Donohue, T. J.; Darst, S. A. A conserved structural module regulates transcriptional responses to diverse stress signals in bacteria. *Molecular cell* **2007**, *27* (5). DOI: 10.1016/j.molcel.2007.07.009.

(63) Greenwell, R.; Nam, T. W.; Donohue, T. J. Features of Rhodobacter sphaeroides ChrR required for stimuli to promote the dissociation of σ(E)/ChrR complexes. *Journal of molecular biology* **2011**, *407* (4). DOI: 10.1016/j.jmb.2011.01.055.

(64) Maillard, A. P.; Girard, E.; Ziani, W.; Petit-Härtlein, I.; Kahn, R.; Covès, J. The crystal structure of the anti-σ factor CnrY in complex with the σ factor CnrH shows a new structural class of anti-σ factors targeting extracytoplasmic function σ factors. *Journal of molecular biology* **2014**, *426* (12). DOI: 10.1016/j.jmb.2014.04.003.

(65) Lonetto, M. A.; Brown, K. L.; Rudd, K. E.; Buttner, M. J. Analysis of the Streptomyces coelicolor sigE gene reveals the existence of a subfamily of eubacterial RNA polymerase sigma factors involved in the regulation of extracytoplasmic functions. *Proceedings of the National Academy of Sciences of the United States of America* **1994**, *91* (16). DOI: 10.1073/pnas.91.16.7573.

(66) Haugen, S. P.; Ross, W.; Gourse, R. L. Advances in bacterial promoter recognition and its control by factors that do not bind DNA. *Nature reviews. Microbiology* **2008**, *6* (7). DOI: 10.1038/nrmicro1912.

(67) Young, B. A.; Anthony, L. C.; Gruber, T. M.; Arthur, T. M.; Heyduk, E.; Lu, C. Z.; Sharp, M. M.; Heyduk, T.; Burgess, R. R.; Gross, C. A. A coiled-coil from the RNA polymerase beta' subunit allosterically induces selective nontemplate strand binding by sigma(70). *Cell* **2001**, *105* (7). DOI: 10.1016/s0092-8674(01)00398-1.

(68) Lonetto, M.; Gribskov, M.; Gross, C. A. The sigma 70 family: sequence conservation and evolutionary relationships. *Journal of bacteriology* **1992**, *174* (12). DOI: 10.1128/jb.174.12.3843-3849.1992.

(69) Ades, S. E.; Connolly, L. E.; Alba, B. M.; Gross, C. A. The Escherichia coli sigma(E)-dependent extracytoplasmic stress response is controlled by the regulated proteolysis of an anti-sigma factor. *Genes & development* **1999**, *13* (18). DOI: 10.1101/gad.13.18.2449.

(70) Campbell, E. A.; Tupy, J. L.; Gruber, T. M.; Wang, S.; Sharp, M. M.; Gross, C. A.; Darst, S. A. Crystal structure of Escherichia coli sigmaE with the cytoplasmic domain of its anti-sigma RseA. *Molecular cell* **2003**, *11* (4). DOI: 10.1016/s1097-2765(03)00148-5.

(71) Newman, J. D.; Anthony, J. R.; Donohue, T. J. The importance of zinc-binding to the function of Rhodobacter sphaeroides ChrR as an anti-sigma factor. *Journal of molecular biology* **2001**, *313* (3). DOI: 10.1006/jmbi.2001.5069.

(72) Mettrick, K. A.; Lamont, I. L. Different roles for anti-sigma factors in siderophore signalling pathways of Pseudomonas aeruginosa. *Molecular microbiology* **2009**, *74* (5). DOI: 10.1111/j.1365-2958.2009.06932.x.

(73) Ochs, M.; Veitinger, S.; Kim, I.; Welz, D.; Angerer, A.; Braun, V. Regulation of citrate-dependent iron transport of Escherichia coli: fecR is required for transcription activation by FecI. *Molecular microbiology* **1995**, *15* (1). DOI: 10.1111/j.1365-2958.1995.tb02226.x.

(74) Koster, M.; van de Vossenberg, J.; Leong, J.; Weisbeek, P. J. Identification and characterization of the pupB gene encoding an inducible ferric-pseudobactin receptor of Pseudomonas putida WCS358. *Molecular microbiology* **1993**, *8* (3). DOI: 10.1111/j.1365-2958.1993.tb01603.x.

(75) Koster, M.; van Klompenburg, W.; Bitter, W.; Leong, J.; Weisbeek, P. Role for the outer membrane ferric siderophore receptor PupB in signal transduction across the bacterial cell envelope. *The EMBO journal* **1994**, *13* (12).

(76) Draper, R. C.; Martin, L. W.; Beare, P. A.; Lamont, I. L. Differential proteolysis of sigma regulators controls cell-surface signalling in Pseudomonas aeruginosa. *Mol Microbiol* **2011**, *82* (6), 1444-1453. DOI: 10.1111/j.1365-2958.2011.07901.x From NLM.

(77) Kim, D. Y.; Kwon, E.; Choi, J.; Hwang, H. Y.; Kim, K. K. Structural basis for the negative regulation of bacterial stress response by RseB. *Protein science : a publication of the Protein Society* **2010**, *19* (6). DOI: 10.1002/pro.393.

(78) Bastiaansen, K. C.; Ibañez, A.; Ramos, J. L.; Bitter, W.; Llamas, M. A. The Prc and RseP proteases control bacterial cell-surface signalling activity. *Environmental microbiology* **2014**, *16* (8). DOI: 10.1111/1462-2920.12371.

(79) Keiler, K. C.; Silber, K. R.; Downard, K. M.; Papayannopoulos, I. A.; Biemann, K.; Sauer, R. T. C-terminal specific protein degradation: activity and substrate specificity of

the Tsp protease. *Protein science : a publication of the Protein Society* **1995**, *4* (8). DOI: 10.1002/pro.5560040808.

(80) Silber, K. R.; Keiler, K. C.; Sauer, R. T. Tsp: a tail-specific protease that selectively degrades proteins with nonpolar C termini. *Proceedings of the National Academy of Sciences of the United States of America* **1992**, *89* (1). DOI: 10.1073/pnas.89.1.295.

(81) Su, M.-Y.; Som, N.; Wu, C.-Y.; Su, S.-C.; Kuo, Y.-T.; Ke, L.-C.; Ho, M.-R.; Tzeng, S.-R.; Teng, C.-H.; Mengin-Lecreulx, D.; et al. Structural basis of adaptor-mediated protein degradation by the tail-specific PDZ-protease Prc. *Nature Communications* **2017**, *8* (1), 1-13, OriginalPaper. DOI: doi:10.1038/s41467-017-01697-9.

(82) Yokoyama, T.; Niinae, T.; Tsumagari, K.; Imami, K.; Ishihama, Y.; Hizukuri, Y.; Akiyama, Y. The Escherichia coli S2P intramembrane protease RseP regulates ferric citrate uptake by cleaving the sigma factor regulator FecR. *The Journal of biological chemistry* **2021**, *296*. DOI: 10.1016/j.jbc.2021.100673.

(83) Stiefel, A.; Mahren, S.; Ochs, M.; Schindler, P. T.; Enz, S.; Braun, V. Control of the ferric citrate transport system of Escherichia coli: mutations in region 2.1 of the FecI extracytoplasmic-function sigma factor suppress mutations in the FecR transmembrane regulatory protein. *Journal of bacteriology* **2001**, *183* (1). DOI: 10.1128/JB.183.1.162-170.2001.

(84) Wriedt, K.; Angerer, A.; Braun, V. Transcriptional regulation from the cell surface: conformational changes in the transmembrane protein FecR lead to altered transcription of the ferric citrate transport genes in Escherichia coli. *Journal of bacteriology* **1995**, *177* (11). DOI: 10.1128/jb.177.11.3320-3322.1995.

(85) Luscher, A.; Moynié, L.; Auguste, P. S.; Bumann, D.; Mazza, L.; Pletzer, D.; Naismith, J. H.; Köhler, T. TonB-Dependent Receptor Repertoire of Pseudomonas aeruginosa for Uptake of Siderophore-Drug Conjugates. *Antimicrobial agents and chemotherapy* **2018**, *62* (6). DOI: 10.1128/AAC.00097-18.

(86) Edgar, R. J.; Xu, X.; Shirley, M.; Konings, A. F.; Martin, L. W.; Ackerley, D. F.; Lamont, I. L. Interactions between an anti-sigma protein and two sigma factors that regulate the pyoverdine signaling pathway in Pseudomonas aeruginosa. *BMC microbiology* **2014**, *14*. DOI: 10.1186/s12866-014-0287-2.

(87) Alba, B. M.; Leeds, J. A.; Onufryk, C.; Zen, Z. L.; Gross, C. A. DegS and YaeL participate sequentially in the cleavage of RseA to activate the ϛE-dependent extracytoplasmic stress response. *Genes and Development* **2002**, *16*, 2156-2168.

(88) Bishop, T. F.; Martin, L. W.; Lamont, I. L. Activation of a Cell Surface Signaling Pathway in Pseudomonas aeruginosa Requires ClpP Protease and New Sigma Factor Synthesis. *Frontiers in microbiology* **2017**, *8*. DOI: 10.3389/fmicb.2017.02442.

(89) Bastiaansen, K. C.; Otero-Asman, J. R.; Luirink, J.; Bitter, W.; Llamas, M. A. Processing of cell-surface signalling anti-sigma factors prior to signal recognition is a conserved

autoproteolytic mechanism that produces two functional domains. *Environmental microbiology* **2015**, *17* (9). DOI: 10.1111/1462-2920.12776.

(90) Bastiaansen, K. C.; Ulsen, P. v.; Wijtmans, M.; Bitter, W.; Llamas, M. A. Self-cleavage of the Pseudomonas aeruginosa cell-surface signaling anti-sigma factor FoxR occurs through an N-O acyl rearrangement. *Journal of Biological Chemistry* **2015**, *290*, 12237-12246.

(91) Sheffield, P.; Garrard, S.; Derewenda, Z. Overcoming expression and purification problems of RhoGDI using a family of "parallel" expression vectors. *Protein expression and purification* **1999**, *15* (1). DOI: 10.1006/prep.1998.1003.

(92) Jensen, J. L.; Wu, Q.; Colbert, C. L. NMR assignments of the N-terminal signaling domain of the TonB-dependent outer membrane transducer PupB. *Biomolecular NMR assignments* **2018**, *12* (1). DOI: 10.1007/s12104-017-9785-0.

(93) Sasse, J.; Gallagher, S. R. Staining proteins in gels. *Current protocols in molecular biology* **2003**, *Chapter 10*. DOI: 10.1002/0471142727.mb1006s63.

(94) Van Duyne, G. D.; Standaert, R. F.; Karplus, P. A.; Schreiber, S. L.; Clardy, J. Atomic structures of the human immunophilin FKBP-12 complexes with FK506 and rapamycin. *Journal of molecular biology* **1993**, *229* (1). DOI: 10.1006/jmbi.1993.1012.

(95) Doublié, S. Preparation of selenomethionyl proteins for phase determination. *Methods in enzymology* **1997**, *276*.

(96) Sreerama, N.; Woody, R. W. Estimation of protein secondary structure from circular dichroism spectra: comparison of CONTIN, SELCON, and CDSSTR methods with an expanded reference set. *Analytical biochemistry* **2000**, *287* (2). DOI: 10.1006/abio.2000.4880.

(97) Scheuermann, T. H.; Stroud, D.; Sleet, C. E.; Bayeh, L.; Shokri, C.; Wang, H.; Caldwell, C. G.; Longgood, J.; MacMillan, J. B.; Bruick, R. K.; et al. Isoform-Selective and Stereoselective Inhibition of Hypoxia Inducible Factor-2. *Journal of medicinal chemistry* **2015**, *58* (15). DOI: 10.1021/acs.jmedchem.5b00529.

(98) Brautigam, C. A. Fitting two- and three-site binding models to isothermal titration calorimetric data. *Methods (San Diego, Calif.)* **2015**, *76*. DOI: 10.1016/j.ymeth.2014.11.018.

(99) Brautigam, C. A.; Zhao, H.; Vargas, C.; Keller, S.; Schuck, P. Integration and global analysis of isothermal titration calorimetry data for studying macromolecular interactions. *Nature protocols* **2016**, *11* (5). DOI: 10.1038/nprot.2016.044.

(100) Zhao, H.; Piszczek, G.; Schuck, P. SEDPHAT--a platform for global ITC analysis and global multi-method analysis of molecular interactions. *Methods (San Diego, Calif.)* **2015**, *76*. DOI: 10.1016/j.ymeth.2014.11.012.

(101) Zhao, H.; Schuck, P. Combining biophysical methods for the analysis of protein complex stoichiometry and affinity in SEDPHAT. *Acta crystallographica. Section D, Biological crystallography* **2015**, *71* (Pt 1). DOI: 10.1107/S1399004714010372.

(102) Houtman, J. C.; Brown, P. H.; Bowden, B.; Yamaguchi, H.; Appella, E.; Samelson, L. E.; Schuck, P. Studying multisite binary and ternary protein interactions by global analysis of isothermal titration calorimetry data in SEDPHAT: application to adaptor protein complexes in cell signaling. *Protein science : a publication of the Protein Society* **2007**, *16* (1). DOI: 10.1110/ps.062558507.

(103) Vonrhein, C.; Flensburg, C.; Keller, P.; Sharff, A.; Smart, O.; Paciorek, W.; Womack, T.; Bricogne, G.; IUCr. Data processing and analysis with the autoPROC toolbox. *Acta Crystallographica Section D: Biological Crystallography* **2011**, *67* (4), 293-302, text. DOI: doi:10.1107/S0907444911007773.

(104) Evans, P. Scaling and assessment of data quality. *Acta crystallographica. Section D, Biological crystallography* **2006**, *62* (Pt 1). DOI: 10.1107/S0907444905036693.

(105) Battye, T. G.; Kontogiannis, L.; Johnson, O.; Powell, H. R.; Leslie, A. G. iMOSFLM: a new graphical interface for diffraction-image processing with MOSFLM. *Acta crystallographica. Section D, Biological crystallography* **2011**, *67* (Pt 4). DOI: 10.1107/S0907444910048675.

(106) Kabsch, W.; IUCr. Integration, scaling, space-group assignment and post-refinement. *Acta Crystallographica Section D: Biological Crystallography* **2010**, *66* (2), 133-144, text. DOI: doi:10.1107/S0907444909047374.

(107) Otwinowski, Z.; Minor, W. Processing of X-ray diffraction data collected in oscillation mode. *Methods in enzymology* **1997**, *276*.

(108) Terwilliger, T. C.; Adams, P. D.; Read, R. J.; McCoy, A. J.; Moriarty, N. W.; Grosse-Kunstleve, R. W.; Afonine, P. V.; Zwart, P. H.; Hung, L. W. Decision-making in structure solution using Bayesian estimates of map quality: the PHENIX AutoSol wizard. *Acta crystallographica. Section D, Biological crystallography* **2009**, *65* (Pt 6). DOI: 10.1107/S0907444909012098.

(109) Terwilliger, T. C.; Grosse-Kunstleve, R. W.; Afonine, P. V.; Moriarty, N. W.; Zwart, P. H.; Hung, L.-W.; Read, R. J.; Adams, P. D.; IUCr. Iterative model building, structure refinement and density modification with the PHENIX AutoBuild wizard. *Acta Crystallographica Section D: Biological Crystallography* **2007**, *64* (1), 61-69, text. DOI: doi:10.1107/S090744490705024X.

(110) Emsley, P.; Cowtan, K. Coot: model-building tools for molecular graphics. *Acta crystallographica. Section D, Biological crystallography* **2004**, *60* (Pt 12 Pt 1). DOI: 10.1107/S0907444904019158.

(111) Adams, P. D.; Afonine, P. V.; Bunkóczi, G.; Chen, V. B.; Davis, I. W.; Echols, N.; Headd, J. J.; Hung, L.-W.; Kapral, G. J.; Grosse-Kunstleve, R. W.; et al. PHENIX: a

comprehensive Python-based system for macromolecular structure solution. *Acta Crystallographica Section D: Biological Crystallography* **2010**, *66* (2), 213-221, text. DOI: doi:10.1107/S0907444909052925.

(112) McCoy, A. J.; Grosse-Kunstleve, R. W.; Adams, P. D.; Winn, M. D.; Storoni, L. C.; Read, R. J. Phaser crystallographic software. *Journal of applied crystallography* **2007**, *40* (Pt 4). DOI: 10.1107/S0021889807021206.

(113) Painter, J.; Merritt, E. A. Optimal description of a protein structure in terms of multiple groups undergoing TLS motion. *Acta crystallographica. Section D, Biological crystallography* **2006**, *62* (Pt 4). DOI: 10.1107/S0907444906005270.

(114) Chen, V. B.; Arendall, W. B.; Headd, J. J.; Keedy, D. A.; Immormino, R. M.; Kapral, G. J.; Murray, L. W.; Richardson, J. S.; Richardson, D. C. MolProbity: all-atom structure validation for macromolecular crystallography. *Acta crystallographica. Section D, Biological crystallography* **2010**, *66* (Pt 1). DOI: 10.1107/S0907444909042073.

(115) Krissinel, E.; Henrick, K. Inference of macromolecular assemblies from crystalline state. *Journal of molecular biology* **2007**, *372* (3). DOI: 10.1016/j.jmb.2007.05.022.

(116) Brünger, A. T.; Adams, P. D.; Clore, G. M.; DeLano, W. L.; Gros, P.; Grosse-Kunstleve, R. W.; Jiang, J. S.; Kuszewski, J.; Nilges, M.; Pannu, N. S.; et al. Crystallography & NMR system: A new software suite for macromolecular structure determination. *Acta crystallographica. Section D, Biological crystallography* **1998**, *54* (Pt 5). DOI: 10.1107/s0907444998003254.

(117) Holm, L. Benchmarking fold detection by DaliLite v.5. *Bioinformatics (Oxford, England)* **2019**, *35* (24). DOI: 10.1093/bioinformatics/btz536.

(118) Franke, D.; Petoukhov, M. V.; Konarev, P. V.; Panjkovich, A.; Tuukkanen, A.; Mertens, H. D. T.; Kikhney, A. G.; Hajizadeh, N. R.; Franklin, J. M.; Jeffries, C. M.; et al. ATSAS 2.8: a comprehensive data analysis suite for small-angle scattering from macromolecular solutions. *Journal of applied crystallography* **2017**, *50* (Pt 4). DOI: 10.1107/S1600576717007786.

(119) Konarev, P. V.; Volkov, V. V.; Sokolova, A. V.; Koch, M. H. J.; Svergun, D. I.; IUCr. PRIMUS: a Windows PC-based system for small-angle scattering data analysis. *Journal of Applied Crystallography* **2003**, *36* (5), 1277-1282, text. DOI: doi:10.1107/S0021889803012779.

(120) Semenyuk, A. V.; Svergun, D. I.; IUCr. GNOM – a program package for small-angle scattering data processing. *Journal of Applied Crystallography* **1991**, *24* (5), 537-540, text. DOI: doi:10.1107/S002188989100081X.

(121) Piiadov, V.; Ares de Araújo, E.; Oliveira Neto, M.; Craievich, A. F.; Polikarpov, I. SAXSMoW 2.0: Online calculator of the molecular weight of proteins in dilute solution from experimental SAXS data measured on a relative scale. *Protein science : a publication of the Protein Society* **2019**, *28* (2). DOI: 10.1002/pro.3528.

(122) Svergun, D.; Barberato, C.; Koch, M. H. J. CRYSOL– a Program to Evaluate X-ray Solution Scattering of Biological Macromolecules from Atomic Coordinates. *Journal of Applied Crystallography* **1995**, *28*, 768-773. DOI: 10.1107/S0021889895007047.

(123) Emekli, U.; Schneidman-Duhovny, D.; Wolfson, H. J.; Nussinov, R.; Haliloglu, T. HingeProt: automated prediction of hinges in protein structures. *Proteins* **2008**, *70* (4). DOI: 10.1002/prot.21613.

(124) Schneidman-Duhovny, D.; Hammel, M.; Tainer, J. A.; Sali, A. FoXS, FoXSDock and MultiFoXS: Single-state and multi-state structural modeling of proteins and their complexes based on SAXS profiles. *Nucleic acids research* **2016**, *44* (W1). DOI: 10.1093/nar/gkw389.

(125) Tria, G.; D. T. Mertens, H.; Kachala, M.; I. Svergun, D. Advanced ensemble modelling of flexible macromolecules using X-ray solution scattering. *IUCrJ* **2015**, *2*, 207-217.

(126) Cole, C.; Barber, J. D.; Barton, G. J. The Jpred 3 secondary structure prediction server. *Nucleic acids research* **2008**, *36* (Web Server issue). DOI: 10.1093/nar/gkn238.

(127) Tusnády, G. E.; Simon, I. The HMMTOP transmembrane topology prediction server. *Bioinformatics (Oxford, England)* **2001**, *17* (9). DOI: 10.1093/bioinformatics/17.9.849.

(128) Schultz, J.; Milpetz, F.; Bork, P.; Ponting, C. P. SMART, a simple modular architecture research tool: identification of signaling domains. *Proceedings of the National Academy of Sciences of the United States of America* **1998**, *95* (11). DOI: 10.1073/pnas.95.11.5857.

(129) Letunic, I.; Doerks, T.; Bork, P. SMART: recent updates, new developments and status in 2015. *Nucleic acids research* **2015**, *43* (Database issue). DOI: 10.1093/nar/gku949.

(130) Ferguson, A. D.; Deisenhofer, J. Metal import through microbial membranes. *Cell* **2004**, *116* (1). DOI: 10.1016/s0092-8674(03)01030-4.

(131) Cobessi, D.; Celia, H.; Folschweiller, N.; Schalk, I. J.; Abdallah, M. A.; Pattus, F. The crystal structure of the pyoverdine outer membrane receptor FpvA from Pseudomonas aeruginosa at 3.6 angstroms resolution. *Journal of Molecular Biology* **2005**, *347* (1), 121-134. DOI: 10.1016/j.jmb.2005.01.021.

(132) Wirth, C.; Meyer-Klaucke, W.; Pattus, F.; Cobessi, D. From the periplasmic signaling domain to the extracellular face of an outer membrane signal transducer of Pseudomonas aeruginosa: crystal structure of the ferric pyoverdine outer membrane receptor. *Journal of molecular biology* **2007**, *368* (2). DOI: 10.1016/j.jmb.2007.02.023.

(133) Härle, C.; Kim, I.; Angerer, A.; Braun, V. Signal transfer through three compartments: transcription initiation of the Escherichia coli ferric citrate transport system from the cell surface. *The EMBO journal* **1995**, *14* (7). DOI: 10.1002/j.1460-2075.1995.tb07129.x.

(134) Beare, P. A.; For, R. J.; Martin, L. W.; Lamont, I. L. Siderophore-mediated cell signalling in Pseudomonas aeruginosa: divergent pathways regulate virulence factor production and siderophore receptor synthesis. *Molecular microbiology* **2003**, *47* (1). DOI: 10.1046/j.1365-2958.2003.03288.x.

(135) Welz, D.; Braun, V. Ferric citrate transport of Escherichia coli: functional regions of the FecR transmembrane regulatory protein. *Journal of bacteriology* **1998**, *180* (9). DOI: 10.1128/JB.180.9.2387-2394.1998.

(136) Braun, V.; Mahren, S.; Ogierman, M. Regulation of the FecI-type ECF sigma factor by transmembrane signalling. *Current opinion in microbiology* **2003**, *6* (2). DOI: 10.1016/s1369-5274(03)00022-5.

(137) Kirby, N.; Cowieson, N.; Hawley, A. M.; Mudie, S. T.; McGillivray, D. J.; Kusel, M.; Samardzic-Boban, V.; Ryan, T. M.; IUCr. Improved radiation dose efficiency in solution SAXS using a sheath flow sample environment. *Acta Crystallographica Section D: Structural Biology* **2016**, *72* (12), 1254-1266, text. DOI: doi:10.1107/S2059798316017174.

(138) Hopkins, J. B.; Gillilan, R. E.; Skou, S. BioXTAS RAW: improvements to a free open-source program for small-angle X-ray scattering data reduction and analysis. *Journal of Applied Crystallography* **2017**, *50* (5), 1545-1553, text. DOI: doi:10.1107/S1600576717011438.

(139) Kozin, M. B.; Svergun, D. Automated matching of high- and low-resolution structural models. *Journal of Applied Crystallography* **2001**, *34*, 33-41.

(140) Franke, D.; Jeffries, C. M.; Svergun, D. I. Correlation Map, a goodness-of-fit test for one-dimensional X-ray scattering spectra. *Nature Methods* **2015**, *12* (5), 419-422, OriginalPaper. DOI: doi:10.1038/nmeth.3358.

(141) Svergun, D. I. Determination of the regularization parameter in indirect-transform methods using perceptual criteria. *Journal of Applied Crystallography* **1992**, *25* (4), 495-503, text. DOI: doi:10.1107/S0021889892001663.

(142) Rambo, R. P.; Tainer, J. A. Accurate assessment of mass, models and resolution by small-angle scattering. *Nature* **2013**, *496* (7446), 477-481, OriginalPaper. DOI: doi:10.1038/nature12070.

(143) Braun, V.; Hartmann, M. D.; Hantke, K. Transcription regulation of iron carrier transport genes by ECF sigma factors through signaling from the cell surface into the cytoplasm. *FEMS microbiology reviews* **2022**. DOI: 10.1093/femsre/fuac010.

(144) Akiyama, Y.; Kanehara, K.; Ito, K. RseP (YaeL), an Escherichia coli RIP protease, cleaves transmembrane sequences. *The EMBO journal* **2004**, *23* (22). DOI: 10.1038/sj.emboj.7600449.

(145) Delgado, C.; Florez, L.; Lollett, I.; Lopez, C.; Kangeyan, S.; Kumari, H.; Stylianou, M.; Smiddy, R. J.; Schneper, L.; Sautter, R. T.; et al. Pseudomonas aeruginosa Regulated Intramembrane Proteolysis: Protease MucP Can Overcome Mutations in the AlgO Periplasmic Protease To Restore Alginate Production in Nonmucoid Revertants. *Journal of Bacteriology* **2018**, *200* (16), 1-16. DOI: 10.1128/JB.00215-18.

(146) Llamas, M. A.; Department of Environmental Protection, E. E. d. Z.-C. S. d. I. C., Granada, Spain; Imperi, F.; Pasteur Institute-Cenci Bolognetti Foundation, D. o. B. a. B., Sapienza University of Rome, Rome, Italy; Visca, P.; Department of Sciences, R. T. U., Rome, Italy; Lamont, I. L.; Department of Biochemistry, U. o. O., Dunedin, New Zealand. Cell-surface signaling in Pseudomonas: stress responses, iron transport, and pathogenicity. *FEMS Microbiology Reviews* **2020**, *38* (4), 569-597. DOI: 10.1111/1574-6976.12078.

(147) Chueh, C.-K.; Som, N.; Ke, L.-C.; Ho, M.-R.; Reddy, M.; Chang, C.-I.; Gottesman, S. Structural Basis for the Differential Regulatory Roles of the PDZ Domain in C-Terminal Processing Proteases. *Molecular Biology and Physiology* **2019**, *10* (4). DOI: 10.1128/mBio.01129-19.

(148) Kabsch, W. XDS. *Acta crystallographica. Section D, Biological crystallography* **2010**, *66* (Pt 2). DOI: 10.1107/S0907444909047337.

(149) Evans, P. R.; Murshudov, G. N. How good are my data and what is the resolution? *Acta crystallographica. Section D, Biological crystallography* **2013**, *69* (Pt 7). DOI: 10.1107/S0907444913000061.

(150) Joosten, R. P.; Long, F.; Murshudov, G. N.; Perrakis, A. The PDB_REDO server for macromolecular structure model optimization. *IUCrJ* **2014**, *1* (Pt 4). DOI: 10.1107/S2052252514009324.

(151) Meisburger, S. P.; Taylor, A. B.; Khan, C. A.; Zhang, S.; Fitzpatrick, P. F.; Ando, N. Domain Movements upon Activation of Phenylalanine Hydroxylase Characterized by Crystallography and Chromatography-Coupled Small-Angle X-ray Scattering. *Journal of American Chemical Society* **2016**, *138*, 6506-6516, research-article. DOI: 10.1021/jacs.6b01563.

(152) Jumper, J.; Evans, R.; Pritzel, A.; Green, T.; Figurnov, M.; Ronneberger, O.; Tunyasuvunakool, K.; Bates, R.; Žídek, A.; Potapenko, A.; et al. Highly accurate protein structure prediction with AlphaFold. *Nature* **2021**, *596* (7873), 583-589, OriginalPaper. DOI: doi:10.1038/s41586-021-03819-2.

(153) Evans, R.; O'Neill, M.; Pritzel, A.; Antropova, N.; Senior, A.; Green, T.; Žídek, A.; Bates, R.; Blackwell, S.; Yim, J.; et al. Protein complex prediction with AlphaFold-Multimer. *bioRxiv* **2021**. DOI: 10.1101/2021.10.04.463034.

(154) Lee, H.-J.; Zheng, J. J. PDZ domains and their binding partners: structure, specificity, and modification. *Cell Communication and Signaling* **2010**, *8* (1), 1-18, ReviewPaper. DOI: doi:10.1186/1478-811X-8-8.

(155) Ernst, A.; Appleton, B. A.; Ivarsson, Y.; Zhang, Y.; Gfeller, D.; Wiesmann, C.; Sidhu, S. S. A structural portrait of the PDZ domain family. *Journal of molecular biology* **2014**, *426* (21). DOI: 10.1016/j.jmb.2014.08.012.

(156) Hsu, H.-C.; Wang, M.; Kovach, A.; Darwin, A. J.; Li, H.; Ehrt, S. Pseudomonas aeruginosa C-Terminal Processing Protease CtpA Assembles into a Hexameric Structure That Requires Activation by a Spiral-Shaped Lipoprotein-Binding Partner. *mBio* **2022**, *13* (1), research-article. DOI: mbio.03680-21.

(157) Mastny, M.; Heuck, A.; Kurzbauer, R.; Heiduk, A.; Boisguerin, P.; Volkmer, R.; Ehrmann, M.; Rodrigues, C. D.; Rudner, D. Z.; Clausen, T. CtpB assembles a gated protease tunnel regulating cell-cell signaling during spore formation in Bacillus subtilis. *Cell* **2013**, *155* (3). DOI: 10.1016/j.cell.2013.09.050.

(158) Liao, D. I.; Qian, J.; Chisholm, D. A.; Jordan, D. B.; Diner, B. A. Crystal structures of the photosystem II D1 C-terminal processing protease. *Nature structural biology* **2000**, *7* (9). DOI: 10.1038/78973.

(159) Pagès, J.-M.; James, C. E.; Winterhalter, M. The porin and the permeating antibiotic: a selective diffusion barrier in Gram-negative bacteria. *Nature Reviews Microbiology* **2008**, *6* (12), 893-903, ReviewPaper. DOI: doi:10.1038/nrmicro1994.

(160) Zeth, K.; Thein, M. Porins in prokaryotes and eukaryotes: common themes and variations. *The Biochemical journal* **2010**, *431* (1). DOI: 10.1042/BJ20100371.

(161) Prajapati, J. D.; Kleinekathöfer, U.; Winterhalter, M. How to Enter a Bacterium: Bacterial Porins and the Permeation of Antibiotics. *Chemical reviews* **2021**, *121* (9). DOI: 10.1021/acs.chemrev.0c01213.

(162) Karla, D.; Krewulak, K. D.; Hans, J.; Vogel, H. J. TonB or not TonB: is that the question? https://doi.org/10.1139/O10-141 **2011**, research-article. DOI: o10-141.

(163) Chang, C.; Mooser, A.; Plückthun, A.; Wlodawer, A. Crystal structure of the dimeric C-terminal domain of TonB reveals a novel fold. *The Journal of biological chemistry* **2001**, *276* (29). DOI: 10.1074/jbc.M102778200.

(164) Peacock, S. R.; Weljie, A. M.; Howard, P. S.; Price, F. D.; Vogel, H. J. The solution structure of the C-terminal domain of TonB and interaction studies with TonB box peptides. *Journal of molecular biology* **2005**, *345* (5). DOI: 10.1016/j.jmb.2004.11.026.

(165) Oeemig, J. S.; Ollila, O. H. S.; Iwaï, H. NMR structure of the C-terminal domain of TonB protein from Pseudomonas aeruginosa. *PeerJ* **2018**, *6*. DOI: 10.7717/peerj.5412.

(166) Madeira, F.; Park, Y. m.; Lee, J.; Buso, N.; Gur, T.; Madhusoodanan, N.; Basutkar, P.; Tivey, A. R. N.; Potter, S. C.; Finn, R. D.; et al. The EMBL-EBI search and sequence analysis tools APIs in 2019. *Nucleic Acids Research* **2019**, *47* (W1). DOI: 10.1093/nar/gkz268.

(167) Robert, X.; Gouet, P. Deciphering key features in protein structures with the new ENDscript server. *Nucleic acids research* **2014**, *42* (Web Server issue). DOI: 10.1093/nar/gku316.

(168) Schneidman-Duhovny, D.; Hammel, M.; Tainer, J. A.; Sali, A. Accurate SAXS profile computation and its assessment by contrast variation experiments. *Biophysical journal* **2013**, *105* (4). DOI: 10.1016/j.bpj.2013.07.020.

(169) Laskowski, R. A.; Jabłońska, J.; Pravda, L.; Vařeková, R. S.; Thornton, J. M. PDBsum: Structural summaries of PDB entries. *Protein science : a publication of the Protein Society* **2018**, *27* (1). DOI: 10.1002/pro.3289.

(170) Freed, D. M.; Lukasik, S. M.; Sikora, A.; Mokdad, A.; Cafiso, D. S. Monomeric TonB and the Ton box are required for the formation of a high-affinity transporter-TonB complex. *Biochemistry* **2013**, *52* (15). DOI: 10.1021/bi3016108.

(171) Navratilova, I.; Sodroski, J.; Myszka, D. G. Solubilization, stabilization, and purification of chemokine receptors using biosensor technology. *Analytical biochemistry* **2005**, *339* (2). DOI: 10.1016/j.ab.2004.12.017.

(172) Wiktor, M.; Hartley, O.; Grzesiek, S. Characterization of structure, dynamics, and detergent interactions of the anti-HIV chemokine variant 5P12-RANTES. *Biophysical journal* **2013**, *105* (11). DOI: 10.1016/j.bpj.2013.10.025.

(173) Ködding, J.; Killig, F.; Polzer, P.; Howard, S. P.; Diederichs, K.; Welte, W. Crystal structure of a 92-residue C-terminal fragment of TonB from Escherichia coli reveals significant conformational changes compared to structures of smaller TonB fragments. *The Journal of biological chemistry* **2005**, *280* (4). DOI: 10.1074/jbc.M411155200.